

# EFFECTS OF PROOF LOADS AND COMBINED MODE LOADINGS ON FRACTURE AND FLAW GROWTH CHARACTERISTICS OF AEROSPACE ALLOYS

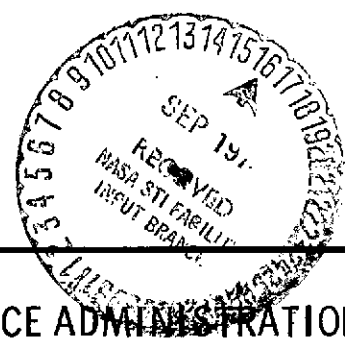
(NASA-CR-134611) EFFECTS OF PROOF LOADS AND COMBINED MODE LOADINGS ON FRACTURE AND FLAW GROWTH CHARACTERISTICS OF AEROSPACE (Boeing Aerospace Co., Seattle, Wash.) 276 p HC \$17.00  
N74-32354  
Unclas 47869  
G3/32

Ramesh C. Shah

**BOEING AEROSPACE** COMPANY

Seattle, Washington

prepared for



NATIONAL AERONAUTICS AND SPACE ADMINISTRATION

NASA Lewis Research Center  
Contract NAS, 3-14346  
Gordon T. Smith - Project Manager

1. Report No. NASA CR-134611	2. Government Accession No.	3. Recipient's Catalog No.	
4. Title and Subtitle Effects of Proof Loads and Combined Mode Loadings on Fracture and Flaw Growth Characteristics of Aerospace Alloys		5. Report Date March 1974	
		6. Performing Organization Code	
7. Author(s) Ramesh C. Shah		8. Performing Organization Report No. D180-17997-1	
		10. Work Unit No.	
9. Performing Organization Name and Address Boeing Aerospace Company Research and Engineering Division Seattle, Washington 98124		11. Contract or Grant No. NAS 3-14346	
		13. Type of Report and Period Covered Contractor Report	
12. Sponsoring Agency Name and Address National Aeronautics and Space Administration Lewis Research Center 2100 Brookpark Road, Cleveland, Ohio 44135		14. Sponsoring Agency Code	
		15. Supplementary Notes Project Manager, Gordon T. Smith Materials and Structures Division NASA Lewis Research Center, Cleveland, Ohio 44135	
16. Abstract			
<p>This experimental program was undertaken to determine the effects of (1) combined tensile and bending loadings, (2) combined tensile and shear loadings, and (3) proof overloads on fracture and flaw growth characteristics of aerospace alloys. Tests were performed on four alloys: 2219-T87 aluminum, 5Al-2.5Sn (ELI) titanium, 6Al-4V <math>\beta</math>STA titanium and high strength 4340 steel. Tests were conducted in room air, gaseous nitrogen at -200F (144K), liquid nitrogen and liquid hydrogen. Flat center cracked and surface flawed specimens, cracked tube specimens, circumferentially notched round bar and surface flawed cylindrical specimens were tested. The three-dimensional photoelastic technique of stress freezing and slicing was used to determine stress intensity factors for surface flawed cylindrical specimens subjected to tension or torsion.</p> <p>Results showed that proof load/temperature histories used in the tests have a small beneficial effect or no effect on subsequent fracture strength and flaw growth rates. For cracks subjected to combined Mode I - II loading, a strong interaction effect was found for the 4340 steel tested at -200F (144K). The empirical relationship <math>K_I + K_{II} \approx K_{IC}</math> or <math>K_I/K_{IC} + K_{II}/K_{IIC} = 1</math> was found to describe the fracture criterion under combined Mode I - II loading. For cracks subjected to combined Mode I - III crack surface deformations, the application of <math>K_{III}</math> up to about 70 percent of <math>K_{IIIcr}</math> has little effect on <math>K_I</math> at which fracture occurs. Similarly, the application of <math>K_I</math> up to about 70 percent of <math>K_{ICr}</math> has little effect on <math>K_{III}</math> at which fracture occurs. The lower bound of the fracture criterion <math>F(K_I, K_{III})</math> can be adequately described by the equation <math>(K_I/K_{ICr})^2 + (K_{III}/K_{IIIcr})^2 = 1</math> for steel, aluminum and titanium.</p>			
17. Key Words (Suggested by Author(s))		18. Distribution Statement	
Fracture Mechanics            Cyclic Life Cracked Specimens            5Al-2.5Sn (ELI) Titanium Combined Tension              6Al-4V $\beta$ STA Titanium and Bending                      2219-T87 Aluminum Combined Mode Loading        4340 Steel		Unclassified, Unlimited	
19. Security Classif. (of this report) Unclassified	20. Security Classif. (of this page) Unclassified	21. No. of Pages 274	22. Price* \$3.00

\* For sale by the National Technical Information Service, Springfield, Virginia 22151

## PREFACE

This report describes an investigation of effects of proof loads and combined mode loadings on fracture and flaw growth characteristics of aerospace alloys performed by Boeing Aerospace Company from August 1970 to November 1973 under Contract NAS 3-14346. The work was administered by Mr. Gordon T. Smith of the NASA Lewis Research Center.

Boeing personnel who participated in the investigation include J. N. Masters, Project Supervisor and R. C. Shah, Principal Investigator. Program support was provided by: A. A. Ottlyk, nonhazardous specimen testing, H. M. Olden, liquid hydrogen testing, Y. F. Cheng, photoelastic testing, and G. C. Buehler, technical illustrations and art work. The author wishes to thank his colleagues, Mr. W. L. Engstrom for his assistance and Drs. L. R. Hall and A. S. Kobayashi for their advice and discussions.

The information released in this report is also released as Boeing Document D180-17997-1.

## TABLE OF CONTENTS

	Page
ABSTRACT	i
SUMMARY	xxi
1.0 INTRODUCTION	1
2.0 BACKGROUND	3
2.1 Stress Intensity Factors for Surface Cracked Specimens in Tension	3
2.2 Relationship of Crack Opening Measurements to Crack Growth Rates for Surface Flaws	4
3.0 MATERIALS AND PROCEDURES	7
3.1 Materials	7
3.2 Procedures	9
4.0 SURFACE FLAWS UNDER COMBINED BENDING AND TENSION STRESSES	13
4.1 Stress Intensity Factors for Surface Cracks Under Combined Tension and Bending	13
4.2 Test Program	14
4.3 Description and Analysis of Results	15
4.3.1 Specimen Calibration	15
4.3.2 Static Fracture Tests Under Combined Bending and Tensile Stresses	16
4.3.3 Static Fracture Tests Under Pure Bending Stresses	17
4.4 Conclusions and Observations	18
5.0 EFFECT OF PROOF TEST TEMPERATURES ON FLAW GROWTH CHARACTERISTICS	21
5.1 Background Information	21
5.2 Analysis	22
5.3 Test Program and Procedures	22
5.3.1 Test Program for 2219-T87 Aluminum	23
5.3.2 Test Program for 6Al-4V $\beta$ STA Titanium	24
5.3.3 Procedures	25
5.4 Description and Analysis of Results	25
5.4.1 2219-T87 Aluminum	25
5.4.2 6Al-4V $\beta$ STA Titanium	28
5.4.2.1 Static Fracture Toughness Tests	28
5.4.2.2 Proof Test Temperature Effects Tests	29

TABLE OF CONTENTS (Cont'd)

	Page
6.0 FRACTURE UNDER COMBINED MODES IN 4340 STEEL	33
6.1 Background and Technical Discussion	33
6.1.1 Crack Tip Stress Fields for Isotropic Elastic Bodies	33
6.1.2 Theories of Fracture Under Combined Mode Loading	35
6.1.2.1 Maximum Stress Criterion	35
6.1.2.2 Strain Energy Density Factor Theory	36
6.1.3 Experimental Work Under Combined Mode Loading	37
6.2 Specimen Configurations and Stress Intensity Factors for Combined Mode Loading Tests	40
6.2.1 Test Specimen Configurations	40
6.2.2 Stress Intensity Factors	40
6.3 Test Program and Procedures	44
6.4 Test Machine and Instrumentation	46
6.5 Test Results and Discussion	47
6.5.1 Fracture Toughness Tests	47
6.5.2 Mode I-II Tests	48
6.5.3 Mode I-III Tests	51
6.5.4 Mode I-II-III Tests with Flat Specimens	52
6.5.5 Mode I-II-III Tests with Round Specimens	53
6.5.6 Fracture Criterion Under Mode I-III	55
6.6 Conclusions	56
7.0 FRACTURE IN COMBINED MODES IN 2219-T87 ALUMINUM AND 6Al-4V $\beta$ STA TITANIUM	57
7.1 Test Program and Procedures	57
7.1.1 Test Program for Static Specimens	57
7.1.2 Test Program for Cyclic Specimens	58
7.1.3 Procedures	58
7.2 Test Results and Discussion	59
7.2.1 Static Fracture Tests of Aluminum	59
7.2.2 Static Fracture Tests of Titanium	61
7.2.3 Cyclic Tests	64

TABLE OF CONTENTS (Cont'd)

	Page	
7.3	Conclusions	66
8.0	EXPERIMENTAL DETERMINATION OF STRESS INTENSITY FACTORS USING PHOTOELASTIC TECHNIQUE	69
8.1	Background for Analysis	69
8.1.1	Three-Dimensional Stress Distribution Near a Blunt Crack	69
8.1.2	Stress Intensity Factors for a Blunt Crack from Isochromatics	71
8.2	Test Program and Experimental Procedures	74
8.2.1	Test Program	74
8.2.2	Experimental Procedures	75
8.3	Results and Discussion	76
8.3.1	Circumferentially Notched Round Bar (Specimen 7)	76
8.3.2	Tension Loaded Surface Flawed Cylindrical Specimens	78
8.3.3	Surface Flawed Cylindrical Specimen in Torsion	80
8.3.3.1	Sliding Mode Stress Intensity Factor, $K_{II}$	80
8.3.3.2	Tearing Mode Stress Intensity Factor, $K_{III}$	82
8.4	Conclusions	83
	REFERENCES	85
	FIGURES	91
	TABLES	195
	APPENDIX A: Photoelastic Data	239
	APPENDIX B: List of Symbols	263

LIST OF FIGURES

Figure No.	Title	Page
2-1	Shape Parameter Curves for Surface Flaws	91
2-2	Estimated Elastic Stress Intensity Magnification Factors at Maximum Crack Depth for Surface Cracks in Tension (Reference 15)	92
3-1	Microstructure for 0.375 in. (9.52 mm) Thick 6Al-4V STA Titanium	93
3-2	Microstructure for 0.375 in. (9.52 mm) Thick 6Al-4V $\beta$ STA Titanium	94
3-3	Microstructure for 1.0 in. (25.4 mm) Thick 6Al-4V $\beta$ STA Titanium	95
3-4	Tensile Specimen for Mechanical Property Measurements	96
3-5	Clip Gage Instrumentation for Large Surface Flaws	97
3-6	Clip Gage Instrumentation for Small Surface Flaws	98
4-1	Estimated Elastic Stress Intensity Magnification Factors for Surface Cracks in Bending (Reference 15 or 22)	99
4-2	Specimen Configuration for Static Fracture Toughness Tests of 5Al-2.5Sn (ELI) Titanium at -320°F (78K)	100
4-3	Specimen Configuration for Combined Bending and Tension Tests of 5Al-2.5 Sn (ELI) Titanium at -320°F (78K)	101
4-4	4 Point Bend Surface Flawed Specimens of 5Al-2.5 Sn (ELI) Titanium for -423°F (20K) Tests	102
4-5	Instrumentation for Calibrations of Combined Bending and Tension Test Specimens	103
4-6	Load-Bending Stress Calibrations for Combined Bending and Tension Specimens	104
4-7	Load-Crack Opening Displacement Curves for Four Point Bend Surface Flawed Specimens at -423°F (20K)	105
5-1	Surface-Flawed 2219-T87 Aluminum Specimens for Ambient Air, LN <sub>2</sub> and LH <sub>2</sub> Testing	106
5-2	Surface-Flawed 6Al-4V $\beta$ STA Titanium Specimen for Ambient Air Testing	107
5-3	Surface-Flawed 6Al-4V $\beta$ STA Titanium Specimen for LN <sub>2</sub> and LH <sub>2</sub> Testing	108
5-4	Surface-Flawed 6Al-4V $\beta$ STA Titanium Specimens for Ambient Air, LN <sub>2</sub> and LH <sub>2</sub> Testing	109
5-5	Load versus Crack Opening Displacement Records for 2219-T87 Aluminum Specimens During Proof Loading at Room Temperature	110

LIST OF FIGURES (Cont'd)

Figure No.	Title	Page
5-6	Load versus Crack Opening Displacement Records for 2219-T87 Aluminum Specimens During Proof Loading at Room Temperature	111
5-7	Load versus Crack Opening Displacement Records for 2219-T87 Aluminum Specimens During Proof Loading at -320°F (78K)	112
5-8	Load versus Crack Opening Displacement Records for 2219-T87 Aluminum Specimens During Proof Loading at -423°F (20K)	113
5-9	Typical Crack Opening Displacement versus Cycles Record for 2219-T87 Aluminum Specimen at Room Temperature	114
5-10	Typical Crack Opening Displacement versus Cycles Record for 2219-T87 Aluminum Specimen at -320°F (78K)	115
5-11	Typical Crack Opening Displacement versus Cycles Record for 2219-T87 Aluminum Specimen at -423°F (20K)	116
5-12	$K_{Ii}/K_{IE}$ Against Cycles to Failure Correlation for 2219-T87 Aluminum at Room Temperature	117
5-13	$K_{Ii}/K_{IE}$ Against Cycles to Failure Correlation for 2219-T87 Aluminum at -320°F (78K)	118
5-14	$K_{Ii}/K_{IE}$ Against Cycles to Failure Correlation for 2219-T87 Aluminum at -423°F (20K)	119
5-15	Load versus Crack Opening Displacement Plots for Surface Flawed Specimens of 6Al-4V $\beta$ STA Titanium Tested at 72°F (295K) and -320°F (78K)	120
5-16	Load versus Crack Opening Displacement Records for 6Al-4V $\beta$ STA Titanium Specimens During Proof Loading and Unloading at 72°F (295K)	121
5-17	Load versus Crack Opening Displacement Records for 6Al-4V $\beta$ STA Titanium Specimens During Proof Loading and Unloading at -320°F (78K)	122
5-18	Load versus Crack Opening Displacement Records for 6Al-4V $\beta$ STA Titanium Specimens During Proof Loading at -423°F (20K)	123
5-19	Typical Crack Opening Displacement versus Cycles Record for 6Al-4V $\beta$ STA Titanium Specimen at Room Temperature	124
5-20	Typical Crack Opening Displacement versus Cycles Record for 6Al-4V $\beta$ STA Titanium Specimen at -320°F (78K)	125



LIST OF FIGURES (Cont'd)

Figure No.	Title	Page
5-21	Typical Crack Opening Displacement versus Cycles Record for 6Al-4V $\beta$ STA Titanium Specimen at $-423^{\circ}\text{F}$ (20K)	126
5-22	Comparisons of Cyclic Flaw Growth Rates for 6Al-4V $\beta$ STA Titanium at Room Temperature With and Without Proof Load Cycles	127
5-23	Comparisons of Cyclic Flaw Growth Rates for 6Al-4V $\beta$ STA Titanium at Room Temperature With and Without Proof Load Cycles	128
5-24	Comparisons of Cyclic Flaw Growth Rates for 6Al-4V $\beta$ STA Titanium at $-320^{\circ}\text{F}$ (78K) With and Without Proof Load Cycles	129
5-25	Comparisons of Cyclic Flaw Growth Rates for 6Al-4V $\beta$ STA Titanium at $-423^{\circ}\text{F}$ (20K) With and Without Proof Load Cycles	130
6-1	Basic Modes of Crack Surface Displacement	131
6-2	Stress Components Near the Crack Tip in Cartesian Coordinates	131
6-3	Stress Components Near the Crack Tip in Cylindrical Coordinates	132
6-4	Cracked Plate Under Uniform Tension	132
6-5	Fracture Angle Versus Crack Angle in a Cracked Plate Under Uniform Tension	133
6-6	Specimens for $\phi$ Degree Inclined Center Cracks for Combined Mode I-II Tests	134
6-7	Through Cracked Tube Specimens for Mode II Tests	135
6-8	Circumferentially Notched Round Bar Specimens for Combined Mode I-III Tests	136
6-9	Specimens for $\phi$ Degree Inclined Surface Flaws for Combined Mode I-II-III Tests	137
6-10	Surface Flawed Cylindrical Specimens for Combined Mode I-II-III Tests	138
6-11	Stress Intensity Factors for Inclined Center Cracked Strips Subjected to Uniaxial Tension Loading	139
6-12	Normalized Stress Intensity Factors for a Tension Plate With Initially Slanted Crack, $\phi = 45$ Degrees (0.79 Rad)	140
6-13	Normalized Stress Intensity Factors for a Tension Plate With Initially Slanted Crack, $\phi = 60$ Degrees	141
6-14	Shell Curvature Correction Factor for a Cracked Tube Subjected to Pure Torsion	142

LIST OF FIGURES (Cont'd)

Figure No.	Title	Page
6-15	Stress Intensities for Circumferentially Cracked Round Bars Subjected to Torsion	143
6-16	Fatigue Crack Grown Under Rotating Bending Fatigue From a Circumferential V-Notch in 4340 Steel	144
6-17	A Round Notched Bar Specimen for Precracking Under Rotating Bending Fatigue	145
6-18	Tension-Torsion Test Machine	146
6-19	Instrumentation for Round Specimens Containing Surface Flaws	147
6-20	Instrumentation for Round Notched Bar Specimens	148
6-21	Surface Flawed and Center Cracked 4340 Steel Specimens for Room Temperature Testing	149
6-22	Load Crack Opening Displacement Records for Surface Flawed Specimens Tested at R.T. and -200°F (144K)	150
6-23	Fracture Surfaces of Inclined Center Cracked Specimens of 4340 Steel Subjected to Combined Modes I and II	151
6-24	$K_I$ versus $K_{II}$ at Fracture for a 4340 Steel Cracked Plate Under Combined Mode I-II Loading at -200°F (144K)	152
6-25	Torque-Angular Deflection Record from Cracked Tube Specimen B of 4340 Steel Subjected to Pure Torsion and Tested at Room Temperature	153
6-26	Fracture Surfaces of Cracked Tube Specimens Subjected to Pure Torsion	154
6-27	$K_I/K_{Icr}$ versus $K_{II}/K_{IIcr}$ for a Cracked Plate Under Combined Mode I-II Loading	155
6-28	Combined Mode I-III Interaction Curve for 4340 Steel at Room Temperature Obtained from Round Notched Bar Specimens	156
6-29	Load-Displacement Records for Round Notched Bar-Specimens Subjected to Tension and Torsion	157
6-30	Fracture Surfaces of Round Notched Bars of 4340 Steel Subjected to Combined Modes I and III	158
6-31	Combined Modes I-III or I-II Interaction for 4340 Steel Specimens Containing Slanted Surface Flaws and Tested at -200°F (144K)	159
6-32	Fracture Surfaces of Inclined Surface Flawed Specimens Subjected to Combined Modes I, II and III	160
6-33	Load-Displacement Records for 4340 Steel Cylindrical Specimens Containing Surface Flaws	161

LIST OF FIGURES (Cont'd)

Figure No.	Title	Page
6-34	Fracture Tests of 4340 Steel Cylindrical Specimens Containing Surface Flaws Subjected to Simultaneous Tension and Torsion	162
6-35	Fracture Surfaces of Surface Flawed Round Specimens of 4340 Steel	163
6-36	$K_I/K_{Icr}$ versus $K_{III}/K_{IIIcr}$ for Round Notched Bar Specimens, Inclined Surface Flawed Flat Specimens and Surface Flawed Round Specimens of 4340 Steel	164
7-1	Surface Flawed Cylindrical Specimen for 2219-T87 Aluminum for Combined Tension and Torsion Tests	165
7-2	Test Program for 2219-T87 Aluminum and 6Al-4V $\beta$ STA Titanium Static Fracture Tests Under Combined Tension and Shear Stresses	166
7-3	Surface Flawed Cylindrical Specimen for 6Al-4V $\beta$ STA Titanium for Combined Tension and Torsion Static Tests	167
7-4	Surface Flawed Cylindrical Specimen for 6Al-4V $\beta$ STA Titanium for Combined Tension and Torsion Cyclic Tests	168
7-5	Load-Displacement Records for 2219-T87 Aluminum Surface Flawed Cylindrical Specimens Subjected to Tension and Torsion	169
7-6	Fracture Tests of 2219-T87 Aluminum Cylindrical Specimens Containing Surface Flaws Subjected to Combined Tension and Torsion	170
7-7	Fracture Tests of 2219-T87 Aluminum Cylindrical Specimens Containing Surface Flaws Subjected to Combined Tension and Torsion	171
7-8	Fracture Tests of 2219-T87 Aluminum Cylindrical Specimens Containing Surface Flaws Subjected to Combined Tension and Torsion	172
7-9	Fracture Surfaces of Surface Flawed Cylindrical Specimens of 2219-T87 Aluminum Subjected to Combined Tension and Torsion (Static Fracture)	173
7-10	$K_I/K_{Icr}$ versus $K_{III}/K_{IIIcr}$ for 2219-T87 Aluminum Cylindrical Specimens Containing Surface Flaws Subjected to Combined Tension and Torsion	174
7-11	Load-Displacement Records for 6Al-4V $\beta$ STA Titanium Surface Flawed Cylindrical Specimens Subjected to Tension and Torsion	175

LIST OF FIGURES (Cont'd)

Figure No.	Title	Page
7-12	Fracture Tests of 6Al-4V $\beta$ STA Titanium Cylindrical Specimens Containing Surface Flaws Subjected to Combined Tension and Torsion	176
7-13	Fracture Tests of 6Al-4V $\beta$ STA Titanium Cylindrical Specimens Containing Surface Flaws Subjected to Combined Tension and Torsion	177
7-14	$K_I/K_{Icr}$ versus $K_{III}/K_{IIIcr}$ for 6Al-4V $\beta$ STA Titanium Cylindrical Specimens Containing Surface Flaws Subjected to Combined Tension and Torsion	178
7-15	Fracture Surfaces of Surface Flawed Cylindrical Specimens of 6Al-4V $\beta$ STA Titanium Subjected to Combined Tension and Torsion (Static Fracture)	179
7-16	Correlation Between Cyclic (Combined Tensile and Shear) Stresses and Cycles to Failure for Surface Flawed Cylindrical Specimens of 2219-T87 Aluminum	180
7-17	Correlation Between Cyclic (Combined Tensile and Shear) Stresses and Cycles to Failure for Surface Flawed Cylindrical Specimens of 6Al-4V $\beta$ STA Titanium	181
7-18	Fracture Surfaces of Surface Flawed Cylindrical Specimens of 2219-T87 Aluminum Subjected to Cyclic Tensile and Torsional Loadings	182
7-19	Fracture Surfaces of Surface Flawed Cylindrical Specimens of 6Al-4V $\beta$ STA Titanium Subjected to Combined Cyclic Tensile and Torsional Loadings	183
8-1	Coordinate System for Stress Field for an Elliptical Notch in an Infinite Plate	184
8-2	Rectangular Stress Components in Plane Normal to Crack Border	184
8-3	Local Coordinate System for a Notch in a Solid	185
8-4	Photoelastic Specimen and Notch Configurations	186
8-5	Notched Photoelastic Specimens in Tension or Torsion Loading in Stress Freezing Oven	187
8-6	Location of Slices for Photoelastic Specimen	188
8-7	Micrographs of Notch Root Radii for Slices in $nz$ Plane of Surface Notched Specimen 1	189
8-8	Measured Fringe Orders for Circumferentially Notched Round Bar (Specimen 7) in Tension	190
8-9	Stress Intensity Factors Calculated for a Circumferentially Notched Round Bar (Specimen 7) Neglecting Effect of Remote Stress Field ( $\rho = 0.002$ in. (0.051 mm))	191

LIST OF FIGURES (Cont'd)

Figure No.	Title	Page
8-10	Stress Intensity Factors Calculated for a Circumferentially Notched Round Bar (Specimen 7) Neglecting Effect of Remote Stress Field ( $\rho = 0.001$ in. (0.025 mm))	192
8-11	Stress Intensity Factors Calculated for a Circumferentially Notched Round Bar (Specimen 7) Neglecting Remote Stress Field ( $\rho = 0.000$ )	193
8-12	Stress Intensity Factors for a Circumferentially Notched Round Bar (Specimen 7) Using Equation (8-12)	194

LIST OF TABLES

Table No.	Title	Page
3-1	Chemical Composition of Materials Tested	195
3-2	Mechanical Properties of Titanium Alloys	196
3-3	Mechanical Properties of 4340 Steel Plate	197
3-4	Mechanical Properties of 2219-T87 Aluminum Plate	198
4-1	Test Program for 5Al-2.5Sn (ELI) Titanium Surface Flawed Specimens Loaded to Fracture in Combined Bending and Tension Stresses at -320°F (78K)	199
4-2	Test Program for 5Al-2.5Sn (ELI) Titanium Surface Flawed Specimens Loaded to Fracture in Pure Bending at -423°F (20K)	200
4-3	Static Fracture Toughness Data for 5Al-2.5Sn (ELI) Titanium at -320°F (78K)	201
4-4	Test Results for 5Al-2.5Sn (ELI) Titanium Surface Flawed Specimens Subjected to Combined Bending and Tension Stresses at -320°F (78K)	202
4-5	Test Results for 5Al-2.5Sn (ELI) Titanium Surface Flawed Specimens Subjected to Pure Bending at -423°F (20K)	203
5-1	Test Program for Proof Test Temperature Effects on 2219-T87 Aluminum	204
5-2	Test Program for Proof Test Temperature Effects on 6Al-4V βSTA Titanium	205
5-3	Proof Test Temperature Effects on Flaw Growth Characteristics of 2219-T87 Aluminum	207
5-4	Fracture Toughness Data for 6Al-4V βSTA Titanium	209
5-5	Proof Test Temperature Effects on Flaw Growth Characteristics of 6Al-4V βSTA Titanium	211
6-1	Test Program for Evaluating Effects of Combined Modes I-II Loading on Fracture in 4340 Steel	213
6-2	Test Program for Evaluating Combined Modes I-III Loading Effects on Fracture in 4340 Steel	214
6-3	Test Program for Evaluating Combined Modes I-II-III Loading Effects on Fracture in 4340 Steel With Surface Flawed Flat Specimens	215
6-4	Test Program for Evaluating Combined Modes I-II-III Loading Effects on Fracture in 4340 Steel With Surface Flawed Round Specimens	216

LIST OF TABLES (Cont'd)

Table No.	Title	Page
6-5	Static Fracture Toughness Test Results for 4340 Steel for Various Crack Propagation Directions	217
6-6	Static Fracture Test Data from Combined Mode I-II Inclined Center Cracked Specimens of 4340 Steel	218
6-7	Fracture Testing of 4340 Steel Hollow Tubes Containing Through Cracks in Pure Torsion	219
6-8	Fracture Data from Combined Mode I-III Tests of Round Notched Bar Specimens of 4340 Steel	220
6-9	Fracture Data from Combined Mode I-II-III Tests of 4340 Steel Flat Specimens Containing Inclined Surface Flaws	221
6-10	Test Results Obtained from Surface Flawed Cylindrical Specimens of 4340 Steel Subjected to Combined Tension and Torsion	222
7-1	Test Program for Static Fracture Specimens at Room Temperature Under Combined Tension and Shear Stresses	223
7-2	Test Program for Cyclic Specimens at Room Temperature Subjected to Combined Tension and Shear Stresses	224
7-3	Results for Fracture Tests of 2219-T87 Aluminum Surface Flawed Cylindrical Specimens Subjected to Combined Tension and Torsion	225
7-4	Results for Fracture Tests of 2219-T87 Aluminum Surface Flawed Cylindrical Specimens Subjected to Combined Tension and Torsion	226
7-5	Results for Fracture Tests of 2219-T87 Aluminum Surface Flawed Cylindrical Specimens Subjected to Combined Tension and Torsion	227
7-6	Fracture Toughness Data of 1.00 in. Thick 6Al-4V $\beta$ STA Titanium	228
7-7	Results for Fracture Tests of 6Al-4V $\beta$ STA Titanium Surface Flawed Cylindrical Specimens Subjected to Combined Tension and Torsion	229
7-8	Results for Fracture Tests of 6Al-4V $\beta$ STA Titanium Surface Flawed Cylindrical Specimens Subjected to Combined Tension and Torsion	230
7-9	Results for Fatigue Tests of 2219-T87 Aluminum Surface Flawed Cylindrical Specimens Subjected to Combined Tension and Torsion Loadings	231
7-10	Results for Fatigue Tests of 6Al-4V $\beta$ STA Titanium Surface Flawed Cylindrical Specimens Subjected to Combined Tension and Torsion Loadings	233

LIST OF TABLES (Cont'd)

Table No.	Title	Page
8-1	Notch Dimensions and Applied Loading for Photoelastic Test Specimens	235
8-2	Stress Intensity Factors $K_I$ at Various Locations of Surface Flaws in Cylindrical Specimens Subjected to Tension from Photoelastic Tests	236
8-3	Stress Intensity Factors $K_{II}$ at Various Locations of Surface Flaws in Cylindrical Specimens Subjected to Torsion from Photoelastic Tests	237



## SUMMARY

This experimental program is one in a series of research programs undertaken by the National Aeronautics and Space Administration to develop methods and data needed for design against fracture in structural components. This experimental and analytical program was directed to determine the effects of (1) combined tensile and bending loadings, (2) combined tensile and shear loadings, and (3) proof overloads on fracture and flaw growth characteristics of aerospace alloys. Tests were performed on four alloys used for aerospace pressure vessels: 2219-T87 aluminum, 5Al-2.5Sn (ELI) titanium, 6Al-4V BSTA titanium and high strength 4340 steel. Twenty surface flawed specimens of 5Al-2.5Sn (ELI) titanium were tested in liquid nitrogen or liquid hydrogen environment to determine the effects of combined tension and bending stresses or pure bending stresses on fracture.

Sixty surface flawed specimens of 2219-T87 aluminum and 6Al-4V BSTA titanium alloys were tested to determine proof test temperature effects on subsequent fracture strength and flaw growth characteristics. These static fracture and fatigue tests were conducted in room air, liquid nitrogen and liquid hydrogen environments.

Eight inclined center cracked flat specimens and two cracked tube specimens of 4340 steel were tested to determine the fracture criterion under combined Modes I and II loadings. Ten circumferentially notched round specimens of 4340 steel were tested to determine the fracture criterion under combined Modes I and III loading. Ten inclined surface flawed flat specimens loaded in tension and sixty-six surface flawed cylindrical specimens of steel, aluminum and titanium subjected to combined tension and torsion were loaded to failure to investigate the fracture criterion under combined Modes, I, II and III loading. Thirty-six surface flawed cylindrical specimens were subjected to simultaneous cyclic tensile and torsional loadings to determine cyclic flaw growth characteristics in the presence of  $K_I$ ,  $K_{II}$  and  $K_{III}$ . These tests were conducted in room air or in gaseous nitrogen environment at  $-200^{\circ}\text{F}$  (144K).

Surface notched photoelastic specimens were tested in pure tension or torsion loading to determine stress intensity factors around the notch periphery.

Results of combined tension and bending stresses showed that good estimates of failure loads can be made for structures containing surface flaws subjected to combined tension and bending stresses.

Results of proof-test-temperatures showed that proof load/temperature histories used in the tests have a small beneficial effect or no effect on subsequent fracture strength and flaw growth rates.

The empirical relationship  $K_I + K_{III} \approx K_{IC}$  or  $K_I/K_{IC} + K_{III}/K_{IIIc} = 1$  adequately represents the fracture criterion under combined Mode I-II loading for 4340 steel at  $-200^\circ\text{F}$  (144K). For cracks subjected to combined Mode I-III or I-II-III crack surface deformations, the application of  $K_{III}$  up to about 70 percent of  $K_{IIIcr}$  has little effect on  $K_I$  at which fracture occurs. Similarly, the application of  $K_I$  up to about 70 percent of  $K_{Icr}$  has little effect on  $K_{III}$  at which fracture occurs. The lower bound of the fracture criterion  $F(K_I, K_{III})$  can be adequately described by a single quadratic equation of  $K_I/K_{Icr}$  and  $K_{III}/K_{IIIcr}$  for steel, aluminum and titanium.

Cyclic lives for surface flawed cylindrical specimens subjected to combined tension and torsion can be predicted from the cyclic lives of the surface flawed specimens subjected to pure tension and the static fracture criterion for the same flaw-specimen configuration under combined tension and torsion.

Results of photoelastic tests showed that for crack geometries tested, for tension loaded surface flawed cylindrical specimens  $K_I$  is maximum at the maximum flaw depth and minimum at the intersection of the flaw periphery and the specimen boundary. Values of  $K_I$  can be calculated with the stress intensity factor solutions of a surface flaw in a plate or a single edge crack in a plate within 15 percent. For torsion loaded surface flawed cylindrical specimens,  $K_{II}$  is minimum at the maximum flaw depth and is maximum at the intersection of the flaw periphery and the specimen boundary. Values of  $K_{II}$  at the former location is approximately 5 percent of  $K_{II}$  at the later location. An equation was developed to calculate  $K_{II}$  at the intersection of the flaw periphery and specimen boundary within an accuracy of about 10 percent for these specimen-flaw configurations.

## 1.0 INTRODUCTION

Structural components and pressure vessels for space shuttle and space vehicle systems may contain crack-like defects due to material processing or fabrication procedures. Experience has shown that such defects can provide origins for brittle fracture either during initial pressurization or after limited service use. Fracture control methods for high strength metallic pressure vessels<sup>(1)</sup> have been developed to ensure that crack-like defects will not grow during service use to a size sufficiently large to impair performance. These methods require knowledge of the fracture toughness and subcritical crack growth characteristics of the constituent materials. Data obtained from tests of surface flawed specimens have proven to be the most useful for fracture control of spacecraft and booster structure. Surface flaws are commonly found in aerospace hardware and are subjected to plane strain crack tip deformations. Since plane strain deformations result in minimum resistance to both brittle fracture and stress corrosion cracking, surface flawed specimens are a severe but realistic mode of potential failure origins in aerospace hardware.

The application of fracture mechanics concepts to selection of materials, operating stress levels, appropriate inspection criteria, and definition of safe operational procedures for aerospace pressure vessels has been the subject of several NASA programs<sup>(2-8)</sup>. A significant body of data on the mechanical properties, fracture toughness, and subcritical flaw growth characteristics for selection of operating and proof test stress levels have been obtained from these programs. The previous programs have generally emphasized testing surface flawed specimens under uniform tension stress fields. However, potential fracture origins are often subjected to combined tensile and bending stress fields, pure bending stress fields and combined tensile and shear stress fields. Fracture criteria under static loading and flaw extension data under cycling loading for these situations are not available and are needed to assist initial design decisions. In the past, proof testing of pressure vessels has been conducted frequently at a relatively higher temperature, such as room ambient temperature, prior to proof testing at a cryogenic temperature. However, the effects on flaw extension characteristics of proof testing at a room ambient temperature prior to proof testing at a cryogenic temperature still need to be evaluated.

This experimental and analytical program was undertaken to investigate the effects of (1) combined tensile and bending loadings, (2) combined tensile and shear loadings, and (3) proof overloads on the flaw growth characteristics of crack-like defects under conditions of plane strain. Tests were performed on four alloys used for aerospace pressure vessels: 2219-T87 aluminum, 5Al-2.5Sn (ELI) titanium, 6Al-4V  $\beta$ STA titanium, and 4340 steel ( $\sigma_{ys} = 210$  ksi (1448 MN/m<sup>2</sup>)). 5Al-2.5Sn (ELI) titanium surface flawed specimens were tested at -320°F (78K) to determine the effects of combined tension and bending stresses and at -423°F (20K) to determine the effects of pure bending stresses. Flat specimens containing center cracks or surface flaws and cylindrical specimens containing circumferential cracks or surface flaws of 4340 steel were tested at -200°F (144K) in a gaseous nitrogen environment and at 72°F (295K) under ambient conditions to study the effects of combined tension and shear. Surface flawed cylindrical specimens of 2219-T87 aluminum and 6Al-4V  $\beta$ STA titanium alloys subjected to combined tension and shear loadings were tested under ambient conditions to determine failure criterion and cyclic flaw growth characteristics. An experimental stress analysis to determine the stress intensity factors of surface flaws in cylindrical specimens under tension or torsion loading was conducted using three-dimensional photoelasticity. Surface flawed specimens of 2219-T87 aluminum and 6Al-4V  $\beta$ STA titanium alloys were tested to investigate proof test temperature effects.

Section 2 gives the technical background for semi-elliptical surface flaws in plates subjected to tension. Description of materials and experimental procedures common to Sections 4, 5, 6 and 7 are included in Section 3. Technical background and experimental procedures pertinent only to a particular series of tests is included in the section where the tests are described. Experimental results and interpretation of results are presented in Sections 4 through 8.

## 2.0 BACKGROUND

The concept of the stress intensity factor employed in fracture mechanics is used to evaluate the experimental results in this report. The part through surface crack represents a common failure origin in many metallic aerospace structures. Surface cracked specimens were tested to develop data for use in life predictions, failure analyses, and fracture prevention of metallic structures. The background information for the expression of stress intensity factors for a semi-elliptical surface crack is given in the following paragraphs. This background information is given only for surface cracked specimens subjected to tensile loading. Tests of this kind of specimen are described in Sections 4, 5 and 6. The expressions for the stress intensity factors and the background information for other crack geometries and loading conditions are described in respective discussion sections.

### 2.1 STRESS INTENSITY FACTORS FOR SURFACE CRACKED SPECIMENS IN TENSION

Irwin<sup>(9)</sup> derived an approximate expression for the stress intensity factor for a surface (semi-elliptical) cracked specimen subjected to uniform tension. This derivation was based on a solution of an elliptical crack in an infinite solid<sup>(10)</sup> and on a solution of an edge-cracked semi-infinite solid<sup>(11)</sup>. The stress intensity factor at the maximum crack depth (point A in Figure 2-1) of the semi-elliptical crack was given as

$$K_I = 1.1 \sigma \sqrt{\frac{\pi a}{Q}} \quad (2-1)$$

where

$$Q = [E(k)]^2 - 0.212 (\sigma/\sigma_{ys})^2$$

$\sigma$  = applied uniform uniaxial gross tensile stress

$\sigma_{ys}$  = yield strength of the material

$E(k)$  = complete elliptical integral of the second kind  
associated with  $k^2 = 1 - a^2/c^2$

$$= \int_0^{\pi/2} \sqrt{1 - k^2 \sin^2 \theta} d\theta$$

$a$  = maximum crack depth

$2c$  = crack length

The above expression for the stress intensity factor was estimated to be applicable for flaw depth to specimen thickness ( $a/t$ ) ratios and flaw depth to length ratios ( $a/2c$ ) less than 0.5. A number of approximate solutions for the stress intensity factor at the maximum depth for surface flaws deeper than 50 percent of the plate thickness have been proposed by many investigators<sup>(5,12-18)</sup>. Of all these solutions, mathematically more rigorous solutions<sup>(15,16)</sup> are all based on the alternating technique suggested by Kantorovich and Krylov<sup>(19)</sup>. Approximate solutions for the stress intensity factor of a semi-elliptical surface flaw in a plate are given in Reference 15 based on the alternating method with an elliptical crack in an infinite solid. Approximate solutions for the stress intensity factor of a part-circular surface flaw in a plate are given in Reference 16 based on the alternating method with a circular crack in an infinite solid. Other approximate solutions for surface flaws are based on model analysis and empirical techniques<sup>(12-14,17)</sup>, finite element analysis<sup>(18)</sup> and experimental results<sup>(5)</sup>. In all these solutions, the stress intensity factor  $K_I$  at the maximum crack depth of a surface flaw in a plate can be expressed by the following equation

$$K_I = M_K \sigma \sqrt{\frac{\pi a}{Q}} \quad (2-2)$$

where  $M_K$  is a stress intensity magnification factor incorporating the effects of the stress free front and back surfaces. The stress intensity magnification factors  $M_K$  based on the numerical analysis of Shah and Kobayashi<sup>(15)</sup>, and the empirical analysis of Masters et al<sup>(5)</sup> agree well with experimental data for a wide range of crack depth to length ratios  $a/2c$  and crack depth to specimen thickness ratios,  $a/t$ . Stress intensity magnification factors,  $M_K$ , given by Reference 15 are available and applicable over a wider range of  $a/2c$  and  $a/t$  ratios. Hence, this solution is used in this report for the evaluation of surface flaw data from tension tests.

Figure 2-1 is a plot of  $Q$  as a function of  $a/2c$ . Figure 2-2 shows stress intensity magnification factors  $M_K$ <sup>(15)</sup> as a function of  $a/t$  and  $a/2c$ .

## 2.2 RELATIONSHIP OF CRACK OPENING MEASUREMENTS TO CRACK GROWTH RATES FOR SURFACE FLAWS

An expression for the crack opening displacement for a completely embedded elliptical crack in an infinite solid subjected to a uniform tensile stress  $\sigma$ , is given in Reference 10. The maximum crack opening displacement,  $\delta$ , occurs at the diametral center of the crack and is given by the following equation

$$\delta = \frac{4(1-\nu^2)}{E} \frac{\sigma a}{E(k)} \quad (2-3)$$

where  $\nu$  and  $E$  are Poisson's ratio and Young's modulus for the material. Although, an exact expression is not available for the crack opening displacement for a semi-elliptical surface flaw, such displacements should also be proportional to  $\sigma$ ,  $a$  and  $E(k)$  for elastic materials. By following Irwin's procedure <sup>(9)</sup> to account for the effect of plastic yielding, the flaw opening displacement for a surface flaw can be approximated by

$$\delta = C \frac{\sigma a}{\sqrt{Q}} \quad (2-4)$$

where the factor  $C$  is a function of the material properties, and the ratios of crack depth to plate thickness,  $a/t$ , and crack depth to crack length,  $a/2c$ . Similar to  $M_k$  in Figure 2-2, factor  $C$  is also affected by the proximities of two stress free surfaces located near a surface flaw in a plate. Thus, the value of  $C$  gradually increases as the flaw depth,  $a$ , increases for a given  $a/2c$  and thickness. This result is also confirmed in the experimental test results of Reference 20.

The value of  $C$  can be determined at test initiation and final (termination) conditions from knowledge of the stress level, initial and final flaw sizes, and the corresponding flaw opening displacements from equation (2-4), as follows

$$C_i = \frac{\delta_i \sqrt{Q_i}}{\sigma a_i} \quad (2-5)$$

$$C_f = \frac{\delta_f \sqrt{Q_f}}{\sigma a_f} \quad (2-6)$$

Subscripts i and f denote initial and final conditions respectively. In order to relate any intermediate value of  $a/\sqrt{Q}$  with  $\delta$  ( or cycles N), C has to be known. Flaw depth and shape changes gradually in a specimen. It was shown in Reference 20 that the C can be assumed to vary linearly between its initial and final values.

In order to determine  $\delta$  or N for a selected flaw depth a, Q needs to be determined. This requires a relationship between flaw depth a and flaw length 2c. Since the relationship between a and 2c is known at initial and final conditions and the flaw shape changes gradually, it is assumed that 2c varies linearly with a, as given by the following equation.

$$\frac{2c - 2c_i}{2c_f - 2c_i} = \frac{a - a_i}{a_f - a_i} \quad (2-7)$$

The flaw shape parameter Q can now be determined as a function of flaw depth a, and, in turn,  $\delta$  can be related to crack depth using equation (2-4). The number of cycles, N, corresponding to each selected flaw depth value, a, can be determined from the test record and, consequently, the change in N for each increment of flaw depth is known. The crack growth rate  $da/dN$  can then be calculated.



### 3.0 MATERIALS AND PROCEDURES

#### 3.1 MATERIALS

A 5Al-2.5Sn (ELI) titanium plate, 0.80 by 36 by 60 in. (20.3 by 914.4 by 1524.0 mm) was obtained in the mill annealed condition per MIL-T-9046E. Ingot composition provided by the vendor is listed in Table 3-1. This plate was from the same heat-batch as that used in Reference 6 tests. As noted in Reference 6, the plate was partially annealed at mid thickness. The plate was annealed at 1550°F (1117K) for 16 hours prior to machining test specimens. Mechanical properties of the alloy at -320°F (78K) and -423°F (20K) are listed in Table 3-2. Surface flawed specimens used to evaluate the effects of pure bending, and combined bending and tension stresses (as described in Section 4) were fabricated from this plate.

6Al-4V titanium plates, 0.375 by 24.0 by 72.0 in. (9.5 by 609.6 by 1828.8 mm) and 1.0 by 24.0 by 36.0 in. (25.4 by 609.6 by 914.4 mm) were purchased in the annealed condition per MIL-T-9046F, Type III, composition C. These plates were solution treated and aged (STA) per BAC 5613 Condition III specifications which are as follows:

Solution Treat	1725°F(1214K)	15 to 25 minutes	Water Quench
Age	1000°F(811K)	4 to 5 hours	Air Cool

Mechanical properties for 0.375 in. (9.5 mm) thick 6Al-4V (STA) titanium plate are given in Table 3.2. As seen from Table 3.2, there is a considerable spread in the strength (yield or ultimate) values of longitudinal and transverse directions. Also, the ultimate strength in the longitudinal direction is considerably higher than that normally encountered for the material. Microstructural examination (Figure 3-1) revealed that the material had a preferentially oriented and a banded microstructure making it behave anisotropically. The microstructural examination also revealed that the rolling direction was not parallel to the length of the plate (72.0 in. (1828.8 mm) side). Instead, it was parallel to the width (24.0 in. (609.6 mm) side). A basal plane 002 pole figure as determined by a computerized X-ray analysis technique <sup>(21)</sup> showed that the STA material had a high anisotropy index.

Beta anneal treatments (1900°F (1311K) for 25 minutes and air cool) were given to these plates to reduce the anisotropy index and to yield a random microstructure. The plates were then solution treated and aged (STA) per BAC 5613, Condition III specifications, as mentioned before. The mechanical properties of 0.375 (9.5 mm) and 1.0 in. (25.4 mm) thick  $\beta$ STA plates are given in Table 3-2. Table 3-2 shows that mechanical properties in longitudinal and transverse directions for  $\beta$ STA plates are essentially identical. Basal plane pole figures determined for  $\beta$ STA plates showed a low anisotropy index. Microstructures for 0.375 in. (9.5 mm) and 1.0 in. (25.4 mm) thick  $\beta$ STA titanium are shown in Figures 3-2 and 3-3, respectively. These microstructures exhibit large equiaxed prior beta grains with a fine  $\alpha/\beta$  platelet structure. Surface flawed specimens tested to investigate effects of proof test temperature and pressure cycles on subsequent fracture strength and cyclic life of pressure vessels (as described in Section 5) were fabricated from the 0.375 in. (9.5 mm) thick  $\beta$ STA titanium plate. Surface flawed cylindrical specimens tested to determine a failure criterion and cyclic flaw growth characteristics under combined tension and torsion (as described in Section 6) were machined from the 1.0 in. (25.4 mm) thick  $\beta$ STA titanium plate.

A 4340 steel plate, 1.0 by 20.0 by 72.0 in. (25.4 by 508.0 by 1828.8 mm), normalized and tempered to a Rockwell C hardness of 33 maximum was purchased according to AMS 6359 specifications. Chemical composition provided by the vendor is listed in Table 3-1. Specimens tested to investigate combined mode (Modes I, II and III) fracture were fabricated from this plate (as described in Section 6). EDM flaws were introduced in the specimens. The specimens were then subjected to heat treatment according to BAC 5617 specifications so that the ultimate strength was 260-280 ksi (1793-1931 MN/m<sup>2</sup>) at room temperature. BAC 5617 specifications are given below.

Austenitize	1550°F (1117K) 30 to 90 minutes depending on specimen thickness
Oil Quench	140°F (333K) maximum
Double Temper	400°F (478K) 3 to 4 hours, depending on specimen thickness.

Mechanical properties of the heat-treated alloy are given in Table 3-3.

2219-aluminum plates, 1.0 by 36.0 by 84 in. (25.4 by 914.4 by 2133.6 mm) and 2.5 by 48.0 by 48.0 in. (63.5 by 1219.2 by 1219.2 mm) were obtained in the T87 condition per BMS 7-1050 (equivalent to MIL-A-8920 ASG) specifications. Specified limits on chemical composition are listed in Table 3-1. The

plates were from the same heat-batch as that tested in Reference 6.

Mechanical properties of these plates are given in Table 3-4. Surface flawed aluminum specimens tested to investigate effects of proof test temperature and pressure cycles on subsequent fracture strength and flaw growth characteristics (as described in Section 5) were machined from 1.0 in. (25.4 mm) thick plate. Surface flawed cylindrical aluminum specimens tested to determine a failure criterion and cyclic flaw growth characteristics under combined tension and torsion were fabricated from 2.5 in. (63.5 mm) thick plate.

### 3.2 PROCEDURES

Experimental procedures used throughout the test program are described in this section. Procedures applicable to a given series of tests only are reported in the section describing those tests.

All test specimens were precracked by growing fatigue cracks from starter slots under low stress tension fatigue loadings. Starter slots with dimensions slightly less than the required final flaw dimensions were introduced using an electrical discharge machine (EDM). The EDM slots were then extended under low stress tension fatigue. The maximum cyclic stress levels used on specimens of different materials are given below:

5Al-2.5Sn (ELI) Titanium specimens	20 to 35 ksi (138 to 241 MN/m <sup>2</sup> )
4340 steel specimens	20 to 35 ksi (138 to 241 MN/m <sup>2</sup> )
2219-T87 aluminum cylindrical specimens	8 to 10 ksi (55 to 69 MN/m <sup>2</sup> )
2219-T87 aluminum flat specimens	12 ksi (83 MN/m <sup>2</sup> )
6Al-4V βSTA flat specimens	40 ksi (276 MN/m <sup>2</sup> )
6Al-4V βSTA cylindrical specimens	25 to 31.5 ksi (172 to 217 MN/m <sup>2</sup> )

Crack surfaces were perpendicular to the rolling direction for the 5Al-2.5 Sn (ELI) and 6Al-4V βSTA titanium specimens and parallel to the rolling direction for the 2219-T87 aluminum alloy specimens.

Tests at  $-423^{\circ}\text{F}$  (20K) were conducted with specimens completely submerged in liquid hydrogen within an enclosed cryostat. The liquid level was monitored by means of liquid level sensors. After the liquid reached the desired level, specimens were soaked for 15 minutes to stabilize test conditions. Maximum cyclic loads applied during the first loading cycle were controlled by means of a hand-operated valve. To avoid overloads, the initially applied maximum load was limited to 90 percent of the required maximum load. Minor load adjustments were made during subsequent cycles to raise the load to the required value. The specified load level was always reached within three to five cycles.

Tests at  $-320^{\circ}\text{F}$  (78K) were conducted by submerging test specimens in liquid nitrogen. Titanium alloy specimens and aluminum alloy specimens less than 16 in. (406.4mm) in length were completely submerged within a closed cryostat. Aluminum alloy specimens greater than 16 in. (406.4mm) in length were submerged only in the gage area using a wrap-around cryostat. Thermocouple temperature measurements showed that the gage areas were maintained at  $-320^{\circ}\text{F}$  (78K).

Prior to the installation of the cyclic test specimens, a dummy specimen was used to adjust cyclic loads to the required values. The test specimen was then substituted for the dummy specimen, cooled to  $-320^{\circ}\text{F}$  (78K), soaked for 15 minutes, and tested. Due to the prior load adjustment, the required maximum cyclic load was applied on the very first loading cycle.

Tests at  $-200^{\circ}\text{F}$  (144K) were conducted by exposing test specimens to a gaseous nitrogen environment in a closed cryostat. The temperature of  $-200^{\circ}\text{F}$  (144K) was maintained in the cryostat by controlling the supply of gaseous nitrogen and liquid nitrogen. A thermocouple mounted on the specimen near the flaw was used to determine the specimen temperature. Loading was commenced 10 to 15 minutes after the specimen had reached a temperature of  $-200^{\circ}\text{F}$  (144K).

Mechanical properties were determined by testing specimens with uniform gage areas as shown in Figure 3-4. All mechanical property specimens were instrumented with a 2.0 in. (50.8mm) gage length extensometer. Mechanical property tests were conducted using a strain rate of 0.0005 per minute until the material yield strength was exceeded; the strain rate was then increased to 0.02 per minute until failure. The loading rates for each static fracture specimen

were such that failure resulted at about one minute after initial load application. All cyclic loading profiles were sinusoidal with a cyclic frequency of 20 cpm (0.33 Hz) at 72°F (295K) and -320°F (78K), and 3 cpm (0.05 Hz) at -423°F (20K).

Most surface flawed flat specimens were instrumented with a crack opening displacement (COD) clip gage to provide a continuous record of COD versus applied load for static tests and COD versus applied cycles for cyclic tests. When flaws were of sufficient size, the clip gage was mounted in the flaw as shown in Figure 3-5. For the smaller flaws, COD brackets were microspot welded on the surface of the specimen as shown in Figure 3-6. COD recordings were used both to calculate crack growth rates and as a basis for terminating tests just prior to failure. Normally, a cyclic test could be terminated within a few cycles of specimen failure by observing the COD output.

#### 4.0 SURFACE FLAWS UNDER COMBINED BENDING AND TENSION STRESSES

Potential flaw locations in aerospace hardware such as weld lands are often subjected to combined bending and tension stresses. Critical flaw size and minimum cyclic life for these conditions can be estimated if a fracture criterion and a solution for the stress intensity factor are known. Very limited experimental data has been generated to investigate effects of combined bending and tension stresses on fracture and fatigue growth of surface flaws<sup>(6)</sup>. Under a NASA program<sup>(6)</sup>, this data was generated from 2219-T87 aluminum and 5Al-2.5Sn (ELI) titanium base metal specimens with simulated weld land build up. The specimens were tested under uniform tension stresses and all static fracture tests were performed at -320°F (78K) in liquid nitrogen. The following describes the experimental program designed to further explore and evaluate effects of the combined bending and tension stresses, and pure bending stresses on fracture criterion of surface flaws. Material selected for the tests is 5Al-2.5Sn (ELI) titanium which is from the same plate as the one tested in the previous program<sup>(6)</sup>.

#### 4.1 STRESS INTENSITY FACTORS FOR SURFACE CRACKS UNDER COMBINED TENSION AND BENDING

Stress intensity factors for a semi-elliptical surface crack in a plate subjected to extensional (tensile) and bending stresses are calculated by the following expression

$$K_I = K_{I_t} + K_{I_b} \quad (4-1)$$

where

$K_I$  = stress intensity factor due to combined extensional and bending loading

$K_{I_t}$  = stress intensity factor due to extensional (tensile) loading only

$K_{I_b}$  = stress intensity factor due to pure bending only.

The stress intensity solution for surface cracks at the maximum depth due to uniform tensile (extensional) loading is discussed in Section 2 (Equation 2-2).

Three approximate solutions are available to calculate the stress intensity factor at the tip (maximum crack depth) of a semi-elliptical surface flaw in a plate subjected to pure bending<sup>(13,15,17,22)</sup>. The stress intensity factor due to pure bending,  $K_{Ib}$ , at the maximum crack depth is expressed in the following form

$$K_{Ib} = M_B \sigma_B \sqrt{\frac{\pi a}{Q}} \quad (4-2)$$

where  $M_B$  is the parameter for the stress intensity factor which is a function of the crack depth to length ratio,  $a/2c$  and the crack depth to specimen thickness ratio,  $a/t$ .  $\sigma_B$  is the maximum bending stress at the outer fibers of the specimen. Approximate  $M_B$  values in Reference 13 were estimated for various values of  $a/2c$  and  $a/t$  ( $a/t \leq 0.5$ ) ratios from the solutions of an edge cracked plate ( $a/2c = 0$ ) subjected to pure bending<sup>(23)</sup> and a semicircular surface flaw ( $a/2c = 0.5$ ) in a thick plate subjected to pure bending<sup>(24)</sup>.  $M_B$  values in References 15 and 22 were obtained from the superposition of the solution of a surface crack in a plate in tension and the solution of an elliptical crack approaching the free surface of a semi-infinite solid and subjected to linearly varying pressure.  $M_B$  values were obtained for various  $a/2c$  ratios and  $a/t$  values up to 0.9. The other approximate solution for a surface crack in bending<sup>(17)</sup> was obtained from the line-spring model. The solution given in References 15 and 22 for  $M_B$  is available and applicable over a wider range of  $a/t$  values and it also seems to be more accurate than other solutions as indicated by three-dimensional photoelastic experiments<sup>(25)</sup>. Hence, this solution was used for evaluation of the test results. The relationship of  $M_B$  with respect to  $a/t$  and  $a/2c$  is given in Figure 4-1.

Two approximate solutions are available to calculate the stress intensity factor at the maximum crack length (point C in Figure 4-1) of surface flaws in a plate subjected to pure bending<sup>(13,26)</sup>. At present, there is no solution available to calculate the stress intensity factor at any intermediate point on the flaw periphery between points A and C in Figure 4-1.

#### 4.2 TEST PROGRAM

Effects of combined bending and tensile stresses on surface flaws were experimentally evaluated on 5Al-2.5Sn (ELI) titanium according to the test

program outlined in Table 4-1. Test specimen configurations are illustrated in Figure 4-2 for  $e = 0$  and in Figure 4-3 for  $e \neq 0$  where  $e$  is the offset of the center section of the specimen with respect to the end section of the specimen, as shown in Figure 4-3. The surface flaws in all these specimens had an  $a/2c$  ratio of approximately 0.25. The specimens with  $e = 0$  were tested for two  $a/t$  ratios of approximately 0.3 and 0.4 under uniform tensile stresses. These uniform thickness specimens were tested to determine the static fracture toughness of the material using flaws nearly identical to those tested under combined bending and tension stresses. Specimens with  $e \approx 0.045$  in. (1.14 mm) and  $e \approx 0.090$  in. (2.29 mm) were tested for two  $a/t$  ratios of approximately 0.3 and 0.5 under applied tensile loadings. All these static fracture tests were conducted at  $-320^{\circ}\text{F}$  (78K) in a liquid nitrogen environment.

Effects of pure bending stresses on the fracture criterion of surface flaws were experimentally studied on 5Al-2.5Sn (ELI) titanium according to the test program outlined in Table 4-2. The test specimen configuration is shown in Figure 4-4. The tests were conducted under four point bending, as shown in Figure 4-4, to obtain a uniform bending moment over the test section of the specimen. The surface flaws in all these specimens had an  $a/2c$  ratio of approximately 0.25. The specimens were tested at four different  $a/t$  ratios of approximately 0.2, 0.3, 0.4 and 0.5. All these static fracture tests were performed at  $-423^{\circ}\text{F}$  (20K) in liquid hydrogen environment.

#### 4.3 DESCRIPTION AND ANALYSIS OF RESULTS

##### 4.3.1 Specimen Calibration

The load-bending stress behavior of the test specimen shown in Figure 4-3 is nonlinear. Therefore it was necessary to generate experimental load versus bending stress calibration curves. These curves were established for two different values of offset,  $e = 0.04$  in. (1.03 mm) and  $e = 0.090$  in. (2.29 mm) by testing unflawed specimens instrumented with four pairs of back-to-back strain gages located at the specimen centerline as illustrated in Figure 4-5. Each specimen was incrementally loaded at  $-320^{\circ}\text{F}$  (78K) in applied stress steps of 25 ksi and strain readings were taken after the addition of each load increment. In both specimens, the measured strains were quite uniform across the specimen width at all load levels. Average tensile strain and average bending strain across the specimen width were determined for each particular



applied load. (If  $\epsilon_1$  and  $\epsilon_2$  are the average strains across the width of the specimen on the surfaces 1 and 2 in Figure 4-5, then the average tensile strain across the specimen section is  $(\epsilon_1 + \epsilon_2)/2$  and the average bending strain across the width at the surface 1 is  $(\epsilon_1 - \epsilon_2)/2$ .) The bending stress for this applied load was then calculated by the following expression.

$$\text{Bending stress} = \text{Applied stress} \times \frac{\text{Average bending strain}}{\text{Average tensile strain}}$$

The resultant load versus bending stress curves are plotted in Figure 4-6. The bending stress in a flawed specimen at fracture was determined from these calibration curves.

#### 4.3.2 Static Fracture Tests under Combined Bending and Tensile Stresses

Results of fracture tests, conducted to determine the fracture toughness  $K_{IE}$  of 5Al-2.5Sn (ELI) titanium at  $-320^\circ\text{F}$  (78K), are summarized in Table 4-3. The average value of the fracture toughness,  $K_{IE}$ , is  $84.0 \text{ ksi}\sqrt{\text{in}}$  ( $92.3 \text{ MN/m}^{3/2}$ ). Fracture surfaces of all four specimens were very flat near the periphery of the surface flaw.  $K_{IE}$  was calculated according to equation (2-2) given in Section 2.

Fracture tests results of the eight surface flawed specimens subjected to combined tension and bending stresses are given in Table 4-4. These specimens (Figure 4-3) were loaded to failure in tension loading in a liquid nitrogen environment. The fracture surfaces were flat around the flaw periphery in these specimens also. The critical stress intensity factor at failure (fracture toughness)  $K_{cr}$  was calculated according to equation (4-1), (4-2) and (2-2). Maximum bending stresses  $\sigma_B$  at the outer fibers at failure were estimated for the failure load and the offset  $e$  by interpolation or extrapolation of the plots of bending stress versus applied load given in Figure 4-6. The resultant values of  $\sigma_B$  are given in Table 4-4. Results of Table 4-4 show that the calculated value of  $K_{cr}$  varies from  $74.4$  to  $96.2 \text{ ksi}\sqrt{\text{in}}$  ( $81.8$  to  $105.8 \text{ MN/m}^{3/2}$ ), compared to a range in fracture toughness  $K_{IE}$  of  $81.0$  to  $89.5 \text{ ksi}\sqrt{\text{in}}$  ( $94.7 \text{ MN/m}^{3/2}$ ) in Table 4-3. The average value of  $K_{cr}$  is  $86.1 \text{ ksi}\sqrt{\text{in}}$  ( $94.7 \text{ MN/m}^{3/2}$ ) and compares well with the average value of  $K_{IE}$  of  $84.0 \text{ ksi}\sqrt{\text{in}}$  ( $92.3 \text{ MN/m}^{3/2}$ ).

The lowest and the highest value of  $K_{cr}$  in Table 4-4 differ only 12 percent from the average value of  $K_{IE}$ . From these results, it can be deduced that good estimates of critical flaw sizes can be made from  $K_{IE}$ , the tensile stress  $\sigma_T$  and the bending stress,  $\sigma_B$  when  $\sigma_B$  is small compared to  $\sigma_T$ . Conversely, good estimates of failure loads can be made for structures containing surface flaws subjected to combined bending and tension stresses when  $K_{IE}$ , flaw size and the relationship between  $\sigma_B$  and  $\sigma_T$  is known. These conclusions are the same as those in Reference 6.

Examination of the results of  $K_{cr}$  with bending stress  $\sigma_B$  and  $a/t$  in Table 4-4 indicates that neither high nor low values of  $K_{cr}$  are directly connected with either high or low values of  $\sigma_B$  or  $a/t$  ratios. Hence, from this limited data it is concluded that this slightly higher range in  $K_{cr}$  values in combined tension and bending tests is due to scatter in the data and cannot be explicitly attributed to approximations in the stress intensity solution.

#### 4.3.3 Static Fracture Tests under Pure Bending Stress

Results of fracture tests of the eight surface flawed specimens subjected to pure bending stresses are summarized in Table 4-5. Fracture surfaces for all eight specimens were flat. Specimens 2TPBH-1 and 2TPBH-2 were instrumented with a clip gage to measure the crack opening displacement. Load versus crack opening displacement records for these two specimens are shown in Figure 4-7. These records show that considerable crack growth occurred prior to fracture. However, the 5 percent secant offset load  $P_5$  as defined in Reference 27 for both of these specimens was approximately 91 percent of the failure load,  $P_F$ . Hence, the critical stress intensity factor  $K_{cr}$  calculated based on the fracture load is less than 10 percent higher than  $K$  calculated based on the load  $P_5$ . Since the other six specimens of Table 4-5 were not instrumented, the  $K_{cr}$  values in Table 4-5 are calculated based on fracture loads to maintain uniformity in data reporting. The ratio of specimen width to flaw length  $W/2c$ , for the last two specimens, 2TPBH-7 and 2TPBH-8, in Table 4-5 was somewhat low at about 2.4. The resulting effect of proximities of the stress free surfaces in the width direction would be to reduce the measured value of stress intensity factor<sup>(16)</sup>. Hence, results of these two data points are ignored.

As mentioned in Section 4-1,  $K_{cr}$  values are calculated at point A (maximum crack depth) as shown in Figure 4-1. Examination of results in Table 4-5 reveals that as the ratio  $a/t$  increases from 0.2 to 0.4, the calculated  $K_{cr}$  drops from 85.6 to 73.6  $\text{ksi}\sqrt{\text{in}}$  (94.1 to 80.9  $\text{MN}/\text{m}^{3/2}$ ). This behavior can be explained as follows.

For a surface flawed specimen subjected to pure bending, the maximum stress intensity factor is not necessarily at the maximum crack depth. Location of the maximum stress intensity factor depends upon the  $a/t$  and  $a/2c$  ratios. If the  $a/2c$  ratio is close to 0.5, the maximum stress intensity factor for pure bending occurs near point C at the surface in Figure 4-1. However, plane stress conditions exist at this point and the applied  $K$  must approach the plane stress fracture toughness for the fracture to originate there. The plane stress fracture toughness is substantially higher than the plane strain fracture toughness and hence, the fracture probably originates at a point on the crack periphery somewhere between points C and A. For a surface flawed specimen with  $a/2c \approx 0.25$ , the maximum stress intensity factor occurs at the maximum crack depth (Point A in Figure 4-1) for small  $a/t$  ratios. However, as the  $a/t$  ratio increases, the location of the maximum stress intensity factor would move from point A towards point C on the periphery in Figure 4-1. In Table 4-5, the stress intensity factor,  $K_{cr}$ , is calculated only at the maximum crack depth (point A) and, as expected, the calculated  $K_{cr}$  values decrease with increasing values of  $a/t$ .

#### 4.4 CONCLUSIONS AND OBSERVATIONS

Limited data developed for surface flaws subjected to combined bending and tension stresses for small ratios of bending stress to tension stress ( $\sigma_B/\sigma_T \leq 1/3$ ) shows that  $K_{cr}$  calculated with equations (4-1), (4-2) and (2-2) compares quite well with the fracture toughness  $K_{IE}$ . Data developed in this program and a previous program<sup>(6)</sup> indicate that good estimates of failure loads can be made for structures containing surface flaws subjected to combined bending and tension stresses when the bending stress is small compared to the tension stress. Conversely, good estimates of critical flaw sizes for structures can also be determined for given applied stresses.

Limited results of surface flawed tests under pure bending show that as the ratio  $a/t$  increases from 0.2 to 0.4, the calculated  $K_{cr}$  at point A (maximum crack depth) decreases from 85.6 to 73.6  $\text{ksi}\sqrt{\text{in}}$  (94.1 to 80.9  $\text{MN}/\text{m}^{3/2}$ ). It is concluded that the location of maximum plane strain stress intensity factor and fracture initiation probably moves increasingly away from the point of maximum crack depth with increasing values of  $a/t$ . This possibility could not be quantitatively evaluated due to the lack of stress intensity solution for locations on the crack periphery other than the maximum crack depth.

## 5.0 EFFECT OF PROOF TEST TEMPERATURES ON FLAW GROWTH CHARACTERISTICS

Proof testing of pressure vessels has been conducted frequently at room ambient temperature, prior to proof testing at a cryogenic temperature. Examples of such proof testing are Saturn S-II liquid hydrogen tank, Mariner Mars 1971 Propulsion System Tanks, and the Apollo Lunar Module Descent Propellant Tanks. However, the effects of this test sequence on the flaw growth characteristics has not been investigated. The following describes an experimental program designed to evaluate the effects of proof testing at a higher temperature prior to proof testing at a cryogenic temperature on subsequent plane strain fracture strength and flaw growth characteristics. 2219-T87 aluminum and 6Al-4V BETA titanium materials are used for the investigation.

### 5.1 BACKGROUND INFORMATION

It is a normal practice to perform a proof test on a pressure vessel at a temperature at or near the expected operating temperature of the vessel. It has been pointed out that a successful proof test to a pressure  $(\alpha)X$  (the maximum operating pressure) indicates that the maximum possible  $K_{II}/K_{IC}$  at the maximum operating pressure is equal to  $1/\alpha$ , if flaw growth occurring during the proof test cycle is negligible<sup>(1, 28)</sup>. ( $K_{II}$  is the stress intensity factor based on initial conditions and the maximum operating pressure.) This value of  $K_{II}/K_{IC}$  can then be used in conjunction with subcritical flaw growth data to estimate the minimum life of the vessel.

If the proof test is performed at a temperature different from the operating temperature, the required minimum proof test factor is dependent upon the maximum allowable  $K_{II}/K_{IC}$  value at operating temperature, and the variation in  $K_{IC}$  of parent metal and welds with temperature<sup>(1)</sup>. For cryogenic vessels made from materials which exhibit either a constant or increasing fracture toughness with decreasing temperature, a room temperature proof test can be designed to assure successful operation. The major advantage of this approach is reduced cost of proof testing. An example of such testing practice is the Saturn S-1C liquid oxygen tank. For vessels made from materials which exhibit a decrease in fracture toughness with decreasing temperature, proof testing may

be undertaken at a temperature lower than the operating temperature. The advantage of testing at a temperature at which the  $K_{IC}$  is lower than at operating temperature is that either a lower proof test factor can be used, or a longer operation life can be assured. The primary disadvantage is a possibly higher risk of proof test failure. Examples of this proof testing procedure are the Mariner Mars 1971 Propulsion System Tanks, and the Apollo LM descent propellant tanks. These titanium vessels were subjected to a service temperature of about 70 to 100°F (294 to 311K). The proof test was conducted in liquid nitrogen at -320°F (78K). In each case, the cryogenic pressure cycle was preceded by a lower stress room temperature pressure cycle. Very little work has been done to define the effects of this prior load cycle. References (29) and (30) involved studies of flaw growth in titanium which can occur during the proof cycle, but little data is available on the effects of the proof cycle on subsequent life. References (31) and (32) report the results of experimental work performed on 2014 aluminum weldments applicable to Saturn S-II liquid hydrogen proof test requirements. This vessel, designed for -423°F (20K) operation, received an ambient proof cycle followed by a -423°F (20K) proof cycle. Test specimens<sup>(31)</sup> showed that addition of the room temperature pre-stress resulted in a higher failure stress at -423°F (20K).

## 5.2 ANALYSIS

Stress intensity factors for the surface flaws were calculated according to equation 2-2 using stress intensity magnification factors obtained in Reference 15.

Cyclic flaw growth rates,  $da/dN$ , for the surface flawed specimens were determined from the instantaneous values of crack opening displacements according to the procedure described in Section 2-2.

## 5.3 TEST PROGRAM AND PROCEDURES

An experimental program was undertaken to investigate the effects of proof test temperatures on fracture strength and flaw growth characteristics of pressure vessels fabricated from 2219-T87 aluminum and 6Al-4V  $\beta$ STA titanium alloys. Test programs and procedure for studying the effects of proof test temperatures on 2219-T87 aluminum and 6Al-4V  $\beta$ STA titanium are discussed

separately in the following two subsections.

### 5.3.1 Test Program for 2219-T87 Aluminum

Test program for the surface flawed specimens of 2219-T87 aluminum is shown in Table 5-1. Test program in Table 5-1 investigates the effects on fracture strength and flaw growth characteristics caused by proof loading at room temperature prior to proof loading at a cryogenic temperature. The test program provides a direct evaluation and comparison of these effects with those of direct proof loading at the cryogenic temperature or at the room temperature, as applicable. Fracture toughness at different temperatures for a plate of the same heat, thickness, and rolling batch were obtained in a previous program<sup>(6)</sup>. Fracture toughness,  $K_{IE}$ , for the material in the TS crack propagation direction in the environments of ambient room temperature at 72°F (295K), liquid nitrogen at -320°F (78K), and liquid hydrogen at -423°F (20K) are 41.9, 43.0 and 45.0 ksi√in (45.1, 47.3 and 49.5 MN/m<sup>3/2</sup>), respectively. The specimen was designed such that both flaw depth  $a$ , and uncracked ligament  $t-a$  are greater than the plane strain plastic zone size. Surface flaws in all specimens had a flaw depth to length ratio of  $a/2c \approx 0.25$ , and a flaw depth to specimen thickness ratio of  $a/t \approx 0.35$ . The proof stress at room temperature was selected as 85 percent of the tensile yield strength. The flaw size was selected such that the stress intensity factor at proof stress is approximately 90 percent of the fracture toughness at room temperature. Based on the above considerations, the flaw depth  $a$ , length  $2c$  and the specimen thickness,  $t$ , were selected as 0.21, 0.84 and 0.60 in. (5.3, 21.3 and 15.2 mm), respectively. The specimen configuration used is shown in Figure 5-1.

Proof stresses at -320°F (78K) and -423°F (20K) were selected such that the stress intensity factor at the proof stress was 90 percent of the fracture toughness,  $K_{IE}$ , at the corresponding temperature. Selected proof stresses  $P_1$  at room temperature,  $P_2$  at -320°F (78K) and  $P_3$  at -423°F (20K) in Table 5-1 are 47.6, 58.0, and 55.0 ksi (328.2, 399.9 and 379.2 MN/m<sup>2</sup>), respectively.

As seen from Table 5-1, for each combination of proof operational sequences investigated, three specimens were tested. Specimens were first proof loaded to the indicated proof stress level at the shown proof test temperature or temperatures. One of the specimens was then statically fractured to assess

the effect of prior proof test temperatures on the fracture strength. The remaining two specimens were cycled to failure using two different peak cyclic stress levels. Operational peak cyclic stress levels were selected from the previous results of  $K_{II}/K_{IE}$  versus cycles to failure data<sup>(8)</sup> so that the cyclic life of the specimens was greater than 400 cycles (minimum cyclic life required for space shuttle orbiter pressure vessels). Operational cyclic stress levels  $C_1$  and  $C_2$  at room temperature,  $C_3$  and  $C_4$  at  $-320^\circ\text{F}$  (78K) and  $C_5$  and  $C_6$  at  $-423^\circ\text{F}$  (20K) in Table 5-1 are 40.6, 44.0, 42.6, 46.4, 46.8 and 51.0 ksi (279.9, 303.4, 293.7, 319.9, 322.7, 351.6  $\text{MN}/\text{m}^2$ ), respectively.

### 5.3.2 Test Program for 6Al-4V $\beta$ STA Titanium

Prior to conducting the test program to investigate the effects of proof test temperatures, a few tests were conducted to determine fracture toughness of 6Al-4V  $\beta$ STA titanium at  $72^\circ\text{F}$  (295K),  $-320^\circ\text{F}$  (78K) and  $-423^\circ\text{F}$  (20K) in the LS propagation direction. Two specimens were tested at each of these temperatures. Specimens contained semi-elliptical surface flaws with the ratios  $a/2c \approx 0.25$  and  $a/t < 0.50$ . Specimen configuration is shown in Figure 5-2 for  $72^\circ\text{F}$  (295K) tests and in Figure 5-3 for  $-320^\circ\text{F}$  (78K) and  $-423^\circ\text{F}$  (20K) tests.

The test program for investigating effects of proof test temperatures on fracture strength and flaw growth characteristics in 6Al-4V  $\beta$ STA titanium is summarized in Table 5-2. Test specimens contained semi-elliptical surface flaws with  $a \approx 0.02$  in. (0.51 mm),  $a/t \approx 0.1$  and  $a/2c \approx 0.20$ . Specimen configuration is shown in Figure 5-4. Flaw depth  $a$  was greater than the plane strain plastic zone size for  $-320^\circ\text{F}$  (78K) and  $-423^\circ\text{F}$  (20K). Uncracked ligament  $t-a$  was greater than the plane strain plastic zone size for all temperatures. Proof stress at room temperature was selected as 90 percent of the tensile yield strength. For the other two temperatures, proof stress was selected such that the stress intensity factor at proof stress was approximately 90 percent of the fracture toughness  $K_{IE}$  at the corresponding temperature. Selected proof stresses  $P1$  at  $72^\circ\text{F}$  (295K),  $P2$  at  $-320^\circ\text{F}$  (78K) and  $P3$  at  $-423^\circ\text{F}$  (20K) are 141, 180 and 165 ksi (972.2, 1241.1, 1137.7  $\text{MN}/\text{m}^2$ ), respectively. These proof stresses are typical of proof stresses used in proof tests of Apollo pressure vessels made from 6Al-4V titanium. Peak cyclic stress levels  $C_1$  and  $C_2$  at room



temperature,  $C_3$  and  $C_4$  at  $-320^{\circ}\text{F}$  (78K) and  $C_5$  and  $C_6$  at  $-423^{\circ}\text{F}$  (20K) in Table 5-2 are 125, 110, 159, 138, 138 and 119 ksi (861.9, 758.4, 1096.3, 951.5, 951.5 and 820.5  $\text{MN}/\text{m}^2$ ), respectively.

The test series in the first part of Table 5-2 was designed to obtain baseline cyclic flaw growth rate data (without a proof load cycle) for each of two peak cyclic stress levels at all three temperatures.

The test series in the second part of Table 5-2 was designed to investigate the effects of prior proof loads at room temperature or at room temperature and cryogenic temperature on subsequent fracture strength at cryogenic temperature.

The test series in the remaining portion of Table 5-3 was designed to investigate the effects of proof tests at cryogenic temperature or at room temperature and cryogenic temperature on subsequent cyclic flaw growth rate at operating temperature. When combined with the first portion of the test program, these latter tests provide a direct comparison between basic flaw growth rates, flaw growth rates with a prior cryogenic proof load and flaw growth rates with prior room and cryogenic temperature proof loads.

### 5.3.3 Procedures

Materials and general test procedures are described in Section 3. All specimens of aluminum and titanium were instrumented with a crack opening displacement (COD) clip gage to provide a continuous record of COD versus applied load for proof tests and static fracture tests or of COD versus number of cycles applied for cyclic tests. All cyclic profiles ranged from zero to maximum applied stress and were sinusoidal. Cyclic frequencies were 20 cpm (0.33 Hz) at  $72^{\circ}\text{F}$  (295K) and  $-320^{\circ}\text{F}$  (78K) and 3 cpm (0.05 Hz) at  $-423^{\circ}\text{F}$  (20K).

## 5.4 DESCRIPTION AND ANALYSIS OF RESULTS

### 5.4.1 2219-T87 Aluminum

Test results and specimen details for 2219-T87 aluminum alloy surface flawed specimens are summarized in Table 5-3. Crack propagation direction for these tests was TS. Figures 5-5 and 5-6 contain the plots of COD versus applied load for surface flawed specimens subjected to proof loads at room temperature.

Figures 5-7 and 5-8 show the plots of COD versus applied load for specimens subjected to proof loads at  $-320^{\circ}\text{F}$  (78K) and  $-423^{\circ}\text{F}$  (20K), respectively. Most of these plots show some nonlinear behavior between COD and load starting at approximately 70 percent of maximum applied load. The nonlinear behavior indicates that either flaw growth or plastic yielding or both occurred during loading. As mentioned in Section 5.3.1, the gross applied stress at proof is approximately 80 to 90 percent of tensile yield strength at the corresponding temperature. Plastic yielding must have occurred around the flaw periphery for each specimen. Examination of fractured specimens and fractographs showed that during the proof load cycles at  $-320^{\circ}\text{F}$  (78K) in  $\text{LN}_2$  environment or at  $-423^{\circ}\text{F}$  (20K) in  $\text{LH}_2$  environment, the flaw grew in the depth direction from 0.002 in. (0.051 mm) to 0.010 in. (0.254 mm). No growth occurred in the length direction. Fractographs and fractured surfaces also showed that when a proof cycle was applied to the flawed specimen at room temperature or when the flawed specimen was pulled to failure at room temperature, delamination near the tip (maximum crack depth) of the flaw occurred. The height of the delamination with respect to the flaw plane in these specimens was less than 0.1 in. (2.54 mm).

Specimens 6A-1 and 6A-7 were subjected to proof loads at  $-320^{\circ}\text{F}$  (78K) and  $-423^{\circ}\text{F}$  (20K), respectively prior to loading them to failure at room temperature. Specimens 6A-4 and 6A-10 were proof loaded at room temperature prior to proof loading at  $-320^{\circ}\text{F}$  (78K) or  $-423^{\circ}\text{F}$  (20K). These two specimens were then loaded to failure. Table 5-3 shows that the fracture strength for all four specimens is the same within one percent. Specimen 6A-19 was proof loaded at room temperature and then was pulled to failure at  $-423^{\circ}\text{F}$  (20K). Specimen 6A-22 was proof loaded at room temperature and at  $-423^{\circ}\text{F}$  (20K) and then was pulled to failure at  $-423^{\circ}\text{F}$  (20K). Fracture strength for both these specimens is the same within 0.5 percent. Above results indicate that the fracture strength was unaffected by the proof load histories used in these tests.

Typical plots of COD versus number of cycles are shown in Figures 5-9, 5-10 and 5-11 for room temperature,  $-320^{\circ}\text{F}$  (78K) and  $-423^{\circ}\text{F}$  (20K), respectively. Fracture surfaces showed that the specimens cycled to failure at room temperature had delaminations near the maximum crack depth. The height of delamination with respect to the flaw plane in these specimens was from 0.25 in.

(6.35 mm) to 0.80 in. (20.32 mm). Proof loading, pulling to failure or cycling to failure at  $-320^{\circ}\text{F}$  (78K) or  $-423^{\circ}\text{F}$  (20K) did not cause delaminations to occur. As indicated in Table 5-3, every specimen subjected to cyclic loading had delaminations near the maximum crack depth either due to proof loading at room temperature or due to cycles applied at room temperature. Thus, it was not possible to calculate the flaw growth rates.

The test program did not include any specimens to measure static fracture toughness of the material or cyclic life determination without application of prior proof load cycles. Thus, for the evaluation of the effects of proof load histories, basic data obtained in the previous programs for the same crack propagation direction (TS) in References 2, 6 and 8 had to be used. An extra specimen 6A-18 was tested to measure fracture toughness of the material at  $-423^{\circ}\text{F}$  (20K) in liquid hydrogen environment. As shown in Table 5-3, the fracture toughness  $K_{IE}$  determined from this specimen was  $49.6 \text{ ksi}\sqrt{\text{in}}$  ( $54.5 \text{ MN}/\text{m}^{3/2}$ ). For the material of the same thickness, heat and rolling batch but a different plate in Reference 6, fracture toughness values in environments of room air,  $\text{LN}_2$  and  $\text{LH}_2$  were  $41.0, 43.0, 45.0 \text{ ksi}\sqrt{\text{in}}$  ( $45.1, 47.3, 49.5 \text{ MN}/\text{m}^{3/2}$ ), respectively. For a plate of 2219-T87 aluminum of a different heat and rolling batch tested in Reference 8, the average  $K_{IE}$  values from static tests for 0.4 in. thick specimens (as calculated by equation (2-2)) in environments of room air,  $\text{LN}_2$  and  $\text{LH}_2$  were  $40.8, 42.0$  and  $42.0 \text{ ksi}\sqrt{\text{in}}$  ( $44.9, 46.2, 46.2 \text{ MN}/\text{m}^{3/2}$ ), respectively. The comparison shows that fracture toughness of the material at room temperature compares very well with the previously cited two programs (6,8). However, for  $\text{LN}_2$  and  $\text{LH}_2$  testing, fracture toughness values are higher than reported before (6,8). Another noticeable effect observed in the plate tested here was delamination at room temperature testing. The material tested in Reference 8 did not delaminate at room temperature static or cyclic testing even though the cyclic stress levels used in that program were comparable to the room temperature proof stress level of the present tests.

Figure 5-12 shows a comparison of present room temperature data with previous data (2,8) obtained without prior proof load applications on the basis of  $K_{II}/K_{IE}$  versus cycles to failure. As mentioned before, data of Reference 8 and the present data have nearly the same fracture toughness at room temperature. The data obtained in Reference 8 was at a maximum cyclic stress level equivalent to 90 percent of  $\sigma_{ys}$  as compared to 73 to 79 percent of  $\sigma_{ys}$  in the present

program. From the comparison in Figure 5-12, the cyclic life of a flawed specimen given a proof overload cycle prior to cyclic testing is anywhere from approximately 4 to 10 times that where no proof overload cycle is applied<sup>(8)</sup>. The cyclic stress level differences between these two sets of data would account for only small differences in cyclic life. It is known that the occurrence of delamination near the flaw periphery increases the cyclic life substantially<sup>(2,3,4)</sup>. Hence, the improvement in cyclic life is due to the effects of proof overload cycles and/or delaminations. However, the effect of each parameter cannot be separated since no cyclic data was generated in this program where proof load cycle was not applied.

Figures 5-13 and 5-14 show similar comparisons as Figure 5-12 for LN<sub>2</sub> and LH<sub>2</sub> temperature cyclic lives. From a cursory look, data shows that the pre-load cycles do not have a large effect on cyclic life. However, the material tested in this program has much higher fracture toughness. From the results of References 2 and 8 it can be shown that flaw growth rates are nearly the same at a given  $K_I$  level for both high and low fracture toughness material. Thus, the cyclic life at the same  $K_{Ii}/K_{Ic}$  ratio would be lower for the high toughness material than the low toughness material. Based on the above result, present data with preload effects would show a substantially longer cyclic life. Once again, the improvement in cyclic life is due to the effects of proof overload cycles and/or delaminations.

#### 5.4.2 6Al-4V $\beta$ STA Titanium

Results of tests for static fracture toughness and proof test temperature histories on 6Al-4V  $\beta$ STA titanium surface flawed specimens are described and analyzed in the following two sections. All these tests were conducted for the LS crack propagation direction.

##### 5.4.2.1 Static Fracture Toughness Tests

Results and specimen details of static fracture toughness tests for the 6Al-4V  $\beta$ STA titanium surface flawed specimens are summarized in Table 5-4. For all these tests, the initial  $a/2c$  ratio was 0.25, the initial  $a/t$  was less than 0.5 and the gross applied stress was considerably less than tensile yield strength. Plots of applied load versus crack opening displacement for four

specimens tested at 72°F (295K) and -320°F (78K) are given in Figure 5-15. Figure 5-15 shows no evidence that flaw growth occurred until the applied load approached the fracture load and fracture toughness  $K$  and  $K_{IE}$  calculated with five percent secant offset load  $P_5^{(27)}$  and failure load respectively are identical.  $K_{IE}$  values for the 6Al-4V  $\beta$ STA titanium are 56.9, 52.8, and 44.9  $\text{ks}\sqrt{\text{in}}$  (62.6, 58.1, and 49.4  $\text{MN}/\text{m}^{3/2}$ ) at 72°F (295K), -320°F (78K), and -423°F (20K), respectively.

#### 5.4.2.2 Proof Test Temperature Effects Tests

Results of tests conducted to investigate the effects of proof test temperatures on fracture toughness and flaw growth rates are summarized in Table 5-5. Figures 5-16, 5-17 and 5-18 contain the plots of COD versus applied load for the surface flawed specimens subjected to proof loads at 72°F (295K), -320°F (78K) and -423°F (20K), respectively. Some of the load versus COD plots show some nonlinearity at the maximum applied load. At the maximum proof load, the gross applied stress is up to 90 percent of the tensile yield strength depending upon the proof temperature. This causes plastic yielding around the flaw periphery and thus introduces nonlinearity in the load versus COD curves. For the specimens proof loaded at 72°F (295K) and -320°F (78K), records of COD versus load were also obtained for unloading. These records in Figures 5-16 and 5-17 show that unloading plots are parallel to loading plots. This would indicate that no flaw growth occurred during proof loadings.

Examination of fractured surfaces under low magnification (30X) showed that no growth occurred during the proof load applications in the ambient room air, liquid nitrogen, and liquid hydrogen environments.

Specimen 6T-9 was proof loaded at room temperature and specimen 6T-31 was proof loaded at room temperature and -423°F (20K) and then they were loaded to failure at -423°F (20K), as shown in Table 5-5. The fracture toughness calculated for these specimens is at least 15 percent higher than that calculated from specimens which were not proof loaded prior to loading to failure. This limited data implies that application of proof load cycle may be beneficial in raising the effective fracture toughness,  $K_{IE}$ . Specimen 6T-7 which was proof loaded at room temperature prior to loading to failure at -320°F (78K) also showed a

beneficial effect of proof loading on  $K_{IE}$ . However, specimen 6T-8 which was proof loaded at room and liquid nitrogen temperatures prior to loading to failure at  $-320^{\circ}\text{F}$  (78K) showed no effect on  $K_{IE}$  of the proof cycles. From these tests, it can be concluded that during the specified proof load cycles, flaw growth does not occur, and that the effect on fracture toughness of 6Al-4V  $\beta$ STA titanium ranges from negligible to highly beneficial.

Typical plots of COD versus number of cycles are shown in Figures 5-19, 5-20, and 5-21 for  $72^{\circ}\text{F}$  (295K),  $-320^{\circ}\text{F}$  (78K) and  $-423^{\circ}\text{F}$  (20K), respectively. These plots along with data of initial and final flaw sizes and cyclic stress were used to obtain cyclic flaw growth rates,  $da/dN$ , versus stress intensity factor,  $K_I$ . Figures 5-22 to 5-25 contain the plots of cyclic flaw growth rates (with and without prior proof load cycles) against  $K_I$  for the surface flawed specimens cycled at  $72^{\circ}\text{F}$  (295K),  $-320^{\circ}\text{F}$  (78K) and  $-423^{\circ}\text{F}$  (20K). The basic flaw growth rates obtained without the application of a prior proof load cycle are shown by open or filled circle symbols. Figures 5-22 and 5-23 contain cyclic flaw growth rates for specimens which were cycled at  $72^{\circ}\text{F}$  (295K) under ambient room air environment. Some of the specimens in Figure 5-22 were subjected to proof loads at room and/or  $\text{LN}_2$  temperatures prior to cycling them in a room air environment. Some of the specimens in Figure 5-23 were subjected to proof loads at room and/or  $\text{LN}_2$  temperatures prior to cycling them in a room air environment. The data points indicated with symbol E in Figures 5-22 and 5-23 are used to distinguish crack growth rates and associated stress intensity factors obtained from the end point method<sup>(2)</sup>. (In the end point method, the initial and final dimensions of flaw depths are used with applied number of cycles to calculate an average flaw growth rate  $da/dN$ . The calculated flaw growth rate  $da/dN$  is assumed to correspond with the stress intensity factor which is the average of the initial and final stress intensity factors.) Data of Figures 5-22 and 5-23 indicate that within the scatter of data the flaw growth rates for the specimens subjected to proof loads at room and/or  $\text{LN}_2$  temperatures, or room and/or  $\text{LN}_2$  temperatures are comparable to basic crack growth rates at room temperature without a prior proof load.

Figure 5-24 contains cyclic flaw growth rates for surface flawed specimens which were cycled at  $-320^{\circ}\text{F}$  (78K) under liquid nitrogen environment. Some of these specimens were proof loaded at room and/or  $\text{LN}_2$  temperature prior to cycling at  $\text{LN}_2$ . Data in Figure 5-24 shows that flaw growth rates for specimens

subjected to room and/or  $\text{LN}_2$  temperature proof loads are comparable to basic crack growth rates within the scatter limits of data. Thus, the proof load applications have small or no effects on flaw growth rates of 6Al-4V  $\beta$ STA titanium.

Figure 5-25 contains cyclic flaw growth rates for surface flawed specimens which were cycled at  $-423^\circ\text{F}$  (20K) in a liquid hydrogen environment. Some of these specimens were proof loaded at room and/or  $\text{LH}_2$  temperatures prior to cycling at  $\text{LH}_2$  temperature. Data in Figure 5-25 show that the flaw growth rates for specimens subjected to room and  $\text{LH}_2$  temperature proof loads are slower than the basic crack growth rates. Flaw growth rates for specimens subjected to proof load at  $\text{LH}_2$  temperature alone are comparable to basic flaw growth rates.

From the above results of all cyclic tests, it can be concluded that proof load temperature histories used in these tests have small or no effect on flaw growth rates of surface flawed specimens of 6Al-4V  $\beta$ STA titanium.

## 6.0 FRACTURE UNDER COMBINED MODES IN 4340 STEEL

The majority of past experimental and theoretical fracture and crack growth studies have dealt with the opening mode of deformation (Mode I conditions). Many investigations have shown that under Mode I conditions, crack instability occurs when the stress intensity factor reaches some critical value. Under actual service conditions, cracks may be subjected to loading conditions such that combined modes of crack surface displacements are present. A limited number of theoretical and experimental investigations<sup>(34-45)</sup> have been conducted to determine the effects of combined mode loadings on fracture. These are described briefly in Section 6.1. Section 6.2 includes stress intensity factors for combined mode loading. Section 6.3 deals with test program, specimens and procedures. Section 6.4 describes test machine and instrumentation. Section 6.5 includes test results and a discussion of test results.

### 6.1 BACKGROUND AND TECHNICAL DISCUSSION

#### 6.1.1 Crack Tip Stress Fields for Isotropic Elastic Bodies

Cracks in bodies subjected to combined tension and shear stresses can be subjected to three different types of displacements<sup>(33)</sup>. Each type of displacement is associated with a particular stress field in the immediate vicinity of the crack tip. The elastic stress field is dominated by stress singularities and the strength of the singularity is expressed by a stress intensity factor.

The relative displacement of crack surfaces in the immediate vicinity of a crack tip can be divided into three components or modes. As illustrated in Figure 6-1 the three modes are: the opening Mode I in which crack surfaces displace perpendicular to the plane of the crack; the edge sliding Mode II in which the crack surfaces displace in the plane of the crack perpendicular to the leading edge of the crack; and the tearing Mode III in which the crack surfaces displace in the plane of the crack in a direction parallel to the leading edge of the crack.

Elastic stress fields in the immediate vicinity of a crack tip are related to the mode of crack tip displacement. In terms of the cartesian coordinate system shown in Figure 6-2, plane strain crack tip stress fields corresponding to each mode of displacement are included below. Nonsingular terms are not included in the following expressions for stresses.



It is evident that the stress intensity factors  $K_I$ ,  $K_{II}$  and  $K_{III}$  control the strength of the crack tip stress singularities. These stress intensity factors are functions of the dimensions of both the crack and the body in which the crack is located, and the magnitude and distribution of the loads applied to the body.

### 6.1.2 Theories of Fracture Under Combined Mode Loading

For a cracked component under combined mode loading, two theories of fracture have been advanced; maximum stress criterion<sup>(34)</sup> and strain energy density factor theory<sup>(35,36)</sup>. These theories are explained briefly in the following paragraphs.

#### 6.1.2.1 Maximum Stress Criterion

Erdogan and Sih<sup>(34)</sup> stated the commonly recognized hypothesis for crack extension in a brittle material under slowly applied plane loads as: the crack extension occurs in the plane perpendicular to the direction of the greatest tension. In terms of the coordinate system shown in Figure 6-3, the above hypothesis states that the crack extension starts at  $x = \pm a$  along the radial direction for which  $\sigma_\theta$  is maximum and the shear stress  $\tau_{r\theta}$  is zero. For the mixed mode problem of Figure 6-4, the angle of crack extension,  $\theta_o$  can be shown as

$$K_I \sin\theta_o + K_{II} (3 \cos\theta_o - 1) = 0. \quad (6-4)$$

For the crack and loading configuration of Figure 6-4, the relationship between the crack inclination angle  $\beta$  (shown in Figure 6-4) and fracture angle  $\theta_o$  (angle of crack extension with respect to the initial crack plane) predicted by the above equation is shown in Figure 6-5. In Figure 6-5, the propagation of a crack normal to the applied stress, i.e.,  $\beta + \theta_o = 90^\circ$ , is shown by a straight line.

For materials in which a small plastic zone develops at the crack tip, Erdogan and Sih<sup>(34)</sup> proposed a fracture criterion based on strain energy release rate considerations of Griffith. For the case of plane loadings that impose both Mode I and Mode II crack tip displacements, the fracture criterion is

$$a_{11} K_I^2 + 2a_{12} K_I K_{II} + a_{22} K_{II}^2 = \text{constant} \quad (6-5)$$

where the constants  $a_{ij}$  ( $i, j = 1, 2$ ) are functions of material properties. Since it is not possible to calculate elastic strain energy release per unit crack extension when the crack extension is not coplanar with the original crack plane, the above fracture criterion was deduced by reasoning that the strain energy release rate for a curved crack should be a homogeneous quadratic function of  $K_I$  and  $K_{II}$ <sup>(34)</sup>. In the special case where the crack propagates in its original plane;  $a_{11} = a_{22}$  and  $a_{12} = 0$ <sup>(34)</sup>.

#### 6.1.2.2 Strain Energy Density Factor Theory

Sih<sup>(35,36)</sup> has recently proposed a theory of fracture based on the field strength of local strain energy density to deal with the combined mode crack extension problems. For a crack in an elastic solid subjected to all three modes of crack surface displacements, the strain energy  $dW$  stored in a small elemental volume  $dV$  near the crack tip is represented by the following equation where the terms of order higher than  $1/r$  are neglected.

$$\frac{dW}{dV} = \frac{1}{\pi r} (a_{11} K_I^2 + 2a_{12} K_I K_{II} + a_{22} K_{II}^2 + a_{33} K_{III}^2) \quad (6-6)$$

where

$$\begin{aligned} a_{11} &= \frac{1}{16\mu} [(3 - 4\nu - \cos\theta)(1 + \cos\theta)] \\ a_{12} &= \frac{\sin\theta}{8\mu} [\cos\theta - (1 - 2\nu)] \\ a_{22} &= \frac{1}{16\mu} [4(1 - \nu)(1 - \cos\theta) + (1 + \cos\theta)(3 \cos\theta - 1)] \\ a_{33} &= \frac{1}{4\mu} \end{aligned} \quad (6-7)$$

where  $\nu$  is the Poisson's ratio and  $\mu$  is shear modulus and  $\theta$  is the angle defined in Figure 6-2. The strain energy density function  $\frac{dW}{dV}$  near the crack possesses a  $(1/r)$  singularity. The strain energy density factor  $S$  representing the intensity of the strain energy density field is defined below and varies with the polar angle in Figure 6-2.

$$S = a_{11} K_I^2 + 2a_{12} K_I K_{II} + a_{22} K_{II}^2 + a_{33} K_{III}^2. \quad (6-8)$$

The above formulation is for plane strain conditions. Strain energy density factor theory assumes that the crack initiation starts in a radial direction along which strain energy density or  $S$  is stationary and the critical intensity  $S_c$  governs the onset of crack propagation. According to this theory,  $S_c$  is an intrinsic material property independent of the loading conditions and crack configurations. This implies that if  $S_c$  is obtained for the pure Mode I condition (which is directly related to Griffith-Irwin critical stress intensity factor  $K_{Icr}$ ), the fracture load and crack rotation direction can be predicted for that material environment combination for any mixed mode loading condition. For the planar mixed mode problem of Figure 6-4,  $S_c$  theory predicts the fracture angle  $\theta_o$  with respect to inclined angle  $\beta$  as shown in Figure 6-5. The fracture angle  $\theta_o$  in  $S_c$  theory is dependent upon Poisson's ratio. As seen from Figure 6-5, the fracture angles  $\theta_o$  for a cracked component under an in-plane loading by the maximum stress criterion<sup>(34)</sup>, strain energy density factor theory<sup>(35,36)</sup>, energy theory<sup>(37)</sup> and the crack propagation normal to the applied stress are quite close. Thus, fracture angle is not a sensitive parameter to verify the above theories of fracture under combined mode loading.

### 6.1.3 Experimental Work Under Combined Mode Loading

A limited number of experimental investigations have been conducted to investigate the effect of combined mode loading conditions on fracture at flaws. These experimental studies include the effects of Mode I-II interaction on plaxiglass<sup>(34)</sup>, balsa wood<sup>(38)</sup>, fiberglass<sup>(38)</sup>, and 2000 and 7000 series aluminum alloys<sup>(39-44)</sup> and Mode I-III interaction on 7000 series aluminum alloys<sup>(39,41)</sup> and K-9 tool steel<sup>(41)</sup>. The results of these investigations are presented briefly in the following paragraphs.

Erdogan and Sih<sup>(34)</sup> tested plaxiglass specimens containing through-the-thickness cracks. They found that cracks subjected to pure Mode II loading propagate when  $K_{II}$  reaches some critical value and equation (6-5) was a satisfactory failure criterion when  $K_I$  and  $K_{II}$  were calculated based on the initial crack conditions. Based on these tests they concluded that the final mode of fracture seemed to be always that of an opening mode.

Wu<sup>(38)</sup> tested plates of orthotropic materials (balsa wood and fiberglass) containing cracks under combined Mode I and II loadings. Some of the specimens tested under combined Mode I-II contained slanted cracks and were loaded in pure tension, similar to that in Figure 6-4. Other specimens tested under Mode I and II were first loaded in pure tension (cracks were perpendicular to load) and then were loaded to fracture in pure shear under picture frame type loading while maintaining the tension load. Some specimens were tested in pure shear to obtain critical stress intensity under Mode II, i.e.,  $K_{IIc}$ . All specimens subjected to shear loadings were constrained from buckling. It was found that slow stable crack extension took place prior to sudden fracture. However, under all loading conditions (Mode I, Mode I-II and Mode II), the crack propagated along an essentially straight line collinear with the original crack. It was also found that the applied loading conditions for combined Mode I-II (inclined crack under pure tension or crack subjected to tensile loading and shear) did not have any effect on fracture strength. The experimental data revealed that the empirical equation  $(K_I/K_{Ic}) + (K_{II}/K_{IIc})^2 = 1$  represented adequately the fracture criterion for both balsa wood and fiberglass.

Wilson<sup>(39)</sup> conducted a limited series of tests on 7178-T651 aluminum alloy center cracked plates under combined Mode I-II loading, and on 7075-T651 aluminum alloy round notched bar specimens under combined Mode I-III loading. Directions of slanted cracks in 7178-T651 aluminum coincided with the rolling direction of the plate. Test results showed that equation (6-5) provided a satisfactory failure criterion for both Mode I-II and Mode I-III loading for the particular thicknesses and geometries tested when  $K_{II}$  is replaced by  $K_{III}$  in equation (6-5) for Mode I-III loading.  $K_I$  and  $K_{II}$  were calculated based on the initial crack length and orientation and the fracture load.

Pook<sup>(41)</sup> tested inclined center cracked specimens of DTD 5050 under combined Mode I-II loadings. Inclined cracks were located normal to the rolling direction. Slow, out-of-plane crack growth occurred prior to instability.  $K_I$  and  $K_{II}$ , in these as well as test results of Liu<sup>(42)</sup>, were calculated based on the initial crack length and orientation and the fracture load. Either equation (6-5) or (6-8) provided an adequate fracture criterion<sup>(35)</sup>.

Pook<sup>(41)</sup> also tested single edge cracked and center cracked specimens of DTD 5050 and HE15W aluminum alloys and K9 tool steel under combined Mode I-III crack surface displacements. The cracks were inclined with respect to the plane of the plate and the specimens were loaded in tension. It was found that crack extension started when  $K_I$  was nearly equal to  $K_{Ic}$  and for the applied range of  $K_{III}$ ,  $K_{III}$  had a small effect on initiation of crack growth.

Recently, Liu<sup>(42)</sup> tested panels of 2024-T3 and 7075-T651 aluminum alloys containing fatigue cracks oriented at different angles. The panels were loaded in a picture frame setup to apply shear loads at the edges of the panel so that combined Mode I-II crack surface displacements could be applied. No buckling constraints were applied to avoid buckling in the panels. The cracks were perpendicular to the rolling direction of the materials. Slow, stable, out-of-plane crack growth occurred in all specimens prior to fracture except those loaded in pure Mode II. Experimental data showed that the empirical equation  $(K_I/K_{Icr})^{1.08} + (K_{II}/K_{IIcr})^{1.08} = 1$  represented adequately the fracture criterion. Because this interaction effect was substantially different than that found by Wilson<sup>(39)</sup> and Pook<sup>(41)</sup>, Liu concluded that the  $K_I$  and  $K_{II}$  interaction behavior is a function of the applied loading conditions. However, the tests conducted with the slanted single edge cracked specimens of 7075-T651 aluminum and loaded in tension<sup>(43)</sup> showed very similar results as described above<sup>(42)</sup>. This would indicate that the fracture criterion is not significantly dependent upon loading conditions.

Very little published information exists to date on the crack propagation rates under combined loading of opening and sliding modes. Iida and Kobayashi<sup>(40)</sup> conducted a series of fatigue crack propagation tests under Mode I-II loading in thin 7075-T6 aluminum panels containing inclined center cracks. It was concluded that the crack rotated immediately and propagated in the direction where  $K_I$  was maximum.

Roberts and Kibler<sup>(44)</sup> obtained fatigue crack propagation rates for thin 2024-T3 bare aluminum plates subjected to Mode I extensional loads and Mode II transverse bending loads. They found that the fatigue crack grew in a manner which did not reduce the Mode II component of the load to zero.

Mode I:

$$\sigma_{xx} = \frac{K_I}{\sqrt{2\pi r}} \cos \frac{\theta}{2} \left[ 1 - \sin \frac{\theta}{2} \sin \frac{3\theta}{2} \right] \quad (6-1a)$$

$$\sigma_{yy} = \frac{K_I}{\sqrt{2\pi r}} \cos \frac{\theta}{2} \left[ 1 + \sin \frac{\theta}{2} \sin \frac{3\theta}{2} \right] \quad (6-1b)$$

$$\tau_{xy} = \frac{K_I}{\sqrt{2\pi r}} \sin \frac{\theta}{2} \cos \frac{\theta}{2} \cos \frac{3\theta}{2} \quad (6-1c)$$

$$\sigma_{zz} = \nu(\sigma_{xx} + \sigma_{yy}) \quad (6-1d)$$

$$\tau_{xz} = \tau_{yz} = 0 \quad (6-1e)$$

Mode II:

$$\sigma_{xx} = -\frac{K_{II}}{\sqrt{2\pi r}} \sin \frac{\theta}{2} \left[ 2 + \cos \frac{\theta}{2} \cos \frac{3\theta}{2} \right] \quad (6-2a)$$

$$\sigma_{yy} = \frac{K_{II}}{\sqrt{2\pi r}} \sin \frac{\theta}{2} \cos \frac{\theta}{2} \cos \frac{3\theta}{2} \quad (6-2b)$$

$$\tau_{xy} = \frac{K_{II}}{\sqrt{2\pi r}} \cos \frac{\theta}{2} \left[ 1 - \sin \frac{\theta}{2} \sin \frac{3\theta}{2} \right] \quad (6-2c)$$

$$\sigma_{zz} = \nu(\sigma_{xx} + \sigma_{yy}) \quad (6-2d)$$

$$\tau_{xz} = \tau_{yz} = 0 \quad (6-2e)$$

Mode III:

$$\tau_{xz} = -\frac{K_{III}}{\sqrt{2\pi r}} \sin \frac{\theta}{2} \quad (6-3a)$$

$$\tau_{yz} = \frac{K_{III}}{\sqrt{2\pi r}} \cos \frac{\theta}{2} \quad (6-3b)$$

$$\sigma_{xx} = \sigma_{yy} = \sigma_{zz} = \tau_{xy} = 0 \quad (6-3c)$$

## 6.2 SPECIMEN CONFIGURATIONS AND STRESS INTENSITY FACTORS FOR COMBINED MODE LOADING TESTS

### 6.2.1 Test Specimen Configurations

Specimens for the combined mode loading tests consisted of the following categories. Inclined through cracked flat specimens subjected to uniform tension, as shown in Figure 6-6, were used for combined Mode I-II tests. Through cracked tube specimens, subjected to pure torsion, as shown in Figure 6-7, were used for the Mode II tests. Round notched bar specimens subjected to simultaneous tension and torsion loading, as shown in Figure 6-8, were used for the combined Mode I-III test. Flat specimens with inclined surface cracks and subjected to uniform tension (Figure 6-9) and surface flawed cylindrical specimens subjected to simultaneous tension and torsion loading (Figure 6-10) were utilized for the combined Mode I-II-III tests. Stress intensity factor solutions, used to evaluate the test data of the above specimens, are described in the following paragraphs.

### 6.2.2 Stress Intensity Factors

Utilizing the boundary collocation method, Wilson<sup>(39)</sup> obtained the stress intensity factors  $K_I$  and  $K_{II}$  for a strip containing an inclined center crack (Figure 6-6) and subjected to uniform uniaxial tension. The resulting stress intensity factors  $K_I$  and  $K_{II}$  are shown in Figure 6-11 as a function of the ratio of crack length to the specimen width,  $\frac{2a}{W}$ , for the values of the inclined angles  $\phi = 0, 22.5, 45$  and  $75$  degrees ( $0, 0.39, 0.79$  and  $1.31$  rad). The relationship of  $K_I$  and  $K_{II}$  to the applied stress, crack length, crack angle and specimen width displayed in Figure 6-11 were used to compute stress intensity factors for inclined center cracked specimens.

Iida and Kobayashi<sup>(40)</sup> used the direct stiffness method of finite element analysis and obtained the stress intensity factors for a plate containing a slanted crack and subjected to uniaxial tension. The crack opening displacement (COD) components  $v$ , perpendicular to the crack, and  $u$ , parallel to the crack, were used to determine the stress intensity factors  $K_I$  and  $K_{II}$ . Stress intensity factors, thus obtained from COD are considered to be accurate within ten percent. Figure 6-12 and 6-13 show the stress intensity factors in the non-dimensionalized form for cracks initially inclined at  $45$  and  $60$  degrees

(0.79 and 1.05 rad) to the applied loading direction, respectively. The initial inclined length of the crack is one-twelfth of the width of the plate. The stress intensity factor for the slanted crack is nondimensionalized with respect to  $\sigma\sqrt{\pi a}$  where  $2a$  is the horizontal projection of the crack length. Figure 6-12 shows that prior to any crack extension (no crack rotation),  $K_I = K_{II}$ , as expected for a 45 degrees (0.79 rad) inclined crack. As the crack turns and increases in length (as observed in their experiments),  $K_I$  increases rapidly while  $K_{II}$  decreases sharply. Figure 6-12 also shows Isida's correction factor for a straight (0 deg. inclination) center crack of length  $2a$  in a strip<sup>(33)</sup>. Figure 6-13 shows similar results for a crack initially inclined at 60 degrees (1.05 rad). Both Figures 6-12 and 6-13 show that as the crack turns and extends, the opening mode stress intensity factor,  $K_I$  climbs rapidly to approach  $K_I$  for a horizontal crack with length equal to that of the projected length of the inclined crack and  $K_{II}$  drops rapidly and also changes sign showing the shift in the sliding direction of the  $K_{II}$  mode crack extension.  $K_I$  for an inclined crack is always somewhat lower than the  $K_I$  for a horizontal crack even on the basis of projected crack length. This indicates that the fracture data and fracture criterion under combined mode loading should be evaluated using the crack configuration at the fracture load. Fracture criterion under combined mode loading  $f(K_I, K_{II})$ , based on initial crack length, orientation and fracture load, could be significantly in error if slow crack growth and crack rotation occur prior to fracture.

Stress intensity factors for the circumferentially cracked tubes (Figure 6-7) subjected to pure torsion were calculated from the following equation<sup>(46)</sup>

$$K_{II} = C_m \tau \sqrt{\pi a} \quad (6-9a)$$

where  $C_m$  is the membrane component of the shell curvature correction factor and the relationship between  $C_m$  and the shell parameter  $\lambda$  is given in Figure 6-14<sup>(46)</sup>. The bending part of the stress intensity factor  $K_{II}$  is approximately three orders smaller than the membrane portion and thus it is negligible. The shell parameter  $\lambda$  and the shear stress  $\tau$  are given by the following equation

$$\lambda = a \left[ \frac{12(1-\nu^2)}{r^2 t^2} \right]^{1/4} \quad (6-9b)$$

$$\tau = \frac{T}{2\pi r^2 t} \quad (6-9c)$$



where  $T$  is the applied torque,  $\nu$  is the Poisson's ratio,  $2a$  is the crack length,  $r$  is the average radius of the tube, and  $t$  is the thickness of the tube.

Stress intensity factors for round notched bars subjected to simultaneous tension and torsion loading were calculated by the following equations<sup>(47,48)</sup>.

$$K_I = (1.72 \frac{D}{d} - 1.27) \frac{P}{D^{1.5}} \quad (6-10)$$

$$K_{III} = 0.41 \frac{T}{r^{2.5}} \quad (6-11)$$

where  $D$  is the diameter of the bar,  $d$  and  $r$  are the diameter and the radius of the bar in the plane of the crack, respectively and  $P$  and  $T$  are the applied force and the torque, respectively.

The expression for  $K_I$  is due to Bueckner<sup>(33)</sup>. As mentioned in Section 8.3.1, the expression for  $K_I$  for a round notched bar given by Harris<sup>(48)</sup> is probably more accurate than the above expression. However, the Bueckner expression was used since it is generally accepted. As shown by Figure 6-15, the expression for  $K_{III}$  given by equation 6-11 is approximately the same as given by Wilson<sup>(39)</sup> and Harris<sup>(48)</sup> within 2 percent over the range of  $d/D$  under consideration.

The flaw peripheries of the flat specimens containing inclined semi-elliptical surface cracks and loaded by uniform uniaxial tension are subjected to continuously varying ratios of  $K_I$  to  $K_{II}$  to  $K_{III}$ . Since the stress intensity factor for a surface flawed specimen subjected to uniform shear stress is not available, the stress intensity factors  $K_{II}$  and  $K_{III}$  for the specimens tested were calculated using a solution for an elliptical crack in an infinite solid subjected to uniform shear stress<sup>(49)</sup>. Since ratios of the crack depth to the crack length and the crack depth to the specimen thickness ratios are nearly the same for all test specimens, the effects of the free surfaces would be approximately the same. Hence, in the following expressions for  $K_{II}$  and  $K_{III}$  the effects of the free surfaces are not taken into account. The stress intensity factors  $K_I$  and  $K_{III}$  are maximum at the maximum crack depth and  $K_{II}$  is zero there.  $K_{II}$  is maximum at the surface crack length and  $K_{III}$  is nonexistent there. Hence, the stress intensity factors  $K_I$ ,  $K_{II}$ ,  $K_{III}$  for the test results were calculated at the maximum crack depth and at the surface. The stress

intensity factors at the maximum depth were calculated by the following equations.

$$K_I = M_K \sigma \cos^2 \phi \sqrt{\frac{\pi a}{Q}} \quad (\text{Reference 15}) \quad (6-12)$$

$$K_{II} = 0 \quad (\text{Reference 49}) \quad (6-13)$$

$$K_{III} = M_{III} \sigma \cos \phi \sin \phi \sqrt{\pi a} \quad (\text{Reference 49}) \quad (6-14)$$

where  $M_K^{(15)}$  is a function of  $a/t$  and  $a/2c$  and is given by Figure 2-2 and

$$M_{III} = \frac{(1 - \nu) k^2}{(k^2 - \nu) E(k) + k'^2 K(k)} \quad (6-15)$$

The stress intensity factors at the surface were calculated by the following equations.

$$K_I = 1.11 \sigma \cos^2 \phi \sqrt{\frac{\pi a}{Q}} \sqrt{a/c} \quad (6-16)$$

$$K_{II} = M_{II} \sigma \cos \phi \sin \phi \sqrt{\pi a} \quad (\text{Reference 48}) \quad (6-17)$$

$$K_{III} = 0 \quad (\text{Reference 48}) \quad (6-18)$$

where

$$M_{II} = - \frac{k^2 \sqrt{a/c}}{(k^2 - \nu) E(k) + k'^2 K(k)} \quad (6-19)$$

$\nu$  is the Poisson's ratio,  $k'^2 = a^2/c^2$ ,  $k^2 + k'^2 = 1$ .  $E(k)$ , the complete elliptic integral of the second kind is defined before in Section 2.1 and  $K(k)$ , the complete elliptical integral of the first kind is given by the following equation

$$K(k) = \int_0^{\pi/2} \frac{d\theta}{\sqrt{1 - k^2 \sin^2 \theta}} \quad (6-20)$$

No solution is available for the stress intensity factors for surface flawed cylindrical specimens subjected to tension and/or torsional loading. As discussed in Section 8, the analysis of three dimensional photoelastic data did not give a conclusive expression for the stress intensity factor. Since most of the specimens had approximately the same flaw sizes, as described later in Section 6.5, the failure stresses were used to correlate the effects of the combined modes of loading rather than the stress intensity factors.

### 6.3 TEST PROGRAM AND PROCEDURES

A test program, comprised of surface flawed and center cracked flat specimens under tensile loading, was conducted to determine the effects of the directions of crack propagation on the fracture toughness of 4340 steel. As described in Section 6-5, the crack propagation directions had little or no effect on the fracture toughness for the directions tested. Hence, in the test programs of inclined through cracks and surface cracks in flat plates, the crack propagation directions were not kept in one particular direction. Effects of combined Mode I and II crack surface deformations on fracture were experimentally evaluated according to the test program outlined in Table 6-1. Test specimen configurations are illustrated in Figures 6-6 and 6-7. The inclined center cracked specimens were loaded in uniform uniaxial tension at -200°F (144K) in gaseous nitrogen environment to generate Mode I and combined Mode I-II loading conditions. In order to extend fatigue cracks in the planes of EDM slots in these specimens, the specimens were precracked by loading through 0.75 in. (19 mm) diameter holes whose centers were perpendicular to the EDM slots. In order to reduce the load required for precracking the EDM slots, two slotted holes were machined in the specimen as shown in Figure 6-6. After precracking the EDM slot to the required sized crack, the final specimen was cut such that the crack was oriented at the required angle with respect to the axis of loading. Inclined crack length to the specimen width ratio was approximately 0.5. Through cracked tube specimens (Figure 6-7) were precracked in tension loading and then subjected to torque only to determine the critical sliding mode stress intensity factor,  $K_{IIc}$  at room temperature. These specimens were instrumented with clip gages to continuously measure the angular deflection across the crack plane versus torque.

Effects of the combined Mode I and III crack surface displacements on fracture were experimentally evaluated according to the test program outlined in Table 6-2. Test specimen configuration is illustrated in Figure 6-8. A circumferential V-notch of 60 degree (1.05 rad) terminating with a notch root radius of 0.001 to 0.002 in. (0.025 to 0.051 mm) was machined into each of these round bar specimens. The root diameter of this machined V-notch was approximately 0.55 in. (14.0 mm). Prior to fracture testing, the specimens were precracked under low stress tension fatigue (maximum stress = 30 ksi (207 MN/m<sup>2</sup>), stress ratio = 0.06). It was intended to grow a circumferential fatigue crack of 0.05 in. (1.27 mm) depth from the V-notch root for each specimen. However, the fatigue crack grown from the notch in the first specimen precracked became eccentric. Since the fatigue cracks developing from notches tended to become eccentric, the fatigue cracks were kept small. Fatigue cracks as measured from the notch periphery were from 0.005 to 0.050 in. (0.127 to 1.27 mm). Fatigue cracks grown in two specimens of this material containing circumferential V-notches under rotating bending fatigue were more eccentric than those grown under tension fatigue. Figure 6-16 shows a photograph of a fatigue crack grown under rotating bending fatigue. As shown in Figure 6-17, the specimens to be precracked under rotating bending fatigue required very close tolerances in diametral dimensions. They also required high stresses to initiate fatigue cracking such as 60 ksi (414 MN/m<sup>2</sup>) and more. For these reasons, precracking was not conducted under rotating bending fatigue.

As seen from equations (6-10) and (6-11), since  $K_I$  is dependent on the tensile load  $P$  only and  $K_{III}$  is dependent on the torque  $T$  only, the ratio of  $K_I/K_{III}$  can be controlled by the proper ratio of  $P/T$ . The round notched bar specimens were loaded to failure under simultaneous tensile and torsional loading at a predetermined ratio of  $P/T$  at room temperature. All specimens were instrumented with clip gages to continuously measure the axial deflection and the angular deflection across the crack plane as a function of applied tension and torsion, respectively. The loading machine and the instrumentation are described in Section 6-4.

Effects of combined Mode I, II and III crack surface displacements on fracture were experimentally investigated according to the test programs outlined in

Tables 6-3 and 6-4. Test specimen configurations for the surface flawed flat and round specimens are shown in Figures 6-9 and 6-10. The inclined surface flawed flat specimens were loaded at  $-200^{\circ}\text{F}$  (144K) in a gaseous nitrogen environment in uniform uniaxial tension to create Mode I and combined Mode I-II-III loading conditions. The procedure for precracking the EDM slots was identical to the one described before for the inclined center cracked specimens. The flaw depth to plate thickness ratio was approximately 0.5 to 0.6 and the flaw depth to the flaw length ratio was approximately 0.25 in these specimens. The surface cracked round specimens were loaded at room temperature to failure under simultaneous tensile and torsional loading at a predetermined ratio of P/T. All surface flawed round specimens were instrumented with clip gages to continuously measure axial and angular deflections across the crack plane as a function of applied tensile and torsional loading, respectively. All surface flawed round specimens were intended to have the same flaw sizes, namely, the flaw depth to diameter ratio of 0.3 and a flaw depth to the flaw length ratio of 0.4.

#### 6.4 TEST MACHINE AND INSTRUMENTATION

Round notched bar specimens and cylindrical specimens with surface flaws were subjected to simultaneous tensile and torsional loading. They were loaded in a 150 kip (0.672 MN) capacity tension-compression machine which was modified to apply simultaneous tensile and torsional loading, as shown in Figure 6-18. The specimen was loaded in tension by a vertical hydraulic cylinder and torque was applied independently by a couple using two horizontal hydraulic cylinders (Figure 6-18). The hydraulic cylinders were actuated by servo valves responding to electrical signals to apply the programmed load. Directly in series with the specimen was a load cell providing a nulling feedback signal when the applied load reached the programmed value, thus forming a closed-loop control system. The load cell was made of a circular tube so that it could carry a relatively high axial load and be sensitive to torsional measurements. Axial load was measured and controlled by two independent four arm strain gage bridge circuits installed in the axial direction and torque was measured and controlled by two independent four arm strain gage circuits with the gages installed at a 45 degree (0.79 rad) angle with respect to the axial direction. The required ratio of the tension load with respect to the simultaneous torque

was maintained by a drum programmer.

The axial and angular displacement across the flawed cross-section were measured by electrical displacement indicators. Load versus displacement curves were generated independently for axial and for angular displacement by X-Y plotters. For round specimens containing surface flaws, crack opening displacement measurements in the axial direction were taken using clip gages, as shown in Figure 6-19. Holding-tabs with knife edges were microspot welded with one spot weld close to the flaw edge along the centerline of the flaw, and the other end of the tab held down by a slip-joint. For round notched bar specimens, axial displacement measurements were taken by using two electrical displacement indicators of the horseshoe type attached to clamps one inch apart on the specimen, as shown in Figure 6-20. The average output of the two displacement indicators was used to generate the load-displacement curves. For angular displacement measurements, two clamps, one inch apart along the specimen were attached to the specimen as shown in Figures 6-19 and 6-20. Knife edges were machined at the end of arms extended from the clamps to hold clip gages for angular displacement measurements. For convenience, the knife edges, where the clip gages were attached, were located one inch away from the vertical centerline of the specimen.

## 6.5 TEST RESULTS AND DISCUSSION

### 6.5.1 Fracture Toughness Tests

The plane strain fracture toughness of 4340 steel at room temperature was determined in LS and LT crack propagation directions by testing flat specimens containing semi-elliptical surface cracks, and central through-the-thickness cracks, respectively (Figure 6-21). The fracture toughness at  $-200^{\circ}\text{F}$  (144K) under gaseous nitrogen environment was determined in LS and TS directions of crack propagation by testing surface flawed specimens and in LT direction by testing center cracked specimens. All surface flawed specimens were instrumented with clip gages to measure crack opening displacement (COD) versus applied load. Typical records of load versus COD for each crack propagation direction and test temperature are shown in Figure 6-22. Figure 6-22 shows that the relationship between the load and crack opening displacement is linear almost up to the fracture load. This is especially true for the tests at  $-200^{\circ}\text{F}$  (144K) which indicates that little or no crack growth occurred

prior to fracture. Detailed test results are presented in Table 6-5. As observed from Table 6-5, the plane strain fracture toughness values for the LS and LT directions at room temperature were 72.2 and 73.9 ksi $\sqrt{\text{in}}$ , (79.4 and 81.2 MN/m<sup>3/2</sup>), respectively. The plane strain fracture toughness values in LS, TS and LT directions at -200°F (144K) were 40.1, 40.6, and 41.6 ksi $\sqrt{\text{in}}$  (44.1, 44.6, 45.7 MN/m<sup>3/2</sup>), respectively. The test results indicate that fracture toughness is essentially independent of the crack propagation directions in these planes.

### 6.5.2 Mode I-II Tests

Test results and specimen details for 4340 steel specimens containing inclined through cracks and loaded to failure in tension at -200°F (144K) in a gaseous nitrogen environment are summarized in Table 6-6. The photograph in Figure 6-23 shows fracture surfaces of these specimens. As seen from Figure 6-23, fracture (crack propagation) surfaces were oriented perpendicular to the applied tension. Examination of fracture surfaces did not reveal any apparent slow crack growth. These specimens were not instrumented with COD gages. However, instrumented surface flawed specimens of the same thickness tested under identical conditions did not show COD evidence of slow crack growth prior to fracture (Figure 6-22). Stress intensity factors  $K_I$  and  $K_{II}$  in Table 6-6 were calculated according to equations given in Figure 6-11. Initial crack length and orientation and the fracture stress were used to calculate  $K_I$  and  $K_{II}$ . Results of Table 6-6 are plotted in Figure 6-24 as  $K_I$  at fracture versus  $K_{II}$  at fracture. The plot in Figure 6-24 shows that the fracture criterion  $f(K_I, K_{II})$  for 4340 steel under combined Modes I-II loading at -200°F (144K) is well represented by a straight line relationship between  $K_I$  and  $K_{II}$  and this relationship can be well described by the equation  $K_I + K_{II} \approx K_{IC}$ . The fracture criterion  $f(K_I, K_{II})$  for 4340 steel is significantly different than that defined by either equation (6-5) or (6-8) or that inferred from the test data of Wilson<sup>(39)</sup> or Pook<sup>(41)</sup>. In order to compare directly with the existing test data, a comparison has to be made on the basis of  $K_I/K_{IC}$  versus  $K_{II}/K_{IIc}$ . Thus,  $K_{IIc}$  for the material needs to be determined.

Test results and specimen details for two cracked tube specimens of 4340 steel (Figure 6-7) are summarized in Table 6-7. These two cracked tubes were loaded to failure in pure torsion to obtain Mode II critical stress intensity factor,  $K_{IIc}$  at 72°F (295K) in ambient room air environment. As mentioned before, both

specimens were instrumented with clip gages to measure angular deflection across the crack plane against the applied torque. A typical plot of angular deflection versus applied torque is given in Figure 6-25. As seen from this plot for the tube specimen B, abrupt crack extension (pop-in) occurred at an applied torque of 9200 in-lb (1060 joules) and the complete fracture occurred at an applied torque of 11,250 in-lb (1270 joules). The applied gross shear stress at failure is 116 ksi which is slightly below the shear yield stress of 124 ksi. (Shear yield stress is assumed to be equal to tensile yield stress divided by  $\sqrt{3}$  from Mises's yield condition.) Visual observation as well as results of Figure 6-25 indicated that considerable crack growth had taken place prior to fracture. Fracture surfaces of the two tube specimens are shown in Figure 6-26. Fracture for these specimens initiated at a point A shown in Figure 6-26, and the fracture angles (angle between the crack extension and the initial crack) were 70 and 75 degrees (1.22 and 1.31 rad) for specimens A and B, respectively. This compares very favorably with the fracture angles predicted by equation (6-4) of the maximum stress criterion.

The stress intensity factor  $K_{II}$  for the cracked tube loaded in torsion was calculated according to equations (6-9). The sliding mode stress intensity factors  $K_{III}$ , based on the initial crack lengths and pop-in torques were 65.5 and 67.5 ksi $\sqrt{\text{in}}$  (72.0 and 74.2 MN/m<sup>3/2</sup>) for specimens A and B, respectively. Critical stress intensity factors,  $K_{IIIc}$ , based on initial crack lengths and fracture torque were 78.5 and 82.4 ksi $\sqrt{\text{in}}$  (86.3 and 90.6 MN/m<sup>3/2</sup>) for specimens A and B, respectively. Thus, average  $K_{IIIc}$  was 80.4 ksi $\sqrt{\text{in}}$  (88.4 MN/m<sup>3/2</sup>). Assuming the ratio of  $K_{IIIc}$  at -200°F (144K) to  $K_{IIIc}$  at 72°F (295K) is the same as  $K_{Ic}$  at -200°F (144K) to  $K_{Ic}$  at 72°F (295K), the calculated value of  $K_{IIIc}$  for -200°F (144K) is 45.2 ksi $\sqrt{\text{in}}$  (49.7 MN/m<sup>3/2</sup>). A  $K_{IIIc}$  of 45.2 ksi $\sqrt{\text{in}}$  (49.7 MN/m<sup>3/2</sup>) was used for 4340 steel at -200°F (144K) to calculate  $K_{II}/K_{IIIc}$  ratios in Figure 6.27, to be discussed later. If  $K_{IIIc}$  was based on the pop-in torque and the initial crack length, it would have been 37.4 ksi $\sqrt{\text{in}}$  (41.1 MN/m<sup>3/2</sup>).

Some uncertainty exists in the determination of the exact value of critical plane strain sliding stress intensity factor,  $K_{IIIc}$  as the thickness of the tube does not meet the plane strain criterion for the minimum thickness for tension-loaded-specimen and the applied shear stress is high with respect to the shear yield stress. It is possible that the value of  $K_{IIIc}$  is lower than



45.2 ksi $\sqrt{\text{in}}$  (49.7 MN/m<sup>3/2</sup>). This will change the shape of  $K_I/K_{Ic}$  versus  $K_{II}/K_{IIc}$  curve in Figure 6-27 from a straight line to a slightly convex (elliptical shape) curve. However, as shown in Figure 6-24,  $K_{IIc}$  cannot be much lower than 35.0 ksi $\sqrt{\text{in}}$  (38.5 MN/m<sup>3/2</sup>) since it required an applied  $K_{II}$  of 35.0 ksi $\sqrt{\text{in}}$  (38.5 MN/m<sup>3/2</sup>) in the presence of an applied  $K_I$  of 10.5 ksi $\sqrt{\text{in}}$  (11.5 MN/m<sup>3/2</sup>) to fracture the specimen. Also, the linear fracture criterion in Figure 6-24 indicates that  $K_{IIc}$  is around 45.5 ksi $\sqrt{\text{in}}$  (50.0 MN/m<sup>3/2</sup>).

The data of combined mode loading I-II of 4340 steel at -200°F (144K) are compared in Figure 6-27 on the basis of  $K_I/K_{Icr}$  versus  $K_{II}/K_{IIcr}$  with the Mode I-II data at room temperature obtained by: (1) Wilson<sup>(39)</sup> for 7178-T651 aluminum alloy from inclined center cracked specimens loaded in tension, (2) Pook<sup>(41)</sup> for DTD 5050 aluminum alloy from inclined center cracked specimens loaded in tension, (3) Liu<sup>(42)</sup> for 7075-T7651 and 2024-T3 aluminum alloys from cracked panels loaded in shear and; (4) unpublished data at Boeing<sup>(43)</sup> for 7075-T651 aluminum alloy from inclined edge cracked specimens loaded in tension. From Figure 6-27, the fracture criterion under combined Mode I-II for 4340 steel at -200°F (144K) can also be well described by  $K_I/K_{Ic} + K_{II}/K_{IIc} = 1$ . The fracture criterion  $f(K_I, K_{II})$  is significantly different from that implied by data of the aluminum specimens of Wilson<sup>(39)</sup> and Pook<sup>(41)</sup> or that defined by equations (6-5) or (6-8). Thus, for 4340 steel specimens under combined mode loading I-II, presence of Mode II stress intensity factor has highly significant effect on Mode I stress intensity factor at which fracture occurs, i.e.,  $K_I$  at fracture can be significantly less than  $K_{Ic}$  in the presence of  $K_{II}$ . Figure 6-27 suggests that the fracture criterion under combined Mode I-II crack surface deformations may be dependent on material, thickness and test temperature combination. It needs to be emphasized that for all data presented in Figure 6-27 and in References (39, 41-43),  $K_I$  and  $K_{II}$  were calculated based on initial crack length and orientation and fracture load even though the tests conducted by Pook<sup>(41)</sup>, Liu<sup>(42)</sup> and at Boeing<sup>(43)</sup> did show that slow, stable, out of plane crack growth took place prior to fracture. The finite element solution<sup>(40)</sup> of the inclined thru-crack (Figures 6-12 and 6-13) shows that as the crack turns out of its plane,  $K_I$  increases significantly and  $K_{II}$  decreases significantly. This indicates that the fracture data and criterion under combined mode loading should be evaluated using the crack configuration at the fracture load. The fracture criterion of combined mode  $f(K_I, K_{II})$ ,

obtained disregarding the crack growth and rotation, could be significantly in error.

### 6.5.3 Mode I-III Tests

Test results and specimen details of round notched bar specimens (Figure 6-8) are summarized in Table 6-8. These specimens were loaded to failure at room temperature in pure tension, in combined tension and torsion and in pure torsion to determine the fracture criterion under combined Mode I and III. Details about fatigue crack extension, depth and concentricity are given in Section 6-3 and Table 6-8.

Stress intensity factors  $K_I$  and  $K_{III}$  in Table 6-8 were calculated according to equations (6-10) and (6-11) based on fracture load  $P_F$ , fracture torque  $T_F$  and the initial minimum diameter  $d$  at the cracked section of the bar. Results of Table 6-8 are plotted in Figure 6-28 as  $K_I$  at fracture versus  $K_{III}$  at fracture. The probable fracture criterion under combined mode loading I and III is shown by the curve in Figure 6-28. The results in Figure 6-28 indicate that the fracture criterion under Mode I-III can be reasonably described by a quadratic equation in  $K_I$  and  $K_{III}$  such as given by equations (6-5) or (6-8) when symbol  $K_{II}$  is replaced by  $K_{III}$  in these equations. The results in Figure 6-28 show that an applied tearing mode stress intensity factor ( $K_{III}$ ) approximately equal to or less than 70 percent of  $K_{IIIc}$  has little effect on the opening mode stress intensity factor  $K_I$ , at which the specimen fails. Similar results for the combined Modes I-III interaction have been reported for 7075-T651<sup>(39)</sup>, DTD 5050 and HE 15W aluminum alloys<sup>(41)</sup> and K9 tool steel<sup>(41)</sup>. Similarly, applied  $K_I$  values approximately equal to or less than 70 percent of  $K_{Ic}$  have little effect on the tearing mode stress intensity factor  $K_{III}$  at which the specimen fails.

As mentioned in Section 6-3, these specimens were instrumented with clip gages to measure the axial and angular deflections across the crack plane as a function of applied tension and torsion, respectively. Figure 6-29 shows the tensile load versus tensile axial displacement and torque versus angular displacement for specimens subjected to various  $K_I/K_{III}$  ratios. Tensile load versus displacement curves do not exhibit any nonlinearity almost up to fracture

for any  $K_I/K_{III}$  ratio. However, torque versus angular displacement plots exhibit significant nonlinear behavior for specimens with  $K_I/K_{III}$  ratios smaller than 1.16, indicating plastic flow took place. Net shear stress ( $\tau = 16T_F/\pi d^3$ ) at failure for all specimens subjected to either torque  $T_F$  greater than 3500 in-lb (395 joules) or  $K_I/K_{III}$  ratios less than 1.20 was greater than the shear yield strength while the net tensile stress at failure for all specimens was less than 68 percent of tensile yield stress. For example, the specimen (3 RNB-10) tested under pure tension fractured at a net stress ( $\sigma = 4P_F/\pi d^2$ ) in the cracked section of 68 percent of tensile yield stress while the specimen (3 RNB-5) tested under pure torque failed at a net maximum shear stress ( $\tau = 16T_F/\pi d^3$ ) of 169 percent of shear yield stress. This as well as torque-angular displacement records show that extensive plastic flow took place prior to fracture under pure torsion.

Figure 6-30 shows the fracture surfaces of the specimens subjected to various loading conditions of  $K_I/K_{III}$ . The specimen subjected to pure tension (3 RNB-10) had a flat fracture. Specimens with  $K_I/K_{III}$  ratios of 2.30 and 1.16 (3 RNB-11 and 3 RNB-12) did not have a flat fracture. However, the fracture surfaces had the same texture as that of the pure tension fracture. This, and the Mode I-III fracture interaction results in Figure 6-28, indicate that Mode I ( $K_I$ ) played the predominant role in the fracture of these specimens. The texture of the fracture surface of the specimen subjected to a  $K_I/K_{III}$  ratio of 0.63 (3 RNB-9) was similar to that of the fracture under pure torque indicating Mode III ( $K_{III}$ ) played the dominant role in the fracture. The fracture surface of the specimen subjected to pure torsion was flat with shear rubbing marks.

#### 6.5.4 Mode I-II-III Tests with Flat Specimens

Test results and specimen details of flat slanted surface flawed specimens (Figure 6-9) are summarized in Table 6-9. These specimens were loaded to failure in tension at  $-200^\circ\text{F}$  (144K) in gaseous nitrogen environment to investigate fracture criterion under combined Mode I, II and III. The stress intensity factors  $K_I$  and  $K_{III}$  in Table 6-9 were calculated at the maximum depth (point A in Figure 6-31) according to equations (6-12) and (6-14).  $K_{III}$  at point A is zero. The stress intensity factors  $K_I$  and  $K_{II}$  in Table 6-9 were calculated

at the free surface (point B in Figure 6-31) according to equations (6-16) and (6-17).  $K_{III}$  at point B is zero as given by equation (6-18).

Figure 6-32 shows fracture surfaces for the specimens with  $\phi = 0, 25, 45$  and  $60$  degrees ( $0, 0.44, 0.79, 1.05$  rad). The fracture surfaces were completely flat for Mode I specimens. Fracture surfaces, for specimens with cracks inclined at  $\phi = 25$  and  $45$  degrees ( $0.44$  and  $0.79$  rad) had a stepped appearance near and around the flaw periphery. Fracture surfaces were flat and perpendicular to the applied loading from the end of the crack at the free surface to specimens edge, as shown in Figure 6-32. For specimens with cracks inclined at  $\phi = 0, 25$  and  $45$  degrees ( $0, 0.44, 0.79$  rad), fracture appeared to initiate around the point at the maximum crack depth where  $K_{II}$  is nearly zero and  $K_I$  and  $K_{III}$  are the highest. For the specimens with cracks inclined at  $\phi = 60$  degrees ( $1.05$  rad), the fracture initiated near the point on the crack periphery at the free surface and transverse fracture, perpendicular to applied loading, occurred. The fracture path did not intersect the flaw front other than at the front surface. The combined mode data are evaluated in terms of  $K_I$ - $K_{III}$  at the point of maximum crack depth, A and  $K_I$ - $K_{II}$  at the point near surface, B in Figure 6-31. Figure 6-31 also contains data of Specimens 3TSF-1 and 3TSF-2 of Table 6-5. Figure 6-31 suggests that applying  $K_{III}$  approximately up to 70 percent of  $K_{IIIc}$  has little effect on  $K_I$  at which fracture occurs.

#### 6.5.5 Mode I-II-III Tests with Round Specimens

Test results and specimen details of ten round specimens containing surface cracks (Figure 6-10) are summarized in Table 6-10. These specimens were loaded to failure at room temperature in pure tension, in combined tension and torsion and in pure torsion to study the fracture criterion under combined Mode I, II and III. For the cracked specimen under torsional loading only, both  $K_{II}$  and  $K_{III}$  are present along the periphery of flaw, (as shown by the results of three-dimensional frozen stress photoelastic experiments in Section 8) except  $K_{II}$  is negligible at the maximum crack depth and  $K_{III}$  is negligible near the free surface. Stress intensity factors are not shown in Table 6-10 since good estimates for stress intensity factors are not available for this specimen type.

Figure 6-33 shows a plot of COD (in the axial direction) versus tensile load and angular displacement across the crack plane versus torque for various ratios of applied tension stress to shear stress,  $\sigma/\tau$ . As seen from Figure 6-33, crack opening displacement and angular displacement are linear with respect to tensile load and torque, up to failure for the specimens subjected to  $\sigma/\tau$  ratios greater than 0.27. Specimen 3RSFB-8 was subjected to the simultaneous loading with a  $\sigma/\tau$  ratio of 0.27. Crack opening displacement versus tensile load behavior is linear until fracture occurred. However, angular displacement versus torque is nonlinear. The gross maximum shear stress at the outer fibers for this specimen was 100 ksi (690 MN/m<sup>2</sup>) which is over 70 percent of shear yield stress. The two displacement plots for 3RSFB-8 would indicate that shear yielding and warping occurred and probably flaw growth did not take place. Specimen 3RSFB-11 was subjected to pure torsion. As seen from Figure 6-33, a pop-in occurred at an applied torque of around 7200 in-lb (813 joules). A second pop-in occurred at 8400 in-lb (950 joules). The specimen failed at an applied torque of 10,100 in-lb (1152 joules). The gross maximum shear stress at outer fibers at failure was 149 ksi (1027 MN/m<sup>2</sup>) which is over 110 percent of shear yield stress.

Flaw dimensions in all specimens were comparable except for two specimens which had significantly large flaws. The range of flaw depths and lengths for the other eight specimens were 0.192 to 0.280 in. (4.88 to 7.11 mm) and 0.530 to 0.645 in. (13.46 to 16.38 mm), respectively. In the absence of a good estimate for the stress intensity factor for this problem, the results of these eight specimens are shown in Figure 6.34 in terms of the tensile stress at failure,  $\sigma_F$ , and the shear stress at failure,  $\tau_F$ . The actual failure stresses  $\sigma_F' = 4P_F/\pi D^2$ , and  $\tau_F' = 16T_F/\pi D^3$  for the specimens with flaw depth  $a$  ( $0.192 \text{ in} \leq a \leq 0.280 \text{ in}$  ( $4.88 \text{ mm} \leq a \leq 7.11 \text{ mm}$ )) were converted to failure stresses  $\sigma_F$  and  $\tau_F$  for the flaw depth of 0.240 in (6.10 mm) by multiplying  $\sigma_F'$  and  $\tau_F'$  by the factor  $\sqrt{0.240/a}$  where  $a$  is measured in in. or  $(\sqrt{6.10/a}$  where  $a$  is measured in mm). Failure stresses  $\sigma_F$  and  $\tau_F$  are plotted in Figure 6-34. Once again, the results show that the tensile stress at failure is almost unaffected by the presence of a shear stress up to 100 ksi (690 MN/m<sup>2</sup>) which is approximately 70 percent of shear stress at failure under pure shear.

Figure 6-35 shows a photograph of the fracture surfaces for these surface cracked cylindrical specimens for various ratios of  $\sigma_F/\tau_F$ . The specimen

subjected to pure tension had a completely flat fracture. Most of the middle portion of the fracture surfaces of the specimens subjected to  $\sigma_F/\tau_F = 1.12$  and  $0.61$  had textures similar to that of the pure tension specimens. Shear rubbing marks were observed on the periphery. The fractures appeared to be controlled by Mode I and to start at the maximum depth. The middle left portion of the fracture surface of the specimen subjected to  $\sigma_F/\tau_F = 0.27$  had a texture similar to that of the pure tension specimen and the other portion of the fracture resembled to that of the pure torsion specimen. The specimen subjected to pure torsion had a nearly flat fracture with shear rubbing marks over the fracture surface. From examination of the fracture surfaces, it appears that fracture in all these specimens initiated near the maximum crack depth. Thus, it seems that for this specimen-loading configuration, the fracture originated under combined Mode I-III loading conditions. Since the constraint to crack tip deformation is higher at the maximum crack depth than at the surface of the specimen, and since  $K_I$  and  $K_{III}$  are the highest at the maximum crack depth than at any point on the crack periphery of the specimen (as shown in Section 8), it is not surprising that the fracture did originate near the maximum crack depth.

#### 6.5.6 Fracture Criterion Under Mode I-III

A composite plot for the combined Mode I-III fracture test results is presented in Figure 6-36 as  $K_I/K_{Icr}$  versus  $K_{III}/K_{IIIcr}$  for round notched bar specimens, flat surface flawed specimens with inclined cracks and cylindrical surface flawed specimens of 4340 steel.  $K_{IIIcr}$  at  $-200^\circ\text{F}$  (144K) was not determined experimentally. Hence, the following linear relation was assumed for estimating  $K_{IIIcr}$  at  $-200^\circ\text{F}$  (144K).

$$\left. \frac{K_{IIIcr}}{K_{Icr}} \right|_{-200^\circ\text{F} \text{ (144K)}} = \left. \frac{K_{IIIcr}}{K_{Icr}} \right|_{\text{R.T.}} \quad (6-21)$$

Since all the surface-flawed cylindrical specimens had nearly the same flaw sizes, and the failure stresses  $\sigma_F$  and  $\tau_F$  are adjusted for a single flaw size, the ratios of  $K_I/K_{Icr}$  and  $K_{III}/K_{IIIcr}$  can be calculated with little error by the following equations.

$$K_I/K_{Icr} = \frac{\sigma_F}{\sigma_c} \text{ for the specimen subjected to pure tension} = \frac{\sigma_F}{\sigma_c} \quad (6-22)$$

$$K_{III}/K_{IIIcr} = \frac{\tau_F}{\tau_c} \text{ for the specimen subjected to pure torsion} = \frac{\tau_F}{\tau_c} \quad (6-23)$$

Figure 6-36 shows that the non-dimensionalized data, obtained from the room temperature testing of round notched bar specimens and surface flawed cylindrical specimens, and from -200°F (144K) testing of inclined surface flawed flat specimens, are in general agreement. The results in the plot bear out the same conclusions as drawn previously for the interaction of  $K_I$  and  $K_{III}$  on failure in Section 6.5.3 to 6.5.5. Figure 6-36 shows the probable fracture criterion and the lower bound of the fracture criterion for the combined Mode I-III loadings for 4340 steel. The probable fracture criterion and the lower bound of the fracture criterion are represented by the equations (6-24) and (6-25), respectively.

$$(K_I/K_{Icr})^2 + (K_{III}/K_{IIIcr})^{4.75} = 1 \quad (6-24)$$

$$(K_I/K_{Icr})^2 + (K_{III}/K_{IIIcr})^2 = 1 \quad (6-25)$$

## 6.6 CONCLUSIONS

Cracks subjected to combined Mode I-II crack surface deformations propagate in a plane that is rotated with respect to the original crack plane and the direction of crack propagation can be well predicted. The empirical relationship  $K_I + K_{II} \approx K_{Ic}$  or  $K_I/K_{Ic} + K_{II}/K_{IIc} = 1$  represents the fracture criterion adequately for 4340 steel specimens at -200°F (144K).

For cracks subjected to combined Mode I-III and I-II-III crack surface deformations, it was found that the application of  $K_{III}$  up to about 70 percent of  $K_{IIIc}$  has little effect on  $K_I$  at which fracture occurs. Similarly, the application of  $K_I$  up to about 70 percent of  $K_{Ic}$  has little effect on  $K_{III}$  at which fracture occurs. The lower bound of the fracture criterion  $F(K_I, K_{III})$  for 4340 steel can be adequately described by the quadratic equation  $(K_I/K_{Icr})^2 + (K_{III}/K_{IIIcr})^2$

## 7.0 FRACTURE IN COMBINED MODES IN 2219-T87 ALUMINUM AND 6Al-4V $\beta$ STA TITANIUM

This section describes the results of tests conducted on surface flawed cylindrical specimens of 2219-T87 aluminum and 6Al-4V  $\beta$ STA titanium under ambient room environment to study the effects of combined tension and shear stresses on fracture and cyclic flaw growth characteristics. General background on combined mode loading and objective of tests are described in Section 6.1. Test machine, setup and instrumentation used for these tests are identical to those described in Section 6.4. In Section 7.1, the test program and procedures are described. Section 7.2 contains description and analysis of static tests. Section 7.3 describes and interprets the results of cyclic tests.

### 7.1 TEST PROGRAM AND PROCEDURES

#### 7.1.1 Test Program for Static Specimens

Twenty-eight surface flawed cylindrical specimens of 2219-T87 aluminum, as shown in Figure 7-1, were loaded to failure in an ambient room air environment under combined tension and torsion loadings according to the test program outlined in Table 7-1. Twelve of these specimens had flaw dimensions  $a$  and  $2c$  (as shown in Figure 7-1) of approximately 0.44 in. (11.2 mm) and 1.15 in. (29.2 mm), respectively. The ratios  $a/2c$  and  $a/d$  for these specimens were approximately 0.4 and 0.3, respectively. These specimens were tested as shown in Figure 7-2. Three specimens were axially loaded to failure, one specimen was torqued to failure, four specimens were axially loaded to one of two different tensile stress levels and then were torqued to failure while maintaining the applied tensile load, and four specimens were loaded to one of two different shear stress levels and then were pulled to failure in tension while maintaining the applied torque. Test conditions and flaw dimensions for the other sixteen aluminum specimens are summarized in Table 7-1. Ratios  $a/2c$  and  $a/d$  for twelve specimens were approximately 0.3, and 0.2 and for the remaining four specimens were approximately 0.35 and 0.2, respectively.

Twenty-eight surface flawed cylindrical specimens of 6Al-4V  $\beta$ STA titanium, as shown in Figure 7-3, were tested in an ambient environment under combined tension and torsion loading, according to the test program outlined in Table 7-1.



Flaw dimensions  $a$  and  $2c$  for fourteen specimens were approximately 0.28 in. (7.1 mm) and 0.68 in. (17.3 mm), respectively. Ratios  $a/2c$  and  $a/d$  for these specimens were approximately 0.4 and 0.3, respectively. Flaw dimensions  $a$  and  $2c$  for the remaining fourteen specimens were 0.19 in. (4.8 mm) and 0.61 in. (15.5 mm), respectively. Ratios  $a/2c$  and  $a/d$  for these specimens were approximately 0.3 and 0.2, respectively. Loading combinations are described in Table 7-1.

#### 7.1.2 Test Program for Cyclic Specimens

Eighteen surface flawed cylindrical specimens of 2219-T87 aluminum, as shown in Figure 7-1, were cycled to failure in an ambient environment under combined tension and torsion loadings. Out of these eighteen specimens, nine specimens had flaw dimensions  $a$  and  $2c$  of approximately 0.29 in. (7.4 mm) and 0.95 in. (24.1 mm), respectively. Ratios  $a/2c$  and  $a/d$  for these specimens were nearly 0.3 and 0.2, respectively. The remaining nine specimens had flaw dimensions  $a$  and  $2c$  of approximately 0.42 in. (10.7 mm) and 1.11 in. (28.2 mm), respectively. Ratios  $a/2c$  and  $a/d$  for these specimens were approximately 0.4 and 0.3, respectively. The test program for these specimens is shown in Table 7-2.

Eighteen flawed cylindrical specimens of 6Al-4V BSTA titanium, as shown in Figure 7-4, were cycled to failure in an ambient room environment under combined tension and torsion loadings. The test program for these specimens is summarized in Table 7-2. As shown in Table 7-2, nine specimens had flaw dimensions  $a$  and  $2c$  of 0.19 in. (4.8 mm) and 0.50 in. (12.7 mm), respectively. For these specimens ratios  $a/2c$  and  $a/d$  were approximately 0.4 and 0.2, respectively. The remaining nine specimens had flaw dimensions  $a$  and  $2c$  of 0.28 in. (7.1 mm) and 0.70 in. (17.8 mm), respectively. These specimens had flaws with ratios  $a/2c$  and  $a/d$  as 0.4 and 0.3, respectively.

#### 7.1.3 Procedures

All aluminum specimens were machined from a 2.5 in. (63.5 mm) thick plate such that the crack propagation direction was always TS. All titanium specimens were machined from a 1.0 in. (25.4 mm) thick plate such that the crack propagation direction was LS. All static fracture as well as cyclic specimens of aluminum and titanium were instrumented with clip gages to continuously

measure both axial and angular displacement across the flawed cross section with respect to applied tension and torsion, respectively. Instrumentation and test setup are described in Section 6.4.

Cyclic stress ratio (minimum cyclic stress to maximum cyclic stress) was 0.05 for tension fatigue cycles and 0.0 for shear fatigue cycles. All aluminum and titanium specimens were cycled until either fracture occurred or fracture was imminent. Normally, a cyclic test could be terminated within a few cycles of specimen failure by observing COD output for tension loaded specimens and angular displacement output for the torsion loaded specimens. The tests were terminated just prior to failure so that flaw peripheries could be marked and seen after pulling them to failure in tension. Cyclic specimens subjected to tensile and shear stresses were cycled under simultaneously and synchronously applied axial and torsional loadings. Cyclic frequency was 20 cpm (0.33 Hz) for all specimens.

## 7.2 TEST RESULTS AND DISCUSSION

### 7.2.1 Static Fracture Tests of Aluminum

Specimen details and results of static fracture tests of twenty-eight 2219-T87 aluminum cylindrical specimens (Figure 7-1) are summarized in Tables 7-3 through 7-5. These specimens were loaded to failure at room temperature in combined tension and torsion loadings. Tension and torsion loadings were applied separately and the order of loading is shown in these tables. Shear stress  $\tau$ , given in these tables and subsequent tables, was calculated from the applied torque  $T$  as  $\tau = 16T/(\pi d^3)$ . Shear stress  $\tau$ , thus, is the maximum gross shear stress at the outer fibers of the cylindrical specimen.

Figure 7-5 contains typical plots of crack opening displacement (in the axial direction) versus tensile load and angular displacement across the crack plane versus torque for four specimens subjected to different ratios of tension stress at failure to shear stress at failure  $\sigma_F/\tau_F$ . Specimen 1A1-12 was subjected to a tensile load of 41.1 kips (0.184 MN). COD versus load behavior was linear. The specimen was then subjected to torsion while maintaining the tensile load. As the torque was applied COD remained constant initially and then started to increase as shown in Figure 7-5. Specimen 1A1-3 was subjected to a torque of 20,300 in-lb (2300 joules). While maintaining this torque

constant, the specimen was subjected to tensile load. The angular displacement remained constant initially and then started to increase with increasing load. Nonlinear behavior of the displacement for these two specimens can be due to any or all of the following factors: (1) plastic yielding around the flaw periphery, (2) warping of the flawed cross section, and (3) flaw growth. The possibility of flaw growth could not be ruled out since none of these specimens were unloaded and subjected to low stress fatigue cycles to mark the flaw peripheries. Specimen 1A1-10 was failed in pure torsion. The gross shear stress at the outer fibers of the specimen was 36.1 ksi which is about 10 percent higher than the shear yield strength of the material.

Table 7-3 contains test data for twelve specimens containing surface flaws of depth  $a \approx 0.44$  in. (11.2 mm) and  $2c \approx 1.15$  in. (29.2 mm). Since expressions for stress intensity factors are not available for the specimen-flaw-loading configurations and since flaw dimensions do not vary more than 5 percent between specimens, the results are plotted in terms of gross tensile stress at failure  $\sigma_F$  versus shear stress at failure,  $\tau_F$  in Figure 7-6. Figures 7-7 and 7-8 show similar plots for flaw dimensions of  $a \approx 0.30$  in. (7.6 mm), and  $2c \approx 0.98$  in. (24.9 mm),  $a \approx 0.26$  in. (6.6 mm) and  $2c \approx 0.75$  in. (19.0 mm), respectively. Failure stress  $\tau_F$  in pure shear ( $\sigma_F = 0$ ) in Figure 7-7 was estimated as 40.4 ksi ( $279 \text{ MN/m}^2$ ) from the failure stresses  $\tau_F$  in pure shear of aluminum specimen 1A1-10 and titanium specimens 4TR-12 and 4TR-27. Titanium specimen 4TR-12 has the same flaw shape and geometry ( $a/2c$  and  $a/r$ ) as the specimens in Figure 7-7. Titanium specimen 4TR-27 has the same flaw shape and geometry as the aluminum specimen 1A1-10. From these plots of Figures 7-6, 7-7 and 7-8, two observations can be made. (1) Presence of shear stress up to 30 ksi has small effect on tensile stress at which fracture occurs. (2) For the same flaw size and applied shear stress of approximately 30 ksi, if torque was applied prior to applying tension load, the specimen required higher tensile load to fail than when tensile load was applied prior to torsion.

The later observation may be explained as follows. When high shear stress is applied first, crack surfaces may overlap due to twisting and the crack may blunt due to yielding. Subsequently, when tensile load is applied, the crack would not open up as much as when tensile load is applied first. As a result, the specimen would require higher tensile load to fail when it is first subjected to high shear stress.

Figure 7-9 shows the fracture surfaces for the specimens subjected to various ratios of  $\sigma_F/\tau_F$ . Observations made of fracture surfaces of steel specimens in Section 6.5.5 (Figure 6-35) also apply to fracture surfaces of aluminum specimens. Careful examination of fracture surfaces of the specimens indicated that the fracture originated at the area near the point of maximum crack depth for most specimens. Fracture origin for some specimens, where torsion was applied prior to tensile load, could not be traced definitely. As mentioned before in Section 6.5.5 and as shown in Section 8, stress intensity factor  $K_I$  and  $K_{III}$  are maximum at the maximum crack depth and  $K_{II}$  is negligible there for the specimen subjected to combined tension and torsion. Also the constraint to the crack tip deformation is maximum there. It seems that for this specimen-loading configuration, the fracture originated mainly under combined Mode I-III conditions even though other points on the flaw periphery were subjected to all three modes of crack surface displacements. As described in Section 6.5.6, the ratios  $K_I/K_{Icr}$  and  $K_{III}/K_{IIIcr}$  can be calculated by equations (6-22) and (6-23) with little error from the failure stresses  $\sigma_F$  and  $\tau_F$  of the combined tension and torsion specimens and the failure stresses  $\sigma_c$  and  $\tau_c$  for the identical flawed specimens subjected to pure tension or torsion, respectively. As seen from Figure 7-6,  $\sigma_c$  and  $\tau_c$  for the specimens with flaw dimensions  $a \approx 0.44$  in. (11.2 mm) and  $2c \approx 1.15$  in. (19.2 mm) are 27.0 ksi (186 MN/m<sup>2</sup>) and 36.1 ksi (249 MN/m<sup>2</sup>), respectively. As seen from Figure 7-7,  $\sigma_c$  and  $\tau_c$  for the specimens with flaw dimensions  $a \approx 0.30$  in. (7.6 mm) and  $2c \approx 0.98$  in. (24.9 mm) are 34.2 ksi (236 MN/m<sup>2</sup>) and 40.4 ksi (279 MN/m<sup>2</sup>), respectively. Data of Figures 7-6 and 7-7 are plotted in Figure 7-10 as  $K_I/K_{Icr}$  or  $\sigma_F/\sigma_c$  versus  $K_{III}/K_{IIIcr}$  or  $\tau_F/\tau_c$ . Figure 7-10 also contains the probable fracture criterion (equation (6-24)) and the lower bound of the fracture criterion (equation (6-25)) from Figure 6-36 for 4340 steel specimens subjected to combined Mode I-III loadings. When data points with high shear stresses applied first to the specimens are weighed less or neglected, results in Figure 7-10 show that the fracture results of 2219-T87 aluminum specimens are fairly well described by the failure criterion of 4340 steel under combined Mode I-III given by equation (6-24). The results in Figure 7-10 bear out the same conclusions as drawn previously in Section 6.5.3 to 6.5.6.

### 7.2.2 Static Fracture Tests of Titanium

Static fracture toughness  $K_{IE}$  for 1.0 in. (25.4 mm) thick 6Al-4V  $\beta$ STA titanium

was determined with surface flawed specimens. As shown in Table 7-6, fracture toughness  $K_{Ic}$  at room temperature under an ambient environment was  $69.2 \text{ ksi}\sqrt{\text{in}}$  ( $76.1 \text{ MN/m}^{3/2}$ ) in the crack propagation direction LS. Mechanical properties of the material are given in Section 3.1.

Specimen details and results of static fracture tests of 6Al-4V  $\beta$ STA titanium cylindrical specimens are summarized in Table 7-7 and 7-8. These surface flawed cylindrical specimens were loaded to failure at room temperature in combined tension and torsion loading. Figure 7-11 contains typical plots of crack opening displacement versus tensile load and angular displacement versus torque for six specimens subjected to different ratios of axial tensile stress at failure to shear stress at failure. Observations made in the previous section for load-displacement plots of aluminum (Figure 7-5) apply for plots in Figure 7-11 also.

Table 7-7 contains test data for twelve specimens containing surface flaws of depth  $a \approx 0.19 \text{ in.}$  (4.8 mm) and  $2c \approx 0.61 \text{ in.}$  (15.5 mm). Results of Table 7-7 are plotted in terms of gross tensile stress at failure,  $\sigma_F$ , versus gross maximum shear stress at failure,  $\tau_F$ , in Figure 7-12. Figure 7-13 shows a similar plot for the results of Table 7-8 for flaw dimensions of  $a \approx 0.28 \text{ in.}$  (7.1 mm) and  $2c \approx 0.68 \text{ in.}$  (17.3 mm). Observations similar to those made for aluminum specimens from Figure 7-6 and 7-7 in the previous section, can be made from Figures 7-12 and 7-13. The data in Figures 7-12 and 7-13 show that tensile stresses at failure were affected little by the presence of shear stress up to 70 ksi (about 70 percent of shear stress at failure in pure torsion). Also data in Figures 7-12 and 7-13 show that for constant values of flaw size and applied torque, if torque is applied prior to applying tensile load, slightly higher tensile failure loads are obtained than when the tensile load is applied prior to tension.

Results of Figure 7-12 and 7-13 are shown in terms of  $K_I/K_{Ic}$  or  $\sigma_F/\sigma_c$  versus  $K_{III}/K_{IIIc}$  or  $\tau_F/\tau_c$ . As shown in Figure 7-12,  $\sigma_c$  and  $\tau_c$  for specimens of Table 7-7 ( $a \approx 0.19 \text{ in.}$  (4.8 mm)) are 100.0 ksi (689 MN/m<sup>2</sup>) and 106.2 ksi (732 MN/m<sup>2</sup>), respectively. From Figure 7-13,  $\sigma_c$  and  $\tau_c$  for specimens of Table 7-8 ( $a \approx 0.28 \text{ in.}$  (7.1 mm)) are 78.0 ksi (538 MN/m<sup>2</sup>) and 95.4 ksi (658 MN/m<sup>2</sup>), respectively. The probable fracture criterion and the lower bound of the

fracture criterion under combined Mode I-III of 4340 steel is also shown in Figure 7-14. The failure criterion of 4340 steel describes the combined mode fracture results of titanium quite well.

For pure torsion specimens of aluminum and titanium the gross shear stress at the surface of the specimen (where it is maximum) was higher than the calculated shear yield strength of the material. This could have an effect on the fracture criterion. If Mode I experimental results of surface flaws in the presence of plastic yielding<sup>(5,20)</sup> is used for the interpretation of the above results of pure torsion, it would indicate that the shear stress at failure under elastic conditions would be slightly higher. Thus, ratios  $K_{III}/K_{IIIcr}$  would be slightly smaller than those shown in Figures 7-10 and 7-14 and would have a small effect on the failure criterion.

Figure 7-15 shows fracture surfaces for six titanium specimens subjected to different ratios of  $\sigma_F/\tau_F$ . The specimens subjected to pure tension (4 TR-20) and pure torsion (4 TR-27) had flat fractures. Specimens subjected to tension and torsion both had antisymmetric fracture surfaces, as shown in Figure 7-15. Fracture surfaces of specimens subjected to  $\sigma_F/\tau_F = 2.28$  and 1.10 had textures similar to that of the pure tension specimen. Fracture surfaces of the specimens subjected to  $\sigma_F/\tau_F = 0.58$  and 0.30 had shear rubbing marks over the entire surface similar to pure torsion specimen.

From the results of aluminum (Figure 7-10), titanium (Figure 7-14), and steel (Figure 6-36) and combined Modes I and III results of 7075-T651 aluminum of Reference 39 (results not shown here), it can be concluded that the lower bound of the fracture criterion under combined Modes I and III loading can be well described by the quadratic equation in  $K_I/K_{Icr}$  and  $K_{III}/K_{IIIcr}$  given by the equation (6-25). This suggests that the failure criterion given by equation (6-25) is very likely applicable to other materials where flaws are subjected to Modes I and III crack surface displacements. The results also show that an applied tearing mode stress intensity factor  $K_{III}$  approximately equal to or less than 70 percent of  $K_{IIIcr}$  has little (less than 20 percent of  $K_{Icr}$ ) effect on the opening mode stress intensity factor  $K_I$  at which fracture occurs. Similarly, the application of  $K_I$  up to about 70 percent of  $K_{Icr}$  has little (less than 20 percent of  $K_{IIIcr}$ ) effect on the  $K_{III}$  at which fracture occurs.

### 7.2.3 Cyclic Tests

Specimen details and results of cyclic tests conducted on surface flawed cylindrical specimens of 2219-T87 aluminum (Figure 7-1) and 6Al-4V  $\beta$ STA titanium (Figure 7-4) are summarized in Tables 7-9 and 7-10, respectively. Approximate flaw sizes and ratios of applied tensile stress to shear stress  $\sigma/\tau$  are shown in Table 7-2. Some of the aluminum and titanium specimens were fatigued under pure tensile stresses. Maximum cyclic tensile stresses were approximately 90, 80 and 70 percent of the static failure stresses of the corresponding flaw size and material. Some of the aluminum and titanium specimens were fatigued under synchronously applied tensile and shear stresses. The ratios of applied tensile stress to shear stress,  $\sigma/\tau$ , were generally either 2 or 1. Maximum cyclic tensile and shear stresses were approximately 90, 80 and 70 percent of the static fracture tensile and shear stresses of the corresponding  $\sigma/\tau$  ratio, flaw size and material. As seen in Figures 7-6, 7-7, 7-12 and 7-13, the static tensile stresses at fracture for these two ratios of  $\sigma/\tau$  were at least greater than 80 percent of the static tensile fracture stresses under pure tension for the corresponding flaw sizes. Maximum cyclic shear stresses for the aluminum and titanium specimens cycled under pure torsion were between 60 to 75 percent of the static fracture shear stresses for the corresponding flaw size and material.

For the cyclic tests under combined tensile and shear stresses at a given  $\sigma/\tau$  ratio, each of the maximum cyclic tensile and shear stresses was set at a percentage X of the corresponding static tensile and shear failure stresses given by Figures 7-6, 7-7, 7-12 or 7-13. Previous experimental data<sup>(2-8)</sup> has shown that cyclic lives for precracked specimens are often primarily a function of the ratio of initial stress intensity factor to critical stress intensity factor,  $K_{Ii}/K_{Icr}$ . This ratio is equivalent to the ratio of the maximum cyclic stress to the static fracture stress of the specimen with the same flaw size. Thus,  $K_{Ii}/K_{Icr}$  is the same as X defined before. Hence, an analysis was undertaken to compare the cyclic lives for combined tension and shear tests with those obtained for pure tension tests of surface flawed specimens in which the ratio of initial to critical stress intensity factors  $K_{Ii}/K_{Icr}$  was equal to X<sup>(8)</sup>. Data of Tables 7-9 and 7-10 are shown in figures 7-16 and 7-17,

respectively, as  $X$  versus number of cycles to failure. Limited results of Figures 7-16 and 7-17 show that cyclic lives for combined tension and shear tests can be well predicted from the cyclic lives of the surface flawed specimens subjected to pure tension. However, this requires a knowledge of factor  $X$  which requires a knowledge of static fracture criterion under combined tensile and shear stresses.

Results in Figures 7-16 and 7-17 show that for the same value of  $X$ , cyclic lives for the specimens fatigued under pure tension stresses were significantly less than the cyclic lives for the specimens fatigued under pure shear stresses.  $X$ , here, is  $K_{II}/K_{I,CR}$  or  $K_{III}/K_{III,CR}$  depending upon tension or torsion loading. Results thus indicate that in these tests, at any given value of  $X$ , fatigue crack propagation rates for tension stresses were higher than those for shear stresses.

The fracture criterion under combined tension and shear in Figure 7-12 was obtained for a flaw size of  $a \approx 0.19$  in. (4.8 mm) and  $2c \approx 0.61$  in. (15.5 mm). However, eight cyclic specimens of titanium with small flaws had flaw dimensions  $a \approx 0.194$  in. (4.9 mm) and  $2c \approx 0.50$  in. (12.7 mm). One static specimen, 4TR-1, loaded to failure in pure tension, had a similar sized flaw as those in cyclic specimens. The static failure stress in pure tension of 4TR-1 was compared with the static failure stress in pure tension of other specimens with  $a \approx 0.19$  in. (4.8 mm) and  $2c \approx 0.61$  in. (15.5 mm). This showed that it would require 14 percent higher tensile stress to fail the specimen with  $a \approx 0.194$  in. (4.9 mm) and  $2c \approx 0.50$  in. (12.7 mm) than the stress required to fail the specimen with  $a \approx 0.19$  in. (4.8 mm) and  $2c \approx 0.61$  in. (15.5 mm). It was assumed that the fracture criterion under combined tension and shear for flaws of  $a \approx 0.19$  in. (4.8 mm) and  $2c \approx 0.50$  in. (12.7 mm) can be obtained from that of Figure 7-12 by multiplying tensile stress at failure and shear stress of failure by the factor 1.14. Static fracture stress computed this way was used to calculate factor  $X$  for flaws of  $a \approx 0.19$  in. (4.8 mm) and  $2c \approx 0.50$  in. (12.7 mm) in Figure 7-17.

Figure 7-18 shows the fracture surfaces of five specimens of aluminum fatigued under three different ratios of  $\sigma/\tau$ . Specimen 5A1-12 was fatigued under pure tensile stresses ( $\sigma/\tau = \infty$ ). Specimens 5A1-15 and 5A1-18 were fatigued under



synchronously applied tensile and shear stress with ratio  $\sigma/\tau = 1.0$ . Specimens 5A1-16 and 5A1-17 were fatigued under pure shear stresses ( $\sigma/\tau = 0$ ). Cyclic tests on 5A1-12, 5A1-16 and 5A1-18 were terminated a couple of cycles prior to failure and then the specimens were marked. Specimens cycled under pure tension had flaw growth in the plane of flaw and had a flat fracture. Out of plane flaw growth occurred in specimens subjected to combined tension and torsion loading. For unknown reasons, specimen 5A1-18 fatigued under  $\sigma/\tau = 1.0$  had a one sided out of plane flaw growth. Specimen 5A1-16, fatigued under pure shear stresses ( $\sigma/\tau = 0$ ) had flaw growth largely in the plane of flaw. Flaw growth in Specimen 5A1-17, fatigued under pure shear ( $\sigma/\tau = 0$ ), was also largely in the flaw plane. However, during the last cycle when fracture occurred, the flaw grew out of its plane. The angle between the fracture surface and the flaw plane was approximately 60 degrees (1.05 rad).

Figure 7-19 shows the fracture surfaces of four specimens of titanium fatigued under four different ratios of  $\sigma/\tau$ . As seen from the photograph in Figure 7-19, the flaw growth in specimens fatigued under pure tensile stresses ( $\sigma/\tau = \infty$ ) and combined tensile and shear stresses ( $\sigma/\tau = 2$  and  $\sigma/\tau = 1$ ) was nearly in the plane of the flaw. In fact, flaw growth in all specimens except Specimens 5TC-9 ( $\sigma/\tau = 0$ ), 5TC-18 ( $\sigma/\tau = 0$ ) and 5TC-15 ( $\sigma/\tau = 1.0$ ) was nearly in the plane of the crack. Specimens 5TC-9, 5TC-18 and 5TC-15 were the only specimens where fracture occurred while cycling (Table 7-10). In these three specimens also (as seen for Specimen 5TC-18 from the photograph in Figure 7-19), the flaw growth was nearly in the plane of flaw initially. Thus, it seems that the flaw grew out of its plane largely during the last cycles prior to fracture.

### 7.3 CONCLUSIONS

On the basis of examinations of the fracture surfaces, it was concluded that fractures in surface flawed cylindrical specimens subjected to combined Mode I-II-III crack surface displacements originated at or near the point of maximum crack depth where the constraint to crack tip deformation is maximum and only Mode I-III conditions existed.

Results obtained so far show that the failure criterion for 2219-T87 aluminum, 6Al-4V  $\beta$ STA titanium and high strength 4340 steel under combined Mode I and III

crack surface displacements can be adequately described by the single empirical equation of  $K_I/K_{Icr}$  and  $K_{III}/K_{IIIcr}$  given by equation (6-24). The results show that an applied tearing mode stress intensity factor  $K_{III}$ , less than 70 percent of  $K_{IIIcr}$ , has little (less than 20 percent of  $K_{Icr}$ ) effect on the opening mode stress intensity factor  $K_I$  at which fracture occurs. Similarly, the application of  $K_I$  up to about 70 percent of  $K_{Icr}$  has little (less than 20 percent of  $K_{IIIcr}$ ) effect on the  $K_{III}$  at which fracture occurs.

The lower bound of the fracture criterion under combined Mode I and III loading for the above three materials and 7075-T651 aluminum is well described by the quadratic equation of  $K_I/K_{Icr}$  and  $K_{III}/K_{IIIcr}$  given by equation (6-25). This suggests that the failure criterion given by equation (6-25) is very likely applicable to other materials where flaws are subjected to Mode I and III crack surface displacements.

Cyclic lives for surface flawed cylindrical specimens subjected to combined tension and torsion can be predicted from the cyclic lives of the surface flawed specimens subjected to pure tension and the static fracture criterion for the same specimen-flaw-configuration under combined tension and torsion.

## 8.0 EXPERIMENTAL DETERMINATION OF STRESS INTENSITY FACTORS USING PHOTOELASTIC TECHNIQUE

Two and three-dimensional photoelastic analyses have been used to determine stress distributions near crack tips and stress intensity factors for cracks in plates subjected to static and dynamic loading<sup>(50-62)</sup>.

Since analytical determination of stress intensity factors for surface flawed cylindrical specimens subjected to tensile or torsional loading is extremely difficult, photoelastic experiments utilizing stress freezing and slicing techniques were conducted to determine maximum shear stresses (isochromatics) near the notch tip. These maximum shear stresses were then used to determine stress intensity factors around the flaw periphery.

Stress distributions near a notch tip and their relationships with stress intensity factors are described in Section 8.1 for different loading conditions. Section 8.1 thus gives needed analytical expressions to evaluate data of photoelastic experiments. Test program, specimen preparation and experimental procedures are described in Section 8.2. Section 8.3 contains the photoelastic data and interpretation of data.

### 8.1 BACKGROUND FOR ANALYSIS

#### 8.1.1 Three-Dimensional Stress Distribution Near a Blunt Crack

In order to evaluate stress intensity factors using frozen stress photoelasticity procedures, the effects of inherent crack blunting involved in machining the crack into the specimen as well as the additional crack blunting occurring during the stress freezing cycle must be considered. The blunting changes the stress distribution near the crack tip. Stress distribution near a blunt crack (notch) can be estimated from an available solution for the near field stress distribution for elliptic and hyperbolic notches in a plate for the three modes of local crack deformation<sup>(63)</sup>. The expressions describing the stress distribution for elliptic and hyperbolic notches are identical. These stress field equations are quite similar to the corresponding equations for sharp plane cracks defined by equation (6-1) to (6-3) except the origin of blunt notch coordinate system is located at a distance  $\rho/2$  from the end of the notch as indicated in Figure 8-1 ( $\rho$  is the radius of the curvature

at the tip of the notch). It is assumed that  $\rho \ll a$ ; consequently terms of orders higher than  $\rho/a$  are neglected.

Expressions describing the stress fields near blunt crack tips are given below. Terms of the orders higher than  $(r)^{-1/2}$  are not included in the following expressions for stresses. The stress field expressions remain finite because of the restriction that  $r \geq \rho/2$ .

Mode I:

$$\sigma_{nn} = \frac{K_I}{(2\pi r)^{1/2}} \cos \frac{\theta}{2} (1 - \sin \frac{\theta}{2} \sin \frac{3\theta}{2}) - \frac{K_I}{(2\pi r)^{1/2}} \frac{\rho}{2r} \cos \frac{3\theta}{2} \quad (8-1a)$$

$$\sigma_{zz} = \frac{K_I}{(2\pi r)^{1/2}} \cos \frac{\theta}{2} (1 + \sin \frac{\theta}{2} \sin \frac{3\theta}{2}) + \frac{K_I}{(2\pi r)^{1/2}} \frac{\rho}{2r} \cos \frac{3\theta}{2} \quad (8-1b)$$

$$\tau_{nz} = \frac{K_I}{(2\pi r)^{1/2}} \sin \frac{\theta}{2} \cos \frac{\theta}{2} \cos \frac{3\theta}{2} - \frac{K_I}{(2\pi r)^{1/2}} \frac{\rho}{2r} \sin \frac{3\theta}{2} \quad (8-1c)$$

$$\sigma_{tt} = \nu(\sigma_{nn} + \sigma_{zz}) \quad (8-1d)$$

$$\tau_{nt} = \tau_{zt} = 0 \quad (8-1e)$$

Mode II:

$$\sigma_{nn} = -\frac{K_{II}}{(2\pi r)^{1/2}} \sin \frac{\theta}{2} (2 + \cos \frac{\theta}{2} \cos \frac{3\theta}{2}) + \frac{K_{II}}{(2\pi r)^{1/2}} \frac{\rho}{2r} \sin \frac{3\theta}{2} \quad (8-2a)$$

$$\sigma_{zz} = \frac{K_{II}}{(2\pi r)^{1/2}} \sin \frac{\theta}{2} \cos \frac{\theta}{2} \cos \frac{3\theta}{2} - \frac{K_{II}}{(2\pi r)^{1/2}} \frac{\rho}{2r} \sin \frac{3\theta}{2} \quad (8-2b)$$

$$\tau_{nz} = \frac{K_{II}}{(2\pi r)^{1/2}} \cos \frac{\theta}{2} (1 - \sin \frac{\theta}{2} \sin \frac{3\theta}{2}) - \frac{K_{II}}{(2\pi r)^{1/2}} \frac{\rho}{2r} \cos \frac{3\theta}{2} \quad (8-2c)$$

$$\sigma_{tt} = \nu(\sigma_{nn} + \sigma_{zz}) \quad (8-2d)$$

$$\tau_{nt} = \tau_{zt} = 0 \quad (8-2e)$$

Mode III:

$$\tau_{nt} = - \frac{K_{III}}{(2\pi r)^{1/2}} \sin \frac{\theta}{2} \quad (8-3a)$$

$$\tau_{zt} = \frac{K_{III}}{(2\pi r)^{1/2}} \cos \frac{\theta}{2} \quad (8-3b)$$

$$\sigma_{nn} = \sigma_{zz} = \sigma_{tt} = \tau_{nz} = 0 \quad (8-3c)$$

When the above stress field equations are compared with the corresponding equations of a sharp crack (equations (6-1), (6-2), (6-3)), it is seen that the above equations have an additional term for Modes I and II given by the second term containing  $\rho/2r$  in each equation. For Mode III, the stress equations for blunt notches and sharp cracks are identical. It is emphasized that  $r$  is defined differently for the blunt notch and the sharp crack.

Kassir and Sih<sup>(49)</sup>, and Shah and Kobayashi<sup>(64)</sup> have shown that the three-dimensional stress distribution near the boundary of a sharp planar crack bounded by a smooth curve (such as an elliptical crack or a crack shown in Figure 8-2) is given by equations (6-1) to (6-3) for two-dimensions when a local coordinate system, as shown in Figure 8-2, is used. For three-dimensional crack problems,  $n, z, t, r$  and  $\theta$  are defined as shown in Figure 8-2. It would be safe to assume that the three-dimensional stresses near a blunt planar crack bounded by a smooth curve would be the same as those given by equations (8-1) to (8-3) when  $r, \theta$  and  $\rho$  are defined as shown in Figure 8-3.

### 8.1.2 Stress Intensity Factors for a Blunt Crack from Isochromatics

From the frozen stress technique of three-dimensional photoelasticity, a pattern of isochromatics (maximum shear stress in the plane of slice) can be obtained. The photoelastic slices are taken in an  $n$ - $z$  plane for the notched specimens subjected to tension and the measured fringe orders (isochromatics) give the maximum shear stress  $\tau_{nz}$ , denoted by symbol  $\tau_{nz}|_{\max}$ .

$$\tau_{nz}|_{\max} = \left[ \left( \frac{\sigma_{nn} - \sigma_{zz}}{2} \right)^2 + \tau_{nz}^2 \right]^{1/2} \quad (8-4)$$

If the effect of the remote stress field (stresses described by terms of orders  $r$  higher than  $r^{-1/2}$ ) is neglected, then, the stress intensity factor  $K_I$  is expressed by the following equation when isochromatics are measured at a point  $(r, \theta)$  very near the crack tip ( $r \ll$  crack dimension).

$$K_I = \tau_{nz} \Big|_{\max} \left[ \frac{8\pi r}{\sin^2 \theta + (\rho^2/r^2)} \right]^{1/2} \quad (8-5)$$

If a solid containing a blunt crack is subjected to a loading which introduces either Mode II or both Mode II and III crack surface displacements (such as a surface flawed cylindrical bar subjected to pure torsion), the photoelastic slices are taken in an  $n$ - $z$  plane. The maximum shear stress  $\tau_{nz}$  given by the measured isochromatics is defined by equation (8-4). The stress intensity factor  $K_{II}$  is expressed by the following equation when isochromatics are measured at a point very near the crack tip.

$$K_{II} = \tau_{nz} \Big|_{\max} \left[ \frac{2\pi r}{1 + (0.25\rho^2/r^2) - (\rho/r) \cos \theta - 0.75 \sin^2 \theta} \right]^{1/2} \quad (8-6)$$

The Mode III stress intensity factor can be obtained from a slice taken in an  $n$ - $t$  plane. If the solid containing a blunt or sharp crack is subjected to a loading which introduces only Mode III crack surface displacement,  $K_{III}$  is given by the following equation when the isochromatics are measured near the crack tip.

$$K_{III} = - \frac{\tau_{nt} \sqrt{2\pi r}}{\sin(\theta/2)} \quad (8-7)$$

As seen from equation (8-3), for pure Mode III crack surface displacement,  $\sigma_{nn}$  and  $\sigma_{tt}$  are zero near the crack tip and hence the maximum shear stress  $\tau_{nt}$  is the same as  $\tau_{nt}$  given by equation (8-3a). If the solid containing a blunt crack is subjected to a loading which introduces both Mode II and III crack surface displacements,  $\sigma_{nn}$  and  $\sigma_{tt}$  are not zero near the crack tip for Mode II (as seen from equations (8-2)). Maximum  $\tau_{nt}$  measured by isochromatics of the slice in the  $n$ - $t$  plane is given by the following equation.

$$\tau_{nt} \Big|_{\max} = \left[ \left( \frac{\sigma_{nn} - \sigma_{tt}}{2} \right)^2 + \tau_{nt}^2 \right]^{1/2} \quad (8-8)$$

As observed from equations (8-2) and (8-3), stresses near the crack tip  $\sigma_{nn}$  and  $\sigma_{tt}$  involve only Mode II stress intensity factor  $K_{II}$  and  $\tau_{nt}$  involves only Mode III stress intensity factor  $K_{III}$ .  $K_{II}$  can be determined from a slice in the n-z plane with equation (8-6). Stress  $\sigma_{tt}$  in equation (8-2d) involves Poisson's ratio,  $\nu$ . Poisson's ratio for epoxy at freezing temperature is approximately 0.5. With equation (8-2d), equation (8-8) can be written as follows.

$$\tau_{nt}|_{\max} = \left[ \left( \frac{\sigma_{nn} - \sigma_{zz}}{4} \right)^2 + \tau_{nt}^2 \right]^{1/2} \quad (8-9)$$

$K_{III}$  can then be obtained with the following equations (8-10) and (8-11).

$$K_{III} = \frac{(2\pi r)^{1/2}}{\sin(\theta/2)} \left[ (\tau_{nt}|_{\max})^2 - \left( \frac{\sigma_{nn} - \sigma_{zz}}{4} \right)^2 \right]^{1/2} \quad (8-10)$$

$$\left( \frac{\sigma_{nn} - \sigma_{zz}}{4} \right)^2 = \frac{K_{III}^2}{8\pi r} \left[ \sin \frac{\theta}{2} \left( 1 + \cos \frac{\theta}{2} \cos \frac{3\theta}{2} \right) - \frac{\rho}{2r} \sin \frac{3\theta}{2} \right]^2 \quad (8-11)$$

In derivations of the above equations relating  $K_I$ ,  $K_{II}$  and  $K_{III}$  to the measured maximum shear stresses, nonsingular terms in stress equations (8-1) to (8-3) are not included. However, the remote stress field containing nonsingular constant terms does have an influence on the fringe pattern (maximum shear stress  $\tau_{nz}$ ) of Mode I loading conditions (52,54,58,65). As it happens, the remote stress field does not influence the fringe patterns giving maximum shear stresses  $\tau_{nz}$  and  $\tau_{nt}$  for Mode II and Mode III loadings (58,65,66,67). An estimate of the influence of the remote stresses on the determination of  $K_I$  can be made as follows.

Irwin (52), in a discussion of the photoelastic analysis of a running crack (51), developed a technique for the calculation of  $K_I$  from isochromatic patterns of a sharp crack ( $\rho = 0$ ). This technique involved superposing the remote stress parameter  $-\sigma_o$  to the stress equation of  $\sigma_{nn}$  given by equation (8-1).  $\sigma_o$  represented the applied stress  $\sigma_{nn}$  parallel to the crack at the boundary.  $\sigma_o$  is equal to  $\sigma$  for an infinite plate with a through crack subjected to uniaxial tension  $\sigma$ . The maximum shear stress is related to the stress intensity factor

$K_I$  and  $\sigma_o$  by the following equation for a sharp crack ( $\rho = 0$ ).

$$\tau_{nz}|_{\max} = \frac{1}{2} \left[ \left( \frac{K_I}{\sqrt{2\pi r}} \sin\theta + \sigma_o \sin \frac{3\theta}{2} \right)^2 + \sigma_o^2 \cos^2 \frac{3\theta}{2} \right]^{1/2} \quad (8-12)$$

Irwin also pointed out that a second relation can be obtained to solve for the two constants ( $K_I$  and  $\sigma_o$ ) by noticing that  $\partial\tau_{nz}|_{\max}/\partial\theta = 0$  at the tip of each isochromatic loop. However, this method is very sensitive to the accuracy of measurement<sup>(51)</sup> and additionally requires the isochromatic loops which were not obtained in the point by point experimental procedure used here. Following the work of Bradley and Kobayashi<sup>(54)</sup>,  $\sigma_o$  was taken the same as gross applied tensile stress to the specimen in analyses of photoelastic test data involving Mode I loading. Equation (8-12) has only one unknown constant,  $K_I$ .

## 8.2 TEST PROGRAM AND EXPERIMENTAL PROCEDURES

### 8.2.1 Test Program

Seven round specimens of 1.50 in. (38.1 mm) or 2.50 in. (63.5 mm) diameter and 10.0 in. (254.0 mm) length were machined from 3.0 in. (76.2 mm) diameter, 12.0 in. (304.8 mm) long bars of photoelastic cast epoxy PLM 4B. In specimens number 1 to 6, surface notches of depth "a" and length "2c", as shown in Figure 8-4, were introduced by a circular cutter with notch root radius of less than 0.001 in. (0.025 mm) and the included root angle of 30 degrees (0.52 rad). A notch was used rather than a sharp crack because the crack would be blunted during the thermal cycle and become a notch of varying root radii. Hence, a notch with a predetermined root radius is preferable. As shown in Table 8-1, Specimens 1 and 2 had a surface notch of depth  $a = 0.50$  in. (12.7 mm) and length  $2c = 1.65$  in. (41.9 mm). Ratios  $a/2c$  and  $a/D$  for these specimens were 0.3 and 0.2, respectively. Specimens 3 and 4 had surface notches of depth  $a = 0.75$  in. (19.1 mm) and  $2c = 1.90$  in. (48.3 mm). Ratios  $a/2c$  and  $a/D$  for these specimens were 0.4 and 0.3, respectively. Specimens 5 and 6 had surface notches of depth  $a = 0.30$  in. (7.6 mm) and  $2c = 1.00$  in. (25.4 mm) with ratios  $a/2c$  and  $a/D$  being 0.3 and 0.2, respectively. These flaw geometries were identical to specimens 1 and 2, but the diameter was 1.50 in. (38.1 mm). The purpose of these tests was to investigate whether nondimensional stress intensity factors obtained from photoelastic tests for these two series of tests of



different diameters are nearly the same or not. Flaw shapes and geometries ( $a/2c$  and  $a/D$ ) in photoelastic specimens were nearly identical to those in surface flawed cylindrical specimens of 2219-T87 aluminum and 6Al-4V  $\beta$ STA titanium (Section 7). Specimens 1, 3 and 5 were subjected to tensile loads only. Thus, Specimens 1, 3 and 5 were subjected to opening mode (Mode I) crack surface displacements only. Specimens 2, 4 and 6 were subjected to torsion only. These specimens were subjected to sliding (Mode II) and tearing (Mode III) modes of crack surface displacements.

A half inch (12.7 mm) deep circumferential notch, with similar notch root radius and included angle as surface notched specimens, was machined in Specimen 7. The diameter of the specimen at the notched section,  $d$ , was 1.50 in. (38.1 mm) and  $d/D$  ratio was 0.6 where  $D$  is the diameter of the specimen in the unnotched section. This specimen was loaded in pure tension. A good approximate stress intensity solution is available for this specimen. The purpose of testing this specimen was to compare the stress intensity factor obtained from the photoelastic technique of stress freezing and slicing with that given by the approximate solution and to verify accuracy of the photoelastic method.

### 8.2.2 Experimental Procedures

Specimens 1, 3, 5 and 7 were subjected to small tensile loads and Specimens 2, 4 and 6 were subjected to small torques, as shown in Table 8-1. All specimens were dead weight loaded in a stress freezing oven as shown in Figure 8-5. Ends of tension loaded specimens were wrapped with Teflon strips and were pressed into aluminum cups. Two end bolts in tension loading were self-aligning. In torsion loading, ends of specimens were cemented to aluminum caps or a pulley. In torsion loading, the upper end of the specimen was fixed stationary and the lower end was permitted to deform along a plumbed rod. Torque was applied through the pulley with dead weight, as shown in Figure 8-5. For the torsion loading, the dead weights of the lower half of the specimen and the attached loading jig were counterbalanced by a load applied on the lower end of the fixture. For every specimen a calibration specimen was prepared to determine photoelastic material fringe constant. The loaded specimen along with the calibration specimen were heated from room temperature to the critical temperature of 225°F (380K) at the rate of 3.33°F (1.85K) per hour. The loaded specimens were soaked at 225°F (380K) for 4 hours and then were cooled at 2.5°F

(1.39K) per hour to room temperature. Upon removal of load at the end of this thermal cycle, the specimen retains a frozen fringe pattern which is identical to that produced by the same load at the critical temperature. Moreover, this fringe pattern remains unaltered even when the model is subjected to machining as long as over heating does not take place. Four thin slices of approximately 0.04 in. (1.02 mm) nominal thickness were machined perpendicular to the plane of the crack for each specimen except Specimen number 7. Figure 8-6 shows the locations of the slices. For specimens subjected to torsion (2, 4, and 6), a subslice in the form of a rectangular parallelepiped was prepared from each slice as shown in Figure 8-6. For Specimen 7 (round notched bar in tension), only one diametral slice perpendicular to the plane of notch, was taken.

The notch root radius for each  $nz$  plane slice of tension loaded specimens was measured with a micrograph. Typical micrographs for three slices in  $nz$  planes for Specimen 1 are shown in Figure 8-7. These micrographs were taken with ordinary (nonpolarized light) at a magnification of 400X. Measured notch root radii for each specimen are shown in Table 8-1. At the critical temperature, the modulus of elasticity for the photoelastic material (epoxy) is quite small (around 3 ksi (20.7 MN/m<sup>2</sup>)). Hence, as mentioned before and as seen from Table 8-1, the applied freezing load or torque was kept quite small to avoid plastic deformation. Since the applied load was small and the slices were thin, the resultant photoelastic fringe orders were low. A precision polariscope having a parallel light field and polarizing prisms in combination with a sensitive photometer was used to detect the change of light intensity from point to point in the fringe pattern. Senarmont's principle of compensation in combination with a photometer was used to determine the fractional fringe order at selected points of the slice.

### 8.3 RESULTS AND DISCUSSION

#### 8.3.1 Circumferentially Notched Round Bar (Specimen 7)

A slice of 0.039 in. (0.976 mm) thickness passing through the center of the bar and perpendicular to the notch plane was taken for the circumferentially notched round bar (Specimen 7) in tension. Figure 8-8 shows measured fringe orders at various locations of  $n$  and  $z$  from the notch tip. As seen from

Figure 8-8, the highest fringe order was 0.361. From the calibration specimen and the thickness of the slice, the model fringe constant was determined as 25.0 psi ( $0.172 \text{ MN/m}^2$ ) per fringe order. The maximum shear stress in the plane of a slice at any point is then determined by the product of the model fringe constant and the fringe order at that point. The relationship between this maximum shear stress in the slice plane and the stress intensity factor for a blunt crack is described by equation (8-5) where the effect of the remote stress field (constant term in equation (8-1)) was not taken into account. Utilizing equation (8-5) and fringe order data given in Figure 8-8, stress intensity factors  $K_I$  were calculated for 3 values of notch root radii,  $\rho$ , and are shown in Figure 8-9 to 8-11. In Figure 8-9,  $\rho$  was assumed the same as the measured  $\rho$  of 0.002 in. (0.051 mm). For calculations of  $K_I$ ,  $\rho$  was assumed as 0.001 in. (0.025 mm) and  $\rho = 0.0$  in. (0.0 mm) in Figures 8-10 and 8-11, respectively. Average values of  $K_I$  were 7.18, 7.12 and 6.99  $\text{psi}\sqrt{\text{in}}$  (7.89, 7.82 and 7.68  $\text{KN/m}^{3/2}$ ) for the notch root radii of 0.002, 0.001 and 0.0 in. (0.051, 0.025, 0.0 mm), respectively. These results indicate that notch root radius over this range has a negligible effect on the value of  $K_I$ . Since notch root radii for surface flawed cylindrical specimens were smaller than 0.001 in. (0.025 mm) the notch root radii were assumed as 0.0 for the calculations of stress intensity factors. Results of  $K_I$  in Figures 8-9 to 8-11 show that  $K_I$  does not vary much from one point to another point. The maximum range of  $K_I$ , in these figures is less than 18 percent of the average stress intensity factor.

Based on approximate analyses of Paris and Sih<sup>(33)</sup>, Harris<sup>(48)</sup> and Bueckner<sup>(47)</sup>, the stress intensity factor for this specimen and applied load is 5.68, 5.73 and 6.10  $\text{psi}\sqrt{\text{in}}$  (6.25, 6.30, and 6.71  $\text{KN/m}^{3/2}$ ), respectively. It is seen that the average  $K_I$  from photoelastic results (neglecting the effect of the remote stress field) are about 25 percent higher than  $K_I$  calculated from the solution of Reference 48.

As mentioned before, the notch root radius was taken as zero in all of the subsequent calculations of stress intensity factors ( $K_I$  and  $K_{II}$ ). Equation 8-12 which includes the effect of remote stress field, was used to obtain stress intensity factors  $K_I$  (shown in Figure 8-12) at various points from photoelastic data of Figure 8-8. As seen from Figure 8-12,  $K_I$  varies significantly

from point to point. From equation (8-5) and equation (8-12) isochromatic fringe orders ( $i_{nz}|_{\max}$ ) are expected to be maximum at  $\theta = 90^\circ$  (1.57 rad), i.e., along the  $n = 0$  line. Thus, measurements of isochromatic fringe order would be least sensitive to measurement errors in  $n$  and  $z$  when measurements are made along the  $z$  axis. As seen from Figure 8-8, the fringe orders measured were very small and small errors in measurement could introduce significant errors in value of stress intensity factors. As expected from the above discussion, the least scatter in stress intensity factor existed along the line of  $n = 0.01$  in. (0.25 mm). As seen from Figure 8-12, the maximum percentage difference between any individual value of  $K_I$  along  $n = 0.01$  in. (0.254 mm) and the average value of  $K_I$  was less than 10 percent. For  $n > 0.01$  in. (0.25 mm), the stress intensity varies significantly. This behavior was also observed for every slice taken from tension loaded surface flawed cylindrical specimens. Hence, the calculations of stress intensity factor  $K_I$ , from photoelastic data, were carried out only for  $n = 0.01$  in. (0.25 mm) hereafter. The average value of the stress intensity factor along  $n = 0.01$  in. (0.254 mm) is  $5.79 \text{ psi}\sqrt{\text{in.}}$  ( $6.37 \text{ kN/m}^{3/2}$ ) which compares very well with the calculated value of  $5.73 \text{ psi}\sqrt{\text{in.}}$  ( $6.30 \text{ kN/m}^{3/2}$ ).

From the above results, it seemed that  $K_I$  calculated along the  $n = 0.01$  in. (0.25 mm) line from equation (8-12) (which included effects of remote stresses) was preferable to  $K_I$  calculated from equation (8-5) (which was based on singular stresses only). Hence, in the subsequent analyses of data of tension loaded surface flawed cylindrical specimens, stress intensity factors were calculated only with equation (8-12).

### 8.3.2 Tension Loaded Surface Flawed Cylindrical Specimens

Four slices of thickness ranging from 0.024 in. (0.61 mm) to 0.041 in. (1.04 mm) were taken at the locations shown in Figure 8-6 for each of the surface flawed cylindrical bars subjected to tension loading. Slice 1-2 in Specimen 1 and Specimen 3 broke while machining. Fringe orders were measured at various locations of  $n$ ,  $z$  from the notch tip and they are shown in Appendix A in Figures A-1 through A-10 for Specimens 1, 3 and 5. Figures A-1 through A-10 also show slice location, slice thickness and model fringe constant. Equation (8-12) was used to calculate stress intensity factors along  $n = 0.01$  in.

(0.25 mm) assuming notch root radius  $\rho$  was zero. The individual stress intensity factor at any point along  $n = 0.01$  in. (0.25 mm) for any given location on the flaw (a given slice) did not differ more than +8 percent from the average value of stress intensity factors at that location. Hence, the average value of  $K_I$  at each location is shown in Table 8-2 for Specimens 1, 3 and 5.

For the specimen flaw configurations tested, results in Table 8-2 show that the stress intensity factor  $K_I$  is maximum at the maximum depth of the flaw (location 1-4 in Figure 8-6) and is minimum at the intersection of the flaw periphery (location 1-1 in Figure 8-6) and the specimen surface.

Stress intensity factors  $K_I$  obtained from the photoelastic data at various locations of the flaw periphery were nondimensionalized by the stress intensity factor  $K$  given by each of the following three equations.

$$K = Y\sigma\sqrt{a} \quad (8-13)$$

$$K = 1.95 \sigma\sqrt{a} \quad (8-14)$$

$$K = 1.95 \sigma\sqrt{a/Q} \quad (8-15)$$

where  $\sigma$  is the gross tensile stress applied to the cylindrical specimen,  $a$  and  $2c$  are the flaw depth and the flaw length of the specimen (Figure 8-4).  $Q$  is related to  $a/2c$  and  $\sigma/\sigma_{ys} = 0$  as given by equation (2-1). Equation (8-13) represents the stress intensity factor for an edge cracked specimen with crack length of  $a$  and crack length to specimen width ratio given by  $a/D$ . The relationship between  $Y$  and  $a/D$  is given in Reference 47. Similar to an edge cracked specimen of finite width subjected to uniform tension, the surface flawed cylindrical specimen loaded in tension also experiences considerable bending due to asymmetric cross-section at the flaw plane. It can be shown that the ratio of the area occupied by the surface crack to gross area of the specimen cross section ( $\pi D^2/4$ ) is less than the ratio  $a/D$  for the flaw configurations considered in Table 8-2. Inferring from the above,  $K_I$  at the maximum depth for the surface flawed cylindrical specimen should be less than  $K$  given by equation (8-13). Thus, equation (8-13) would represent the upper bound of the stress intensity solution for a surface crack in a cylindrical specimen.  $K$ , given by equation (8-14) is the stress intensity factor for an edge crack

of length  $a$  in a semi-infinite plate. The lower bound of the stress intensity solution for the surface flawed cylindrical specimen can be represented by the stress intensity factor for a surface crack in a plate of thickness  $D$ . The stress intensity factor for a surface flaw in a plate for  $a/D < 0.5$  is given by equation (8-15).

Results of nondimensionalized stress intensity factors for location 1-4 (maximum crack depth) in Table 8-2 show that equations (8-13) and (8-15) represent upper and lower bound solutions for stress intensity factors for a surface flawed cylindrical specimen in tension.

Specimen 1 and 5 in Table 8-2 have the same flaw geometry, hence, nondimensionalized stress intensity factors obtained from photoelastic tests, ideally, should be the same. However, as seen from Table 8-2, nondimensionalized stress intensity factors for these two specimens at the same location of 1-1, 1-3 or 1-4 (same value of angle  $\theta$  in Figure 8-6) differ as much as 18 percent. This difference has to be due to experimental inaccuracies and scatter.

Table 8-2 also shows the ratios of stress intensity factor at surface  $K_I|_{1-1}$  (location 1-1) to that at maximum crack depth  $K_I|_{1-4}$  (Location 1-4). It is known that for an embedded elliptical crack in an infinite solid with the ratio of semi-minor to major axis as  $a/2c$ , the ratio of stress intensity factor at the semi-major axis to that at the semi-minor axis is given by  $\sqrt{a/c}$ . Table 8-2 shows that the ratio  $(K_I|_{1-1}/K_I|_{1-4})$  is approximately equal to or less than  $\sqrt{a/c}$ . The surface flaw in these specimens were part circular instead of semi-elliptical.

### 8.3.3 Surface Flawed Cylindrical Specimen in Torsion

#### 8.3.3.1 Sliding Mode Stress Intensity Factor, $K_{II}$

Four slices of thickness ranging from 0.025 in. (0.63 mm) to 0.040 in. (1.02 mm) were taken in  $nz$  planes at the locations shown in Figure 8-6 for each of the surface flawed cylindrical bars (Specimens 2, 4 and 6) subjected to pure torsion loading. Measured fringe orders at various locations of  $n, z$  in these slices are shown in Figure A-11 through A-21. Figures A-11 through A-21 also show slice location, slice thickness and fringe constant. From these measured maximum shear stresses,  $\tau_{nz}$ , at various points  $(n, z)$  in a slice, sliding mode

stress intensity factors  $K_{II}$  were computed according to equation (8-6) where the notch root radius  $\rho$  was assumed as 0.001 in. (0.025 mm) or zero. The variation between computed  $K_{II}$  at any point in the slice and the average  $K_{II}$  (arithmetic average of  $K_{II}$  at all points in the slice) for the slice (location) was less than +10 percent of the average  $K_{II}$ . Hence  $K_{II}$  values computed at all points in a slice were used to calculate the average  $K_{II}$  at the location of the slice for the specimen. The average  $K_{II}$  computed for  $\rho$  equal to zero at any location compared within one to three percent with the average  $K_{II}$  computed for  $\rho = 0.001$  in. (0.025 mm) at the same location. Average values of computed  $K_{II}$  at locations 1-1, 1-2, 1-3 and 1-4 (Figure 8-6) are given in Table 8-3 for Specimens 2, 4 and 6. Table 8-3 also shows the maximum gross shear stress  $\tau$  ( $\tau = 16T/\pi D^3$ ) applied to each of the above specimens.

Results in Table 8-3 show that  $K_{II}$  at maximum depth (location 1-4 in Figure 8-6) is less than eight percent of  $K_{II}$  at the intersection of flaw and specimen peripheries (location 1-1 in Figure 8-6). Results also show that for a surface flaw cylindrical specimen subjected to pure torsion,  $K_{II}$  is minimum at maximum flaw depth and  $K_{II}$  increases along the periphery.  $K_{II}$  is maximum at the flaw periphery near free surface of the specimen. Similar results are expected from intuition as well as the results of Kassir and Sih<sup>(49)</sup> for an embedded elliptical crack subjected to uniform shear stress.

Stress intensity factors at the surface of the specimen  $K_{II}|_{1-1}$  are nondimensionalized by the factor  $\tau\sqrt{\pi b}$  in Table 8-3. These nondimensionalized stress intensity factors for Specimens 2 and 6 are 0.80 and 0.67, respectively. Specimens 2 and 6 have similar specimen-flaw configurations. The nondimensionalized stress intensity factors at the surface for Specimens 2 and 6 differ by 16 percent. Once again, this difference has to be attributed to scatter, experimental inaccuracies and inaccuracies in the photoelastic test analysis.

The solution for the stress intensity factor of an embedded elliptical crack subjected to uniform shear  $\tau$  shows that  $K_{II}$  values at the major and minor diameters of the ellipse ( $K_{II}|_{2c}$  and  $K_{II}|_a$ ) are given by the following equations, respectively. (Figures 4(a) and 4(d) of Reference 49.)

$$K_{II}|_{2c} = 0.78 \tau \sqrt{\pi a} \quad 0.25 \leq a/2c \leq 0.50 \quad (8-16)$$

$$K_{II}|_a = 0 \quad 0 \leq a/2c \leq 0.50 \quad (8-17)$$

Stress intensity factors given by equations (8-16) and (8-17) compare very well with computed sliding stress intensity factors  $K_{II}|_{I-1}$  and  $K_{II}|_{I-4}$  (Table 8-3). The effect of linearly varying shear applied on the crack surface is to reduce  $K_{II}$  given by equation (8-16). The effect of the free surface near the flaw is to increase  $K_{II}$  given by equation (8-16). These two opposite effects seem to balance each other for the flaw configurations tested.

From the experimental results and for the range of flaw variables ( $0.3 \leq a/2c \leq 0.4$ ,  $0.2 \leq a/D \leq 0.3$ ), and within experimental accuracy, the stress intensity factor  $K_{II}$  at the surface (Location I-1 in Figure 8-6) can then be estimated by equation (8-16) with little error. Also, from experimental results,  $K_{II}$  at maximum depth (Location I-4 in Figure 8-6) can be estimated by the following equation.

$$\begin{aligned} K_{II}|_a &= 0.05 K_{II}|_{2c} \\ &= 0.04 \tau \sqrt{\pi a} \end{aligned} \quad (8-18)$$

### 8.3.3.2 Tearing Mode Stress Intensity Factor $K_{III}$

For Specimens 2, 4 and 6 loaded in pure torsion, a subslice in the form of a rectangular parallelepiped was prepared for each of the n-z plane slices, as shown in Figure 8-6. Rectangular subslices were taken at  $z = 0.02$  in. (0.51 mm) away from the notch plane. Measured maximum shear stresses  $\tau_{nt}$  at various locations of distance n are given in Table A-1 for these subslices.

Equations (8-10) and (8-11), along with already determined values of  $K_{II}$  at the location of the subslice (Table 8-3), were used to determine  $K_{III}$  at grid points of each subslice. Calculated  $K_{III}$  values varied significantly from point to point in the subslices. Variation in calculated  $K_{III}$  values at different points on the same subslice was as much as over 100 percent. For locations of  $n > 0.015$  in. (0.381 mm),  $K_{III}$  calculated for some subslices at locations I-1, I-2 and I-3 gave imaginary values (numbers) of  $K_{III}$ . As seen from equations



(8-2), (8-3) and (8-9), the maximum shear stress  $\tau_{nt}$  would be zero at  $z = 0$ . Measurement errors in  $z$  (location of the subslice) would significantly change the values of  $K_{III}$ . Computations for  $K_{III}$  were carried out for some cases assuming  $z = 0.01$  in. (0.25 mm). It was found that the effect of changing  $z = 0.02$  in. (0.51 mm) to  $z = 0.01$  in. (0.25 mm) was to decrease  $K_{III}$  at the same location from  $K_{III}$  for  $z = 0.02$  in. (0.51 mm) by as much as 50 percent at slice location 1-1 (Figure 8-6). However,  $K_{III}$  for the assumed value of  $z = 0.01$  in. (0.25 mm) was generally higher than  $K_{III}$  at the same location for  $z = 0.02$  in. (0.51 mm) for subslice location 1-4 (Figure 8-6). Also, for the assumed value of  $z = 0.01$  in. (0.25 mm), values of  $K_{III}$  were real numbers for all locations computed.

Since  $K_{III}$  was quite sensitive to values of  $z$  and since values of  $K_{III}$  at some locations were imaginary numbers, values of  $K_{III}$  are not shown. Basic data is presented in Table A-1.

#### 8.4 CONCLUSIONS

Results of photoelastic tests showed that for surface flawed cylindrical specimens tested in tension loading,  $K_I$  is maximum at the maximum flaw depth.  $K_I$  then gradually decreases along the crack periphery and is minimum at the intersection of the flaw periphery and the specimen boundary. Results also showed that  $K_I$  at maximum depth for this case can be bounded by stress intensity factor solutions for a single edge crack in a plate (equation (8-13)) and a surface flaw in a plate (equation (8-15)). For  $a/D = 0.2$ ,  $K_I$  at the maximum depth calculated by equation (8-15) underestimates the measured  $K_I$  by approximately 15 percent. For  $a/D = 0.3$ ,  $K_I$  at the maximum depth calculated by equation (8-13) overestimates the measured  $K_I$  by approximately 14 percent.

Results of photoelastic tests showed that for surface flawed cylindrical specimens tested under pure torsion,  $K_{III}$  is minimum at the maximum flaw depth and is maximum at the intersection of the flaw periphery and the specimen boundary. Values of  $K_{III}$  at the latter location is approximately 5 percent of  $K_{III}$  at the former location.  $K_{III}$  at the intersection of the flaw periphery and the specimen boundary can be calculated by equation (8-16) within an accuracy of about 10 percent for these specimen flaw configurations.

## REFERENCES

1. Tiffany, C. F., "Fracture Control of Metallic Pressure Vessels," NASA SP-8040, 1971.
2. Tiffany, C. F., Lorenz, P. M. and Hall, L. R., "Investigation of Plane Strain Flaw Growth in Thick-Walled Tanks," NASA CR-54837, 1966.
3. Tiffany, C. F., Lorenz, P. M. and Shah, R. C., "Extended Loading of Cryogenic Tanks," NASA CR-72252, 1967.
4. Hall, L. R., "Plane-Strain Cyclic Flaw Growth in 2014-T62 Aluminum and 6Al-4V (ELI) Titanium," NASA CR-72396, 1968.
5. Masters, J. N., Haese, W. P. and Finger, R. W., "Investigation of Deep Flaws in Thin Walled Tanks," NASA CR-72606, 1969.
6. Hall, L. R. and Finger, R. W., "Investigation of Flaw Geometry and Loading Effects on Plane Strain Fracture in Metallic Structures," NASA CR-72659, 1971.
7. Hall, L. R. and Finger, R. W., "Stress Corrosion Cracking and Fatigue Crack Growth Studies Pertinent to Spacecraft and Booster Pressure Vessels," NASA CR-120823, 1972.
8. Hall, L. R. and Bixler, W. D., "Subcritical Crack Growth of Selected Aerospace Pressure Vessel Materials," NASA CR-120834, 1972.
9. Irwin, G. R., "Crack Extension Force for a Part-Through Crack in a Plate," Journal of Applied Mechanics, Vol. 29, Trans. ASME, Vol. 84, 1962, pp. 651-654.
10. Green, A. E. and Sneddon, I. N., "The Distribution of Stress in the Neighborhood of a Flat Elliptical Crack in an Elastic Solid," Proceedings of the Cambridge Philosophical Society, Vol. 46, 1950, pp. 159-163.
11. Wigglesworth, L. A., "Stress Distribution in a Notched Plate," Mathematica, Vol. 4, 1947, pp. 76-96.
12. Kobayashi, A. S., "On the Magnification Factors of Deep Surface Flaws," Boeing Structural Research Memorandum No. 16, Dec. 1965.
13. Smith, F. W., "Stress Intensity Factors for a Semi-Elliptical Surface Flaw," Boeing Structural Development Research Memorandum No. 17, Aug. 1966.
14. Kobayashi, A. S. and Moss, W. L., "Stress Intensity Magnification Factors for Surface-Flawed Tension and Notched Round Bar," Proceedings of the Second International Conference on Fracture, Brighton, England, 1969.

15. Shah, R. C. and Kobayashi, A. S., "On the Surface Flaw Problem," The Surface Crack: Physical Problems and Computational Solutions, ASME, 1972, pp. 79-124.
16. Smith, F. W., "The Elastic Analysis of the Part-Circular Surface Flaw Problem by the Alternating Method," The Surface Crack: Physical Problems and Computational Solutions, ASME, 1972, pp. 125-152.
17. Rice, J. R. and Levy, N., "The Part-Through Surface Crack in an Elastic Plate," Journal of Applied Mechanics, Vol. 39, Trans. of ASME, Vol. 94, March 1972, pp. 185-194.
18. Miyamoto, H. and Miyoshi, T., "Analysis of Stress Intensity Factor for Surface-Flawed Tension Plate," High Speed Computing of Elastic Structure, Proc. of Symposium of IUTAM, Univ. de Liege, 1971, pp. 137-155.
19. Kantorovich, L. V. and Krylov, V. S., Approximate Methods of Higher Analysis, Wiley, New York, 1964.
20. Masters, J. N., Bixler, W. D. and Finger, R. W., "Fracture Characteristics of Structural Aerospace Alloys Containing Deep Surface Flaws," NASA CR-134587, 1973.
21. Olson, R. H., "Computer Plotting Pole Figures," Metallography, Vol. 5, 1972, pp. 369-371.
22. Shah, R. C. and Kobayashi, A. S., "Stress Intensity Factor for an Elliptical Crack Approaching the Surface of a Plate in Bending," Stress Analysis and Growth of Cracks, ASTM-STP 513, 1972, pp. 3-21.
23. Gross, B., "Stress Intensity Factors for Single Edge Notch Specimens in Bending and Tension by Boundary Collocation of a Stress Function," NASA TN D-2603, 1965.
24. Smith, F. W., Emery, A. F. and Kobayashi, A. S., "Stress Intensity Factors for Semi-Circular Cracks, Part 2 - Semi-Infinite Solid," Journal of Applied Mechanics, Vol. 34, Trans. ASME, Vol. 89, 1967, pp. 953-959.
25. Schroedl, M. A. and Smith, C. W., "Local Stresses Near Deep Surface Flaws under Cylindrical Bending Fields," Progress in Flaw Growth and Fracture Toughness Testing, ASTM-STP 536, 1973, pp. 45-63.
26. Grandt, A. F. and Sinclair, G. M., "Stress Intensity Factors for Surface Cracks in Bending," Stress Analysis and Growth of Cracks, ASTM-STP 513, 1972, pp. 37-58.
27. Anon. "Standard Method of Test for Plane-Strain Fracture Toughness of Metallic Materials, E399-72," Annual Book of ASTM Standards, Part 31.

28. Tiffany, C. F. and Masters, J. N., "Applied Fracture Mechanics," Fracture Toughness and Its Applications, ASTM-STP 381, 1965, pp. 249-278.
29. Bixler, W. D., "Comparison of Flaw Growth Characteristics Under Cryogenic Proof and Ambient Test Conditions for Apollo Titanium Pressure Vessels," Boeing Document D2-121700-1.
30. Hoepfner, D. W. et al, "Determination of Flaw Growth Characteristics of Ti-6Al-4V Sheet in the Solution - Treated and Aged Condition," NASA CR-65811, 1968.
31. Hall, L. R. and Tiffany, C. F., "Fracture and Flaw Growth Investigation for 2014-T6 Aluminum Weldments Used in Saturn II LH<sub>2</sub> Tanks," Boeing Document D5-15737, 1967.
32. Collipriest, J. E. and Kizer, D. E., "Saturn S-II Fracture Mechanics Research Program," NAR Document SD68-659, 1968.
33. Paris, P. C. and Sih, G. C., "Stress Analysis of Cracks," Fracture Toughness and Its Applications, ASTM-STP 381, 1965, pp. 30-83.
34. Erdogan, F. and Sih, G. C., "On the Crack Extension in Plates Under Plane Loading and Transverse Shear," Journal of Basic Engineering, Trans. ASME, Series D. Vol. 85, 1963, pp. 519-527.
35. Sih, G. C., "Introductory Chapter: A Special Theory of Crack Propagation," Methods of Analysis and Solutions of Crack Problems, edited by G. C. Sih, Noordhoff International Publishing, 1972.
36. Sih, G. C. and Macdonald, B., "What the Designer Must Know About Fracture Mechanics," Applications of Fracture Mechanics to Engineering Problems, Lehigh University Report IFSM 72-23, November 1972.
37. Palaniswamy, K. and Knauss, W. G., "Propagation of a Crack Under General, In-Plane Tension," International Journal of Fracture Mechanics, Vol. 8, March 1972, pp. 114-117.
38. Wu, E. M., "Application of Fracture Mechanics to Anisotropic Plates," Journal of Applied Mechanics, Trans. ASME, Series E. Vol. 89, 1967, pp. 967-974.
39. Wilson, W. K., "On Combined Mode Fracture Mechanics," Research Report 69-1E7-FMECH-R1, Westinghouse Research Laboratories, June 1969.
40. Iida, S. and Kobayashi, A. S., "Crack Propagation Rate in 7075-T6 Plates Under Cyclic Tensile and Transverse Shear Loadings," Journal of Basic Engineering, Trans. ASME, Series D. Vol. 91, 1969, pp. 764-769.

41. Pook, L. P., "The Effect of Crack Angle on Fracture Toughness," Journal of Engineering Fracture Mechanics, Vol. 3, No. 3, 1971, pp. 205-218.
42. Liu, A. F., "Crack Growth and Failure of Aluminum Plate under In-Plane Shear," AIAA Paper No. 73-253, 11th Aerospace Sciences Meeting, Washington, D.C., January 1973.
43. Unpublished Data, Boeing Aerospace Co., Seattle, Wash.
44. Roberts, R. and Kibler, J. J., "Mode II Fatigue Crack Propagation," Journal of Basic Engineering, Trans. ASME, Series D. Vol. 93, 1971, pp. 671-680.
45. Shah, R. C., "Fracture Under Combined Modes in 4340 Steel," Fracture Mechanics, ASTM-STP 560, 1974.
46. Erdogan, F. and Ratwani, M., "A Circumferential Crack in a Cylindrical Shell Under Torsion," International Journal of Fracture Mechanics, Vol. 8, 1972, pp. 87-95.
47. Brown, W. F. and Srawley, J. E., "Plane Strain Fracture Toughness Testing of High Strength Metallic Materials," ASTM-STP 410, 1966.
48. Harris, D. O., "Stress Intensity Factors for Hollow Circumferentially Notched Round Bars," Journal of Basic Engineering, Trans. ASME, Series D. Vol. 89, 1967, pp. 49-54.
49. Kassir, M. K. and Sih, G. C., "Three-Dimensional Stress Distribution Around an Elliptical Crack Under Arbitrary Loadings," Journal of Applied Mechanics, Trans. ASME, Series E. Vol. 89, 1966, pp. 601-611.
50. Post, D., "Photoelastic Stress Analysis for an Edge Crack in a Tensile Field," Proceedings of SESA, Vol. XII, 1954, pp. 99-116.
51. Wells, A. A. and Post, D., "The Dynamic Stress Distribution Surrounding a Running Crack - A Photoelastic Analysis," Proceedings of SESA, Vol. XVI, 1958 pp. 69-92.
52. Irwin, G. R., Discussion of Ref.51 above, Proceedings of SESA, Vol. XVI, 1958, pp. 93-96.
53. Fessler, H. and Mansell, D. O., "Photoelastic Study of Stresses Near Cracks in Thick Plates," Journal of Mechanical Engineering Science, Vol. 4, 1962, pp. 213-225.
54. Bradley, W. B. and Kobayashi, A. S., "An Investigation of Propagating Cracks by Dynamic Photoelasticity," Experimental Mechanics, Vol. 10, 1970, pp. 106-113.
55. Bradley, W. B. and Kobayashi, A. S., "Fracture Dynamics A Photoelastic Investigation," Engineering Fracture Mechanics, Vol. 3, 1971, pp. 317-332.

56. Smith, D. G. and Smith, C. W., "Influence of Precatastrophic Extension and Other Effects on Local Stresses in Cracked Plates Under Bending Fields," Experimental Mechanics, Vol. 11, 1971, pp. 394-401.
57. Marloff, R. H., Leven, M. N., Ringler, T. N. and Johnson, R. L., "Photoelastic Determination of Stress Intensity Factors," Experimental Mechanics. Vol. 11, 1971, pp. 529-539.
58. Smith, D. G. and Smith, C. W., "Photoelastic Determination of Mixed Mode Stress Intensity Factors," Engineering Fracture Mechanics, Vol. 4, 1972, pp. 357-366.
59. Marrs, G. R. and Smith, C. W., "A Study of Local Stresses Near Surface Flaws in Bending Fields," Stress Analysis and Growth of Cracks, ASTM STP-518, 1972, pp. 22-36.
60. Schroedl, M. A., McGowan, J. J. and Smith, C. W., "An Assessment of Factors Influencing Data Obtained by the Photoelastic Stress Freezing Technique for Stress Fields Near Crack Tips," Engineering Fracture Mechanics, Vol. 4, 1972, pp. 801-809.
61. Schroedl, M. A., McGowan, J. J. and Smith, C. W., "Determination of Stress Intensity Factors From Photoelastic Data with Application to Surface Flaw Problems," Virginia Polytechnic Institute and State University Report VPI-E-73-1, 1973.
62. Harms, A. E. and Smith, C. W., "Stress Intensity Factors for Long, Deep Surface Flaws in Plates Under Extensional Fields," Virginia Polytechnic Institute and State University Report VPI-E-73-6, 1973.
63. Creager, M. and Paris, P. C., "Elastic Field Equations for Blunt Cracks with Reference to Stress Corrosion Cracking," International Journal of Fracture Mechanics, Vol. 3, 1967, pp. 247-252.
64. Shah, R. C. and Kobayashi, A. S., "On the Parabolic Crack in an Elastic Solid," Engineering Fracture Mechanics, Vol. 1, 1968, pp. 309-325.
65. Williams, M. L., "On the Stress Distribution at the Base of a Stationary Crack," Journal of Applied Mechanics, Vol. 24, Trans. ASME, Vol. 79, 1957, pp. 109-114.
66. Hult, J. A. H. and McClintock, F. A., "Elastic Plastic Stress and Strain Distribution Around Sharp Notches Under Repeated Shear," Ninth International Congress of Applied Mechanics, Vol. 8, Brussels, 1956, pp. 51-58
67. Wade, B. G., "A Photoelastic and Numerical Study on Fracture Dynamics of Stressed Panels," Ph.D. Thesis, University of Washington, 1973.

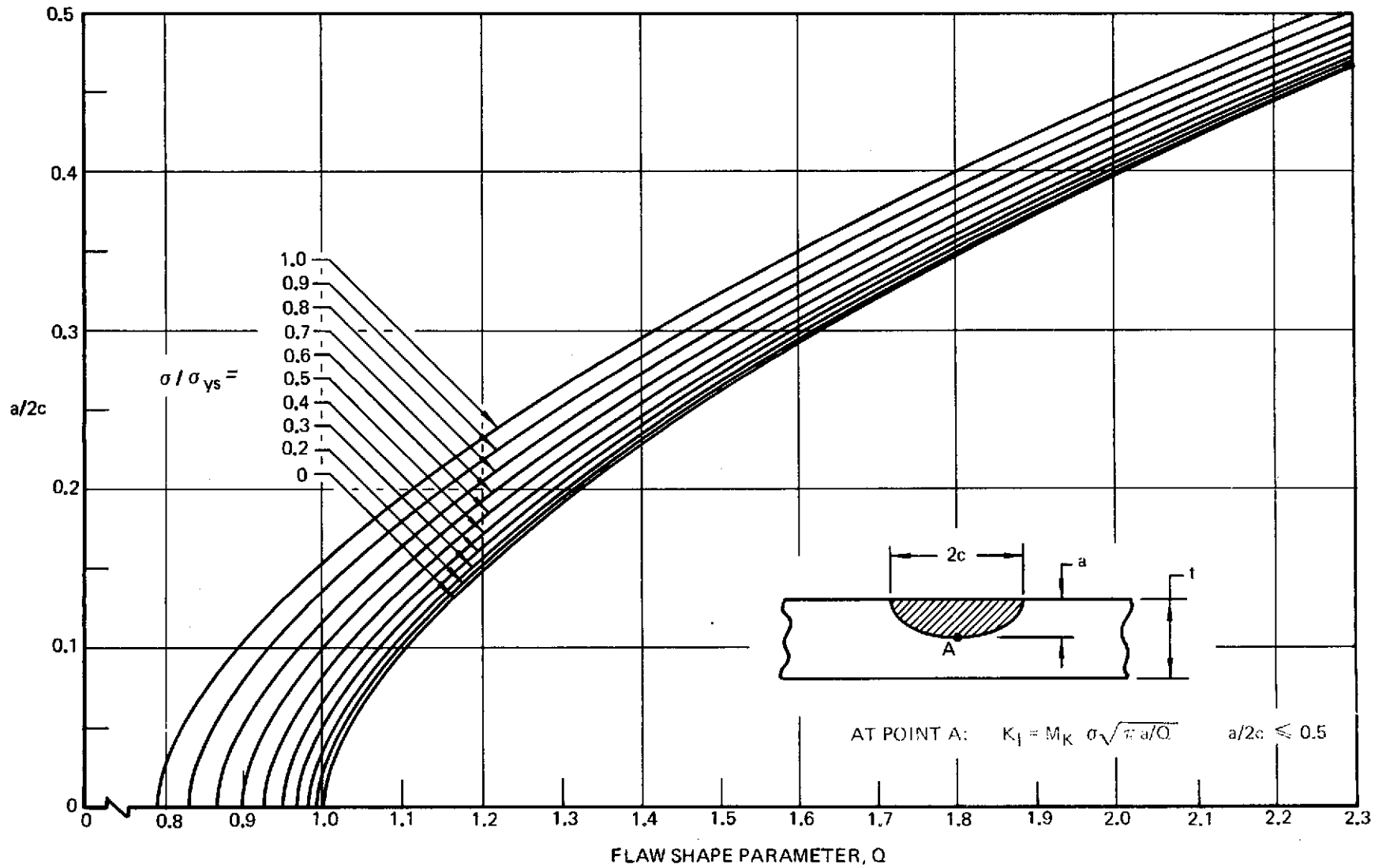


Figure 2-1: Shape Parameter Curves for Surface Flaws

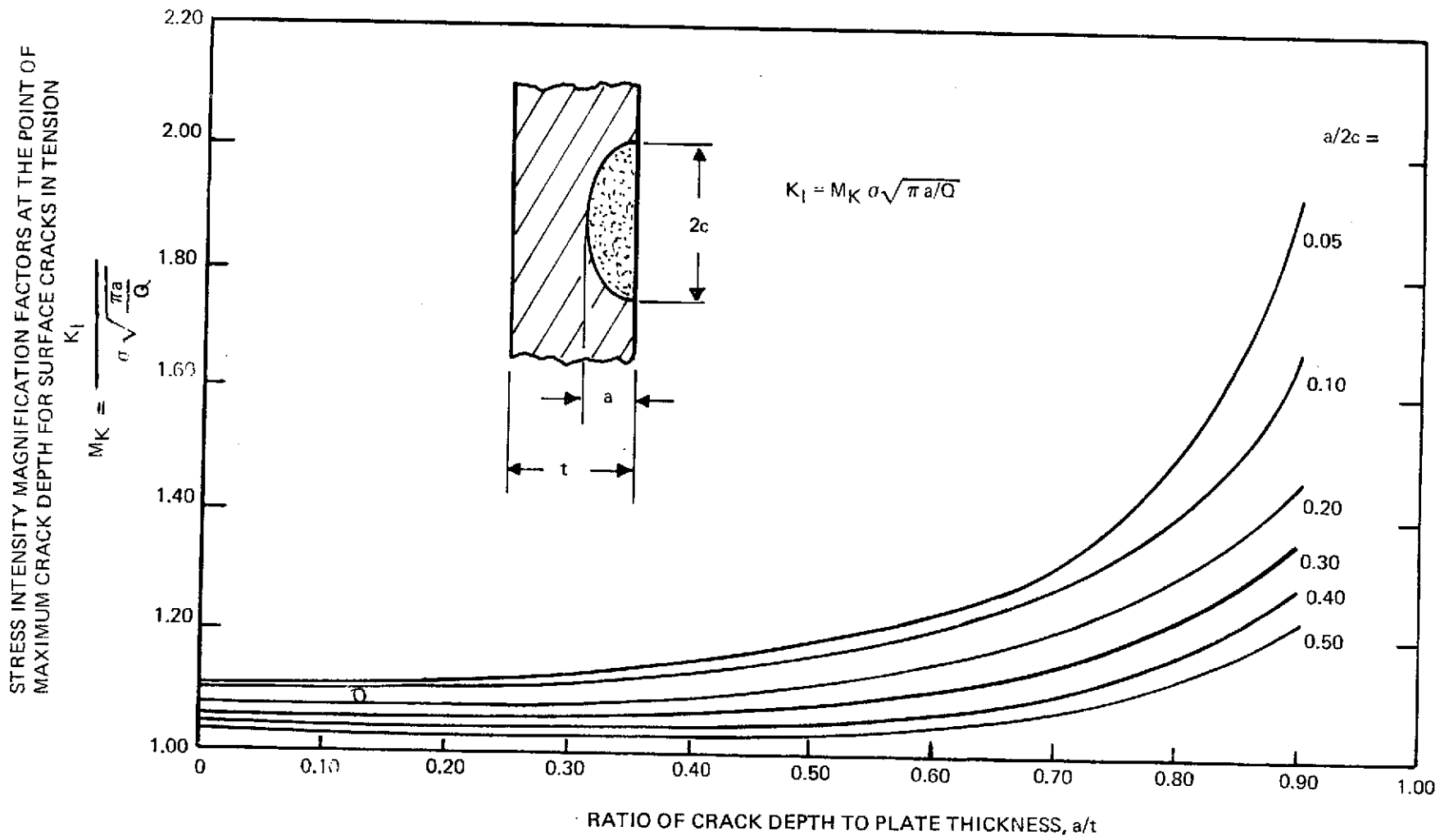
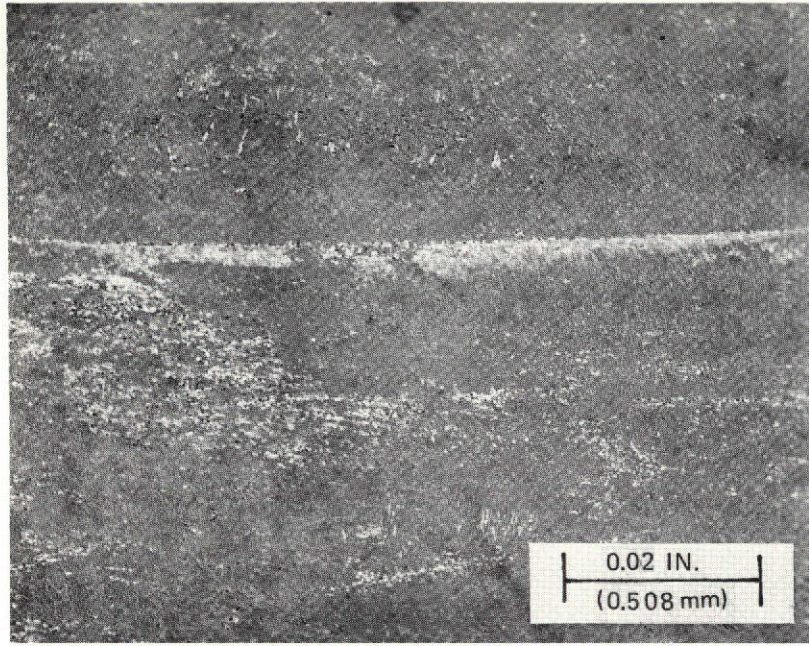


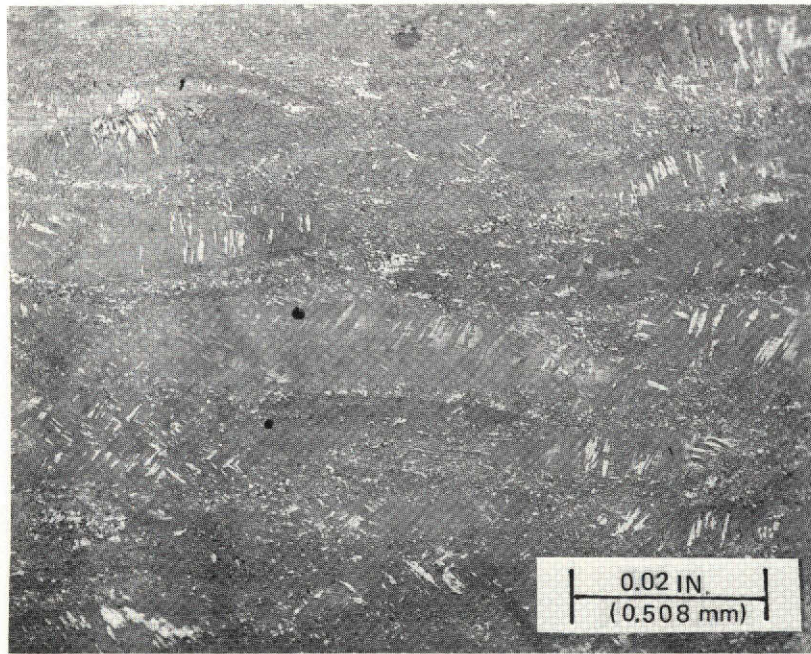
Figure 2-2: Estimated Elastic Stress Intensity Magnification Factors at Maximum Crack Depth for Surface Cracks in Tension (Reference 15)





STA, TOP

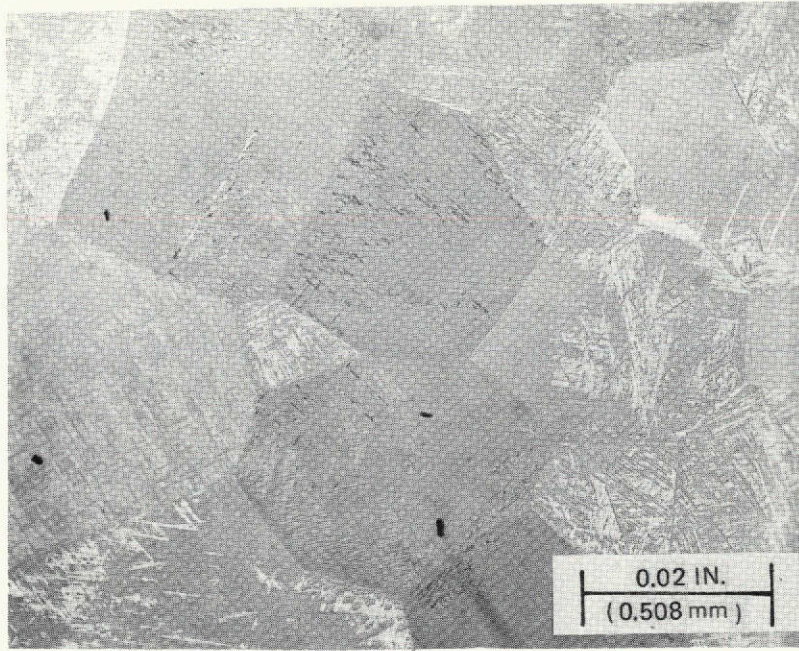
ANODIZE



STA, SIDE

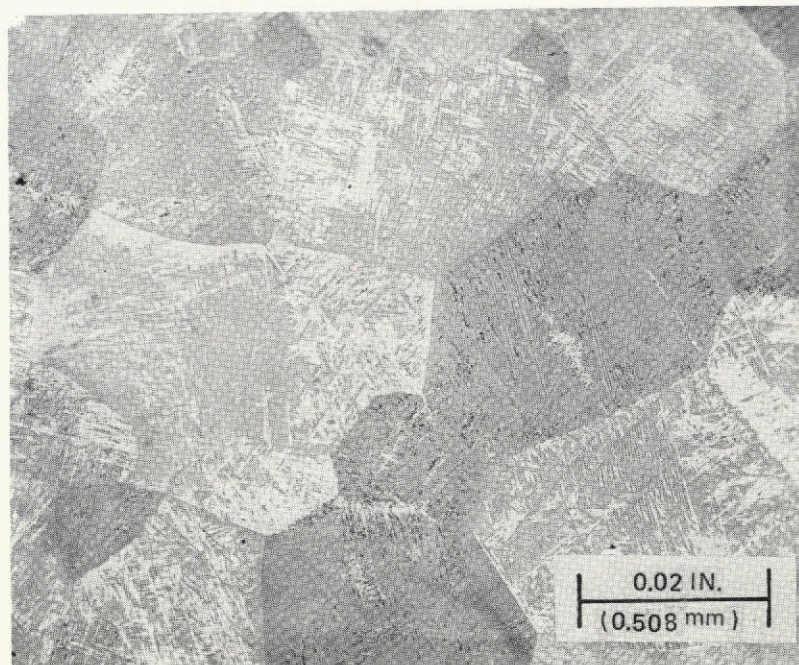
ANODIZE

*Figure 3-1: Microstructure For 0.375 in. (9.52 mm) Thick 6Al-4V STA Titanium*



$\beta$ -STA, TOP

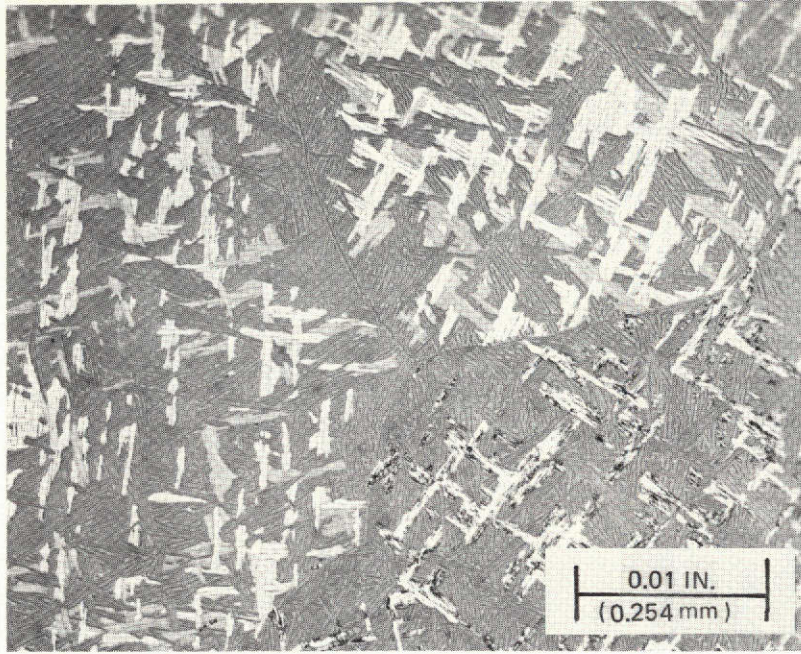
ANODIZE



$\beta$ -STA, SIDE

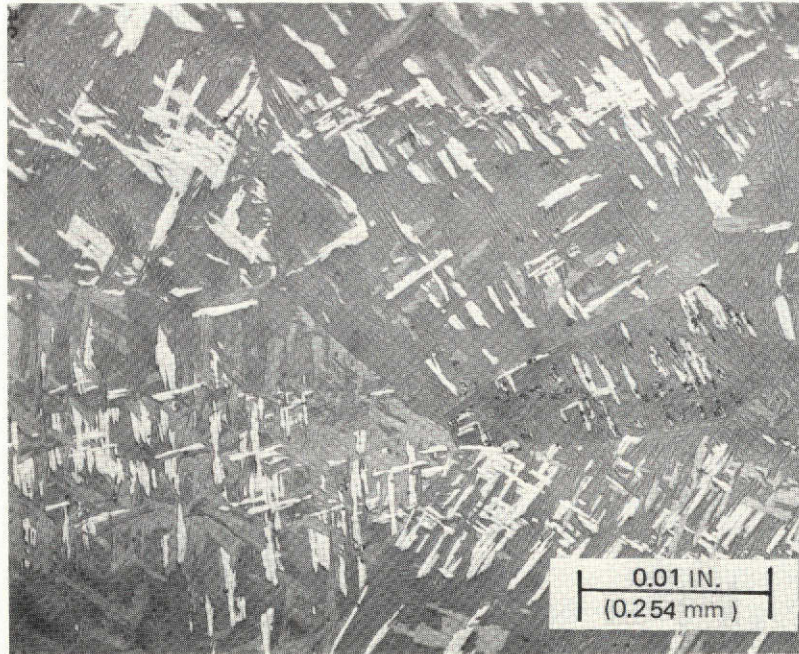
ANODIZE

Figure 3-2: Microstructure For 0.375 in. (9.52 mm) Thick 6Al-4V  $\beta$ -STA Titanium



$\beta$ -STA, TOP

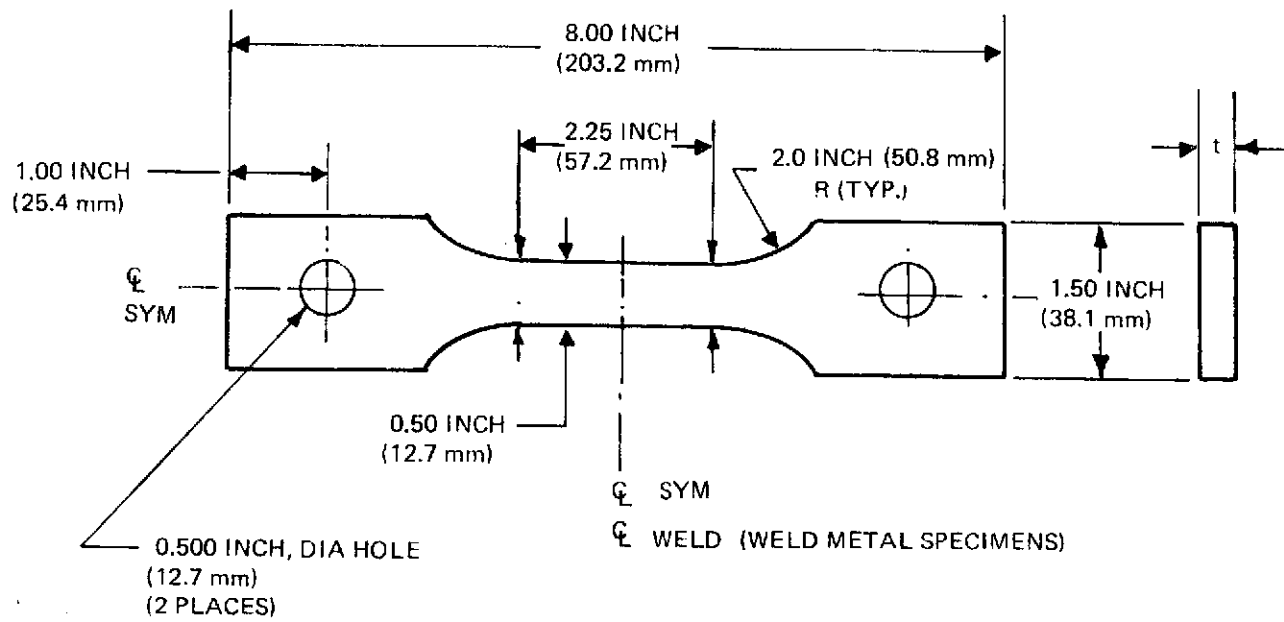
ANODIZE



$\beta$ -STA, SIDE

ANODIZE

Figure 3-3: Microstructure For 1.0 in. (25.4 mm) Thick 6Al-4V  $\beta$ STA Titanium



ALLOY	DIMENSION "t"
2219-T87 ALUMINUM	0.50 INCH (12.7 mm)
5Al-2.5Sn (ELI) TITANIUM	0.37 INCH (9.4 mm)
6Al-4V TITANIUM STA & $\beta$ -STA	0.20 INCH (5.1 mm)
4340 STEEL	0.25 INCH (6.4 mm)

Figure 3-4: Tensile Specimen For Mechanical Property Measurements

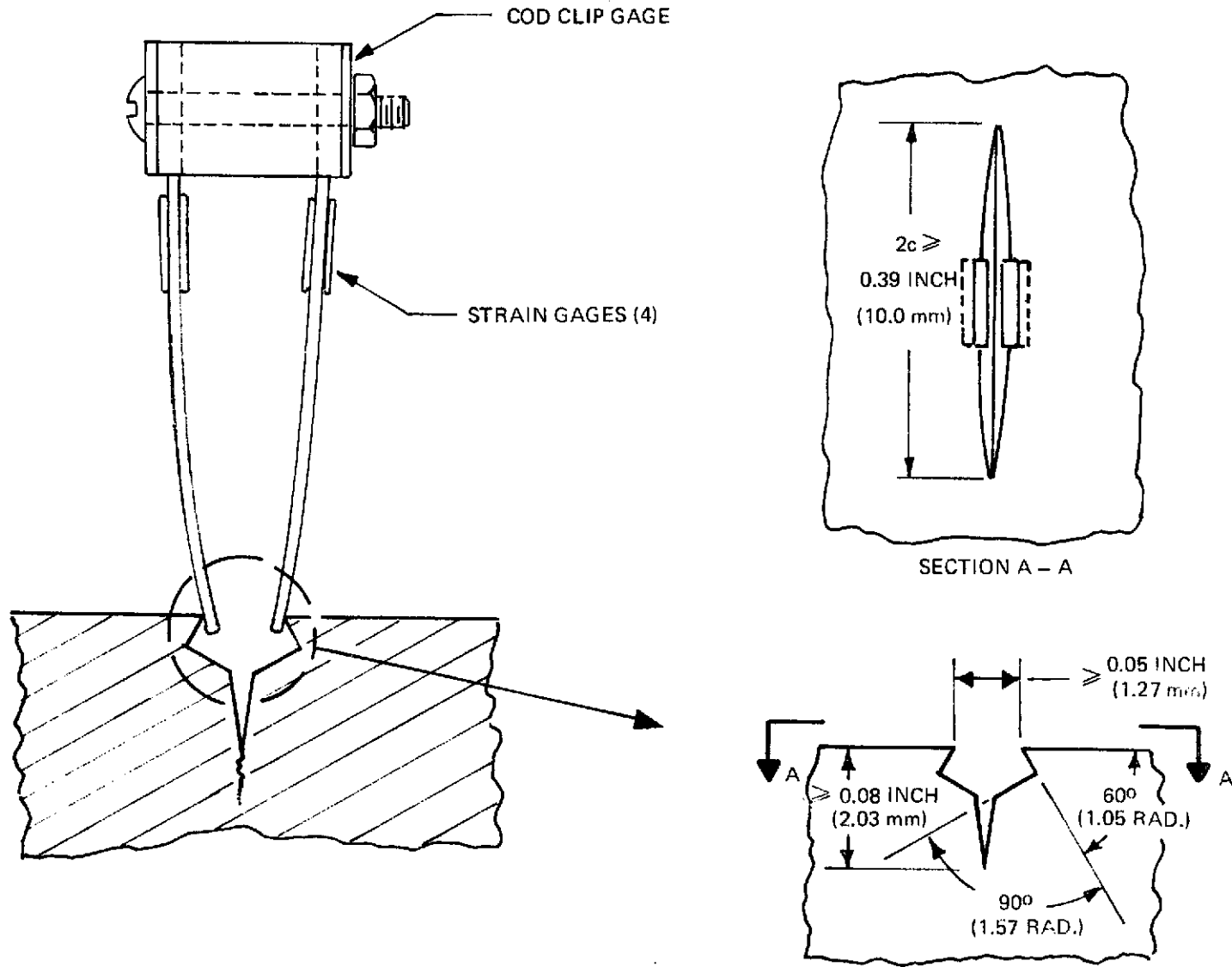


Figure 3-5: Clip Gage Instrumentation for Large Surface Flaws

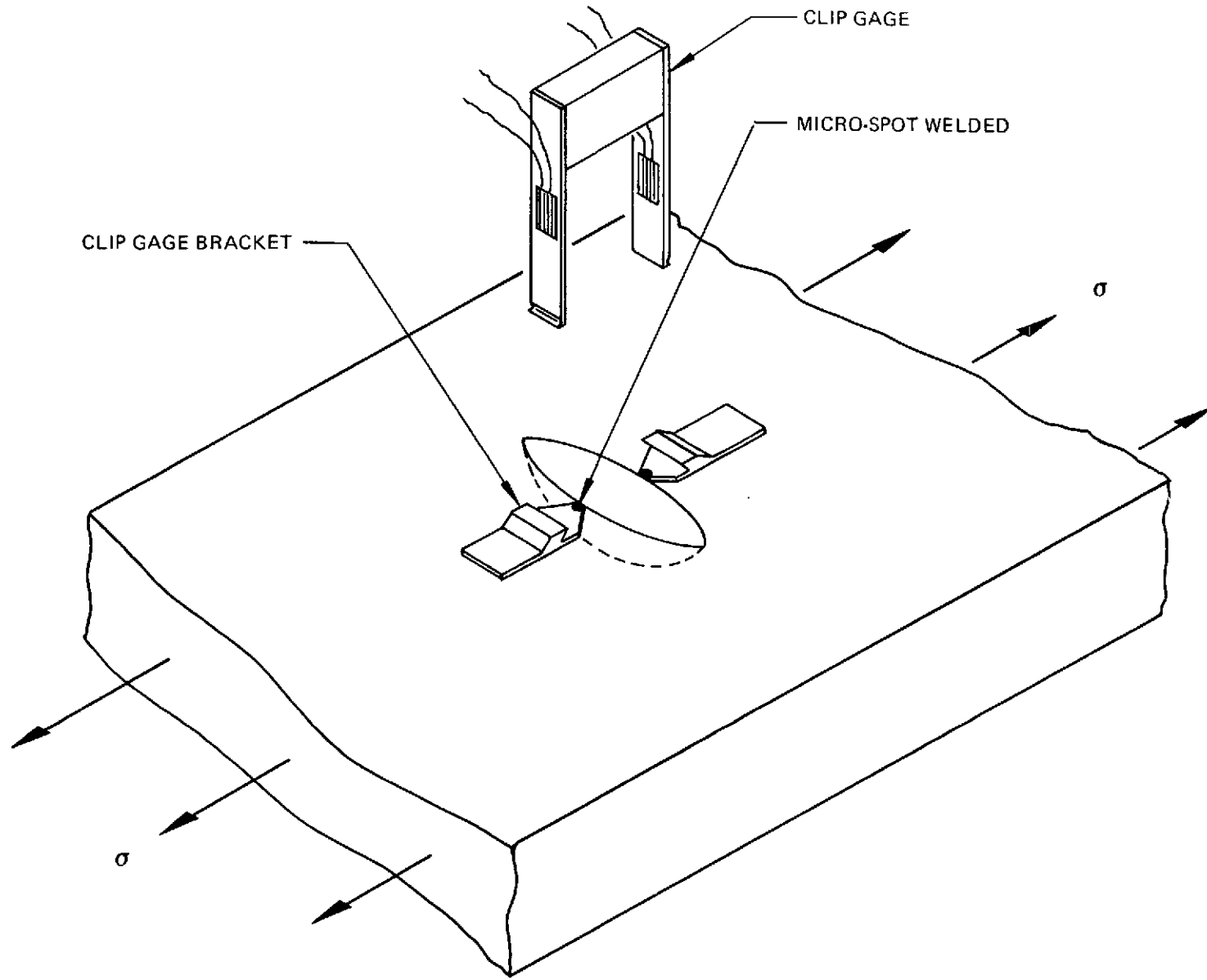


Figure 3-6: Clip Gage Instrumentation for Small Surface Flaws

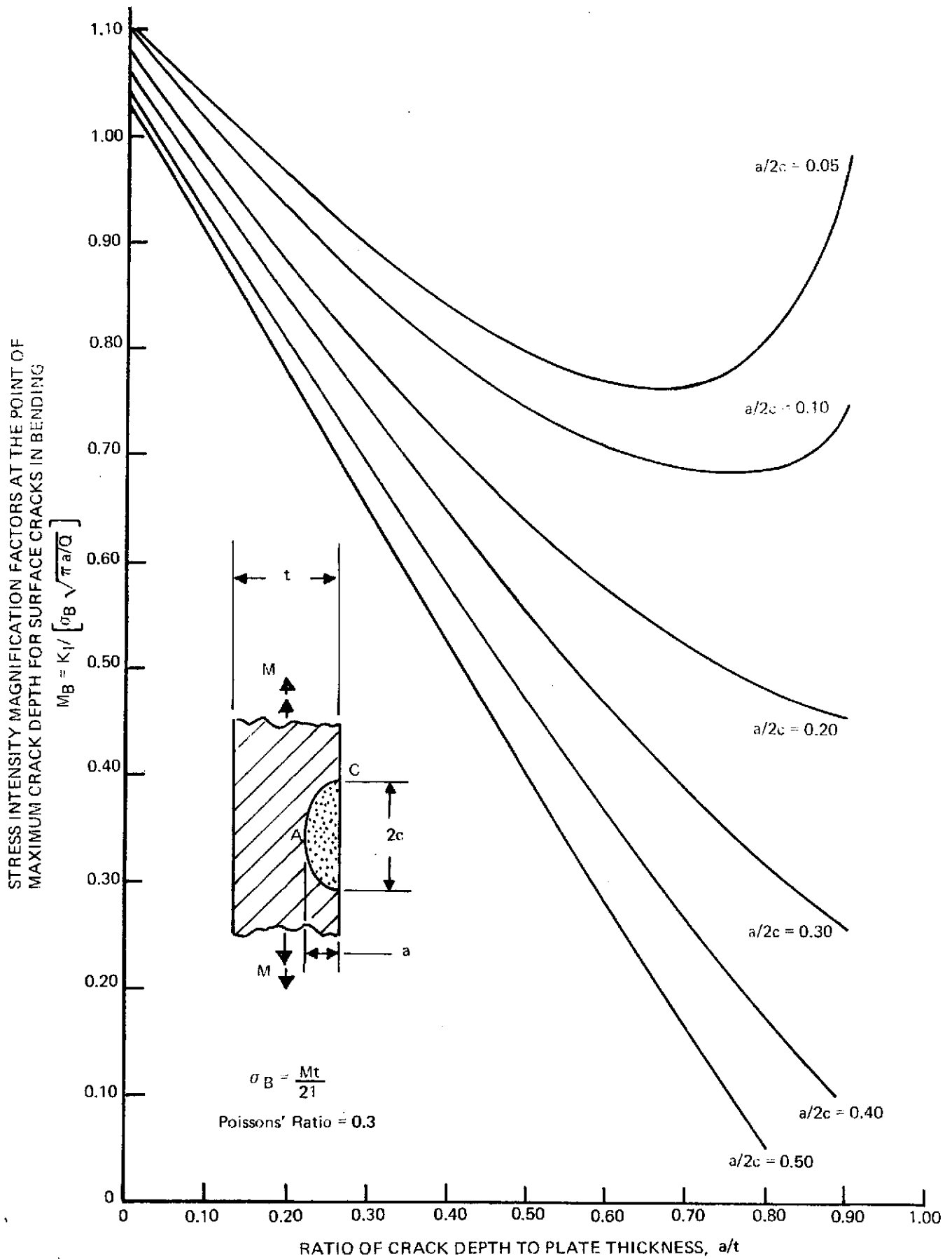
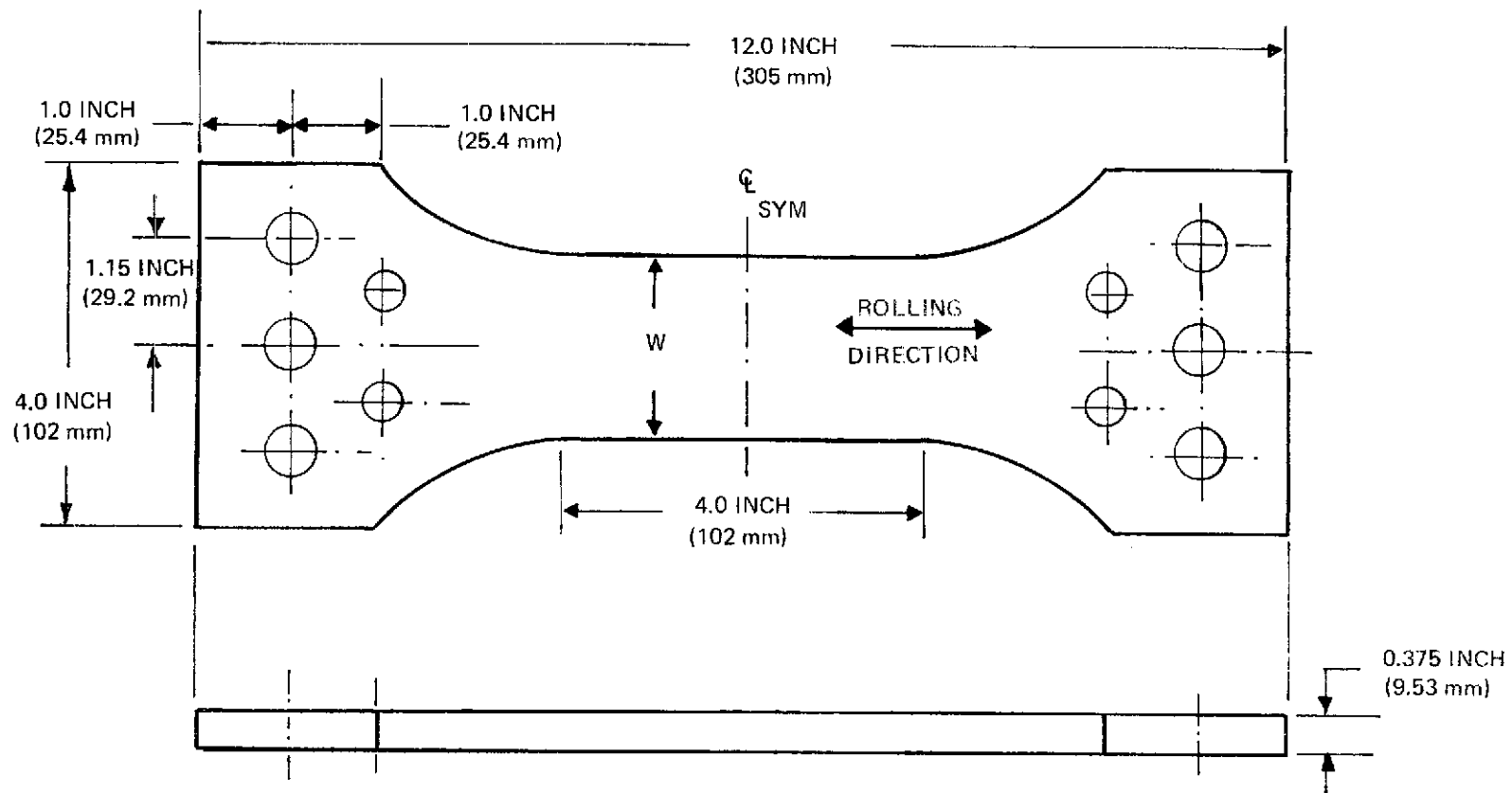


Figure 4-1: Estimated Elastic Stress Intensity Magnification Factors For Surface Cracks in Bending (Reference 15 or 22)



W INCH(mm)	NO. OF SPECIMENS
2.50 (63.5)	2
2.00 (50.8)	2

Figure 4-2: Specimen Configuration for Static Fracture Toughness Tests of 5Al-2.5 Sn (ELI) Titanium at -320F (78K)



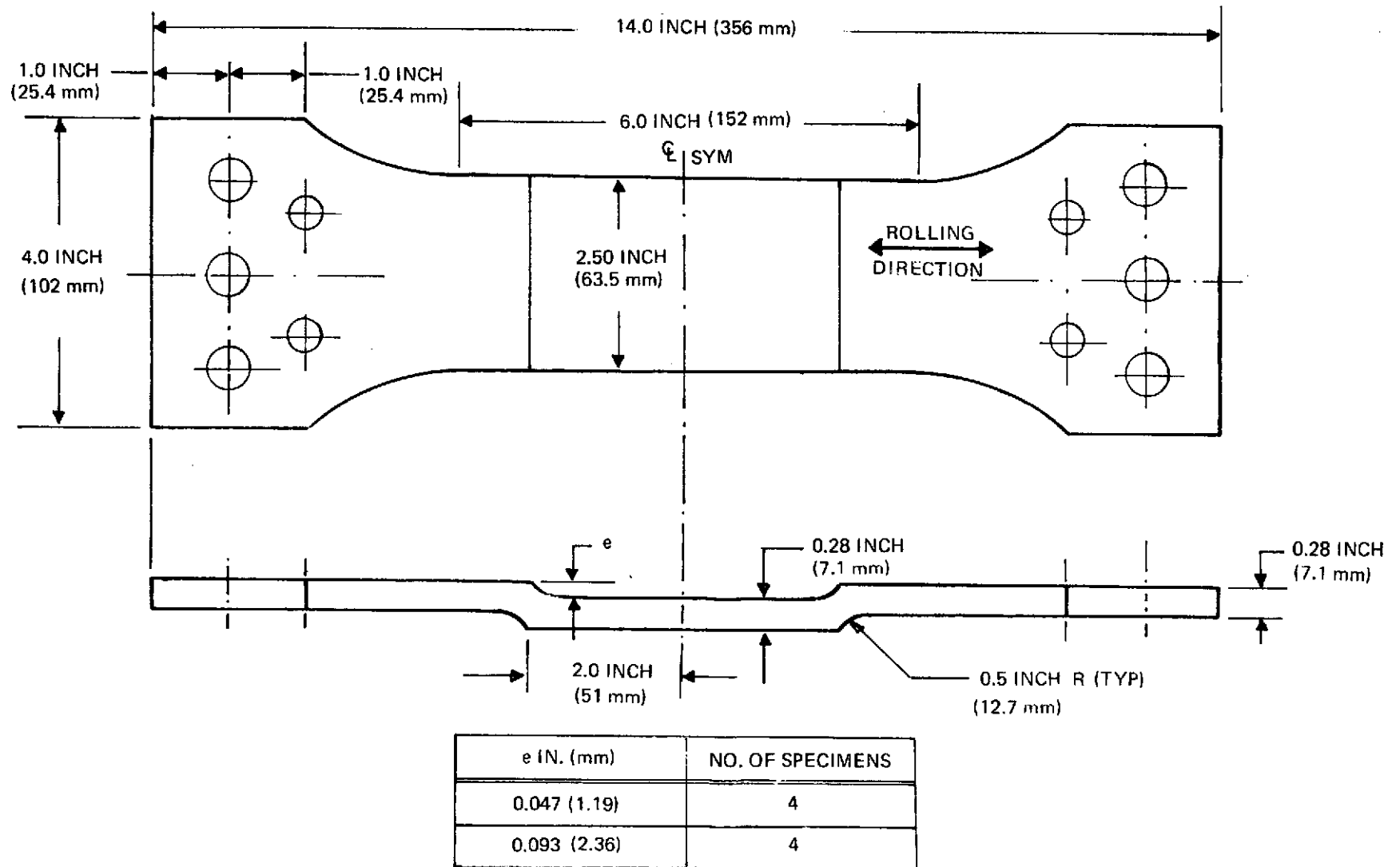


Figure 4-3: Specimen Configuration for Combined Bending and Tension Tests of 5Al-2.5 Sn (ELI) Titanium at -320F (78K)

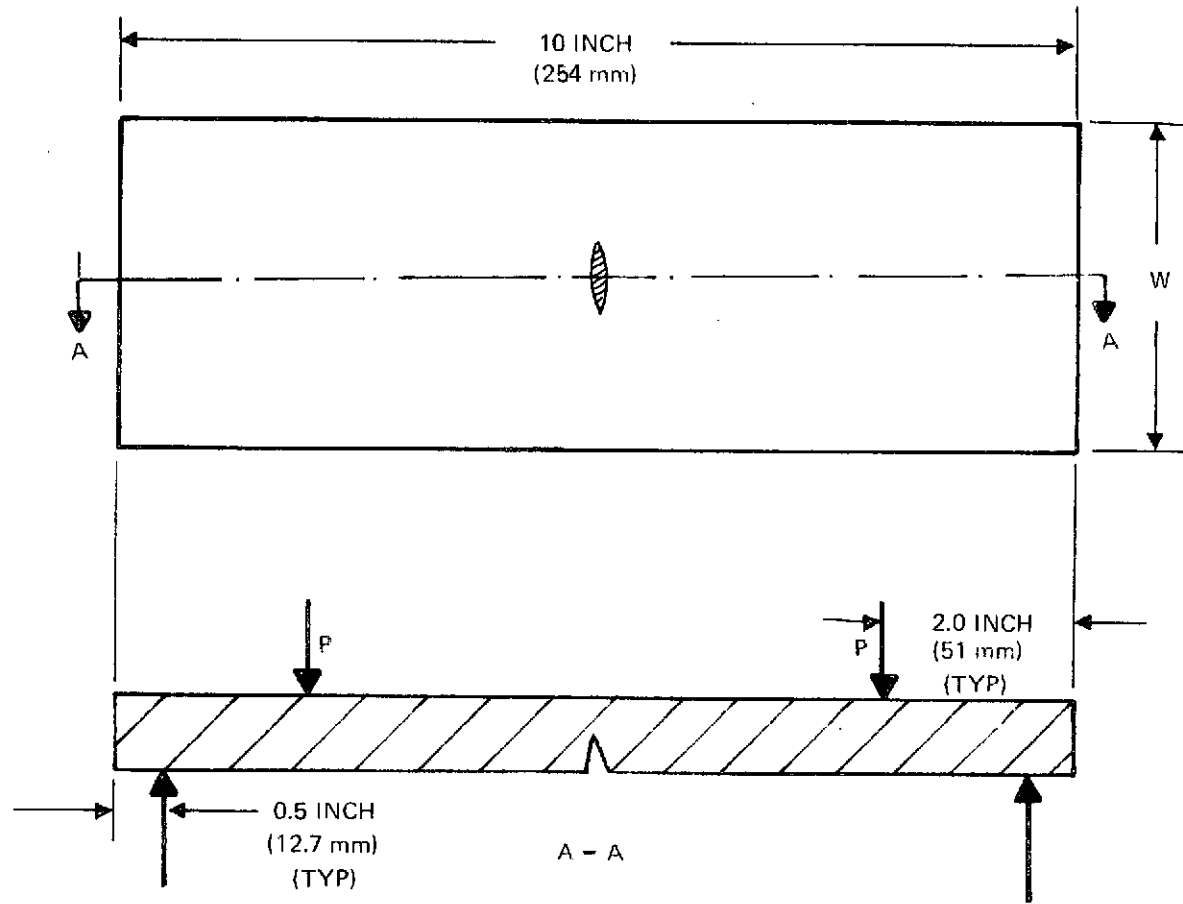


Figure 4-4: 4 Point Bend Surface Flawed Specimens of 5Al-2.5 Sn (ELI) Titanium for -423F (20K) Tests

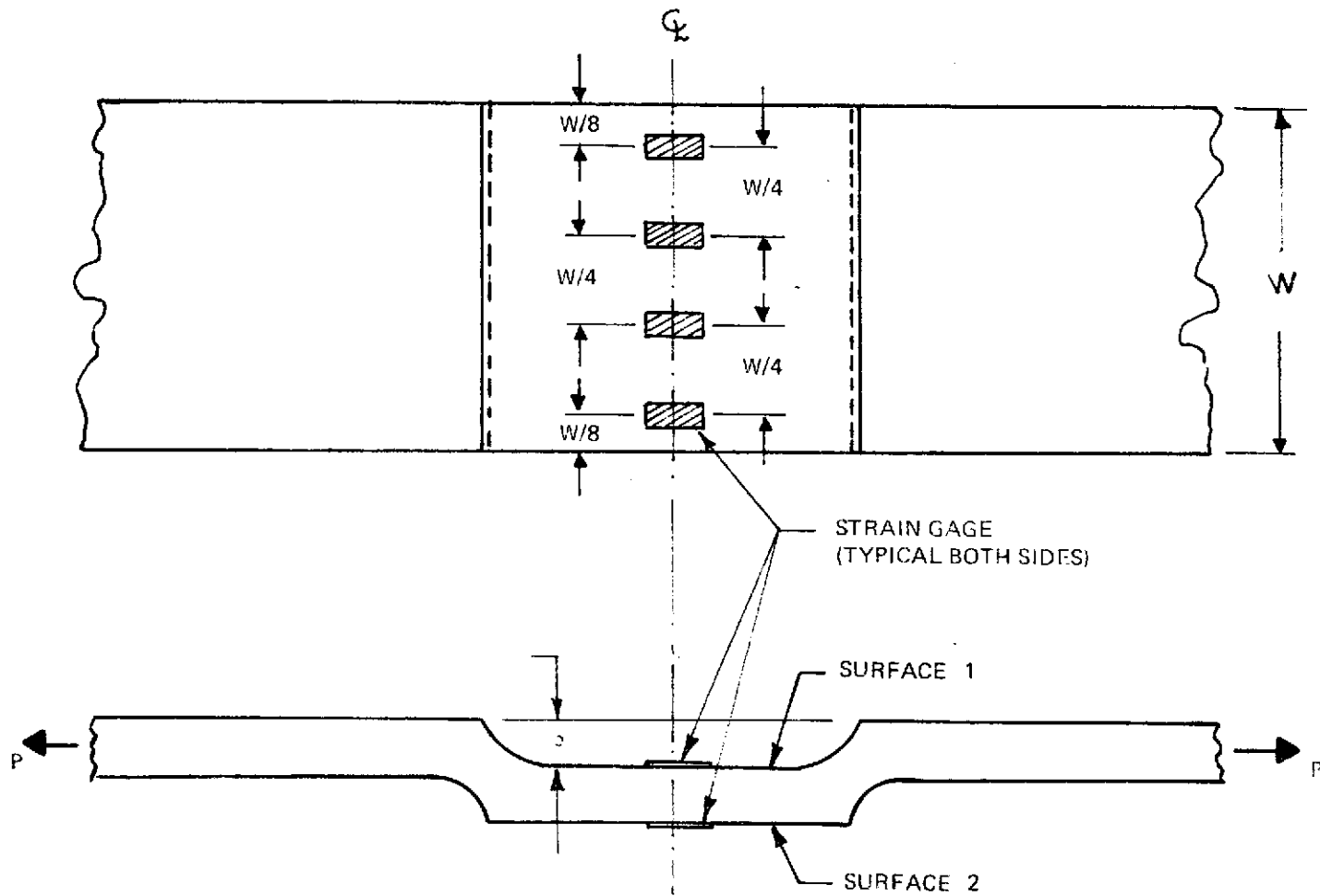


Figure 4-5. Instrumentation For Calibrations of Combined Bending and Tension Test Specimens

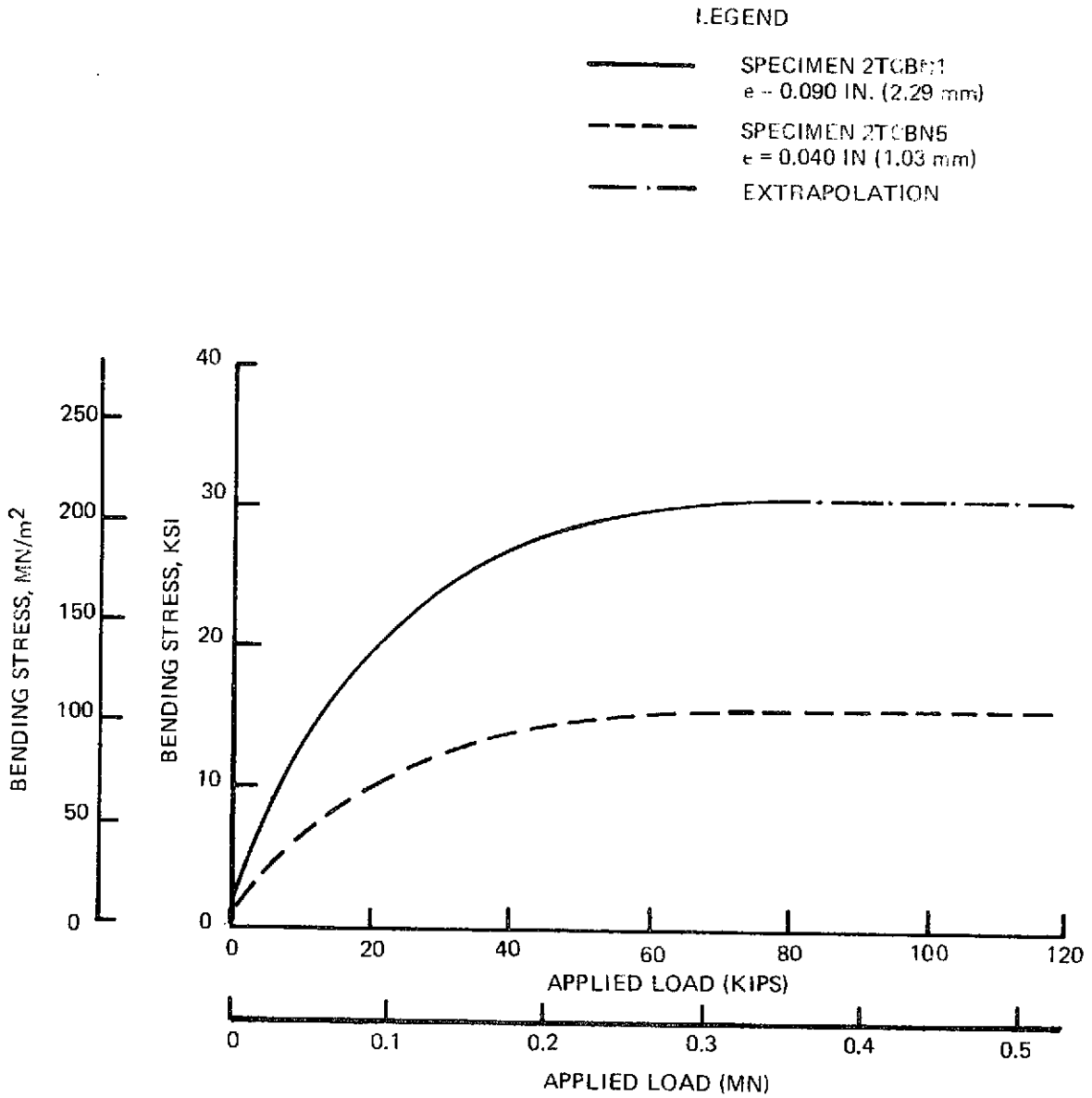


Figure 4-6: Load-Bending Stress Calibrations for Combined Bending and Tension Specimens

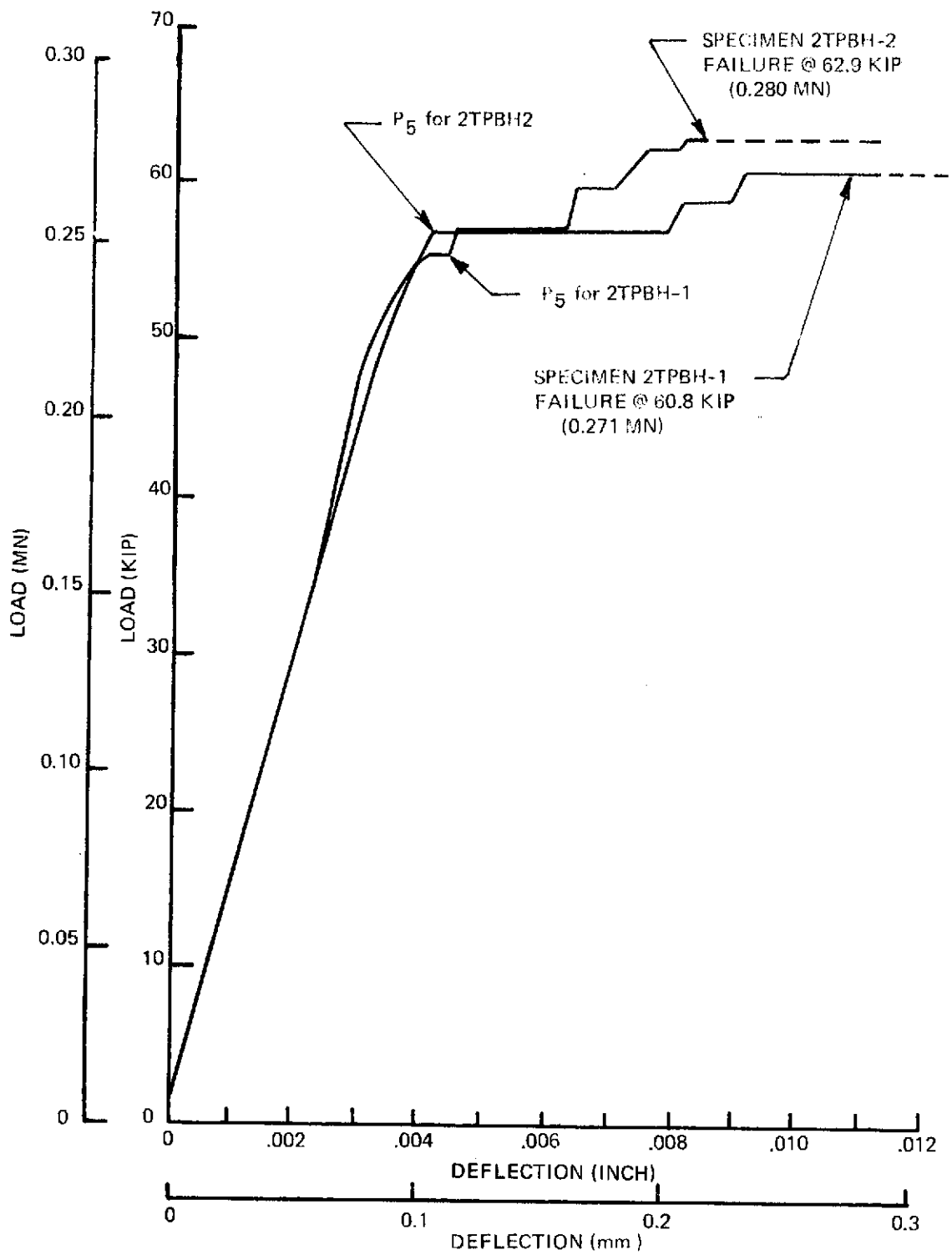


Figure 4-7: Load-Crack Opening Displacement Curves For Four Point Bend Surface Flawed Specimens at -423F (20K)

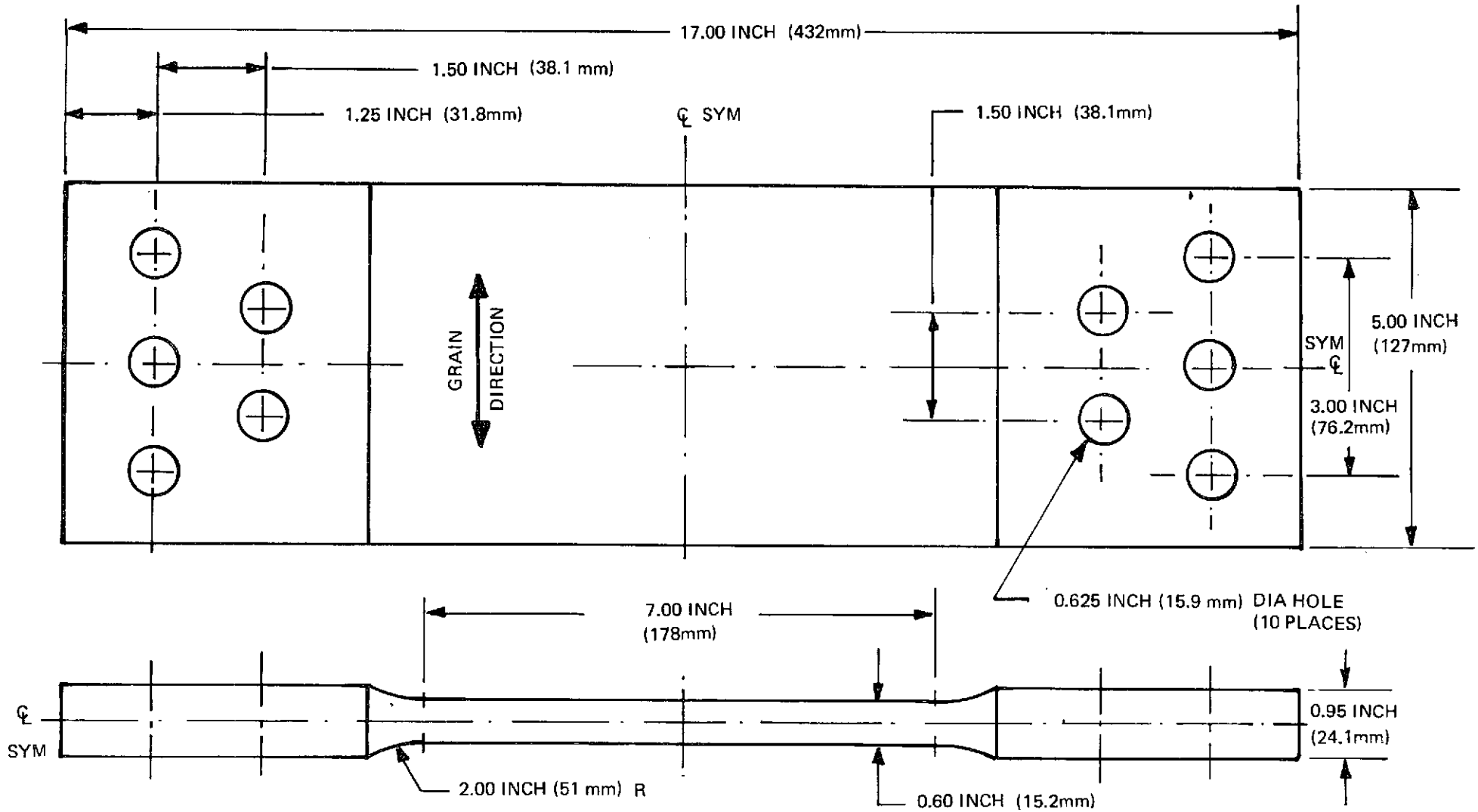


Figure 5-1: Surface-Flawed 2219-T87 Aluminum Specimens For Ambient Air, LN<sub>2</sub> and LH<sub>2</sub> Testing

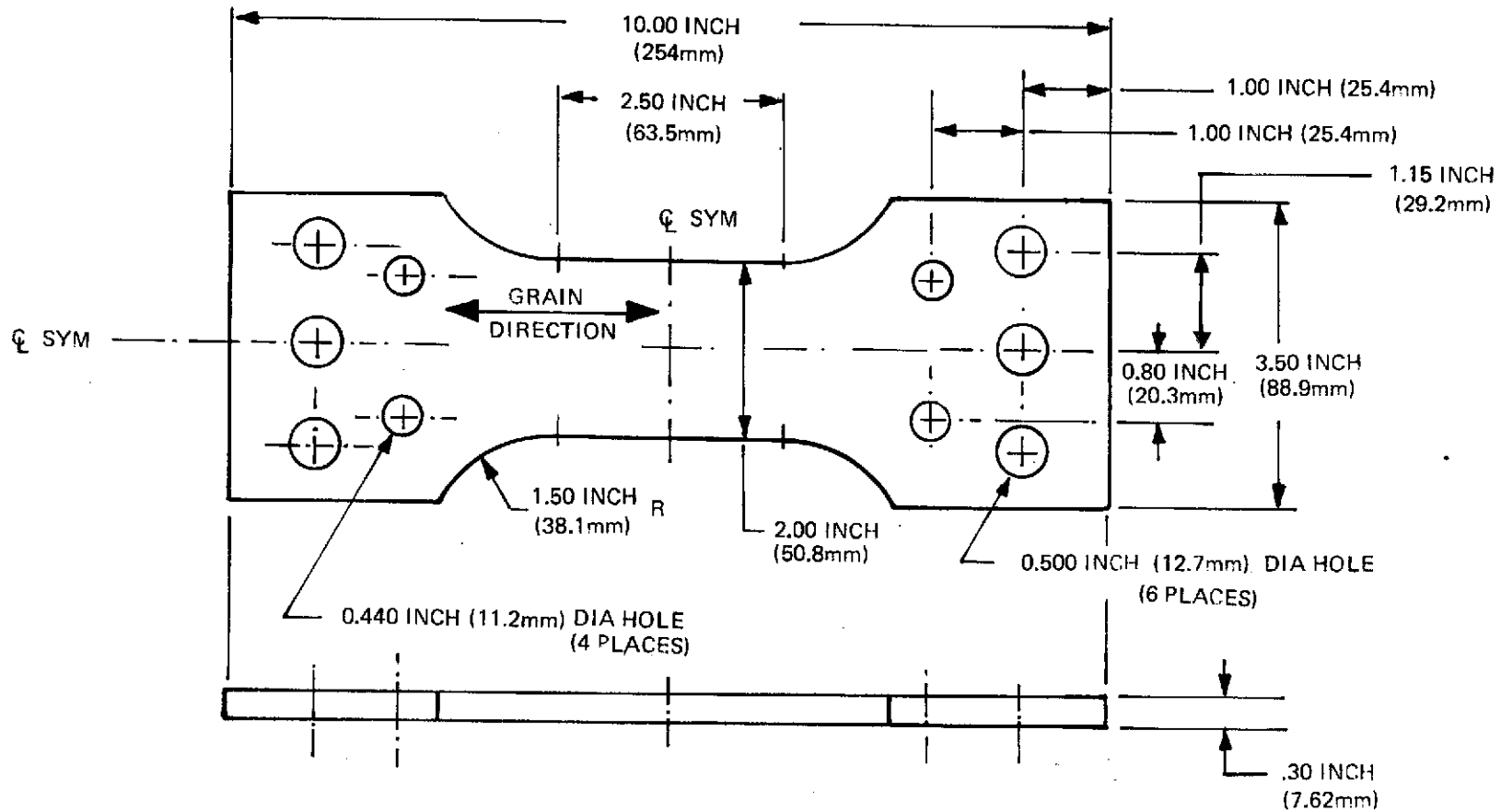


Figure 5-2: Surface-Flawed 6Al-4V  $\beta$  STA Titanium Specimen For Ambient Air Testing

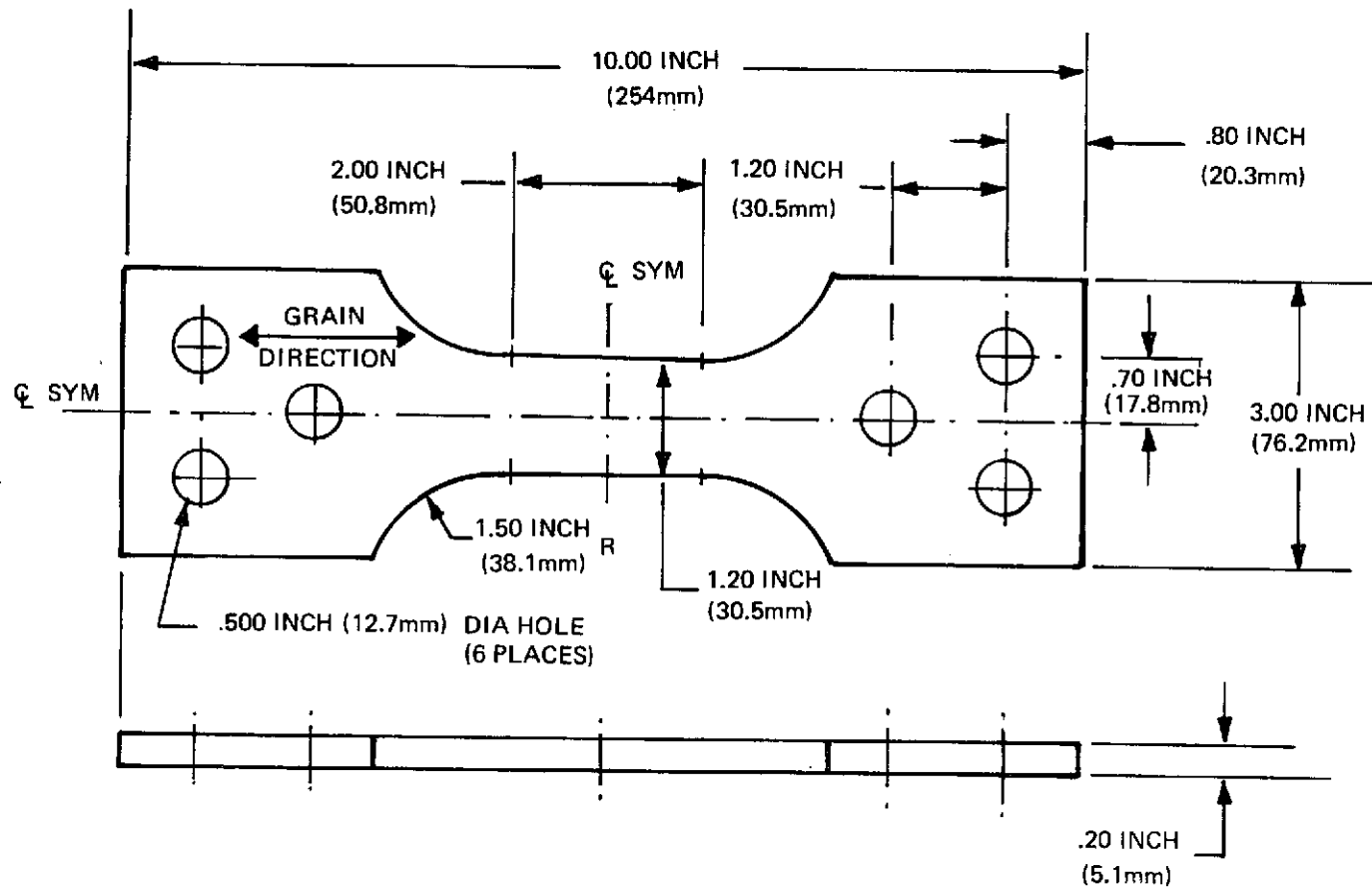


Figure 5-3: Surface-Flawed 6Al-4V  $\beta$ STA Titanium Specimen for  $LN_2$  and  $LH_2$  Testing



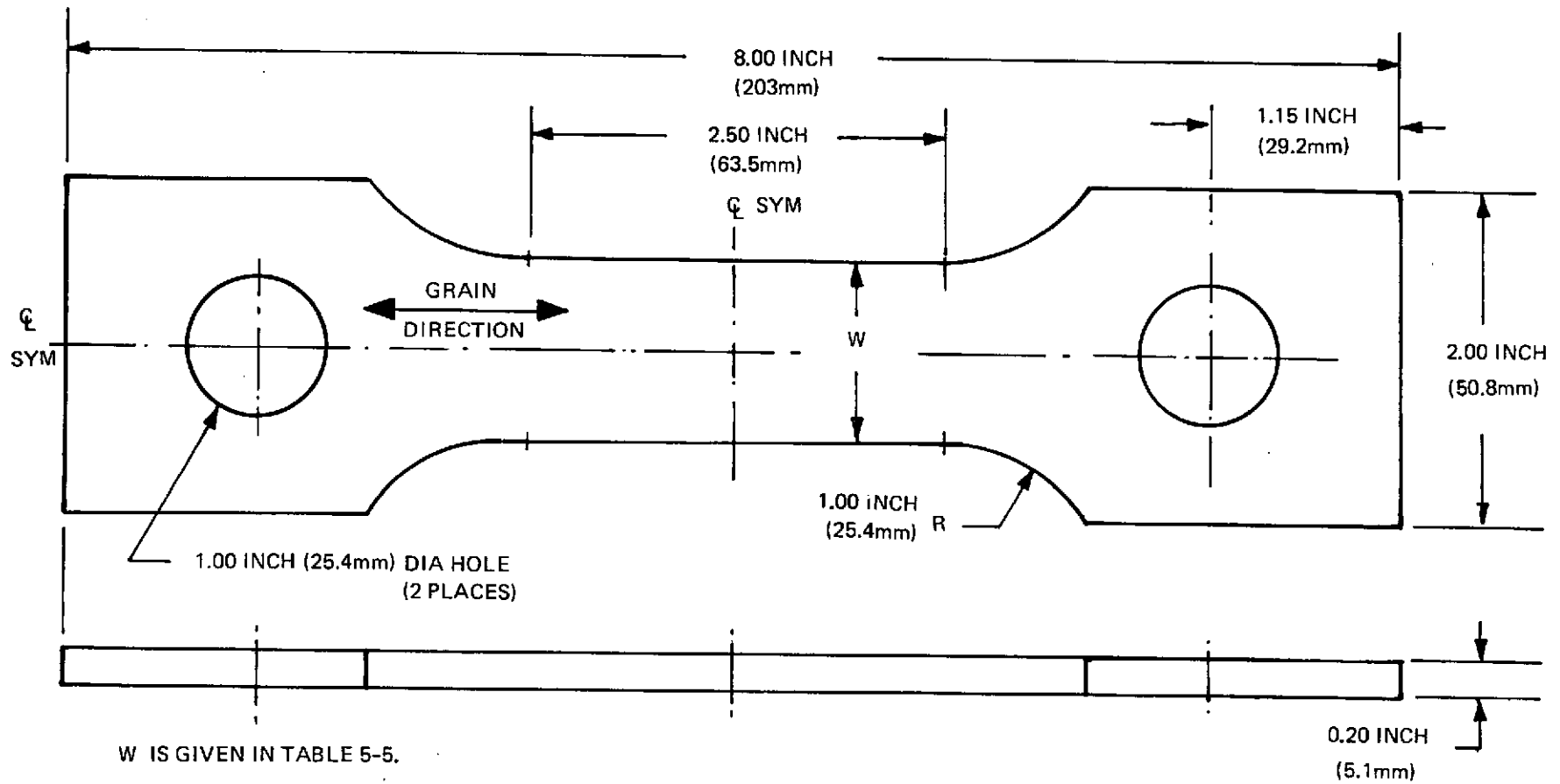


Figure 5-4: Surface-Flawed 6Al-4V  $\beta$  STA Titanium Specimens For Ambient Air, LN<sub>2</sub> and LH<sub>2</sub> Testing

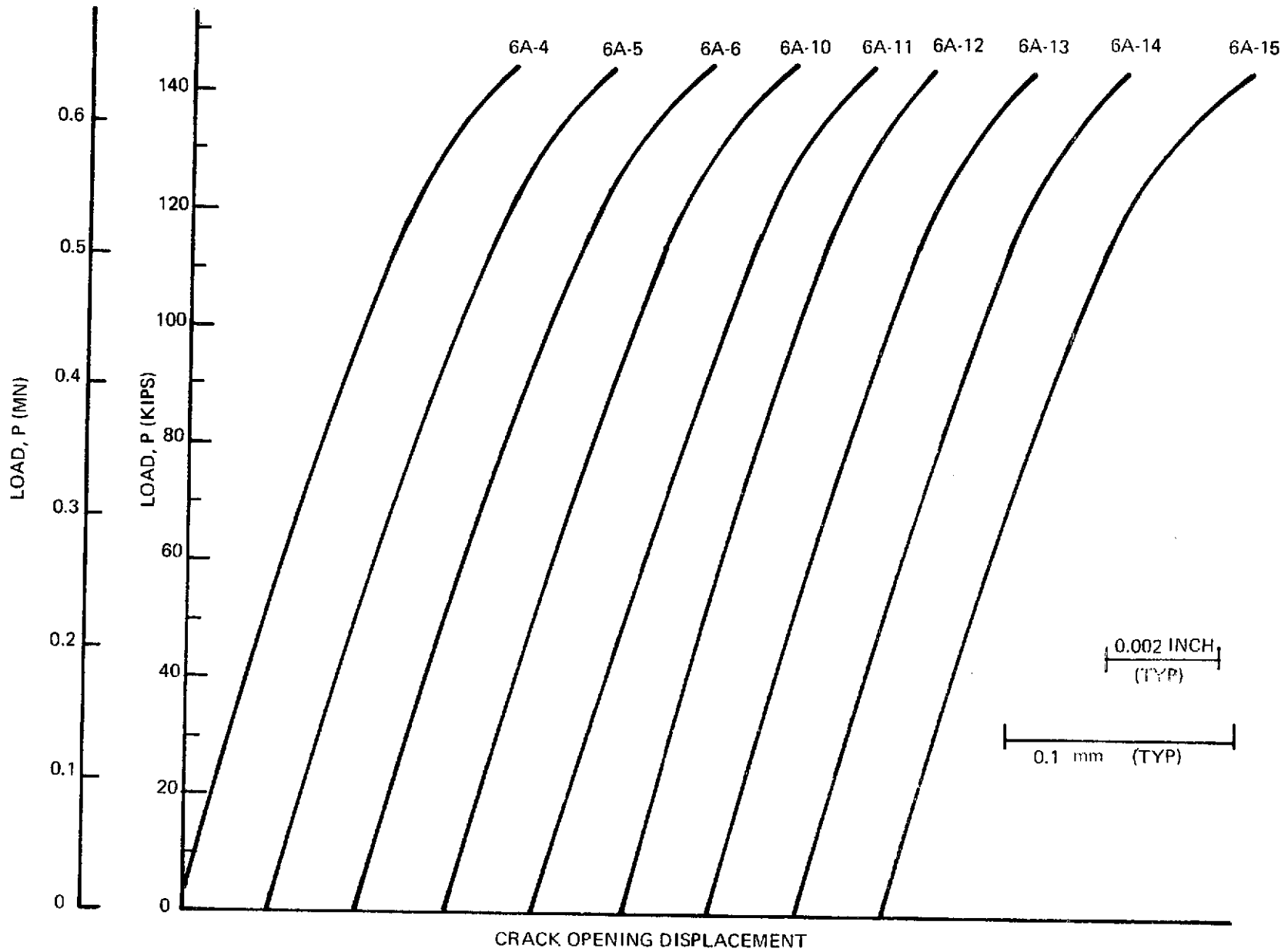


Figure 5-5: Load Vs. Crack Opening Displacement Records for 2219-T87 Aluminum Specimens During Proof Loading at Room Temperature

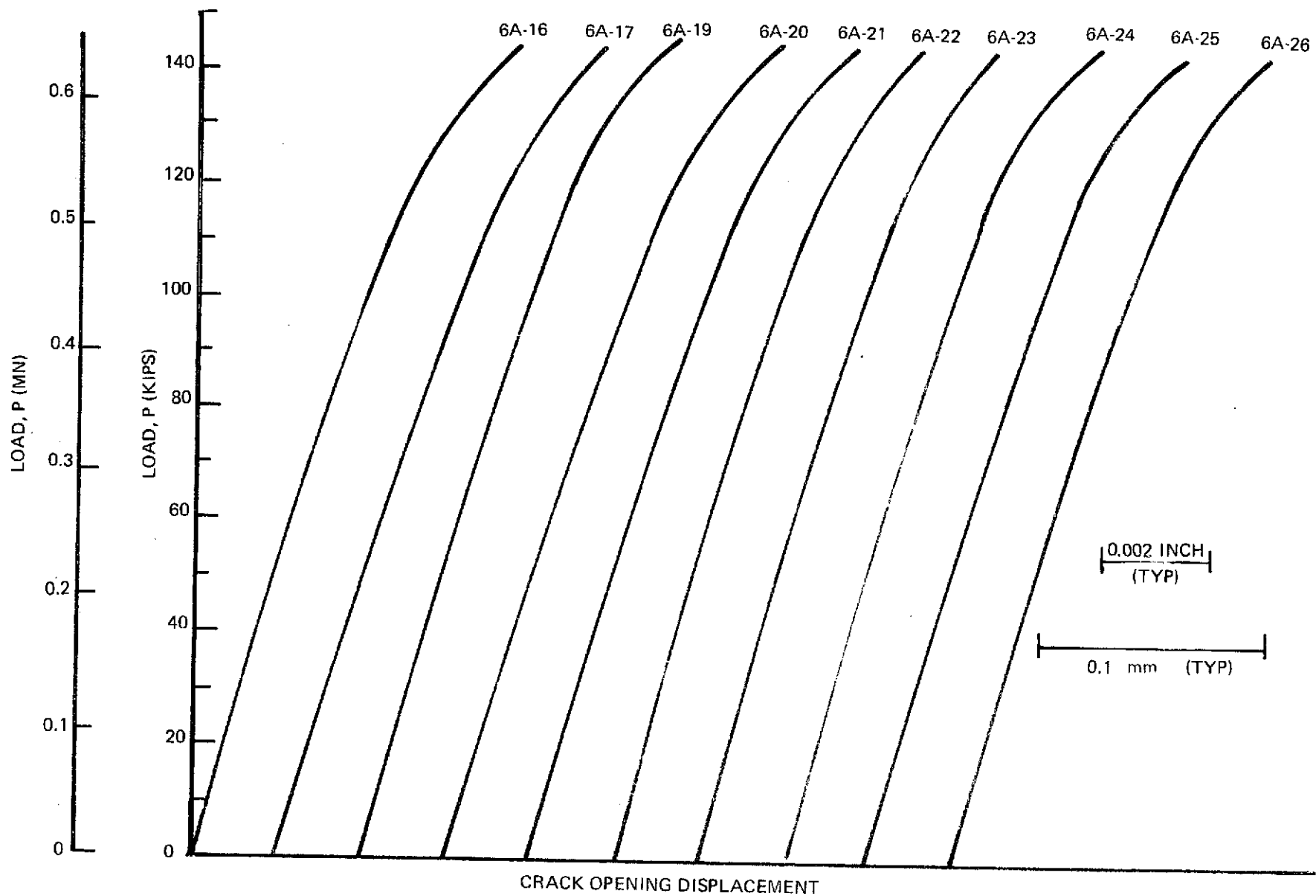


Figure 5-6: Load Vs. Crack Opening Displacement Records for 2219-T87 Aluminum Specimens During Proof Loading at Room Temperature

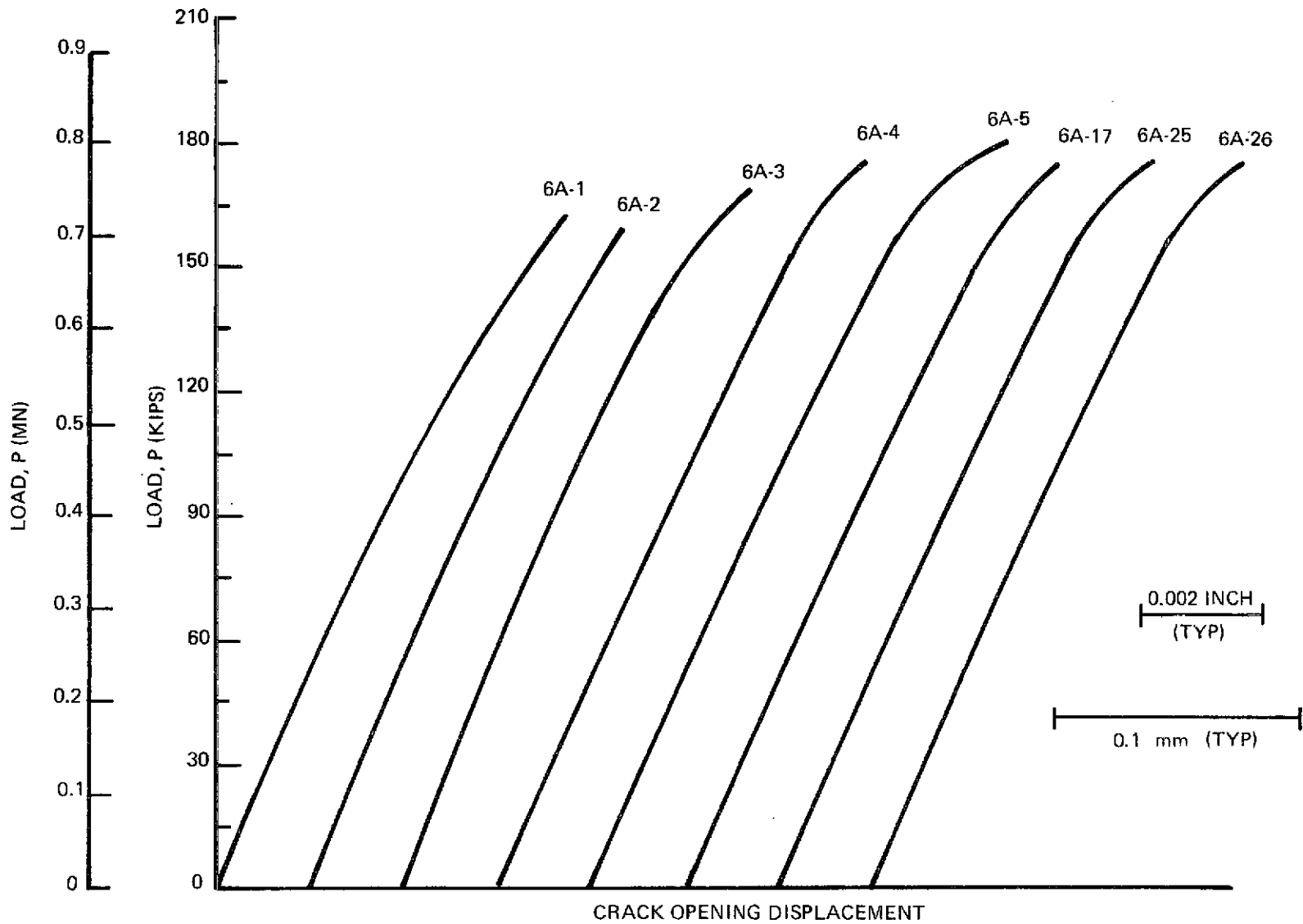


Figure 5-7: Load Vs. Crack Opening Displacement Records for 2219-T87 Aluminum Specimens During Proof Loading at -320F (78K)

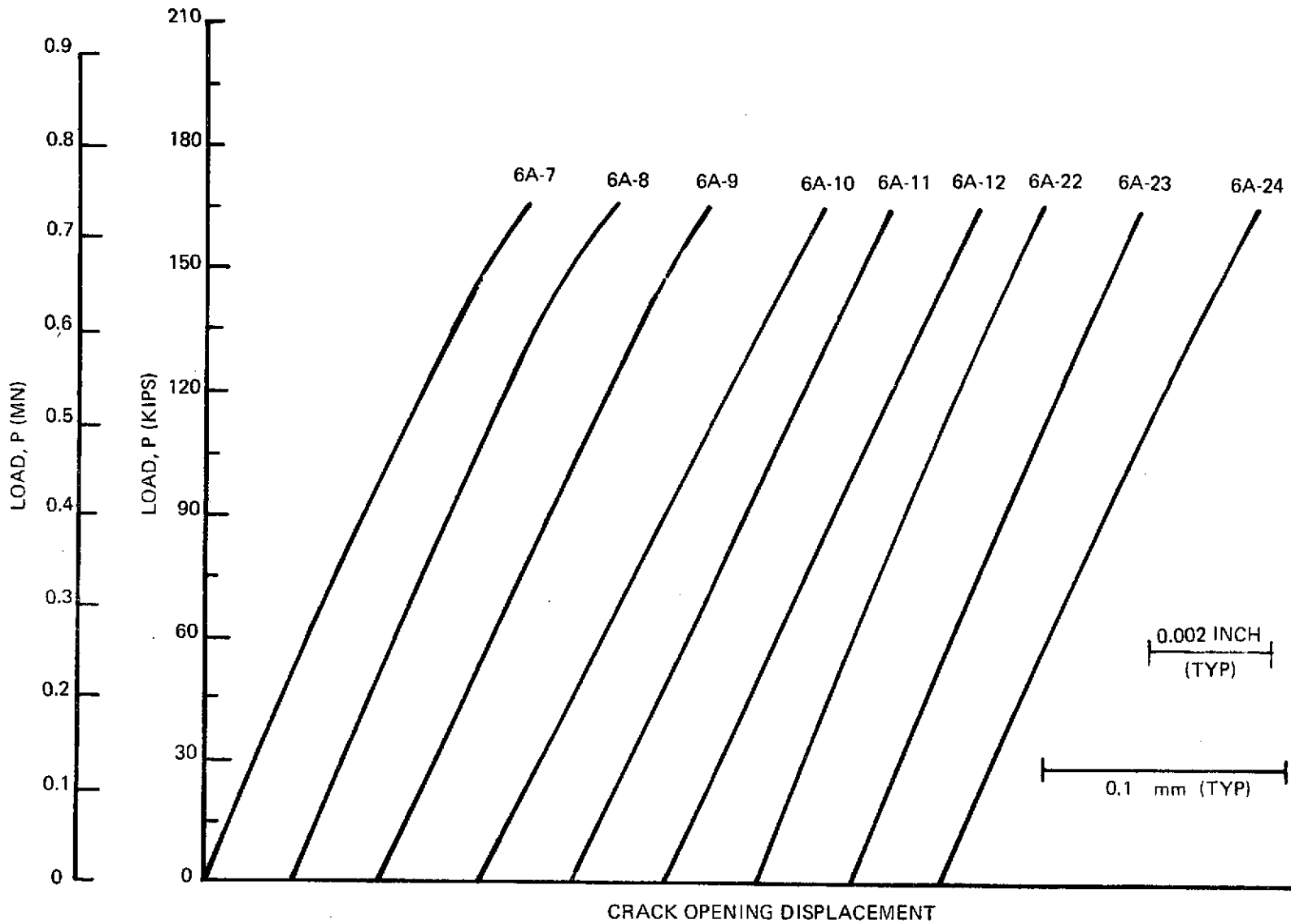


Figure 5-8: Load Vs. Crack Opening Displacement Records for 2219-T87 Aluminum Specimens During Proof Loading at -423F (20K)

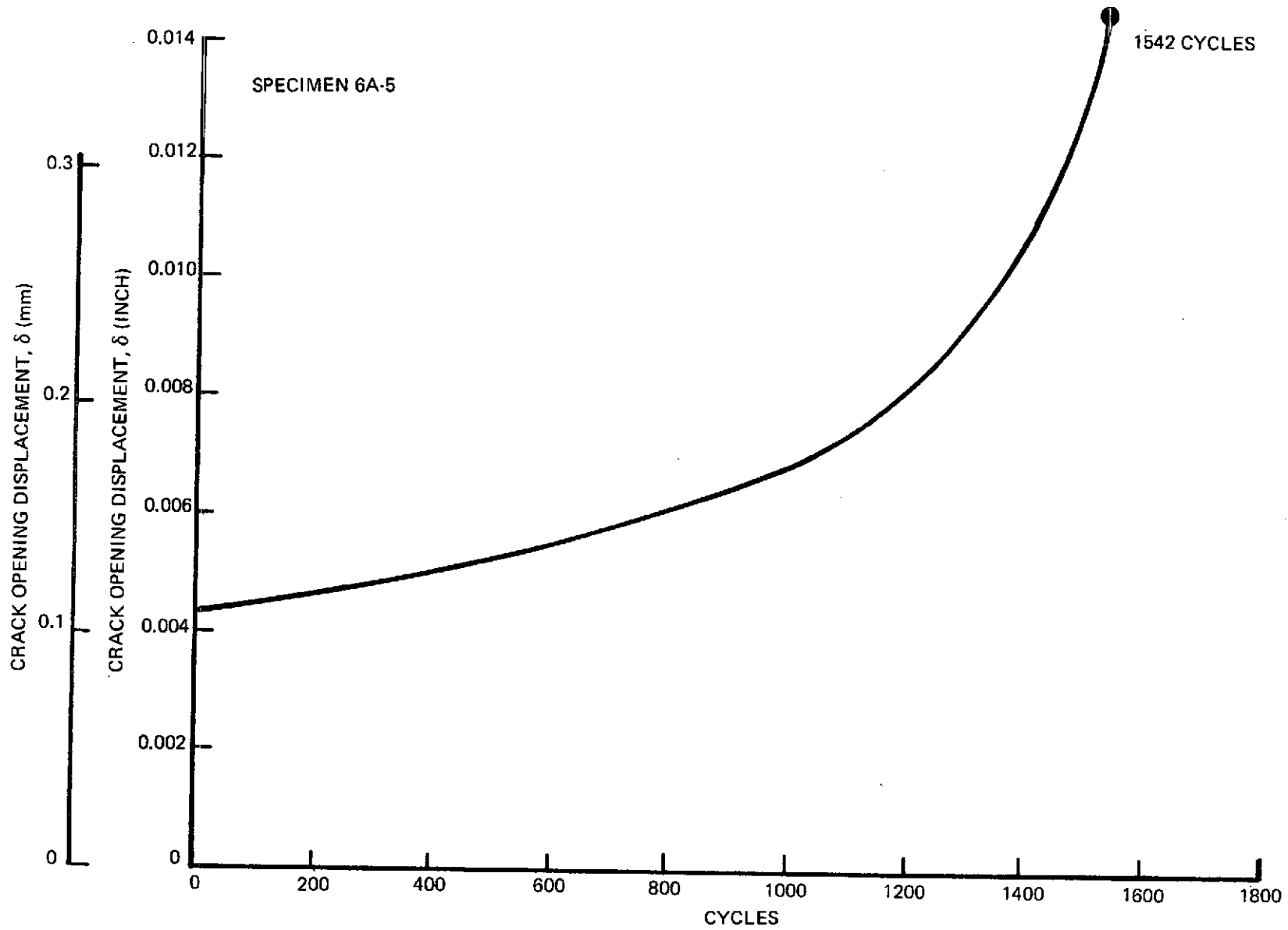


Figure 5-9: Typical Crack Opening Displacement Vs. Cycles Record for 2219-T87 Aluminum Specimen at Room Temperature

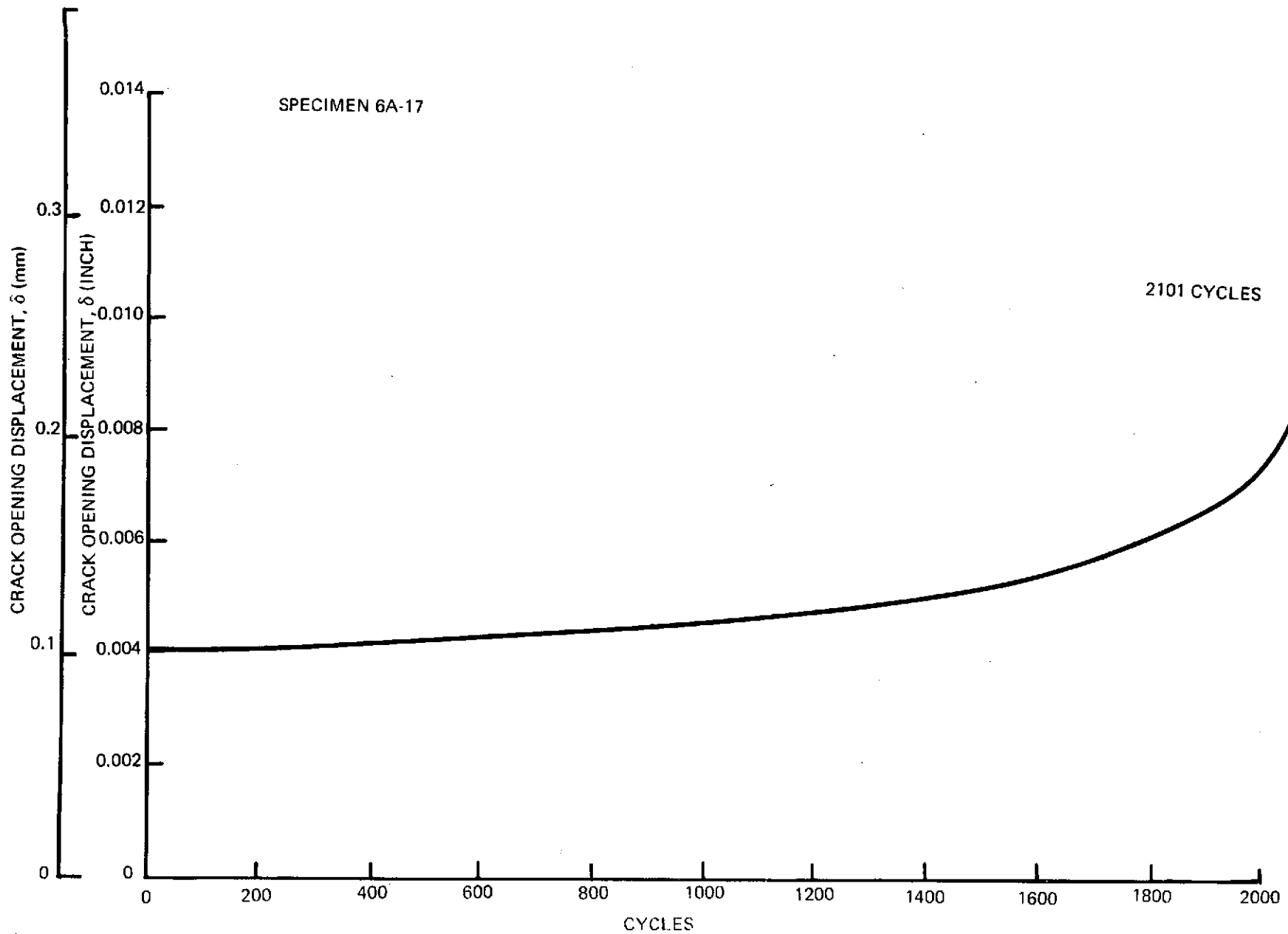


Figure 5-10: Typical Crack Opening Displacement Vs. Cycles Record for 2219-T87 Aluminum Specimen at -320F (78K)

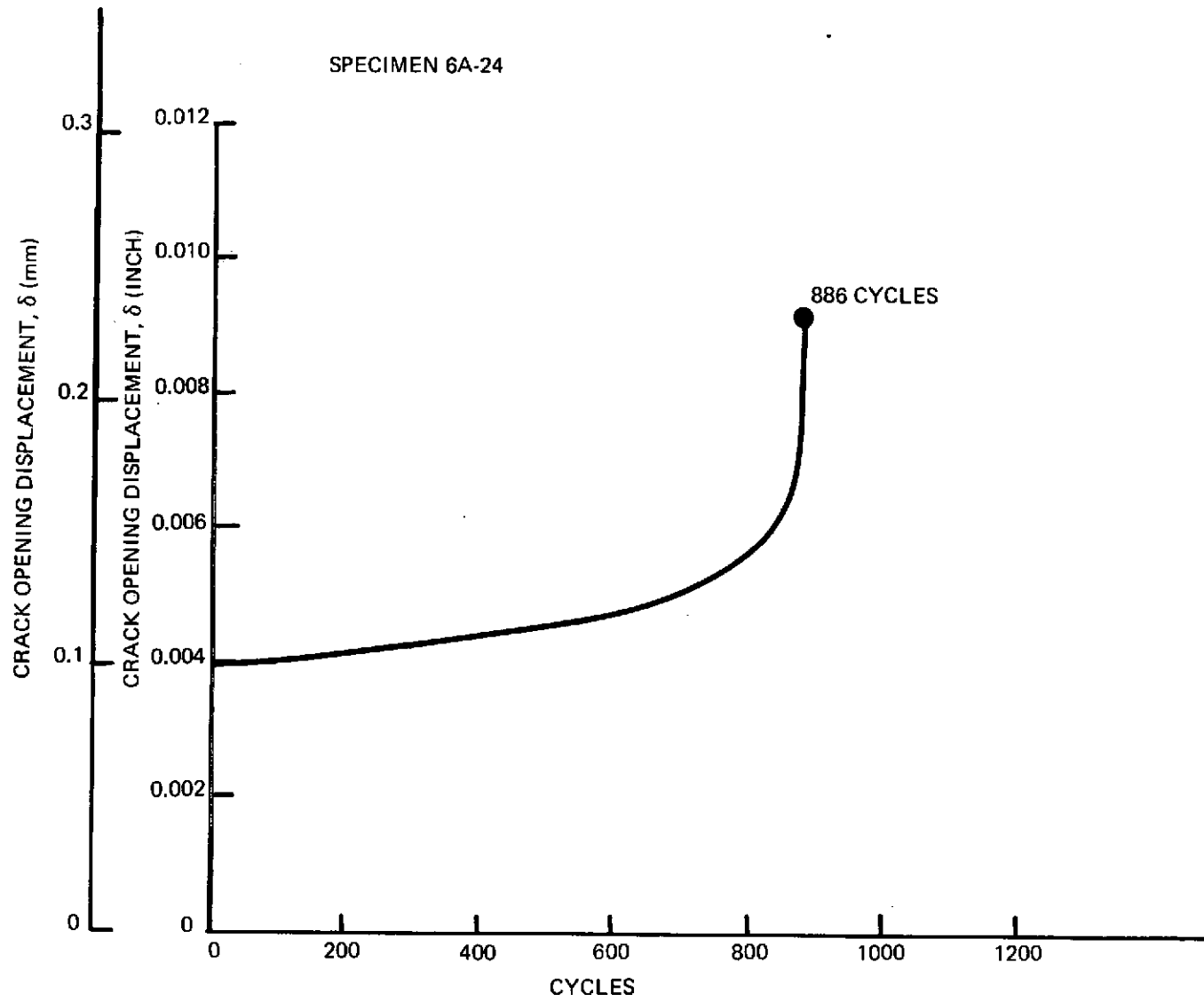


Figure 5-11: Typical Crack Opening Displacement Vs. Cycles Record for 2219-T87 Aluminum Specimen at -423F (20K)



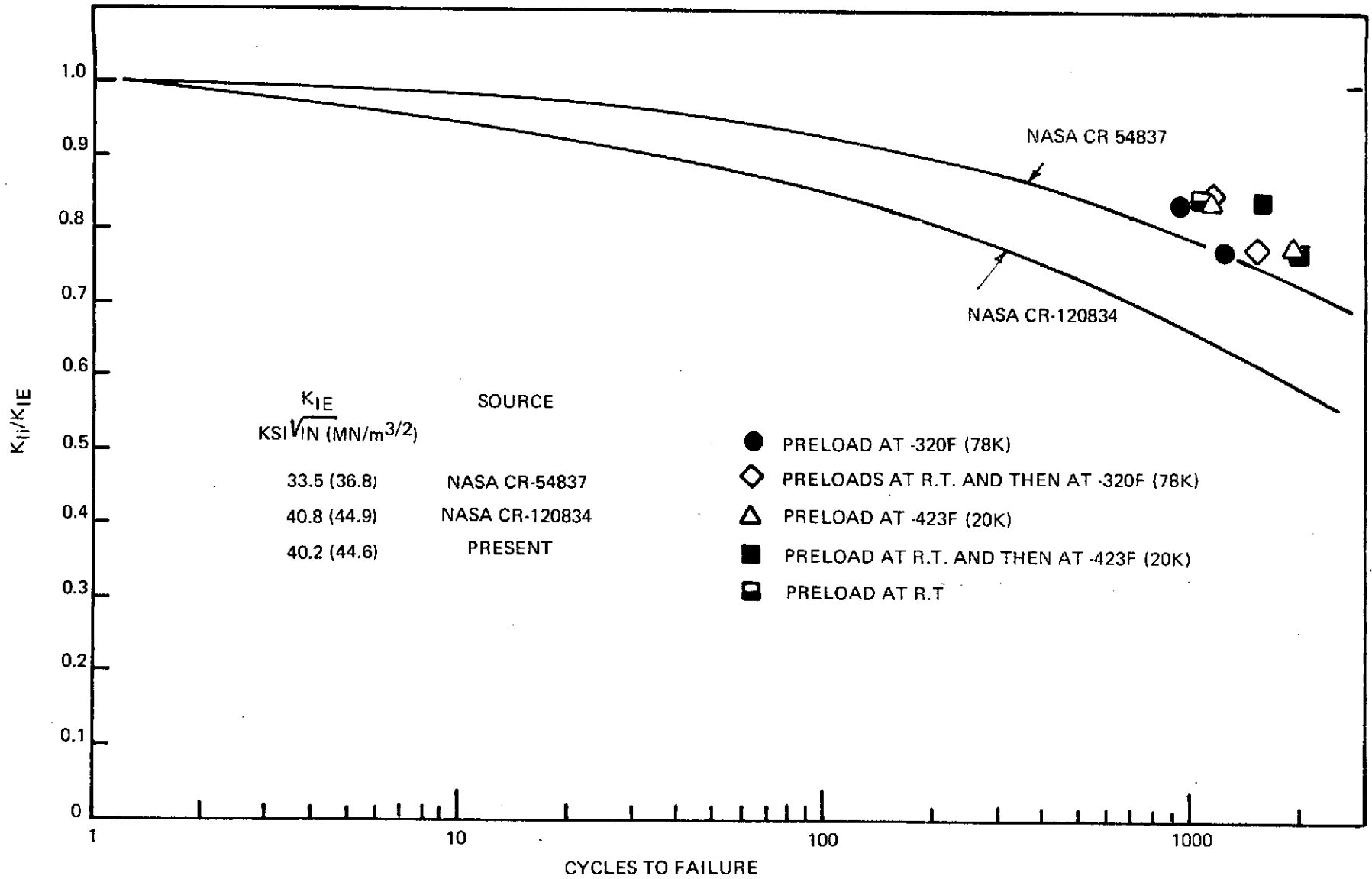


Figure 5-12:  $K_{II}/K_{IE}$  Against Cycles to Failure Correlation for 2219-T87 Aluminum at Room Temperature

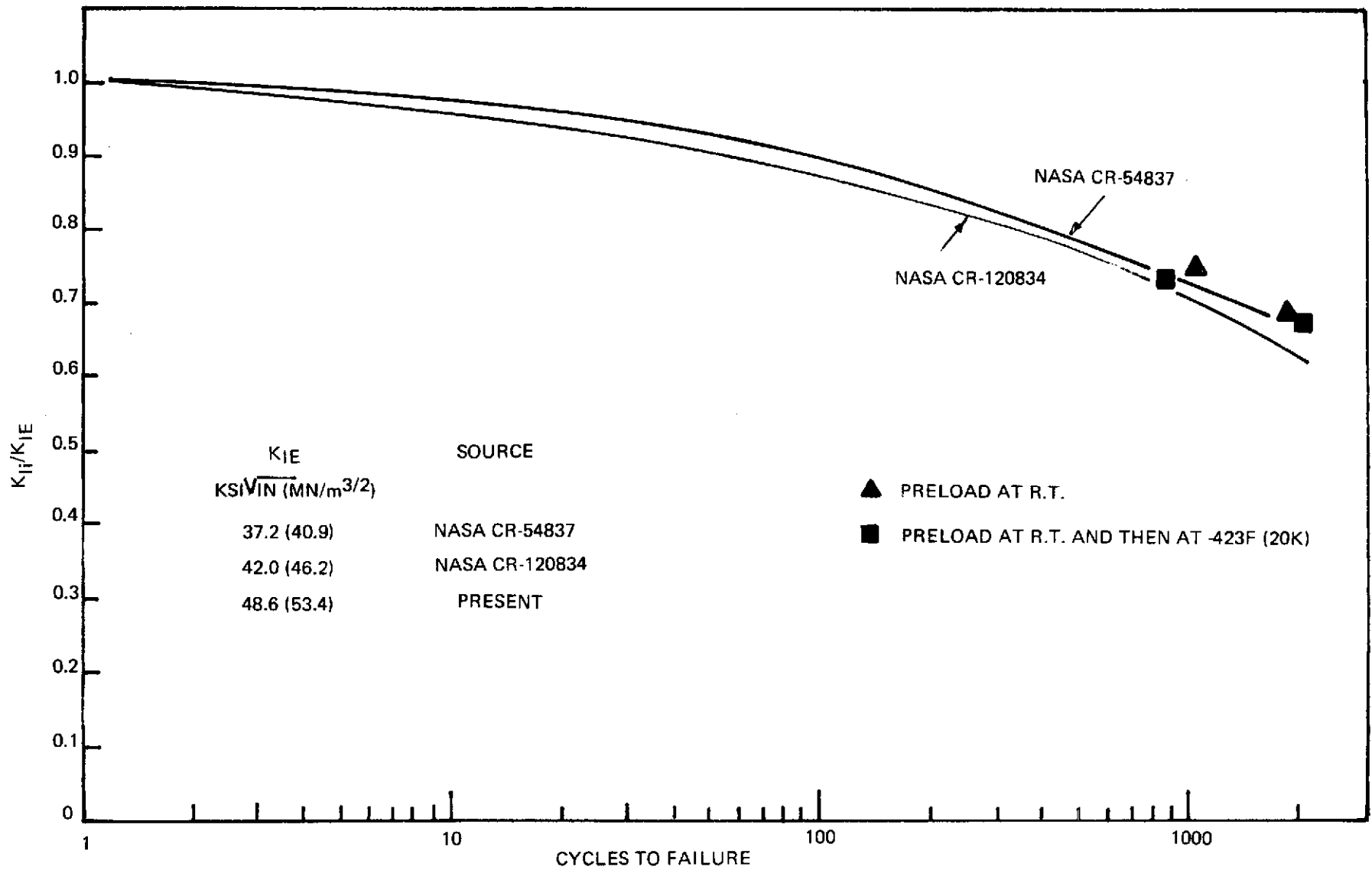


Figure 5-13:  $K_{II}/K_{IE}$  Against Cycles to Failure Correlation for 2219-T87 Aluminum at -320F (78K)

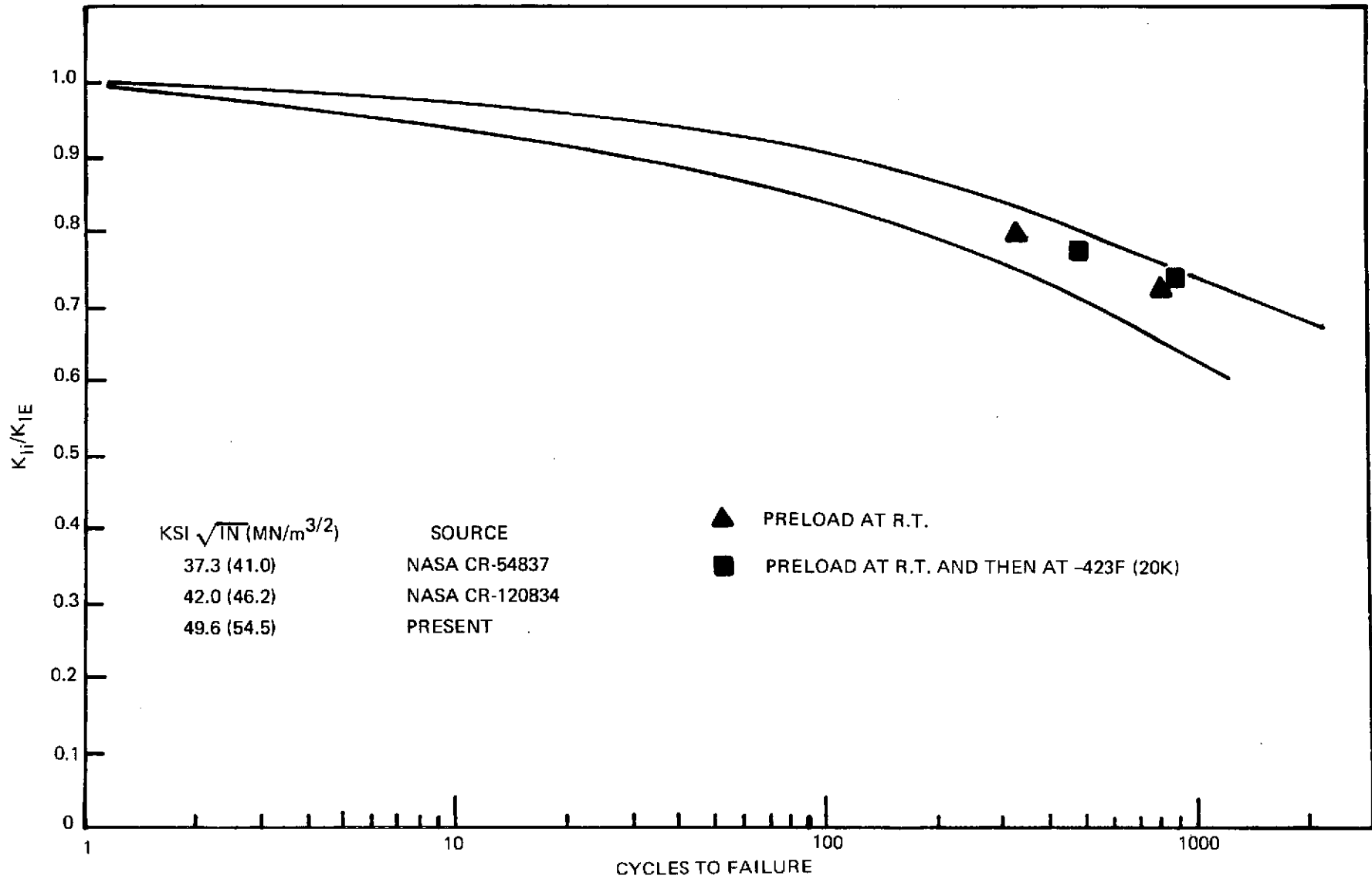


Figure 5-14:  $K_{II}/K_{IE}$  Against Cycles to Failure Correlation for 2219-T87 Aluminum at -423 F (20K)

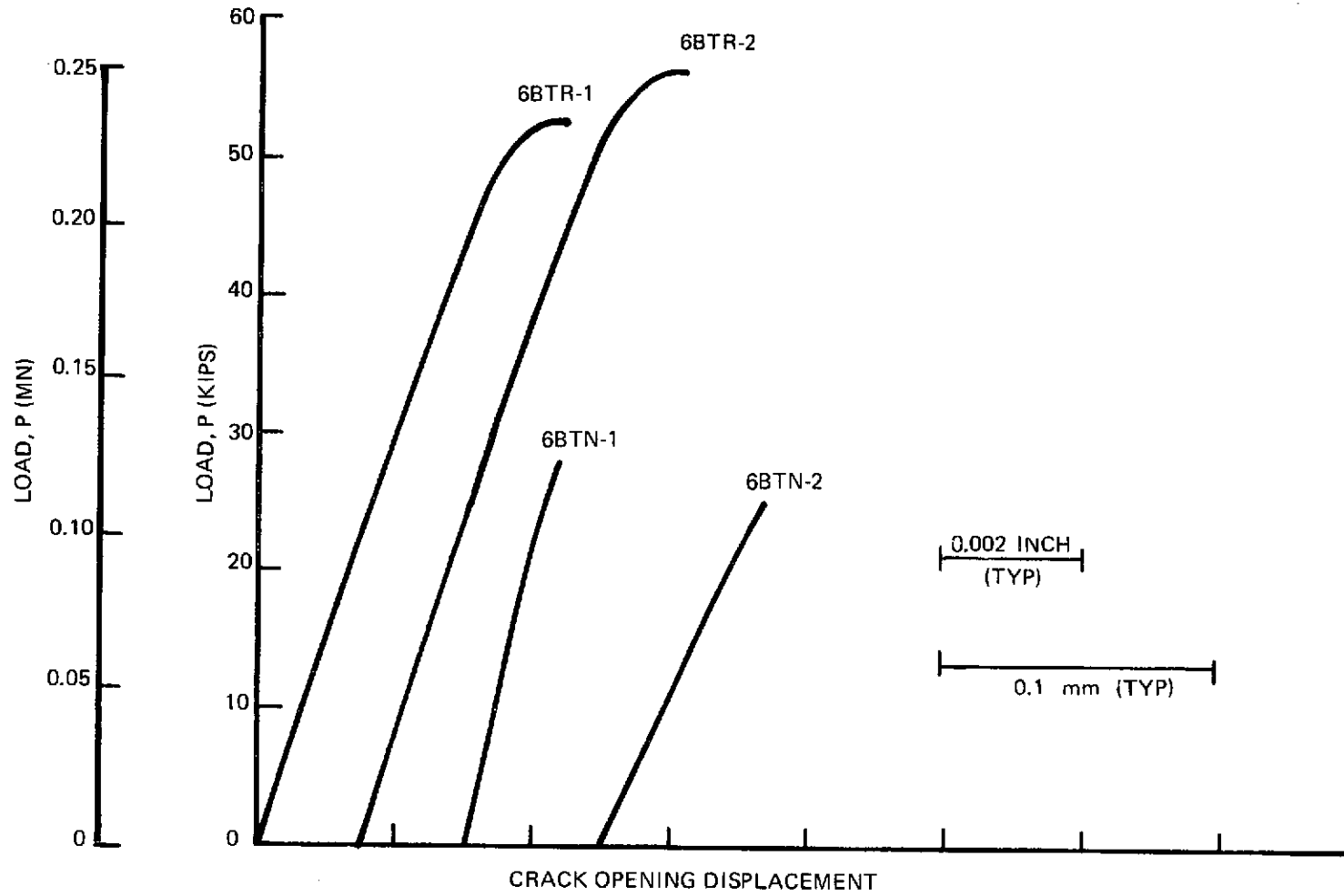


Figure 5-15: Load Vs. Crack Opening Displacement Plots for Surface Flawed Specimens of 6Al-4V  $\beta$ STA Titanium Tested at 72F (295K) and -320F (78K).

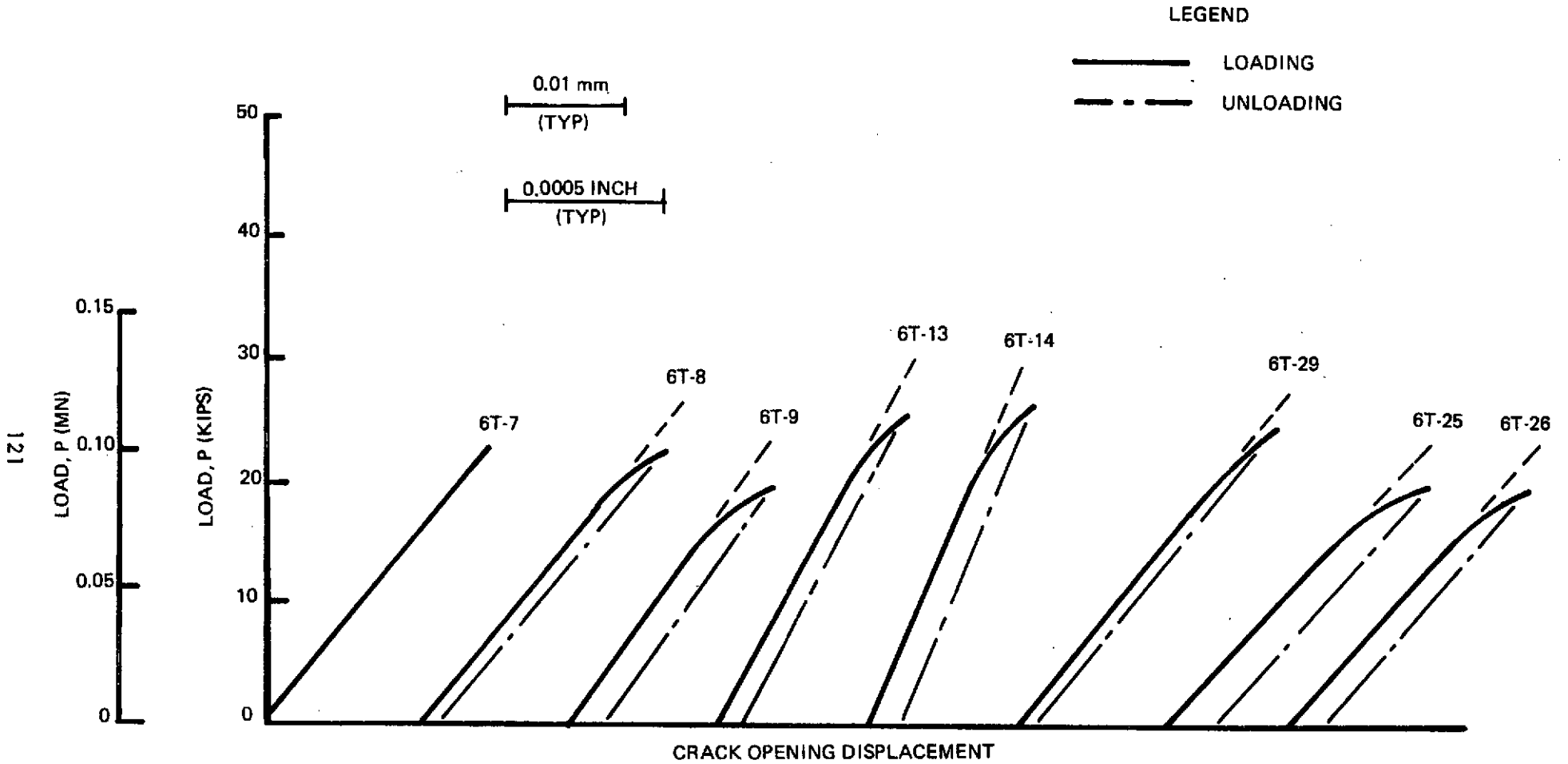


Figure 5-16: Load Vs. Crack Opening Displacement Records for 6Al-4V  $\beta$ STA Titanium Specimens During Proof Loading and Unloading at 72F (295K)

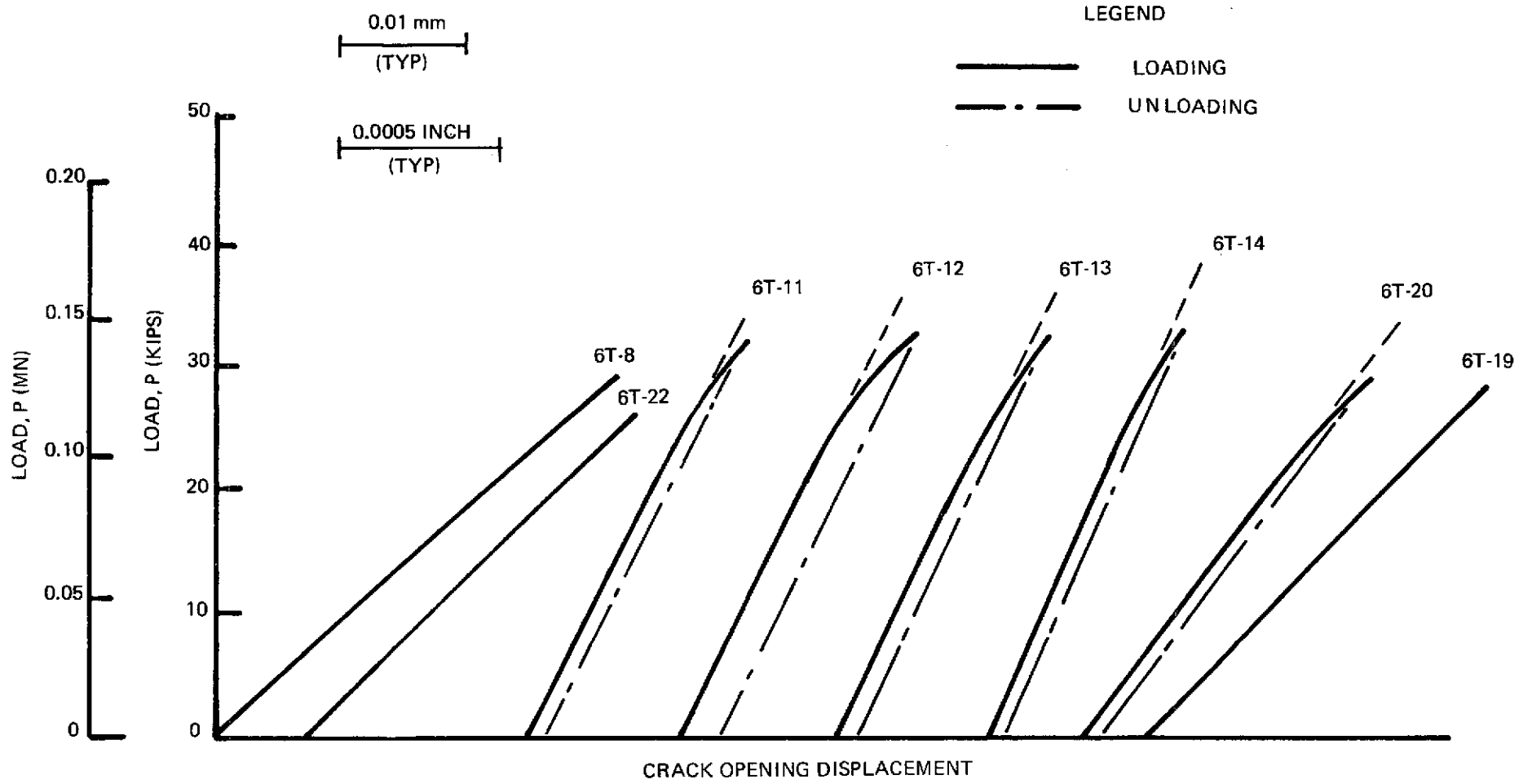


Figure 5-17: Load Vs. Crack Opening Displacement Records for 6Al-4V  $\beta$ STA Titanium Specimens During Proof Loading and Unloading at -320F (78K)

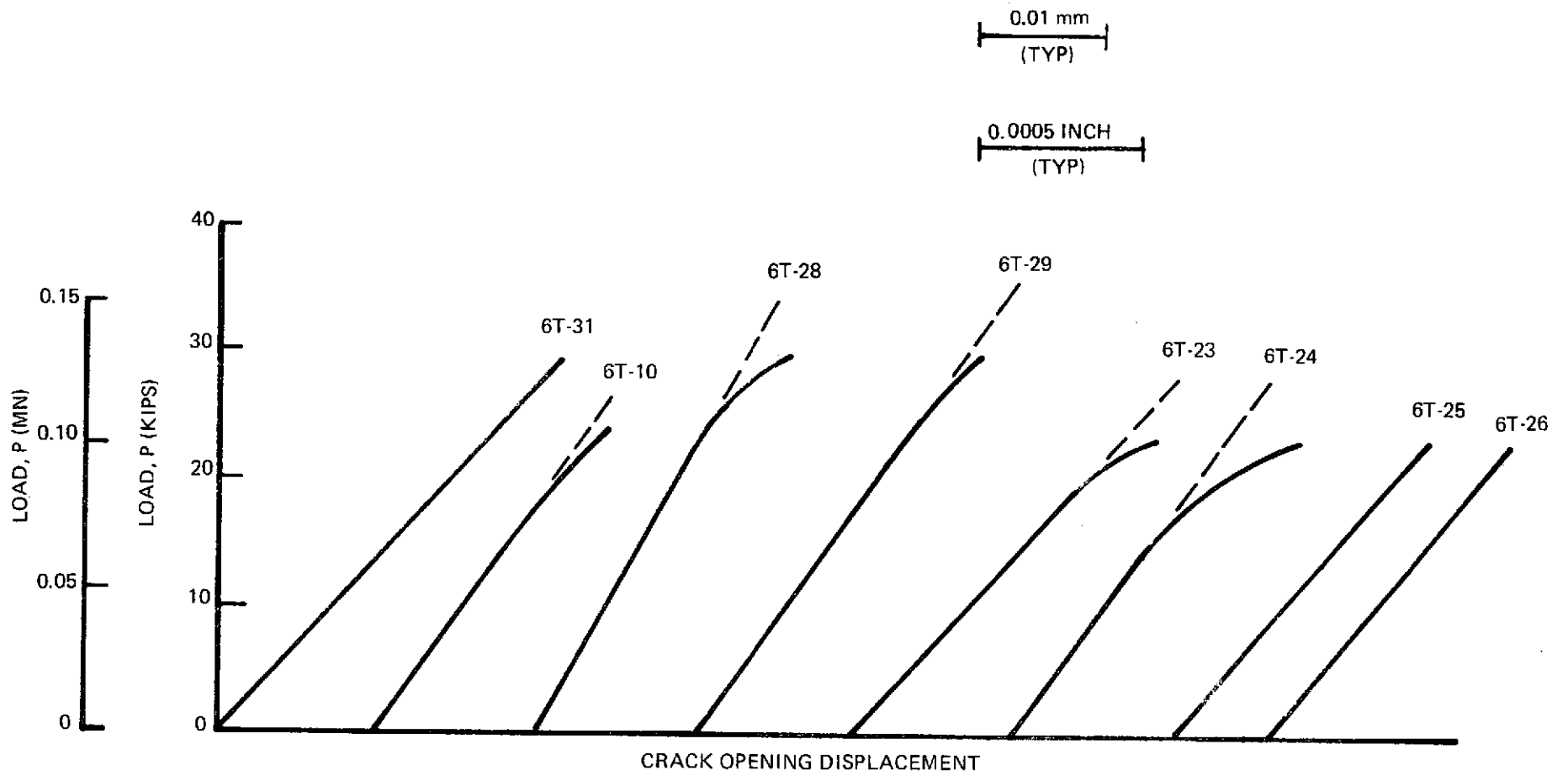


Figure 5-18: Load Vs. Crack Opening Displacement Records for 6Al-4V  $\beta$ STA Titanium Specimens During Proof Loading at -423F (20K)

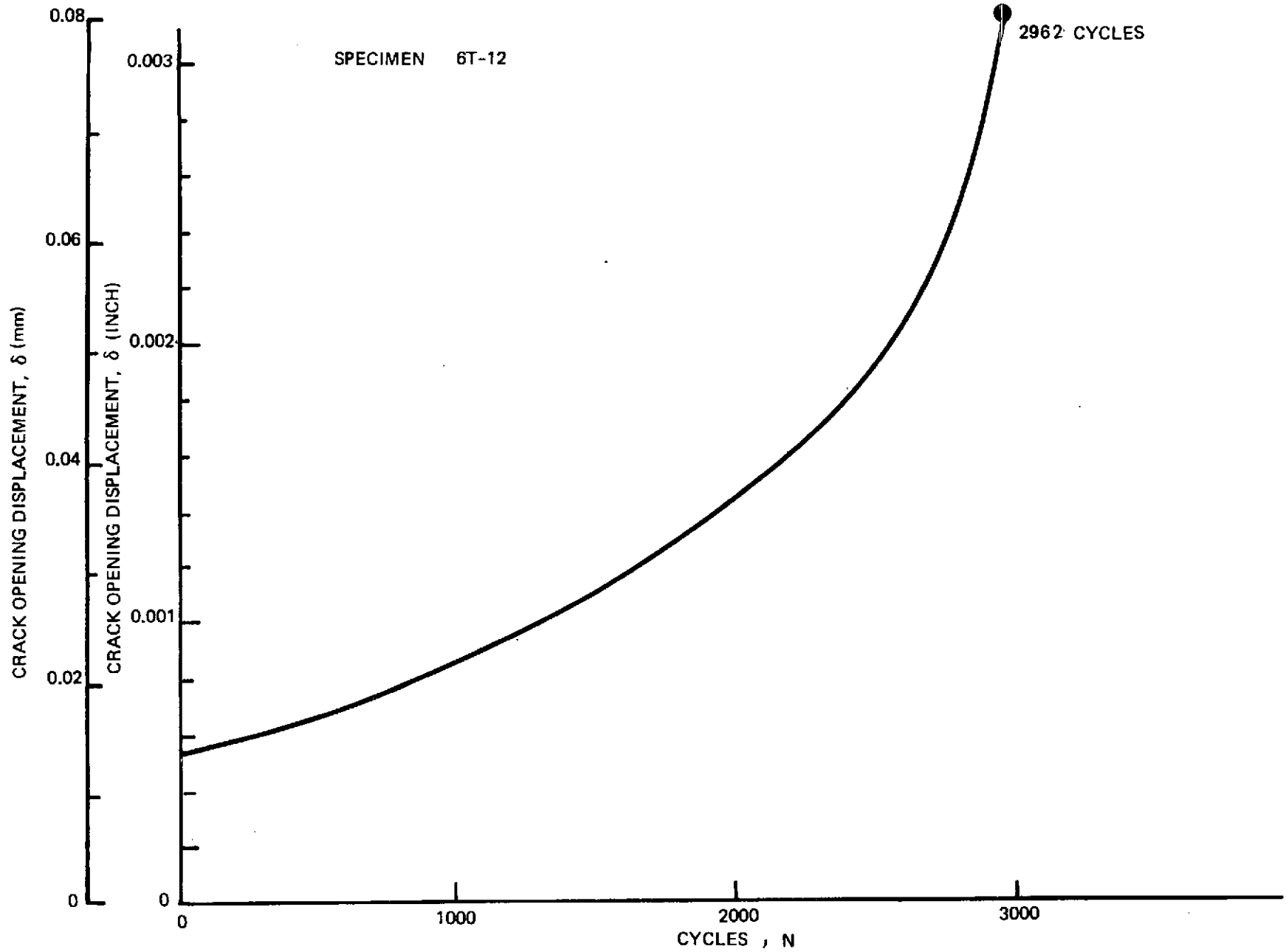


Figure 5-19: Typical Crack Opening Displacement Vs. Cycles Record For 6Al-4V  $\beta$ STA Titanium Specimen at Room Temperature



SPECIMEN 6T-13

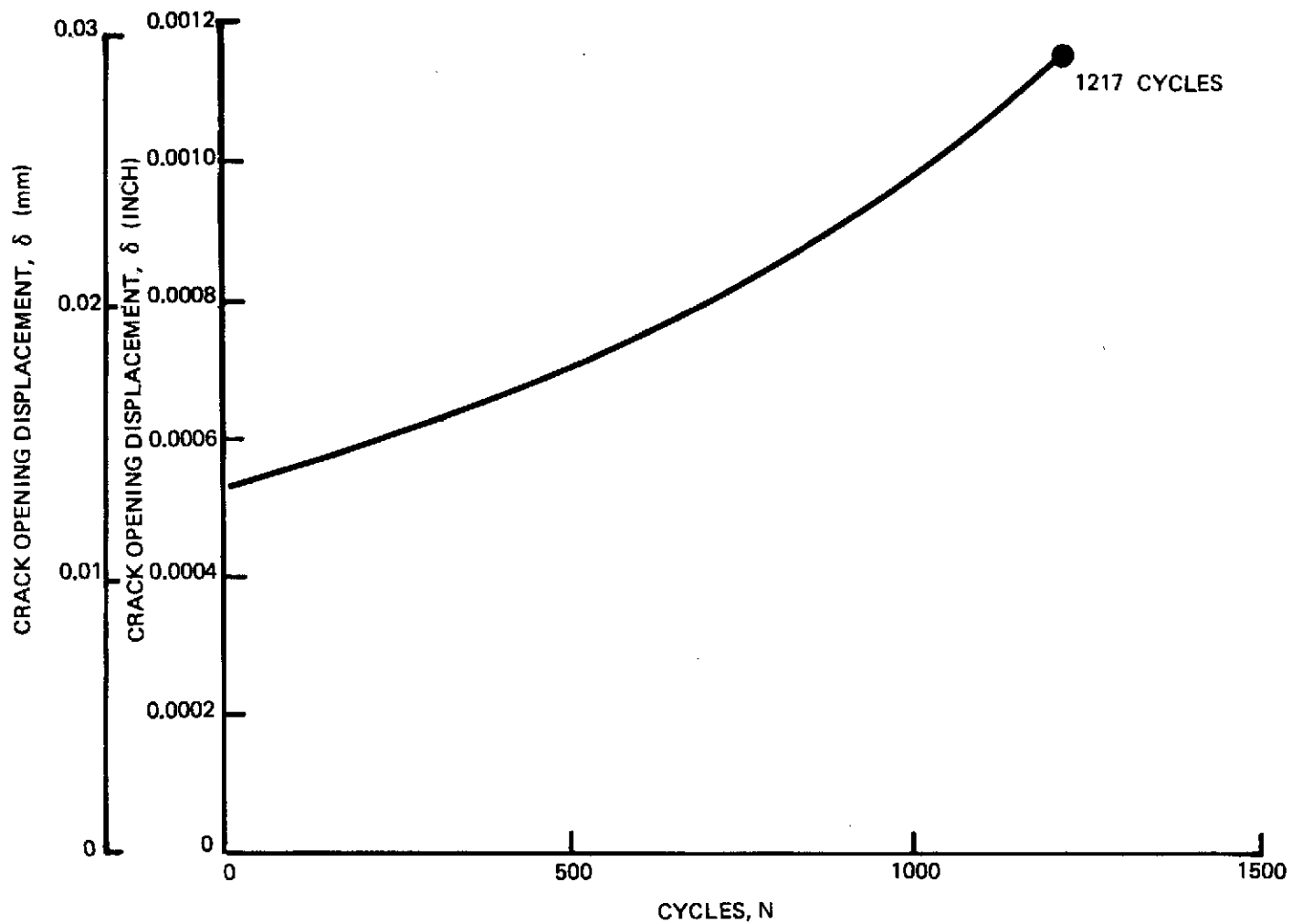


Figure 5-20: Typical Crack Opening Displacement Vs. Cycles Record For 6Al-4V  $\beta$ STA Titanium Specimen at -320F (78K)

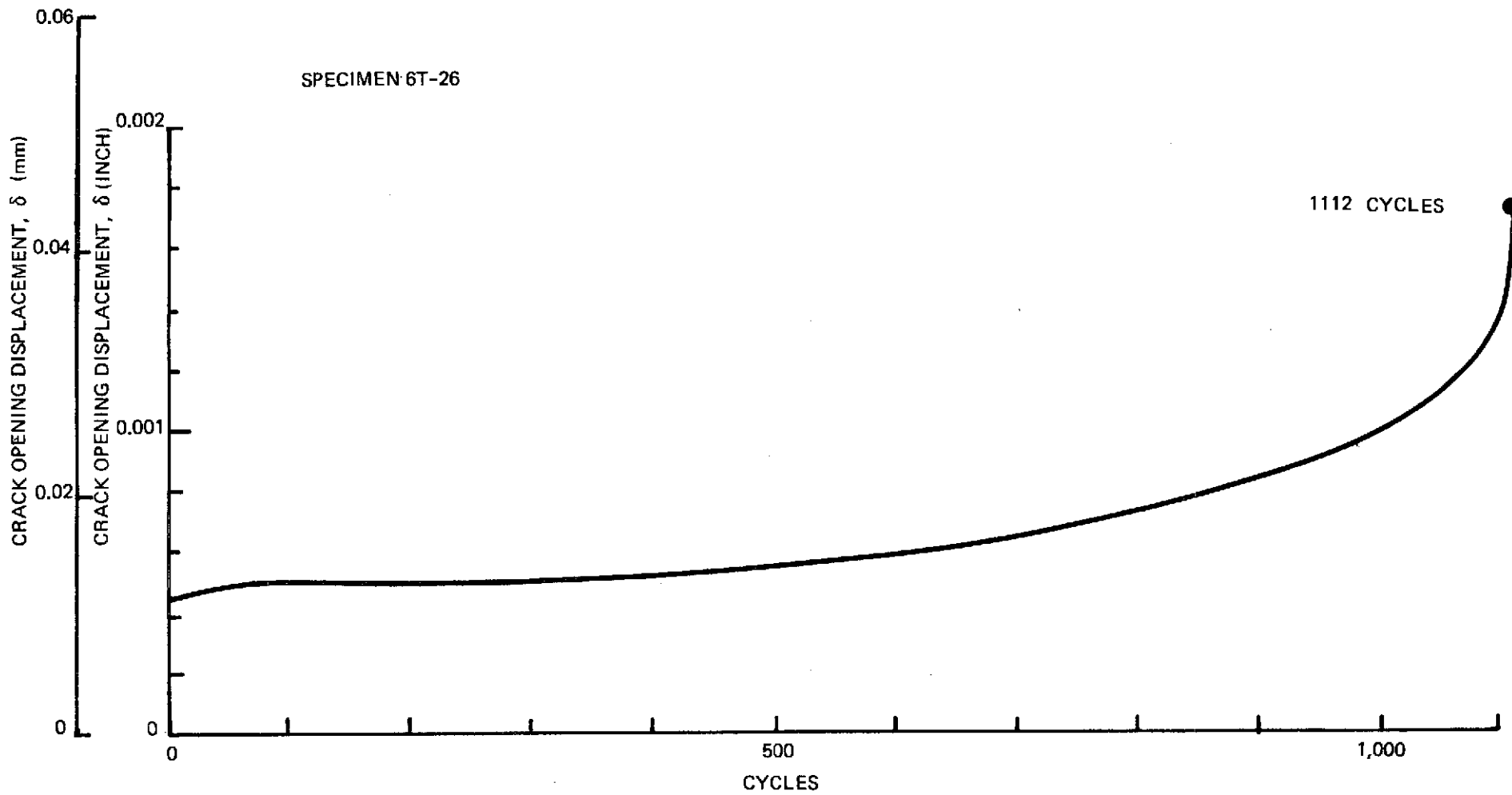


Figure 5-21: Typical Crack Opening Displacement Vs. Cycles Record For 6Al-4V  $\beta$ STA Titanium Specimen at -423F (20K)

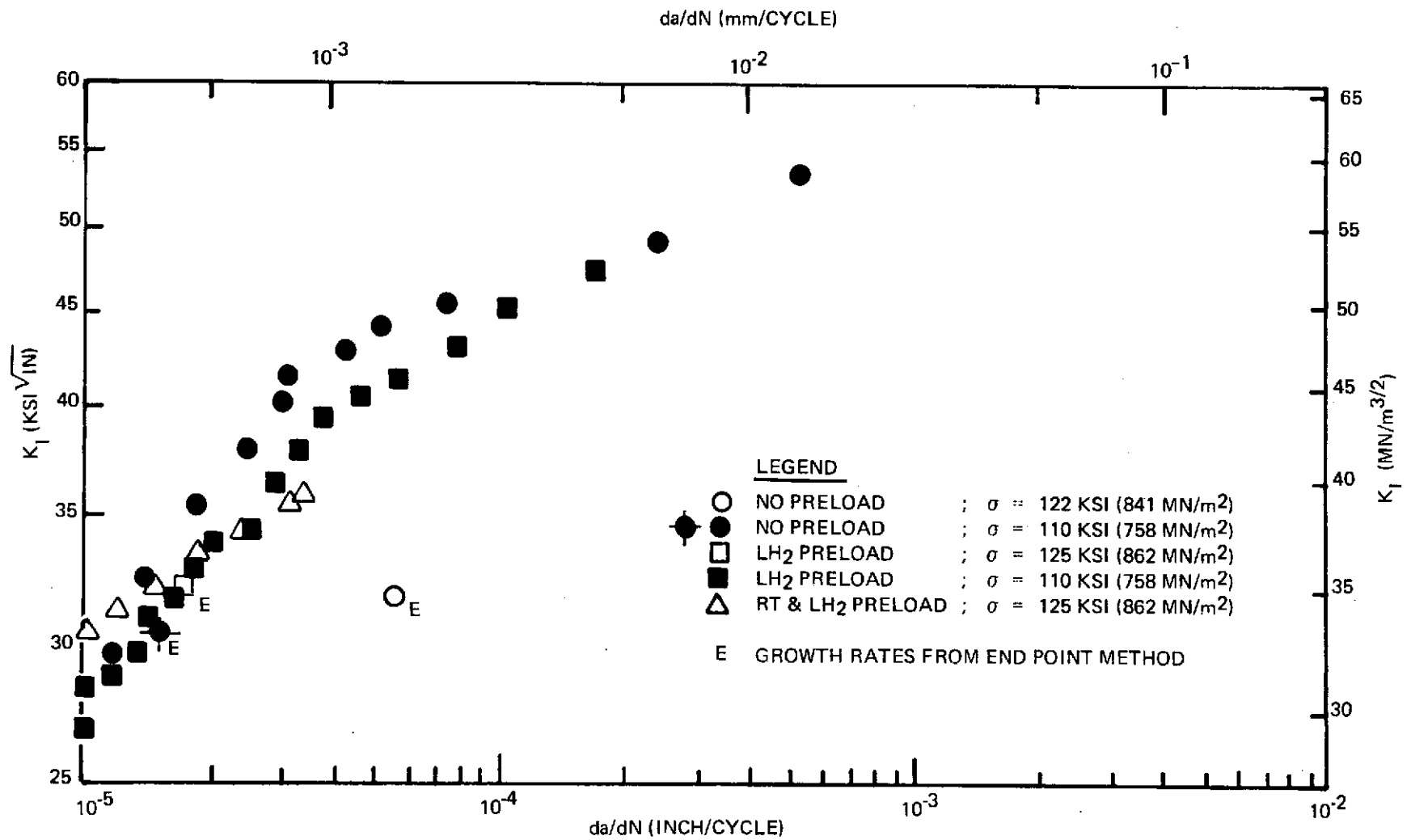


Figure 5-22: Comparisons of Cyclic Flaw Growth Rates For 6Al-4V  $\beta$ -STA Titanium at Room Temperature With and Without Proof Load Cycles

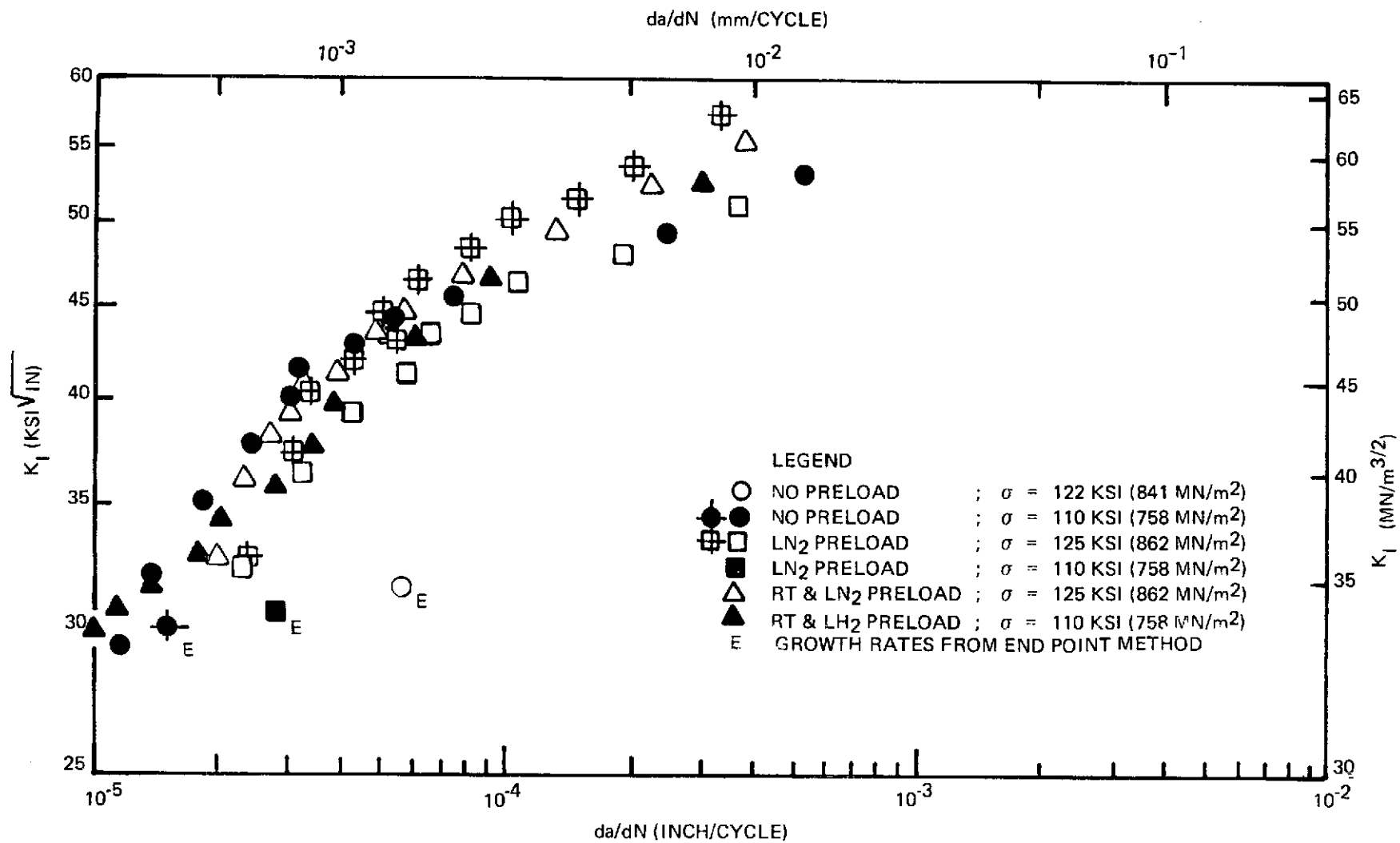


Figure 5-23: Comparisons of Cyclic Flaw Growth Rates For 6Al-4V  $\beta$ -STA Titanium at Room Temperature With and Without Proof Load Cycles

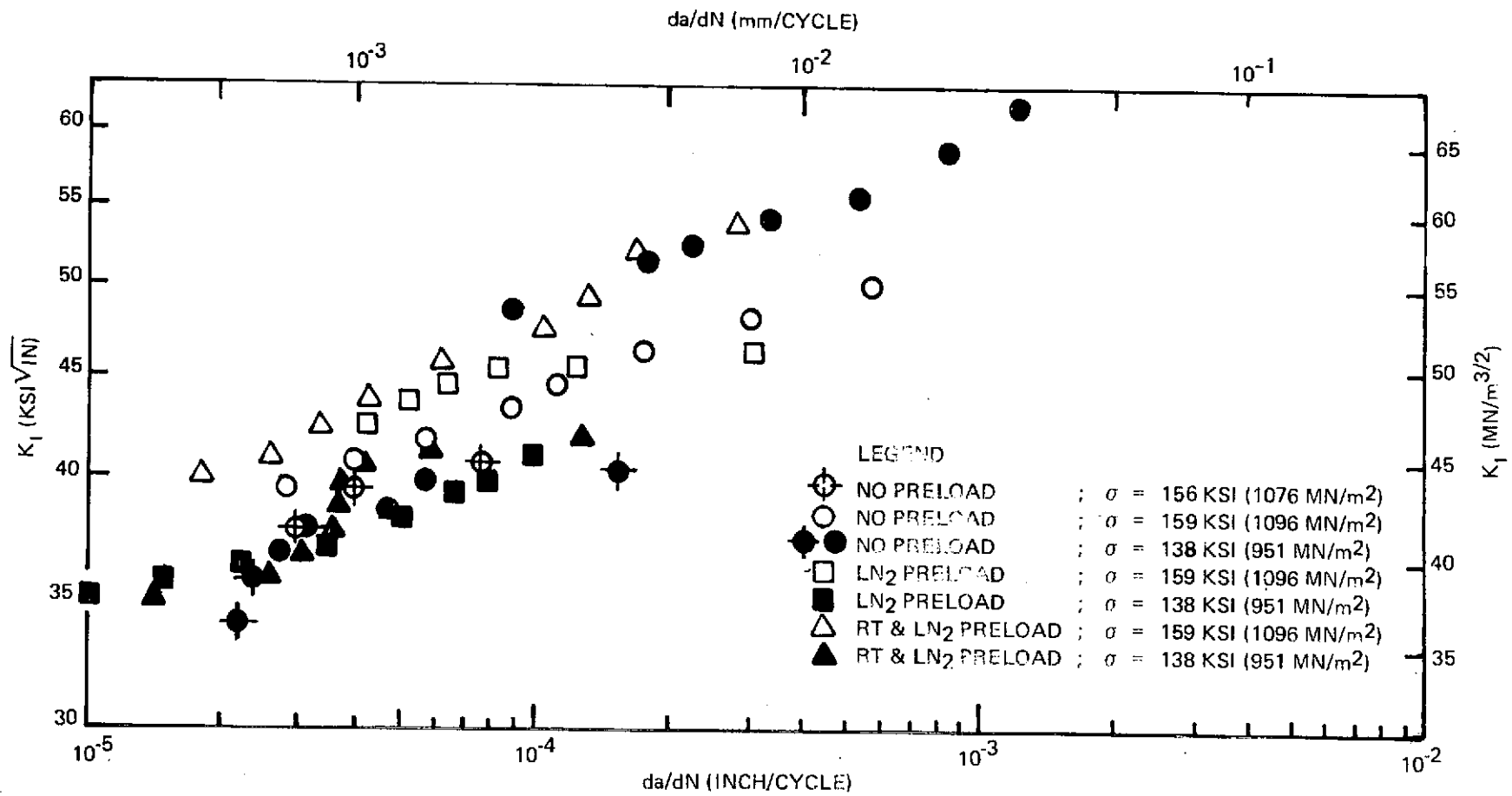


Figure 5-24: Comparisons of Cyclic Flaw Growth Rates For 6Al-4V  $\beta$ -STA Titanium at -320F (78K) With and Without Proof Load Cycles

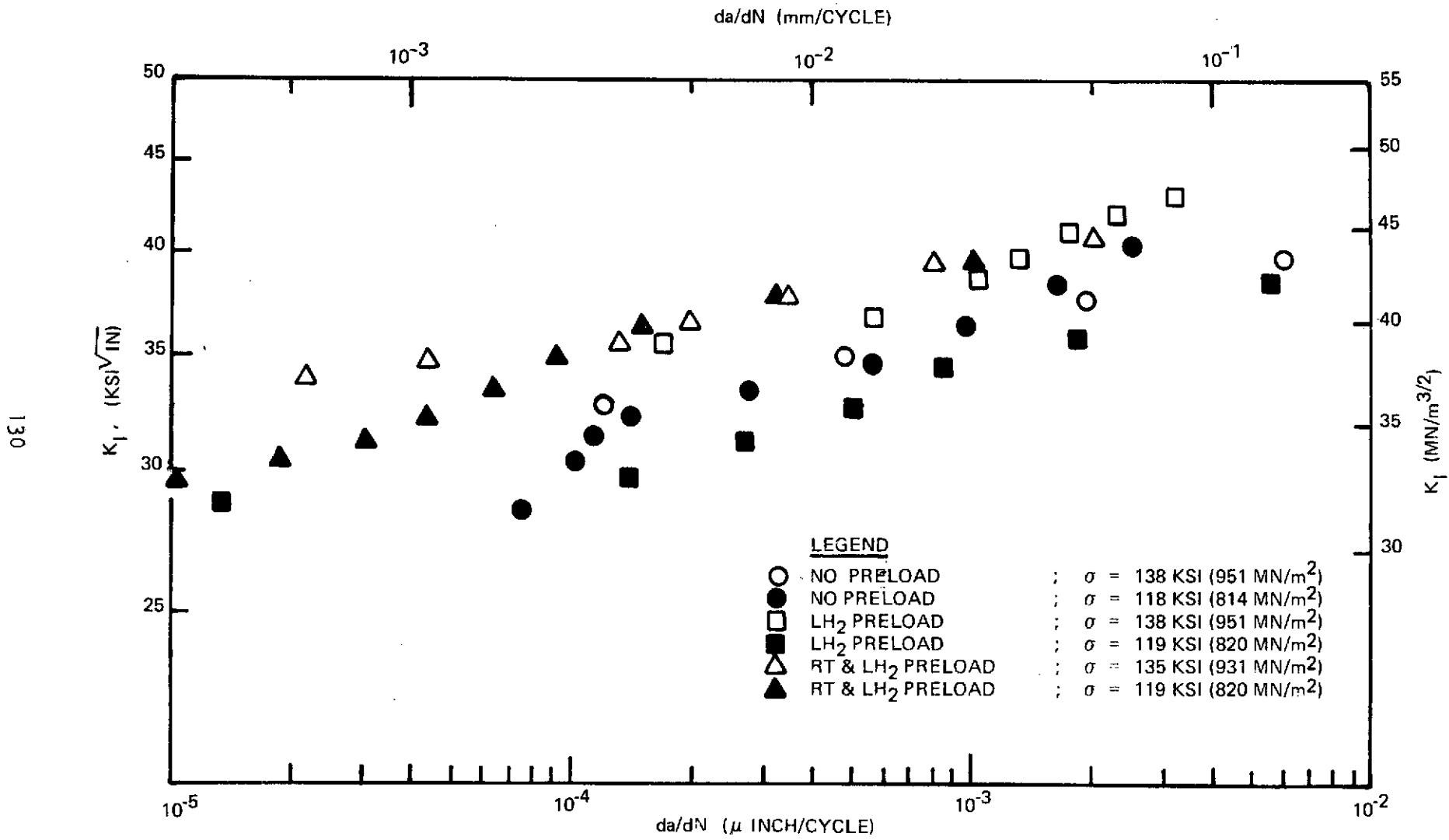


Figure 5-25: Comparisons of Cyclic Flaw Growth Rates For 6Al-4V β-STa Titanium at -423F (20K) With and Without Proof Load Cycles

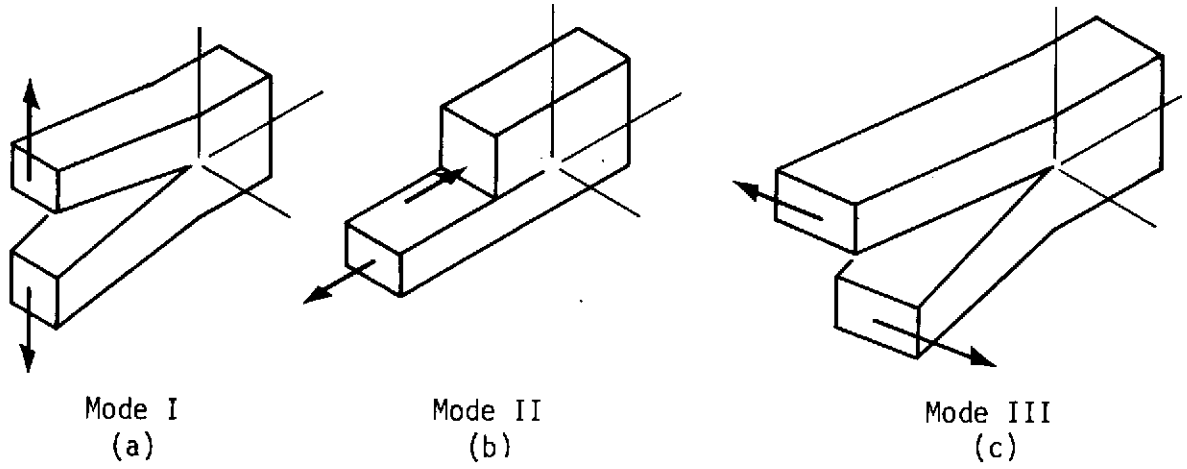


Figure 6-1 : Basic Modes of Crack Surface Displacement

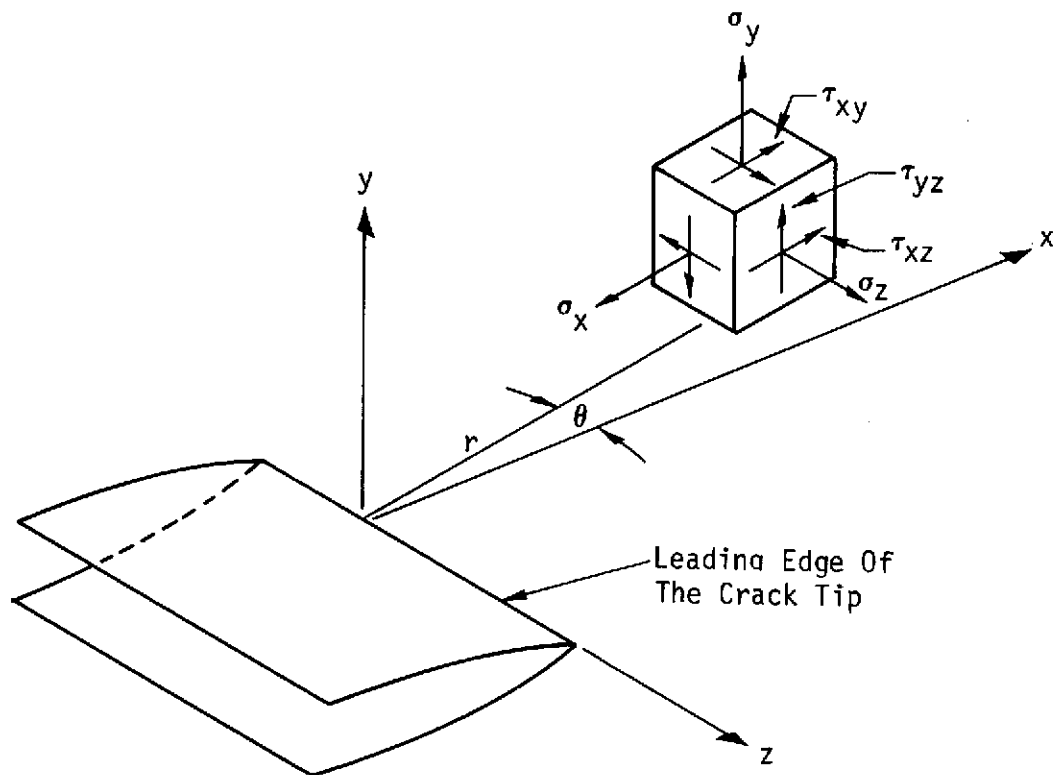


Figure 6-2: Stress Components Near the Crack Tip in Cartesian Coordinates

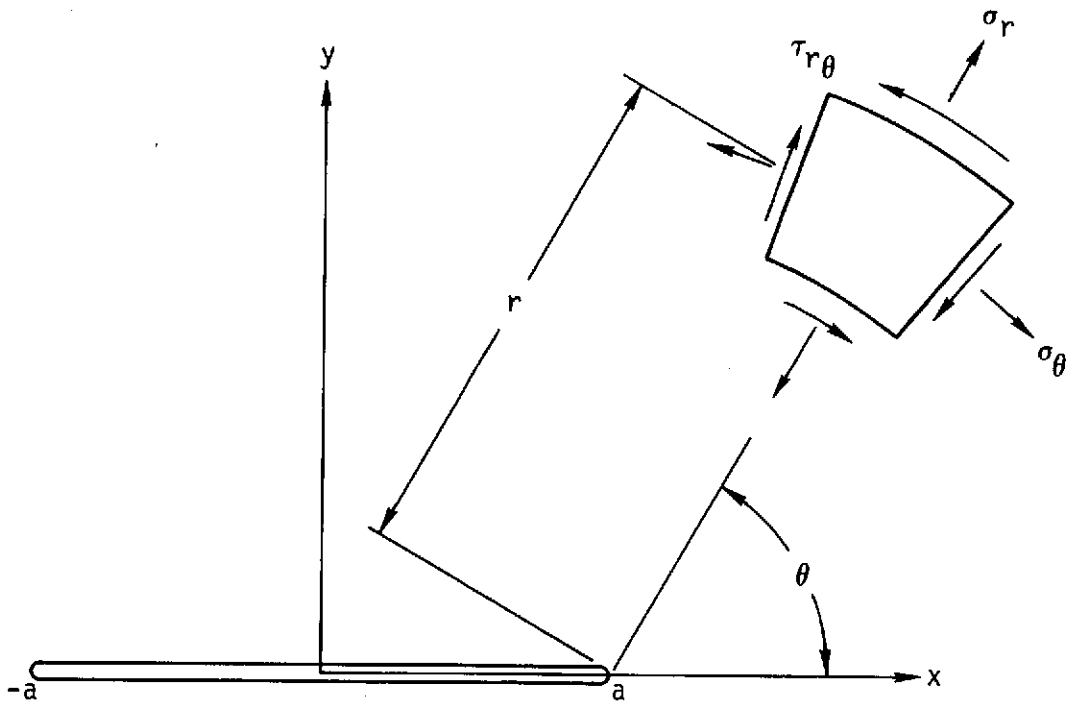


Figure 6-3: Stress Components Near the Crack Tip in Cylindrical Coordinates

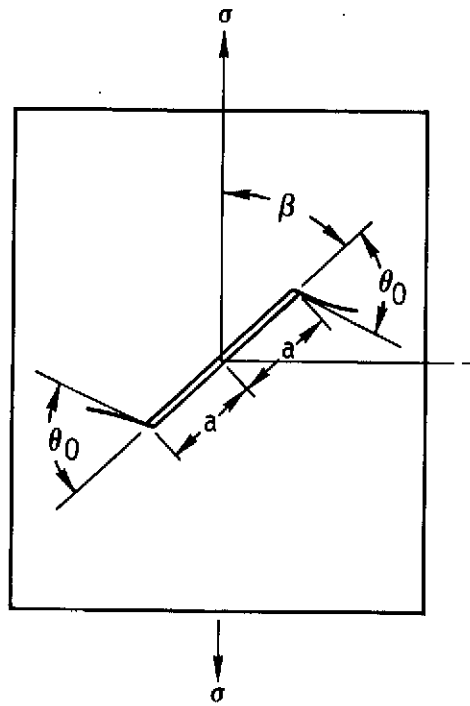


Figure 6-4: Cracked Plate Under Uniform Tension



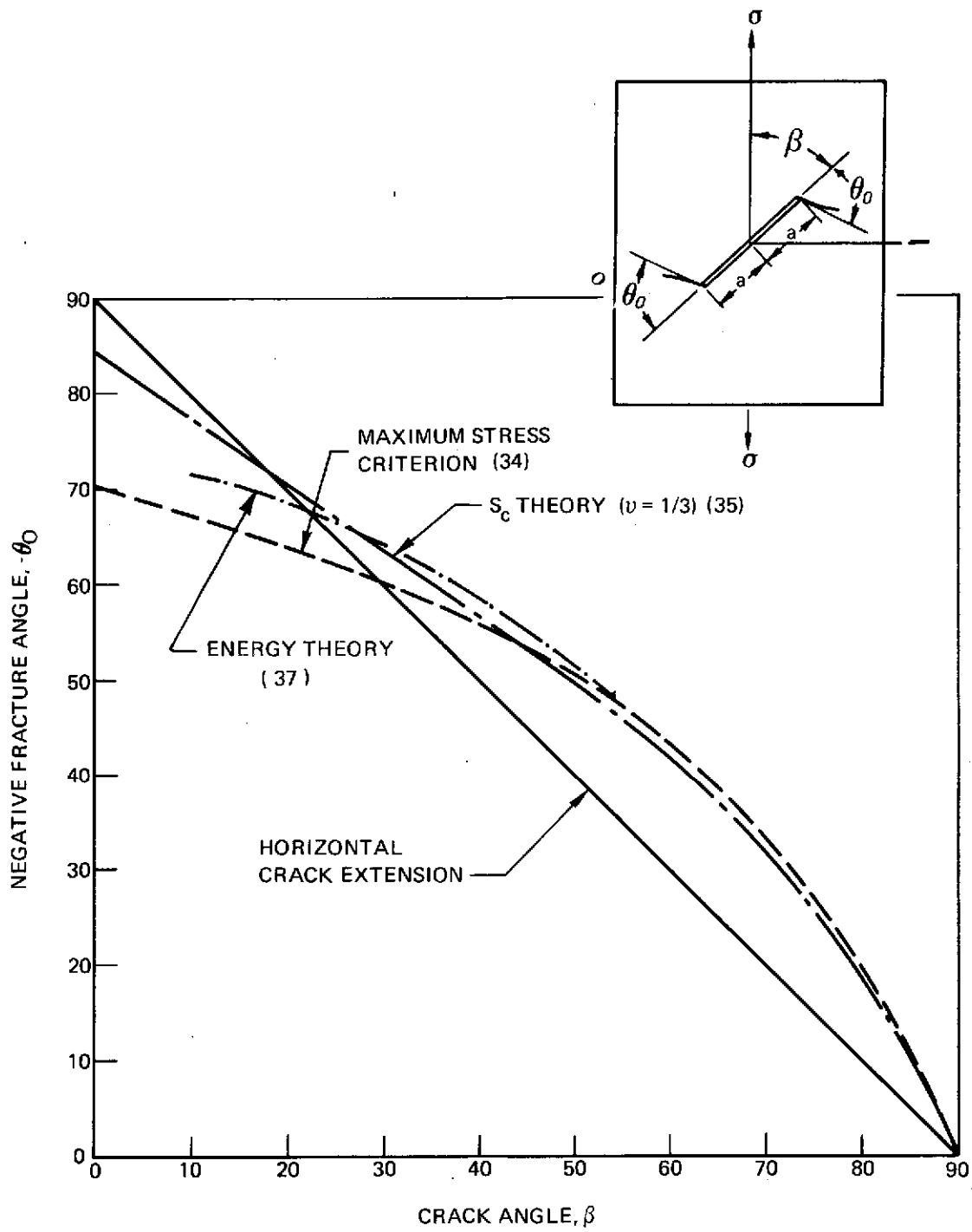
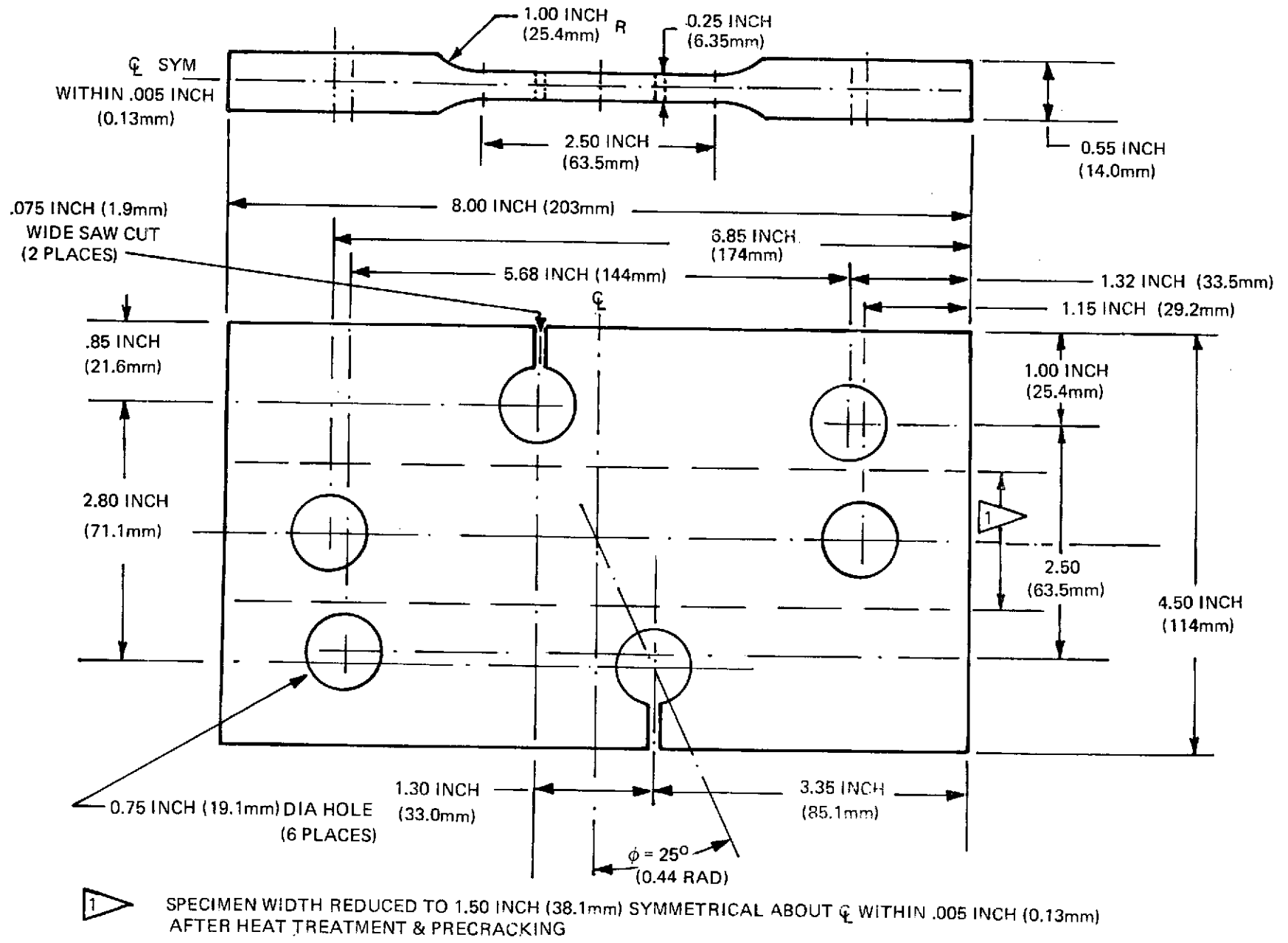


Figure 6-5: Fracture Angle Versus Crack Angle in a Cracked Plate Under Uniform Tension



134

Figure 6-6: Specimens for  $\phi$  Degree Inclined Center Cracks for Combined Mode I-II Tests

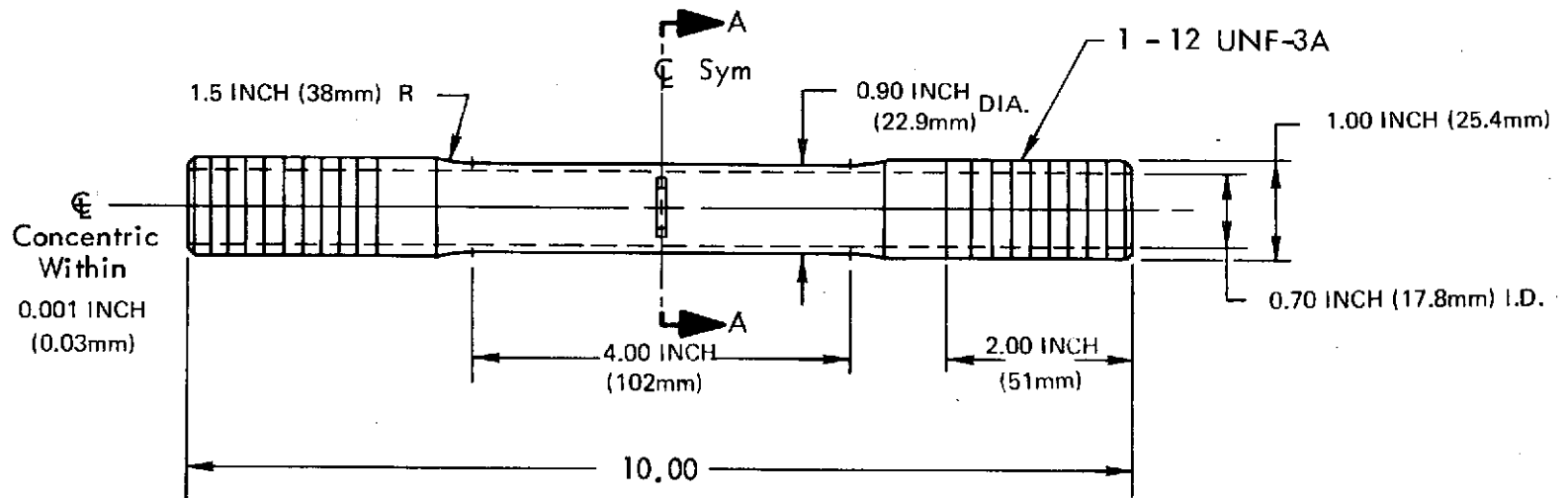
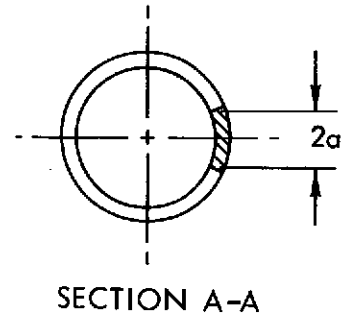


Figure 6-7: Through Cracked Tube Specimens for Mode II Tests

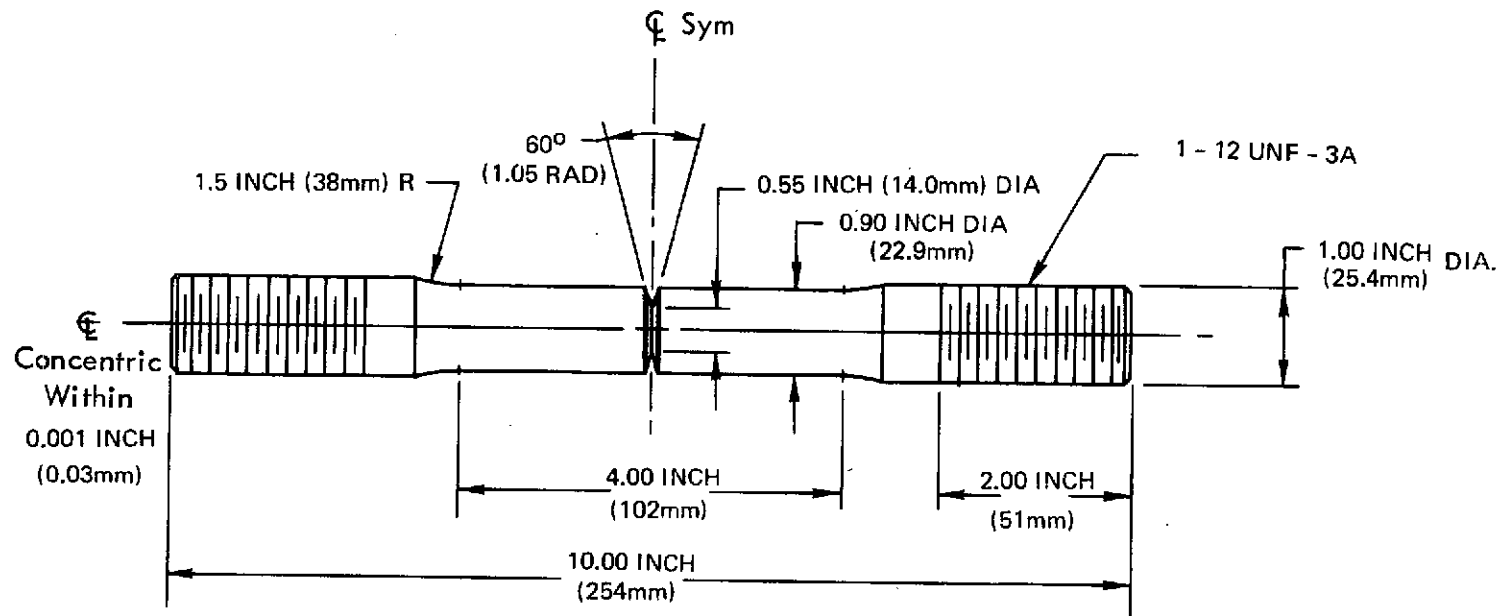


Figure 6-8: Circumferentially Notched Round Bar Specimens for Combined Mode I-III Tests

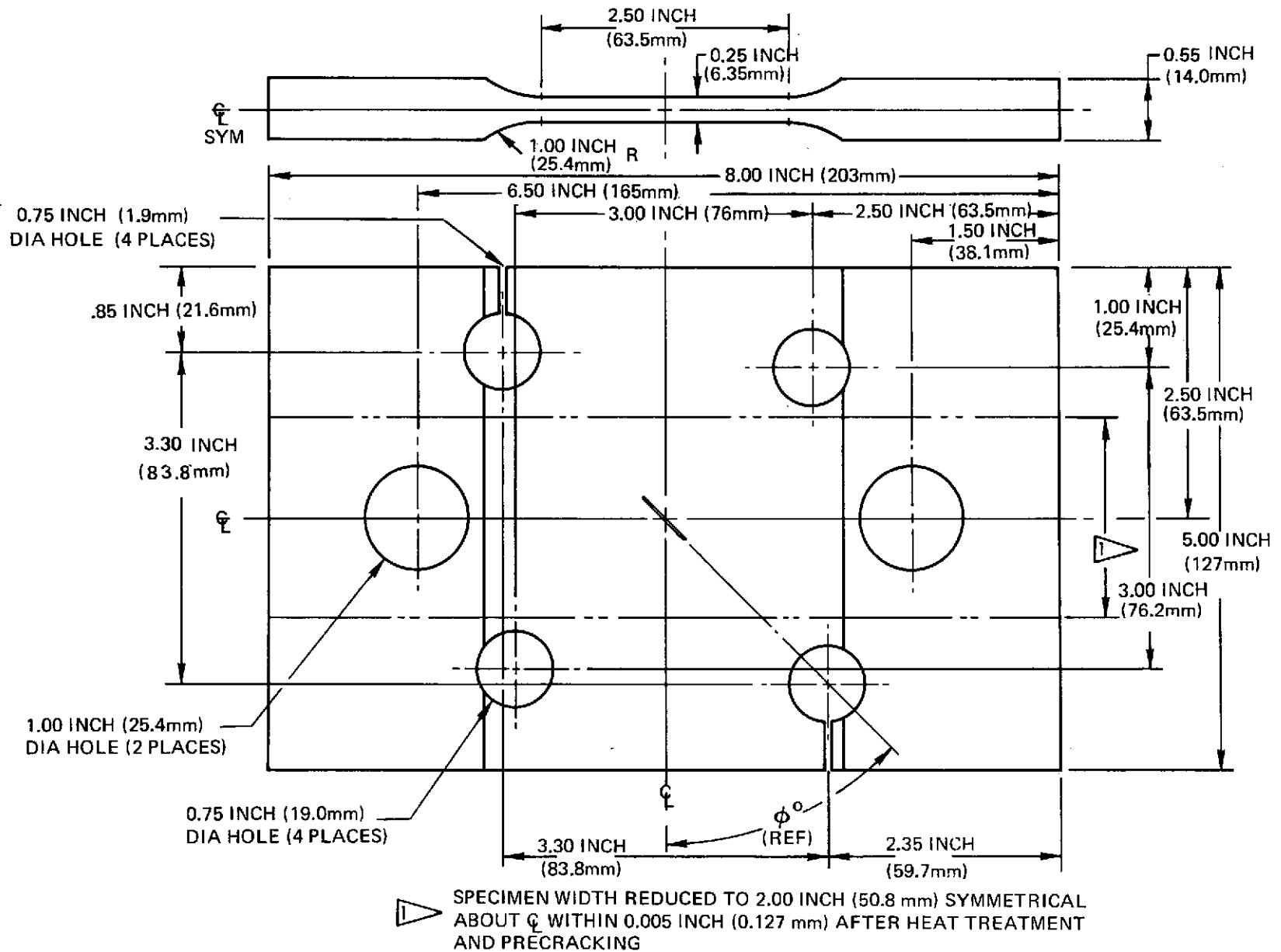


Figure 6-9: Specimens for  $\phi$  Degree Inclined Surface Flaws for Combined Mode I-II-III Tests

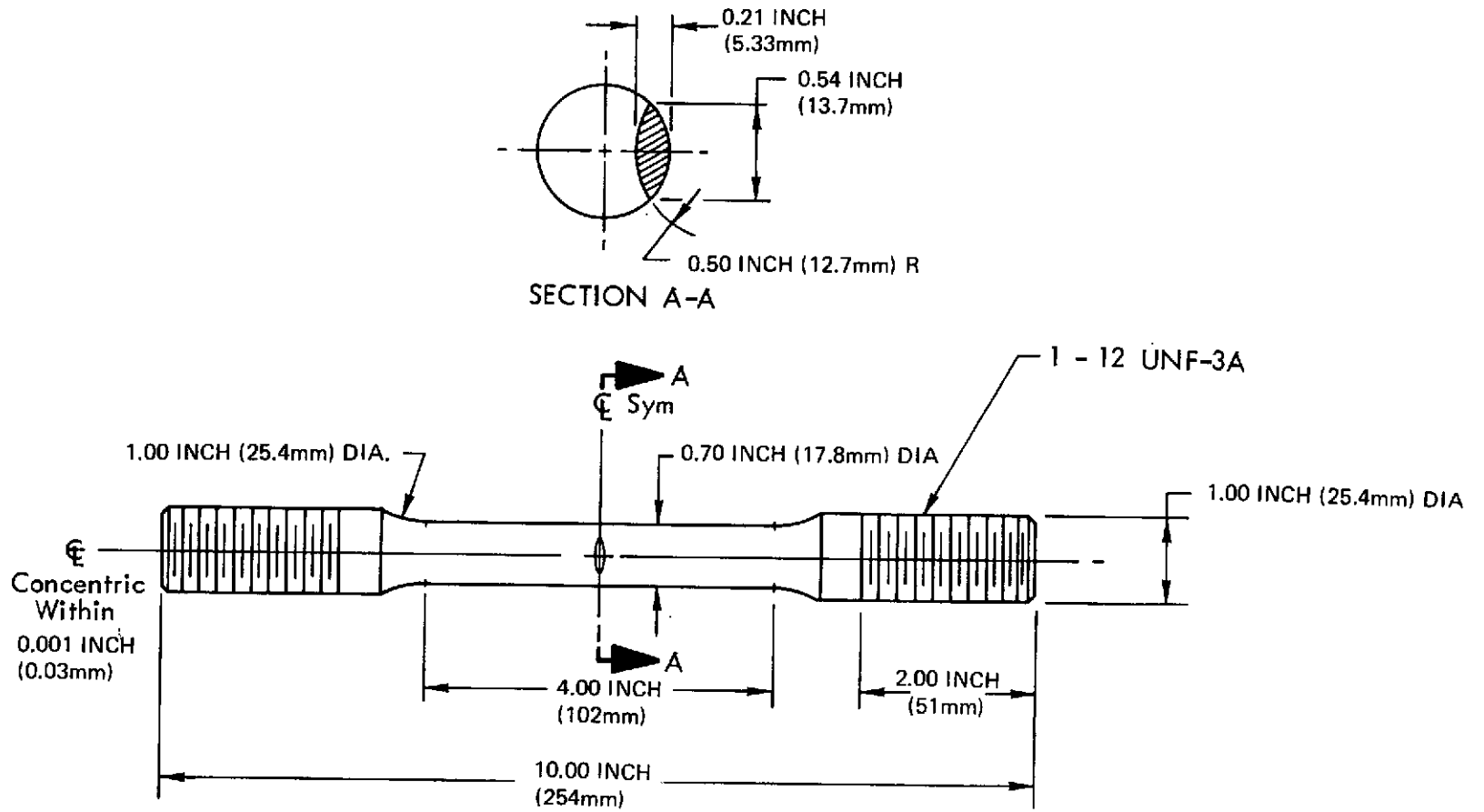


Figure 6-10: Surface Flawed Cylindrical Specimens for Combined Mode I-II-III Tests

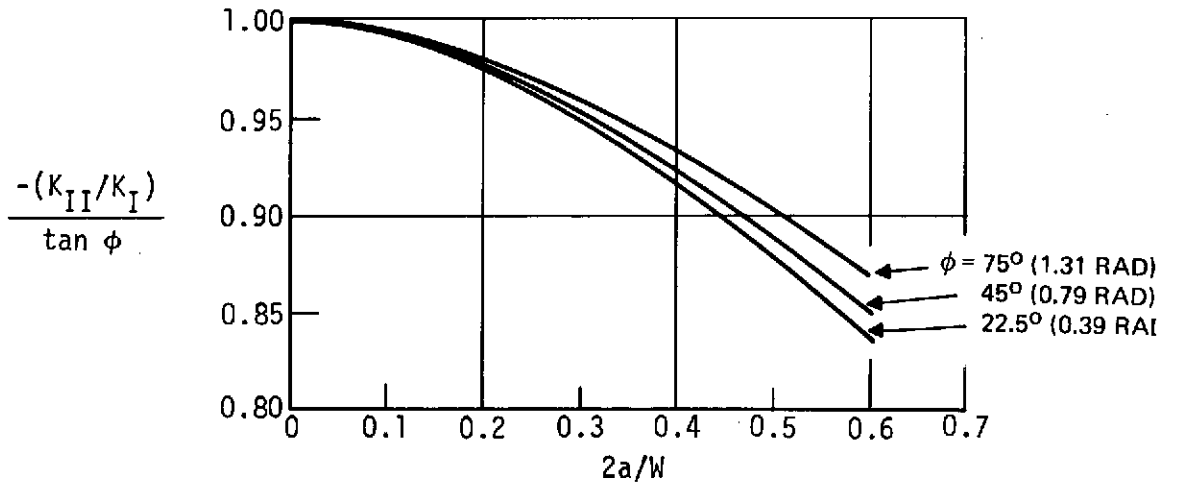
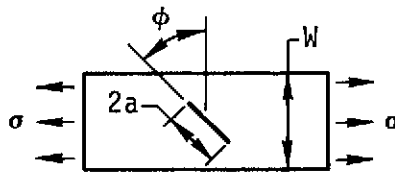
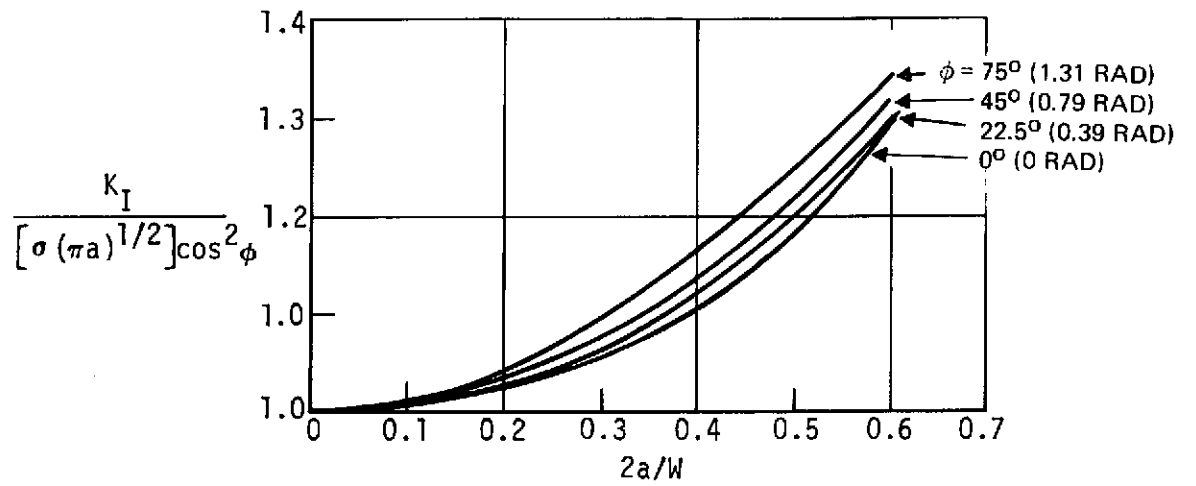


Figure 6-11: Stress Intensity Factors for Inclined Center Cracked Strips Subjected to Uniaxial Tension Loading

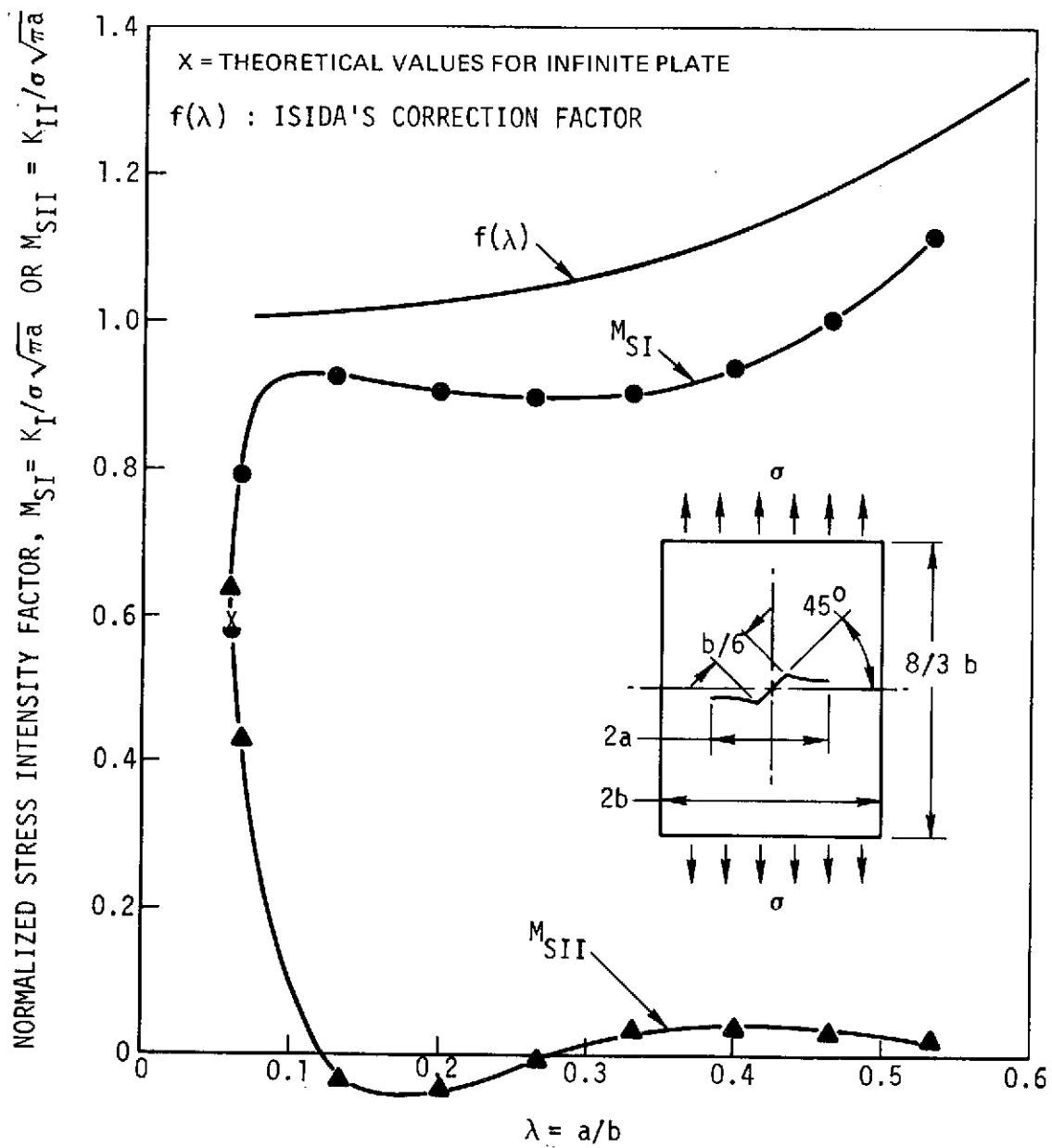


Figure 6-12: Normalized Stress Intensity Factors for a Tension Plate with Initially Slanted Crack,  $\phi = 45$  Degrees (0.79 Rad)



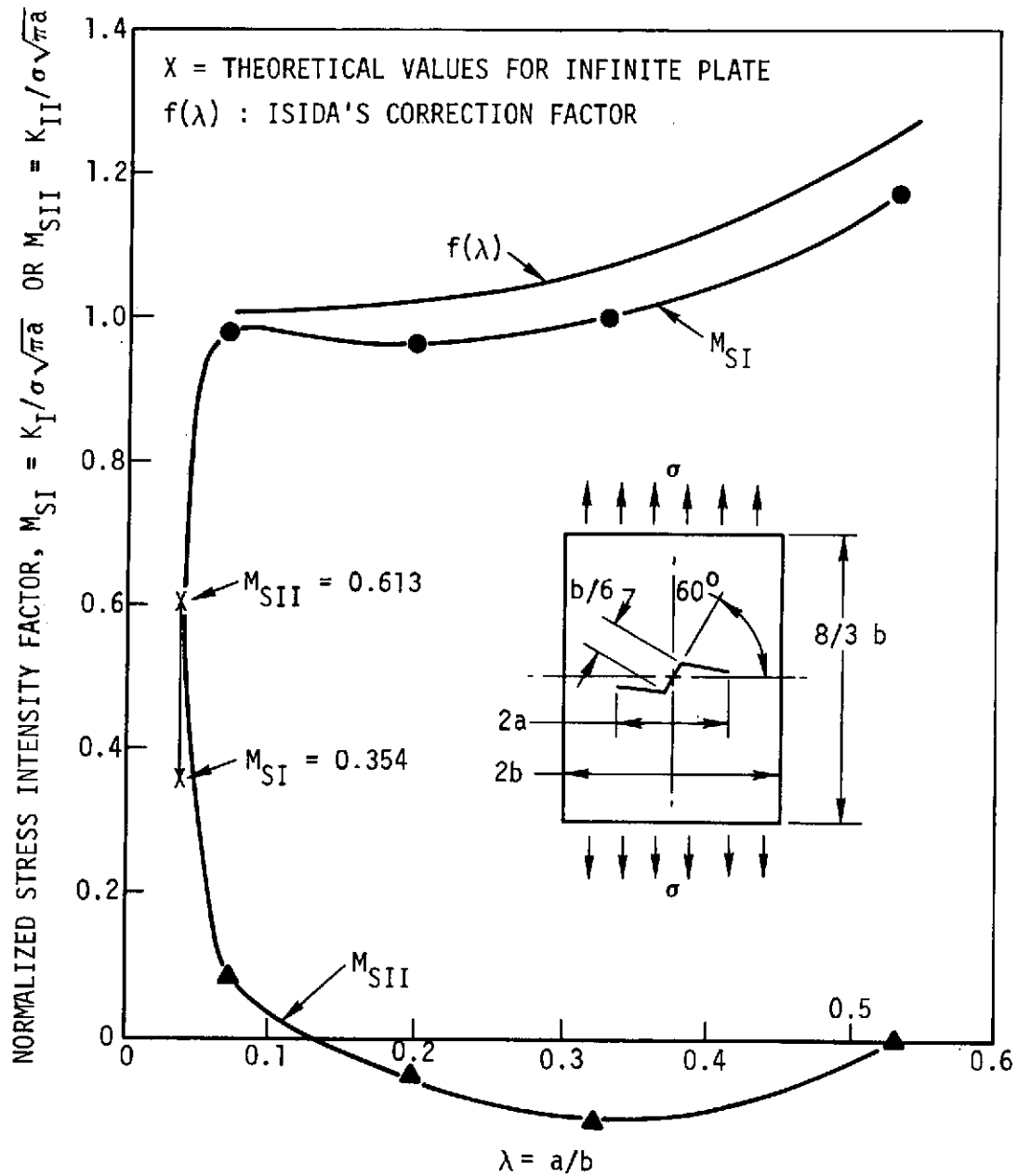


Figure 6-13: Normalized Stress Intensity Factors for a Tension Plate with Initially Slanted Crack,  $\phi = 60$  Degrees (1.05 Rad)

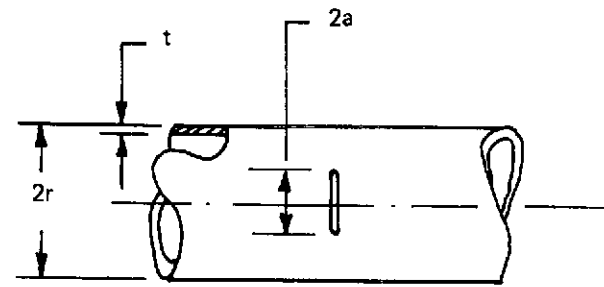
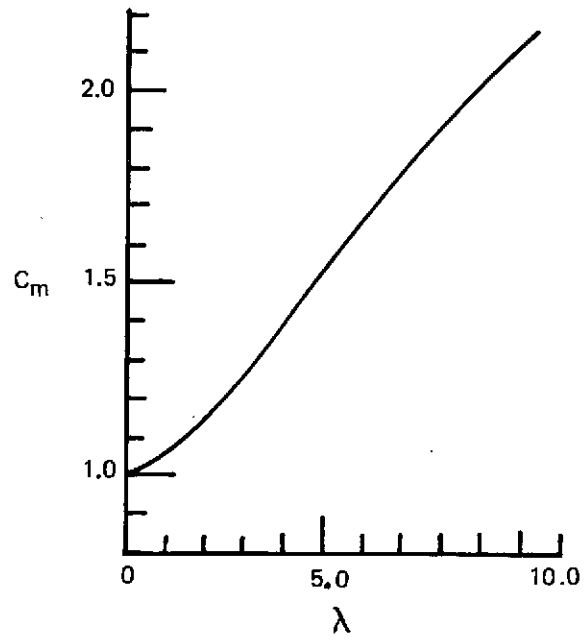


Figure 6-14: Shell Curvature Correction Factor for a Cracked Tube Subjected to Pure Torsion

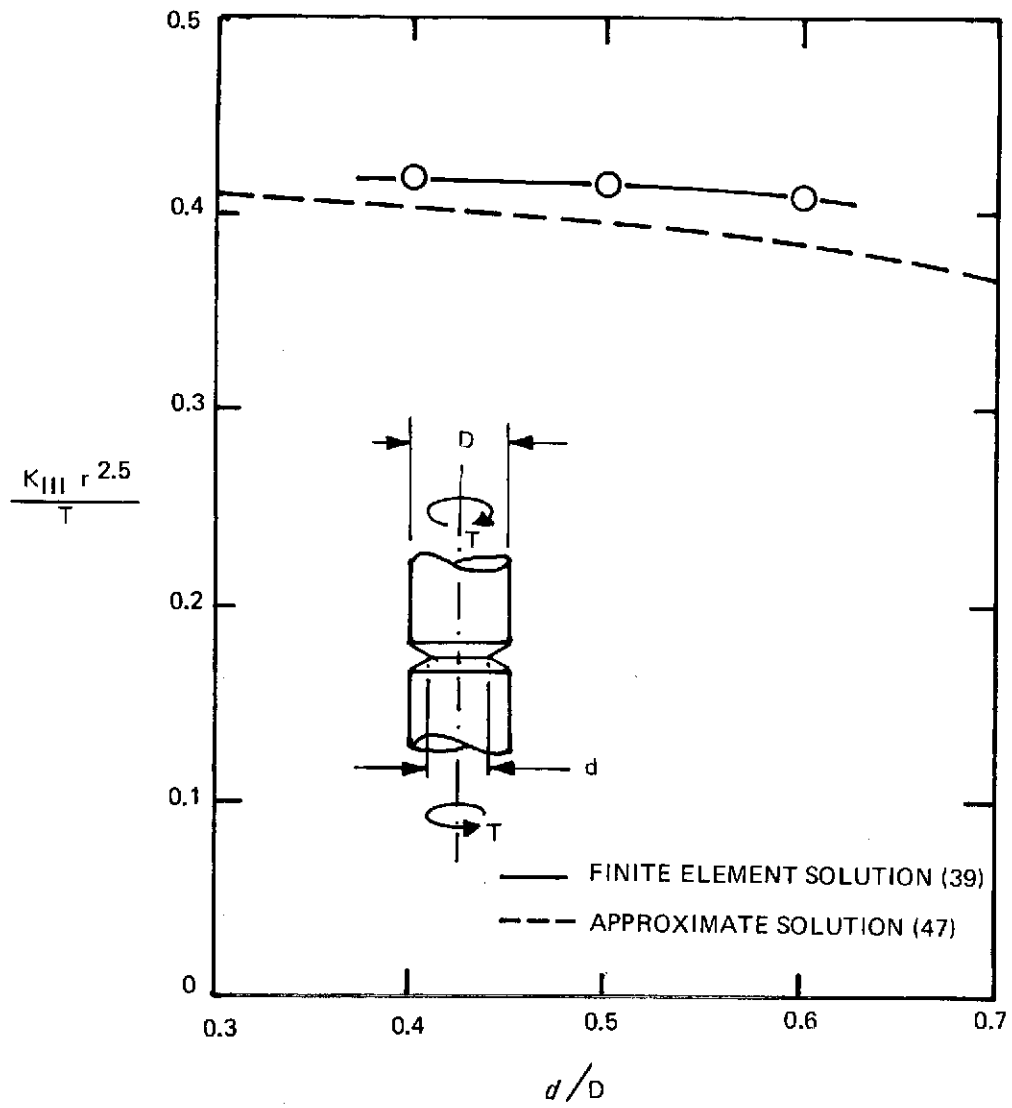
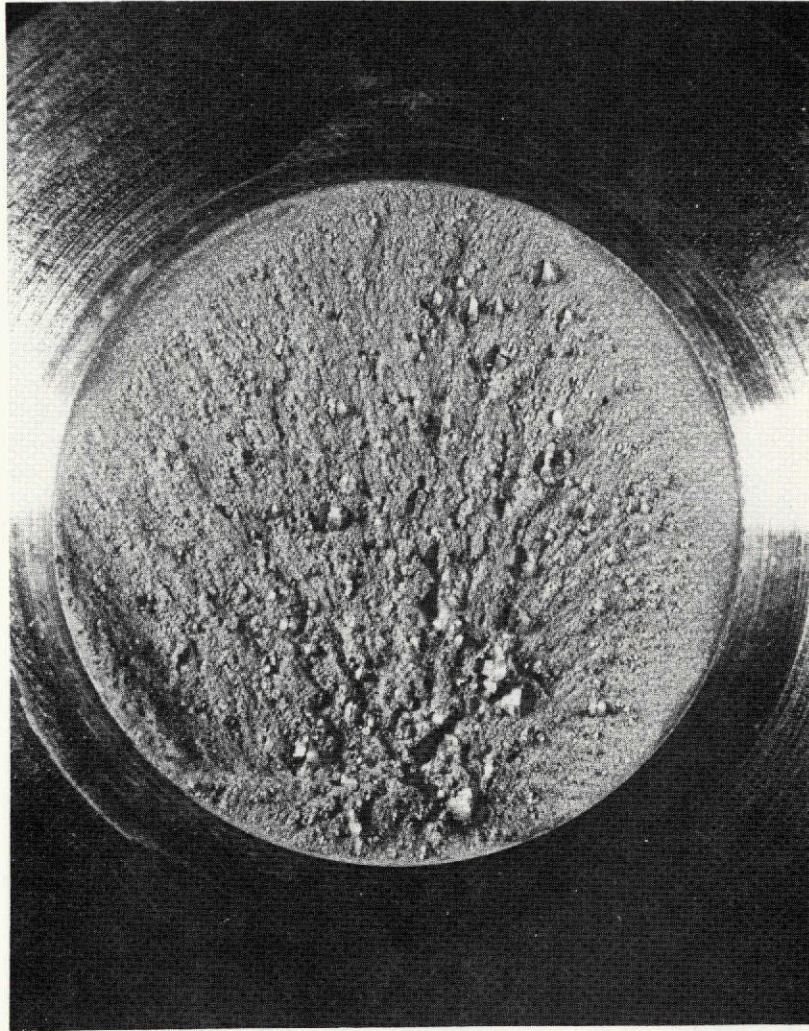
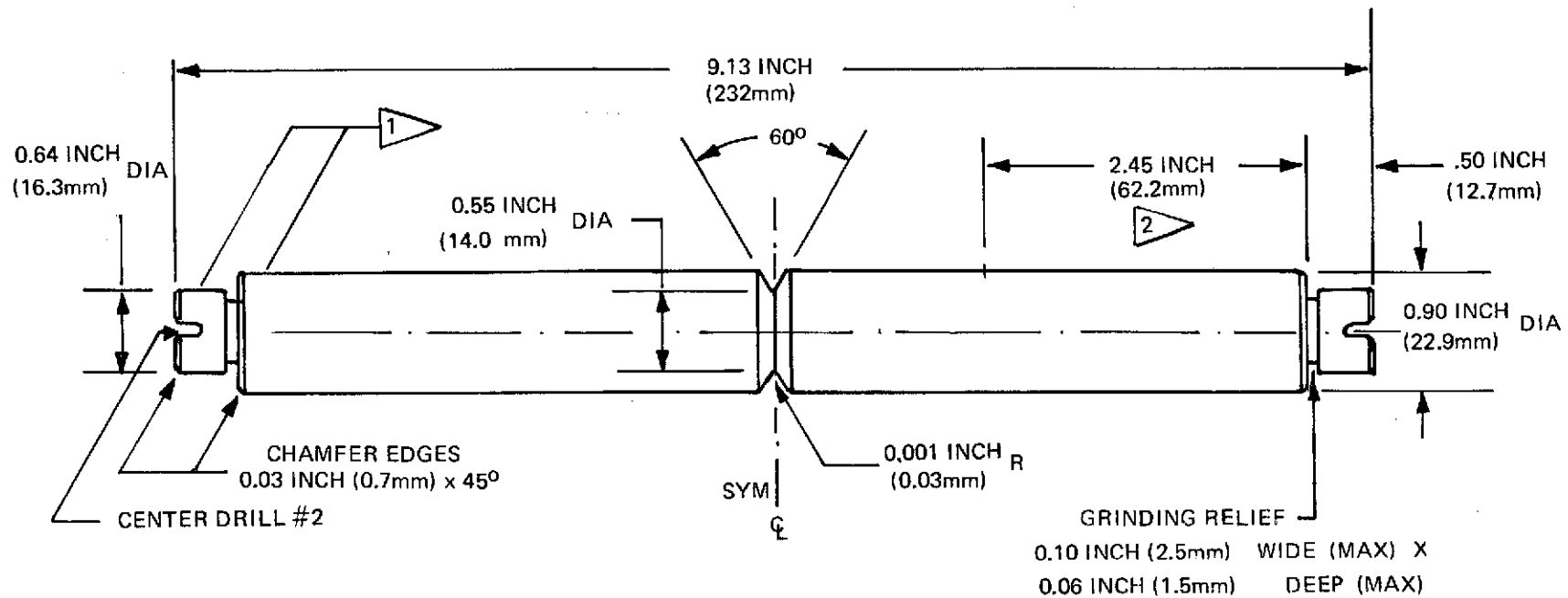


Figure 6-15: Stress Intensities for Circumferentially Cracked Round Bars Subjected to Torsion.



*Figure 6-16: Fatigue Crack Grown Under Rotating Bending Fatigue From A Circumferential V-Notch in 4340 Steel*



LINEAR TOLERANCE  $\pm 0.01$  INCH (0.25mm)

ANGULAR TOLERANCE  $\pm \frac{1}{2}^\circ$



THIS SURFACE CONCENTRIC TO  $\ell$  OF  
LONGITUDINAL AXIS WITHIN .0005 INCH (0.0013mm) TIR.



32  $\sqrt$  FINISH FOR LENGTH INDICATED

Figure 6-17: A Round Notched Bar Specimen For Precracking Under Rotating Bending Fatigue

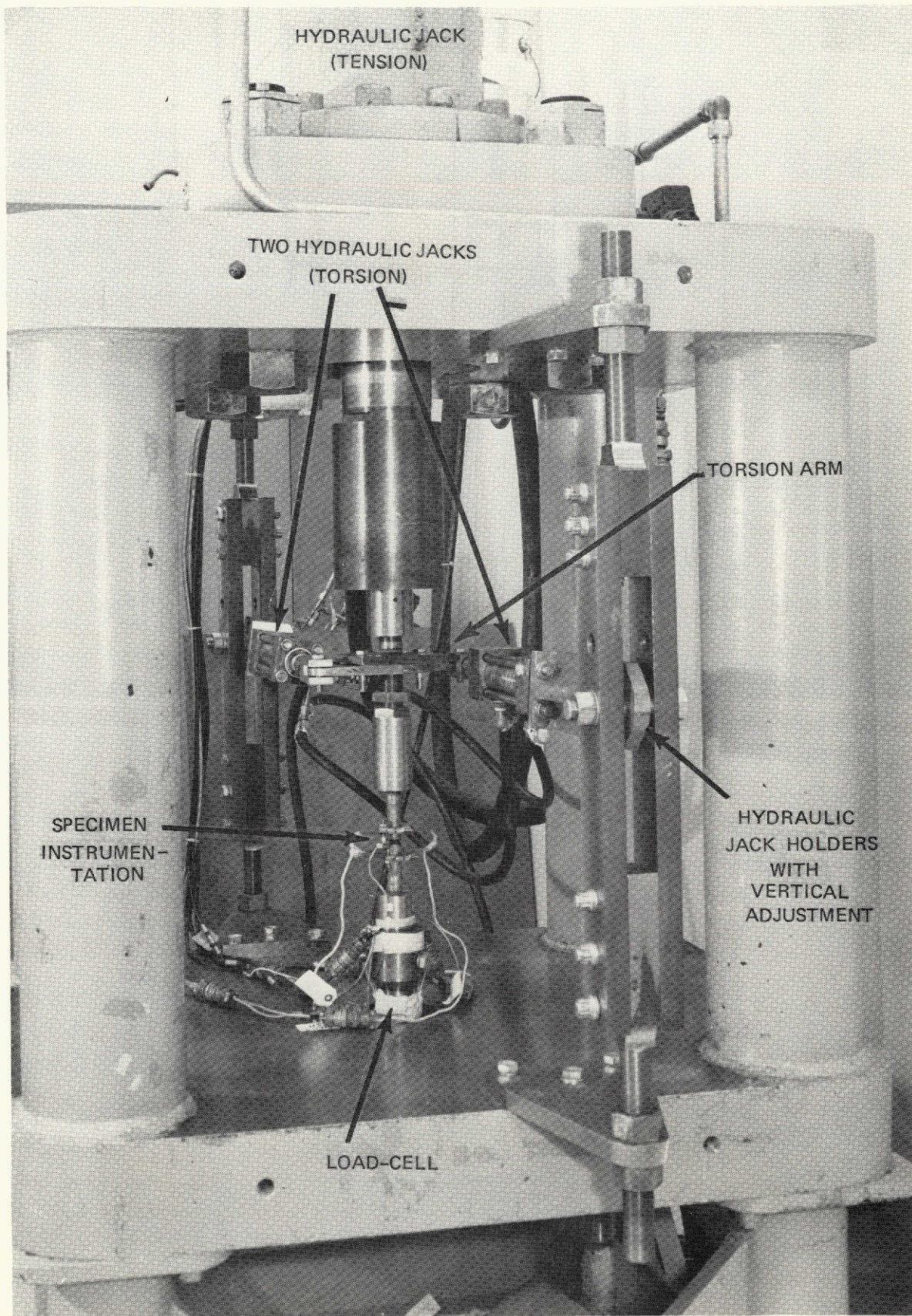


Figure 6-18: Tension-Torsion Test Machine

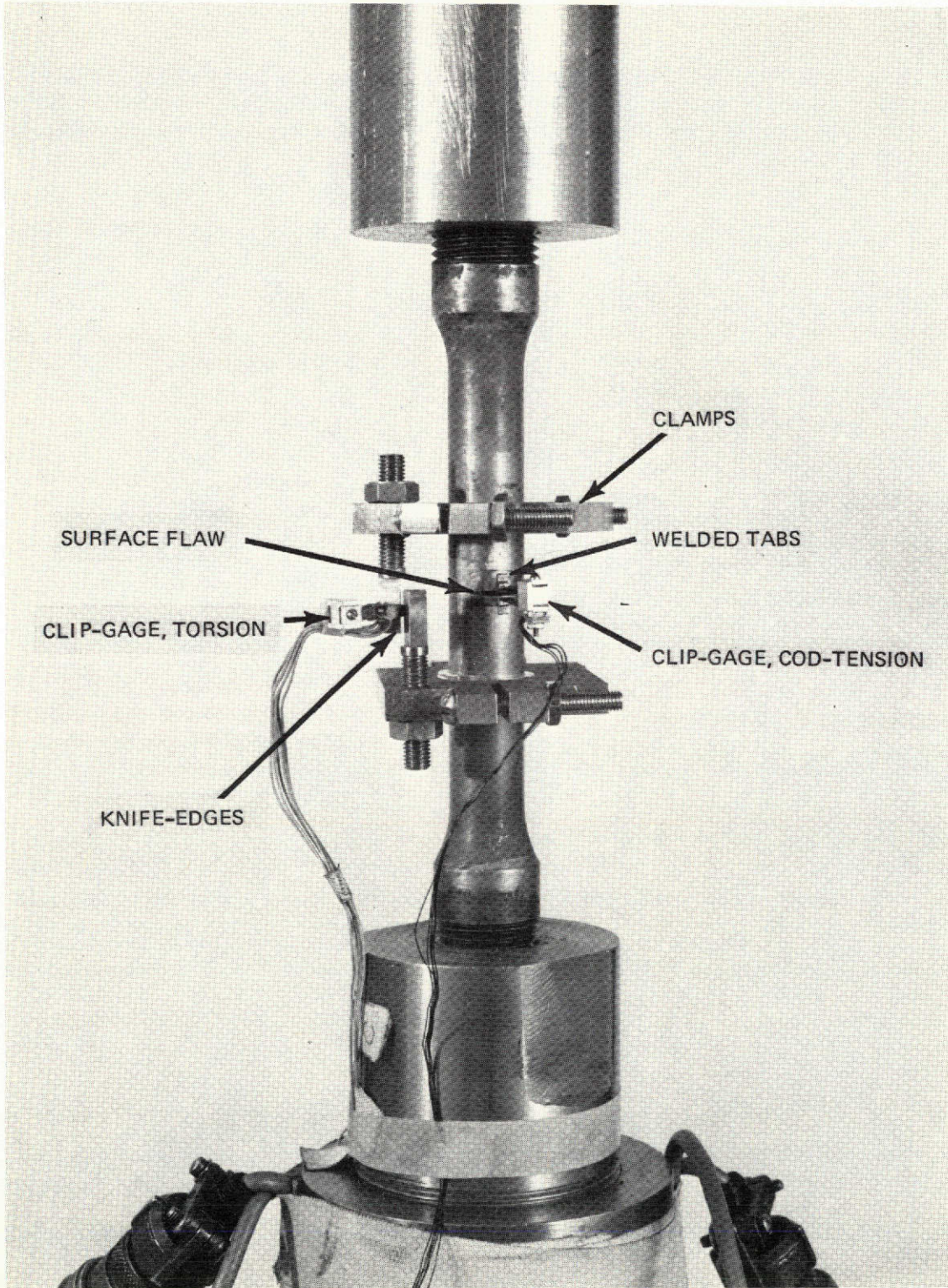


Figure 6-19: Instrumentation for Round Specimens Containing Surface Flaws

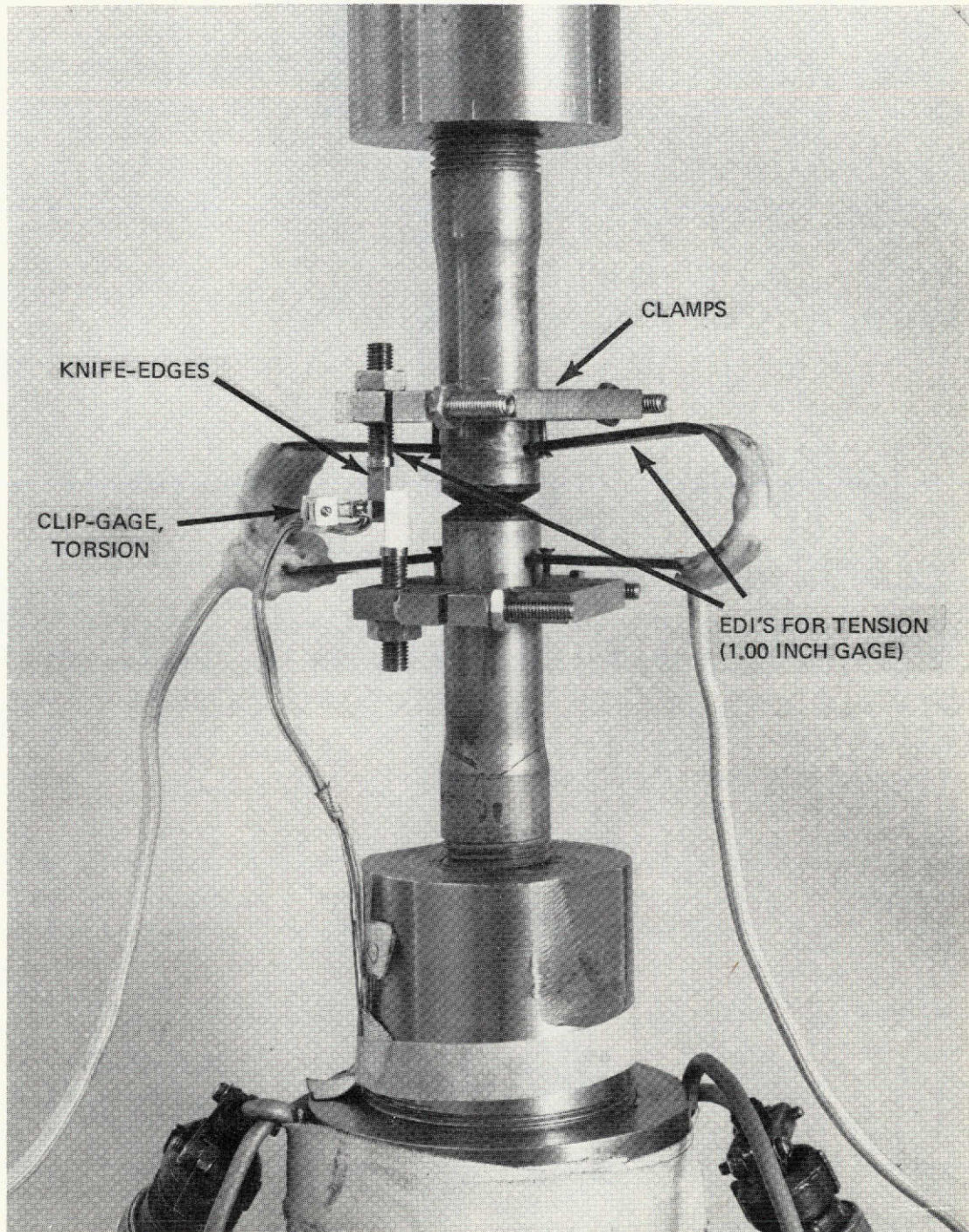
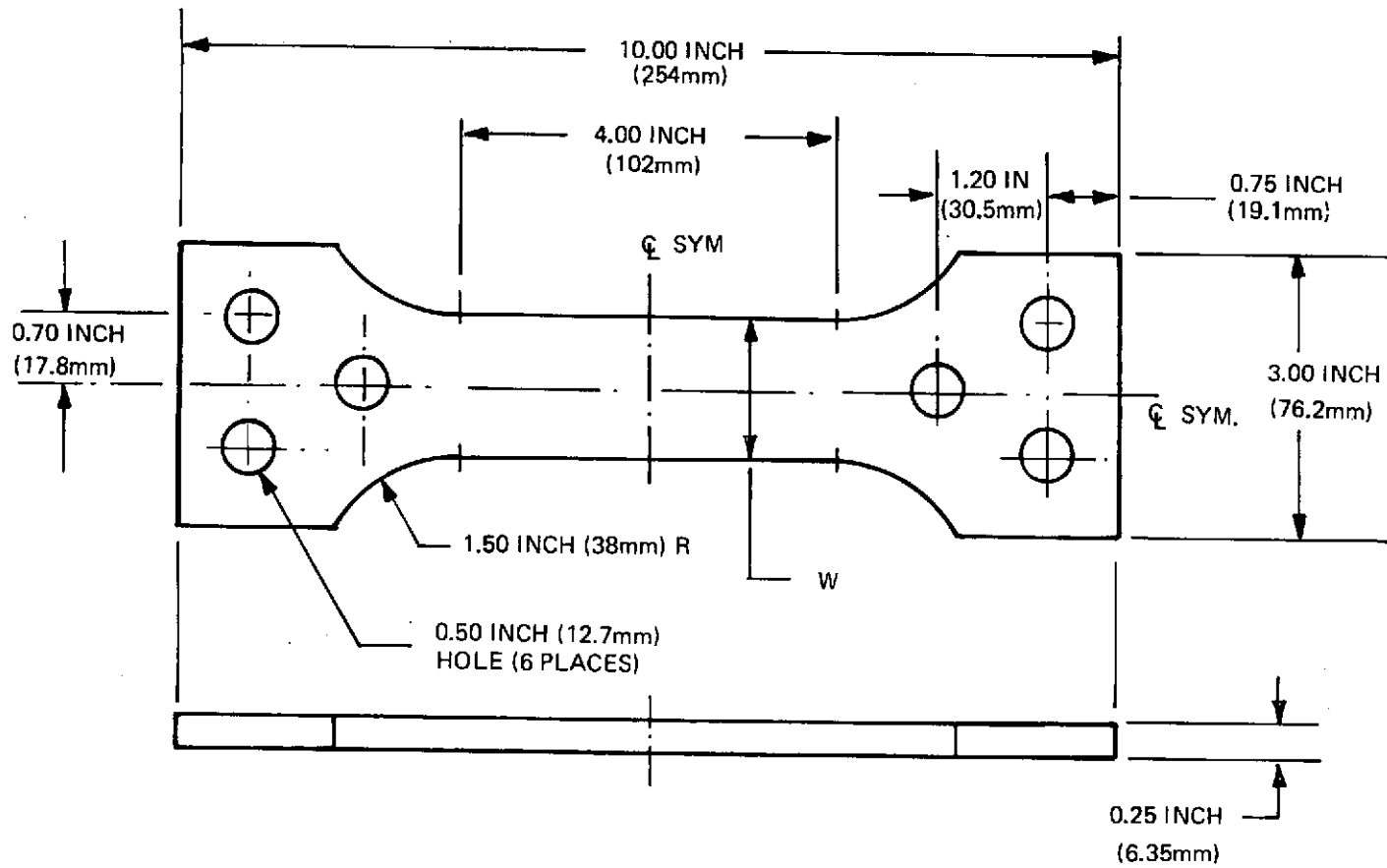


Figure 6-20: Instrumentation for Round Notched Bar Specimens





SPECIMENS	DIMENSION W
CENTER CRACKED	1.50 INCH (38.1mm)
SURFACE FLAWED	1.80 INCH (45.7mm)

Figure 6-21: Surface Flawed and Center Cracked 4340 Steel Specimens For Room Temperature Testing

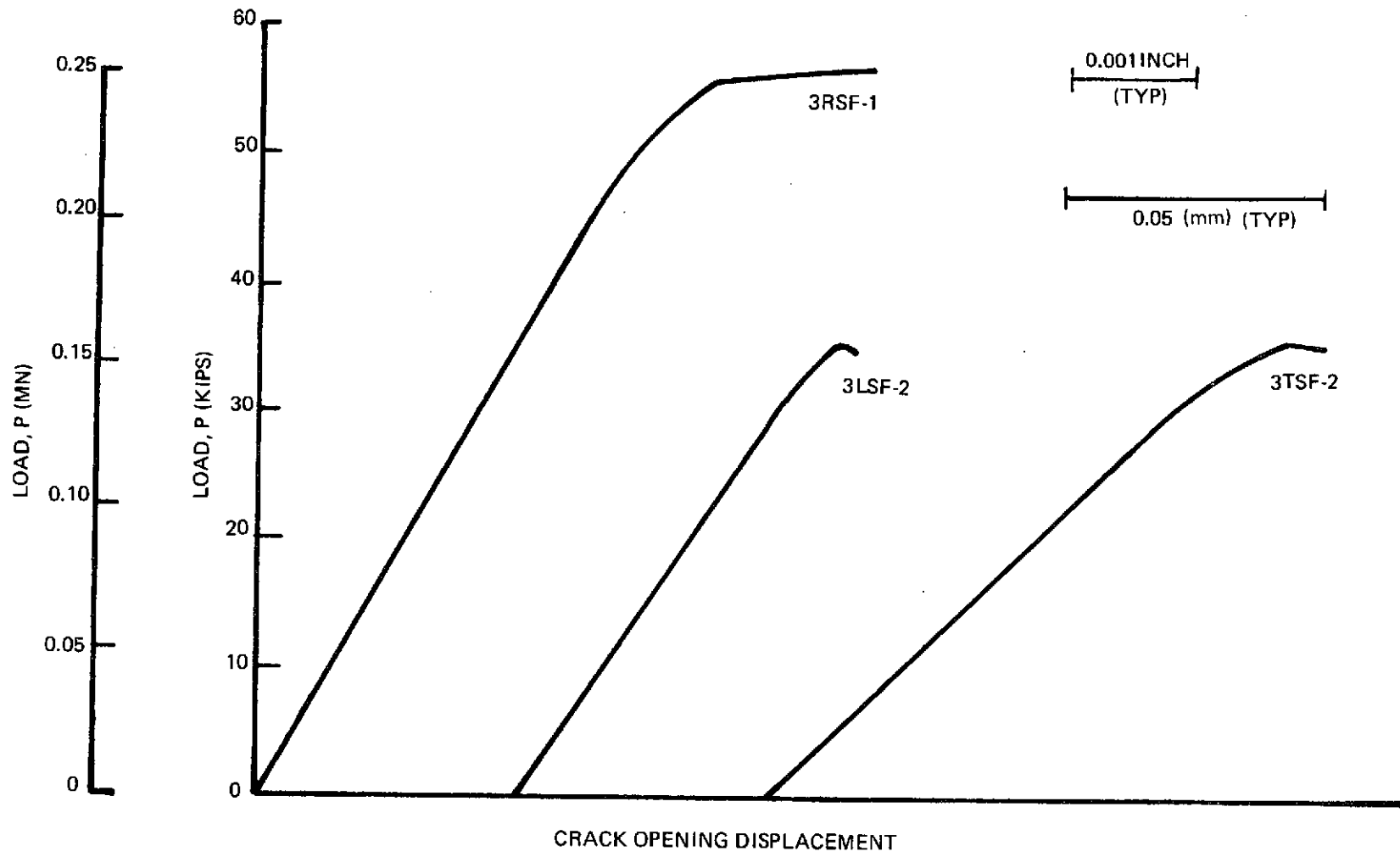


Figure 6-22: Load-Crack Opening Displacement Records for Surface Flawed Specimens Tested at R.T. and -200F (144K)

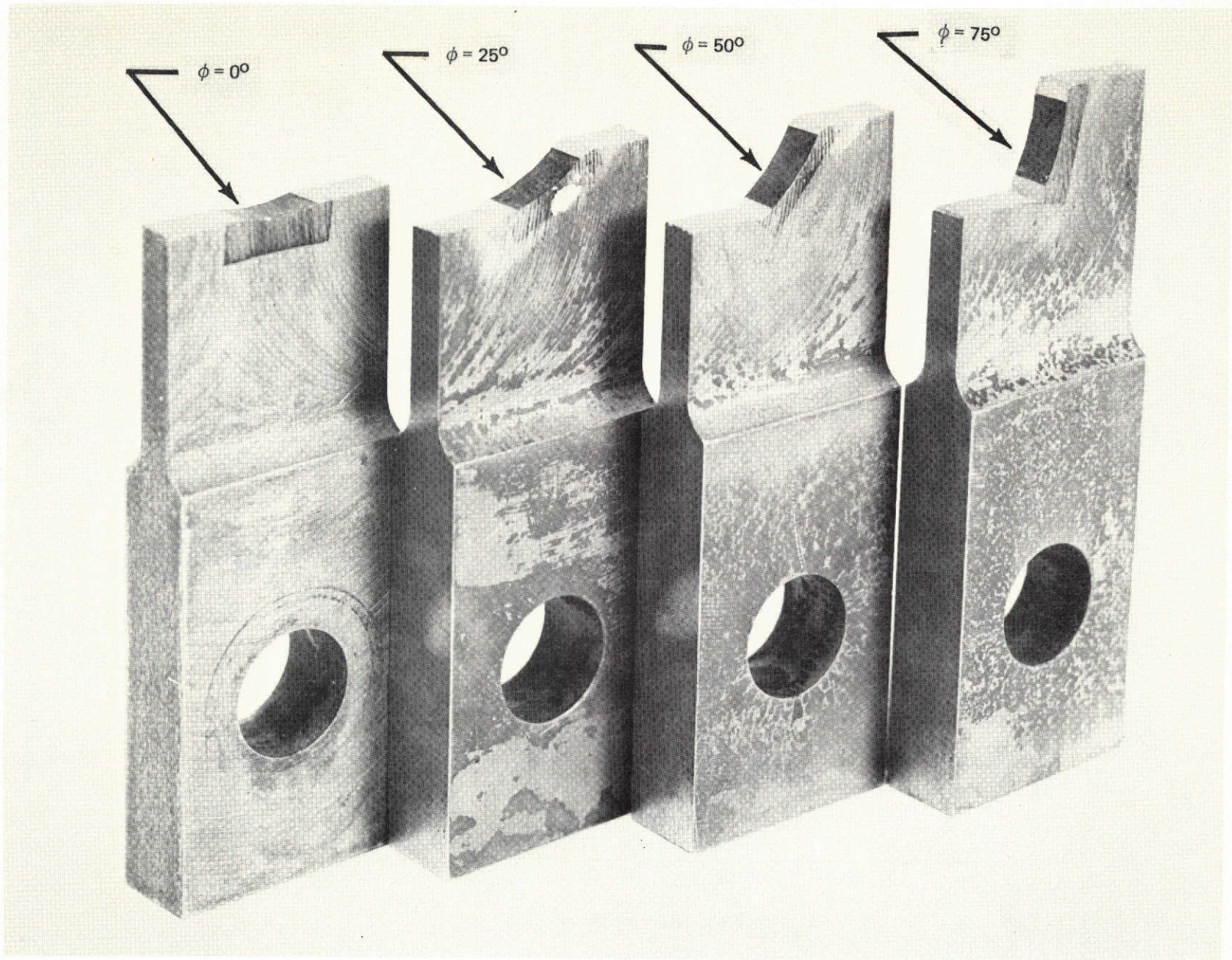


Figure 6-23: Fracture Surfaces of Inclined Center Cracked Specimens of 4340 Steel Subjected to Combined Modes I and II.

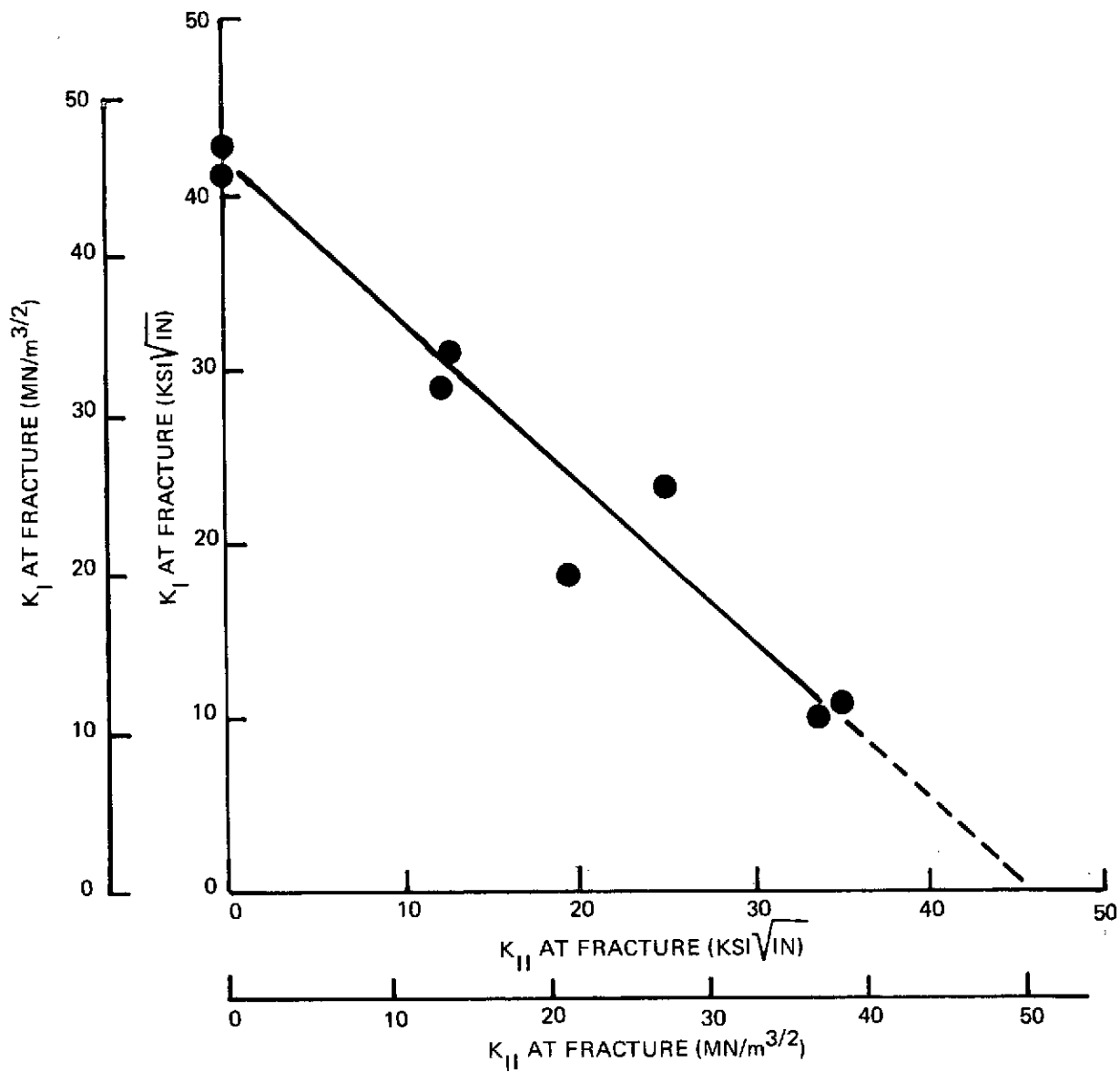


Figure 6-24:  $K_I$  Vs.  $K_{II}$  at Fracture For a 4340 Steel Cracked Plate Under Combined Mode I-II Loading at -200F (144K)

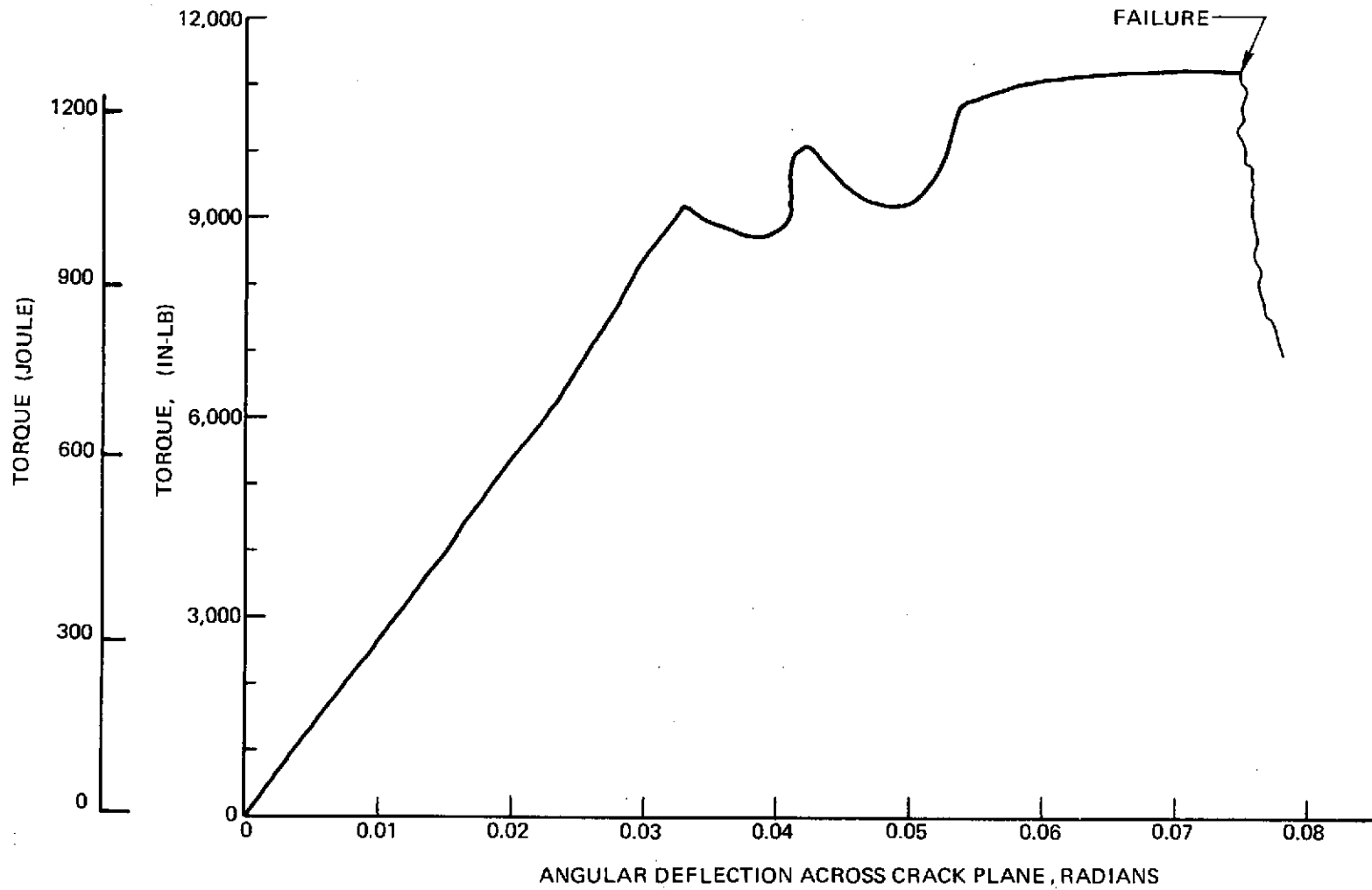
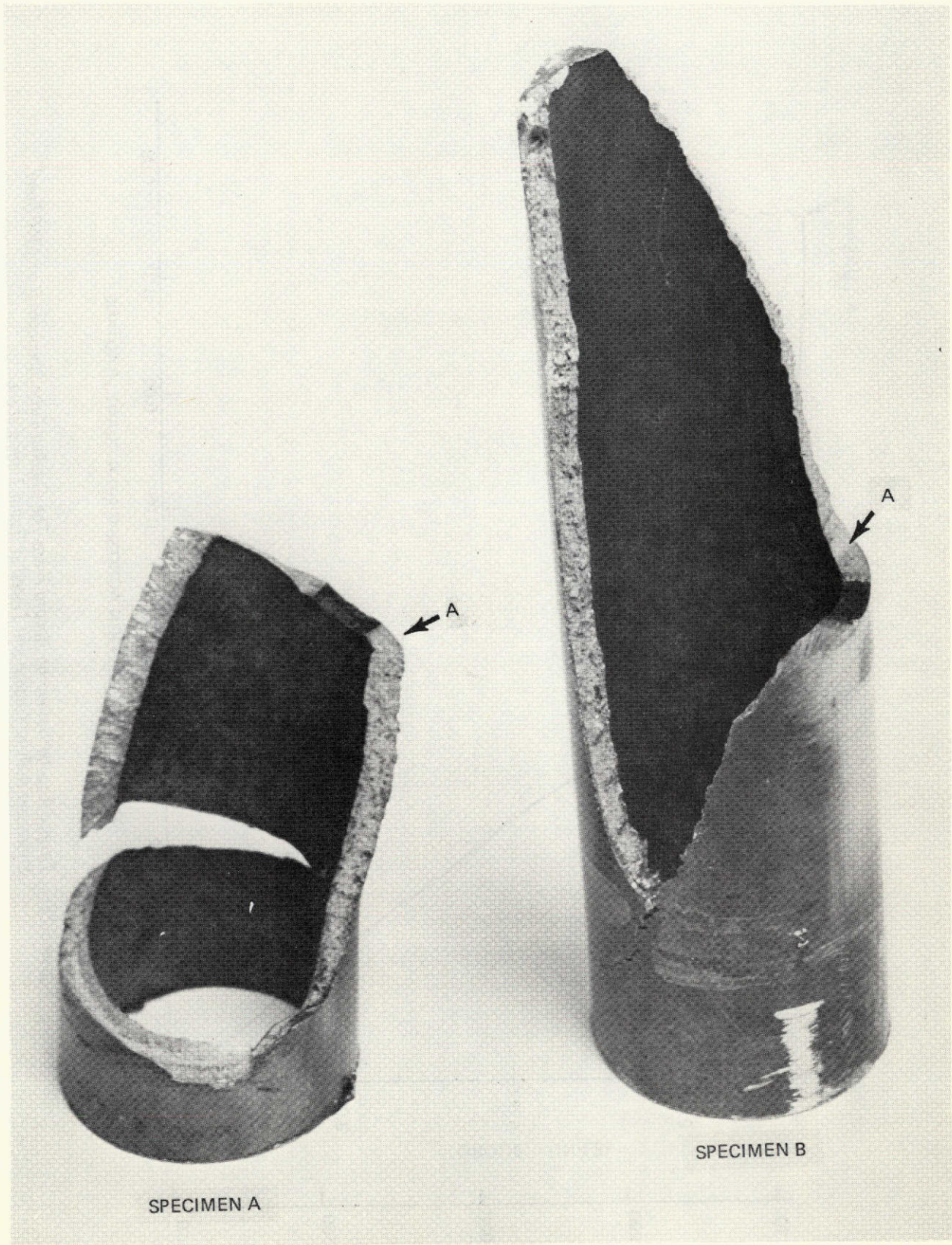


Figure 6-25: Torque-Angular Deflection Record From The Cracked Tube Specimen B of 4340 Steel Subjected to Pure Torsion and Tested at Room Temperature



*Figure 6-26 : Fracture Surfaces of Cracked Tube Specimens Subjected to Pure Torsion*

SYMBOL	SOURCE	MATERIAL	THICKNESS INCH (mm)	$K_{Icr}$ Ksi-In <sup>1/2</sup> (MN/m <sup>3/2</sup> )	$K_{IIcr}$ Ksi-In <sup>1/2</sup> (MN/m <sup>3/2</sup> )
●	PRESENT RESULTS	4340 Steel	0.25 (6.35)	41.6 (45.7)	45.2 (49.7)
◇	LIU (42)	7075-T7651 ALUMINUM	0.3 (7.62)	81.2 (89.2)	81.2 (89.2)
■	BOEING (43)	7075-T651 ALUMINUM	0.3 (7.62)	63.7 (70.0)	63.7 (70.0)
◆	LIU (42)	2024-T3 ALUMINUM	0.312 (7.92)	90.5 (99.5)	67.5 (74.2)

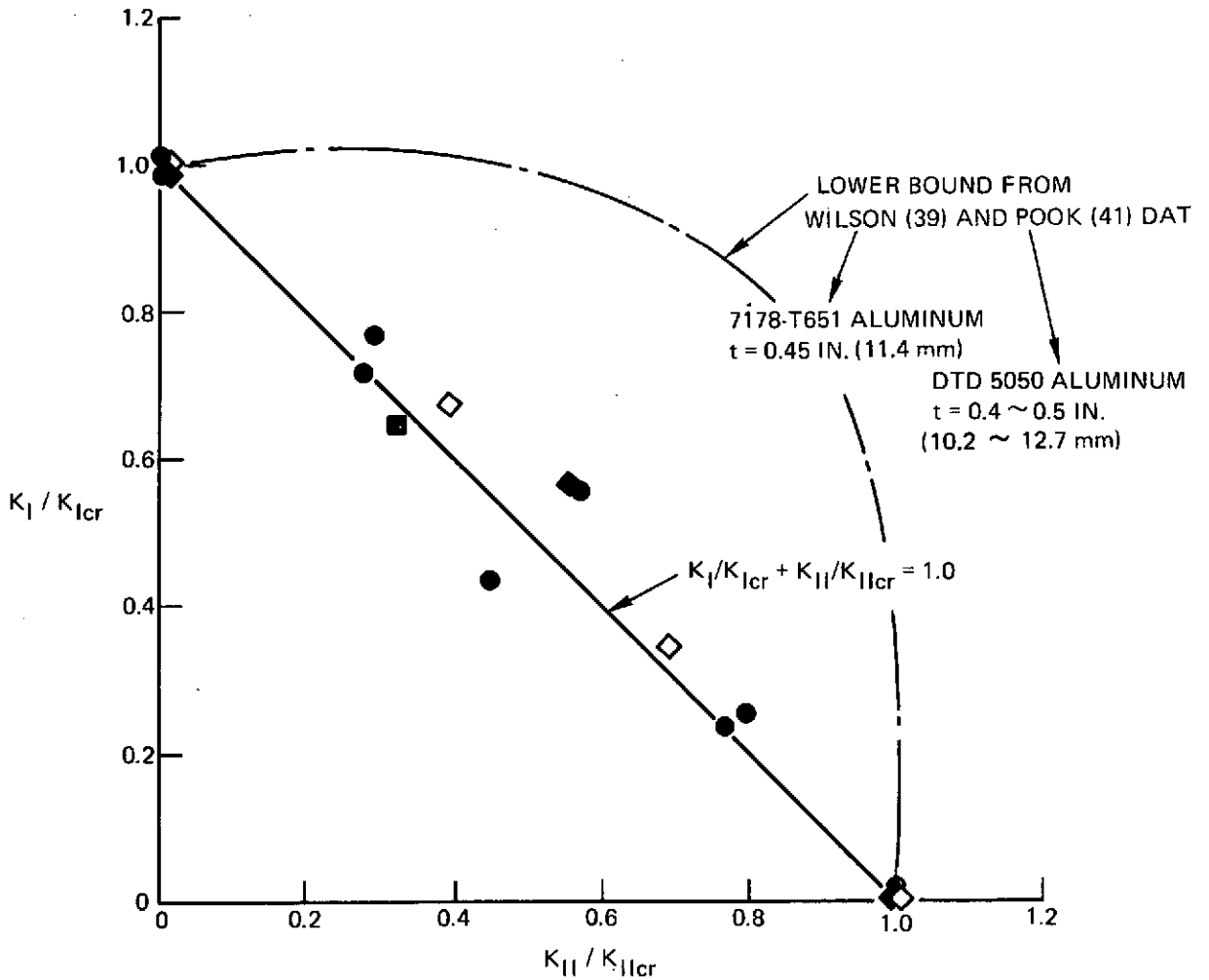


Figure 6-27:  $K_I/K_{Icr}$  Versus  $K_{II}/K_{IIcr}$  For a Cracked Plate Under Combined Mode I-II Loading

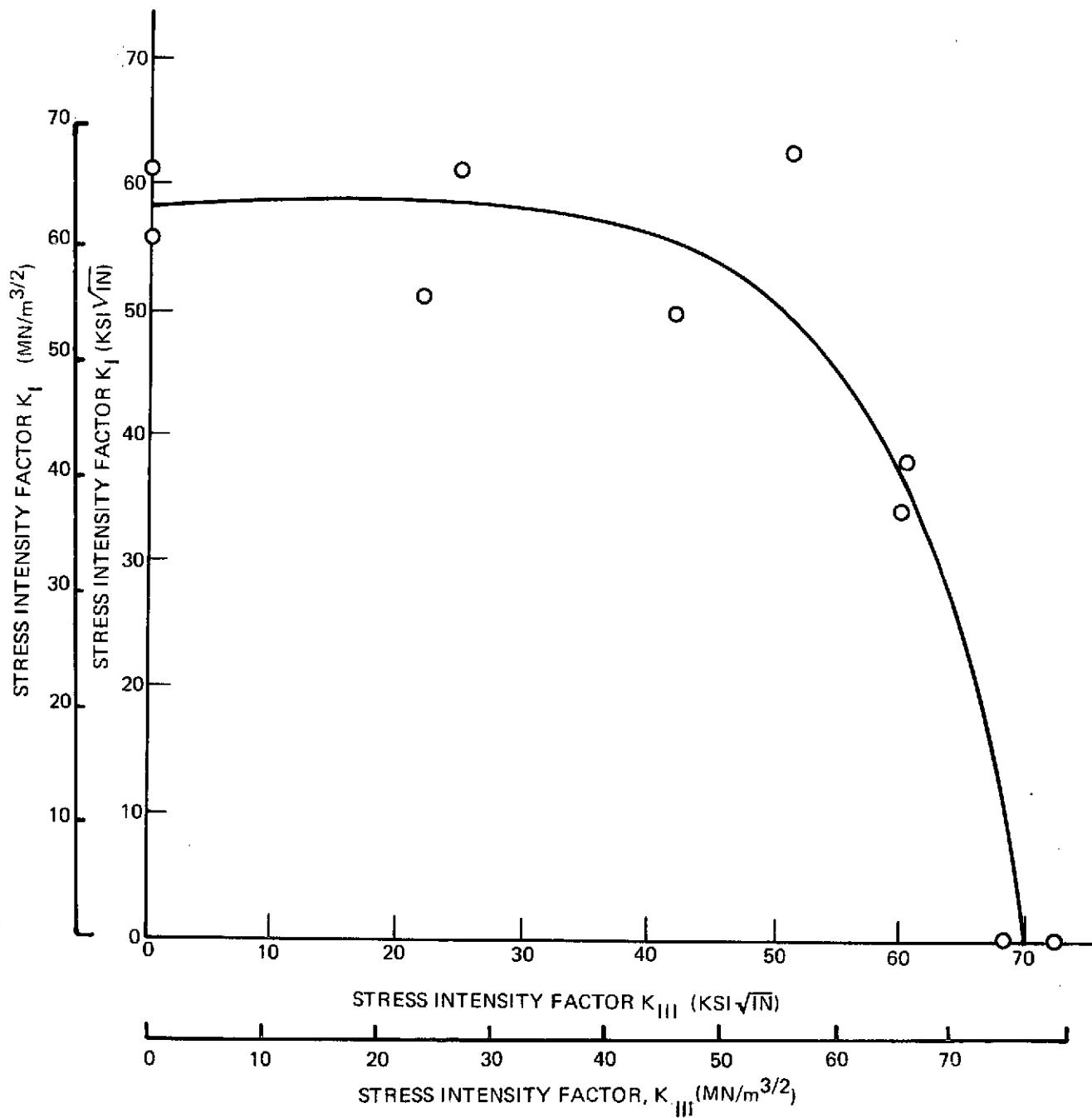


Figure 6-28: Combined Mode I-III Interaction Curve for 4340 Steel at Room Temperature  
Obtained From Round Notched Bar Specimens



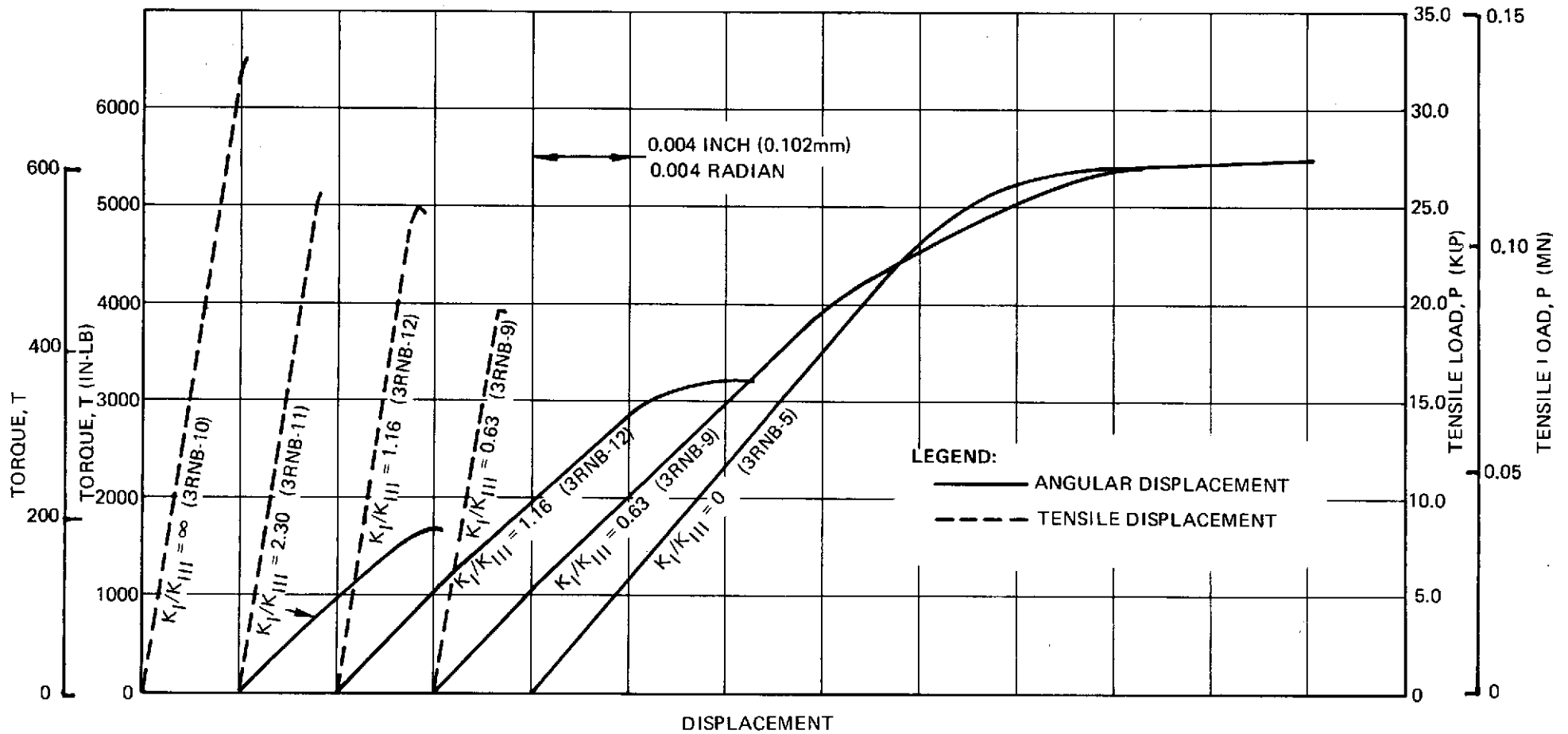
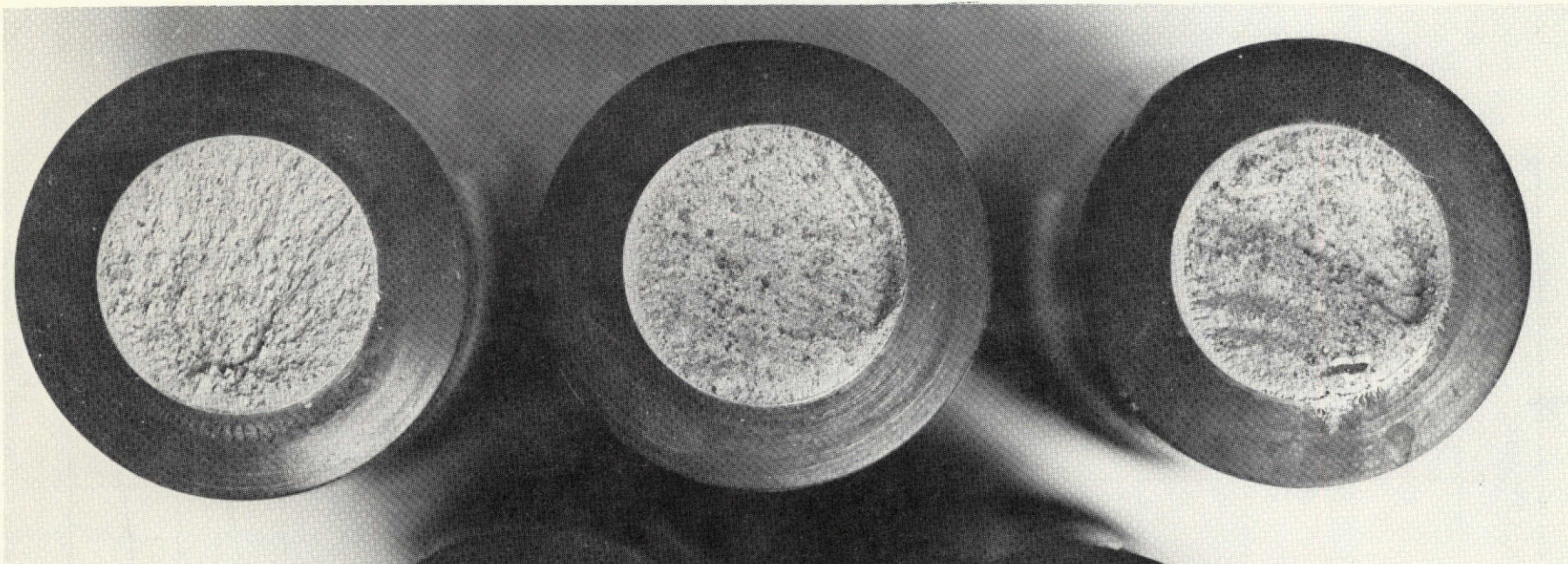


Figure 6-29: Load-Displacement Records for Round Notched Bar-Specimens Subjected to Tension and Torsion

$K_I/K_{III} = \infty$  (3RNB-10)

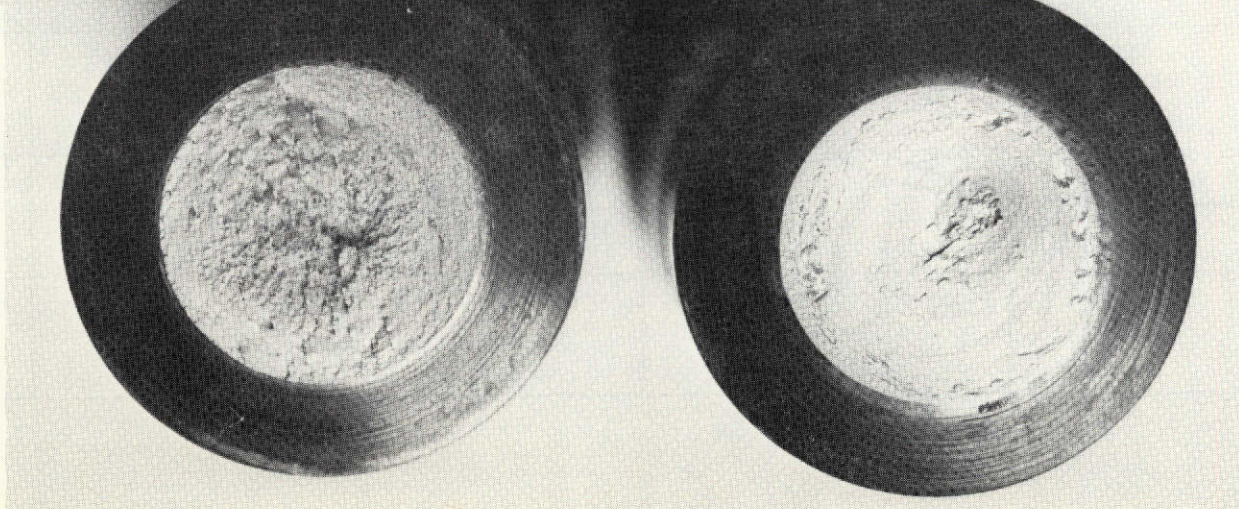
$K_I/K_{III} = 2.30$  (3RNB-11)

$K_I/K_{III} = 1.16$  (3RNB-12)



158

$K_I/K_{III} = 0.63$  (3RNB-9)



$K_I/K_{III} = 0$  (3RNB-5)

Figure 6-30: Fracture Surfaces of Round Notched Bars of 4340 Steel Subjected to Combined Modes I and III

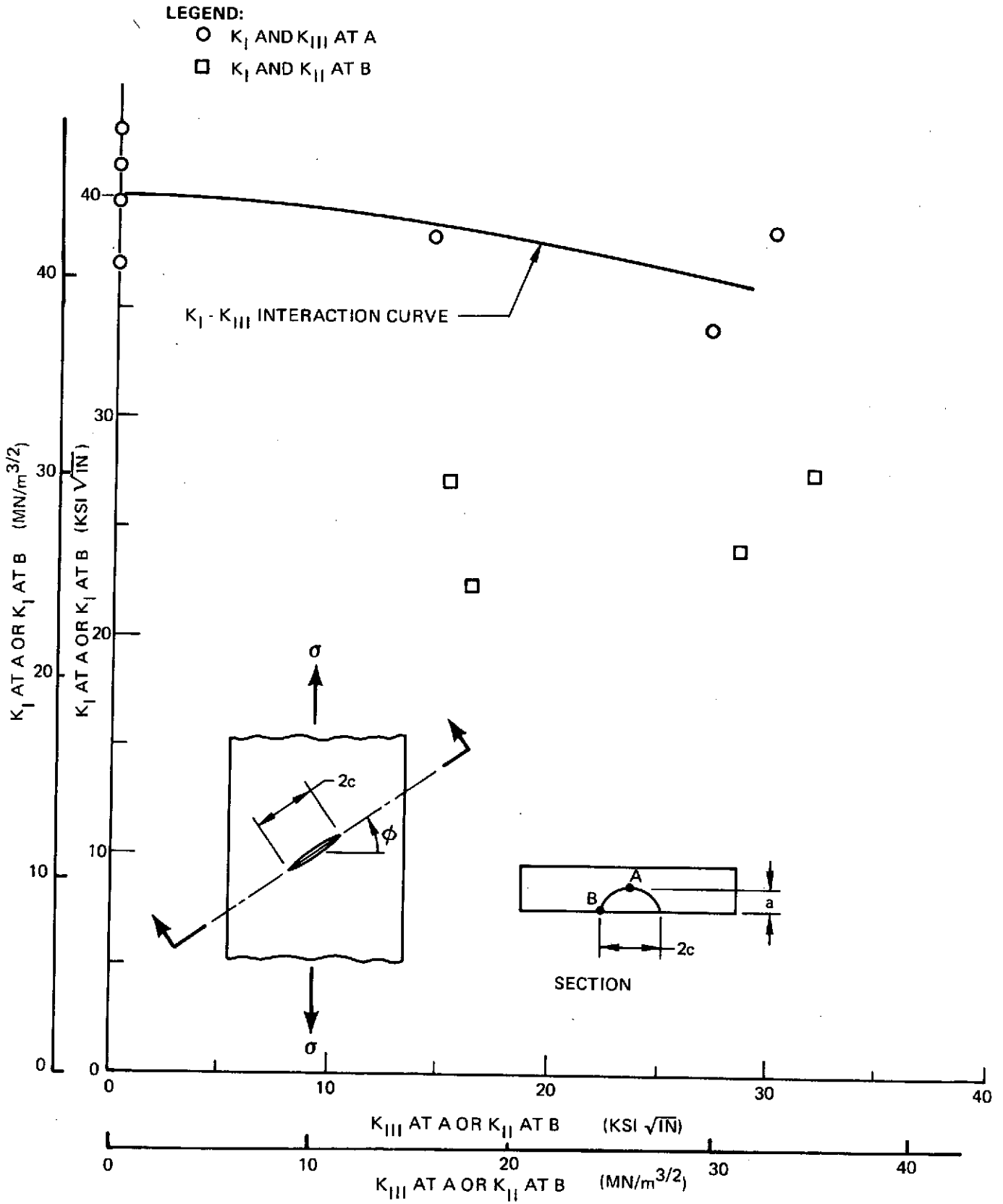


Figure 6-31: Combined Mode I-III or I-II Interaction for 4340 Steel Specimens Containing Slanted Surface Flaws and Tested at -200F (144K)

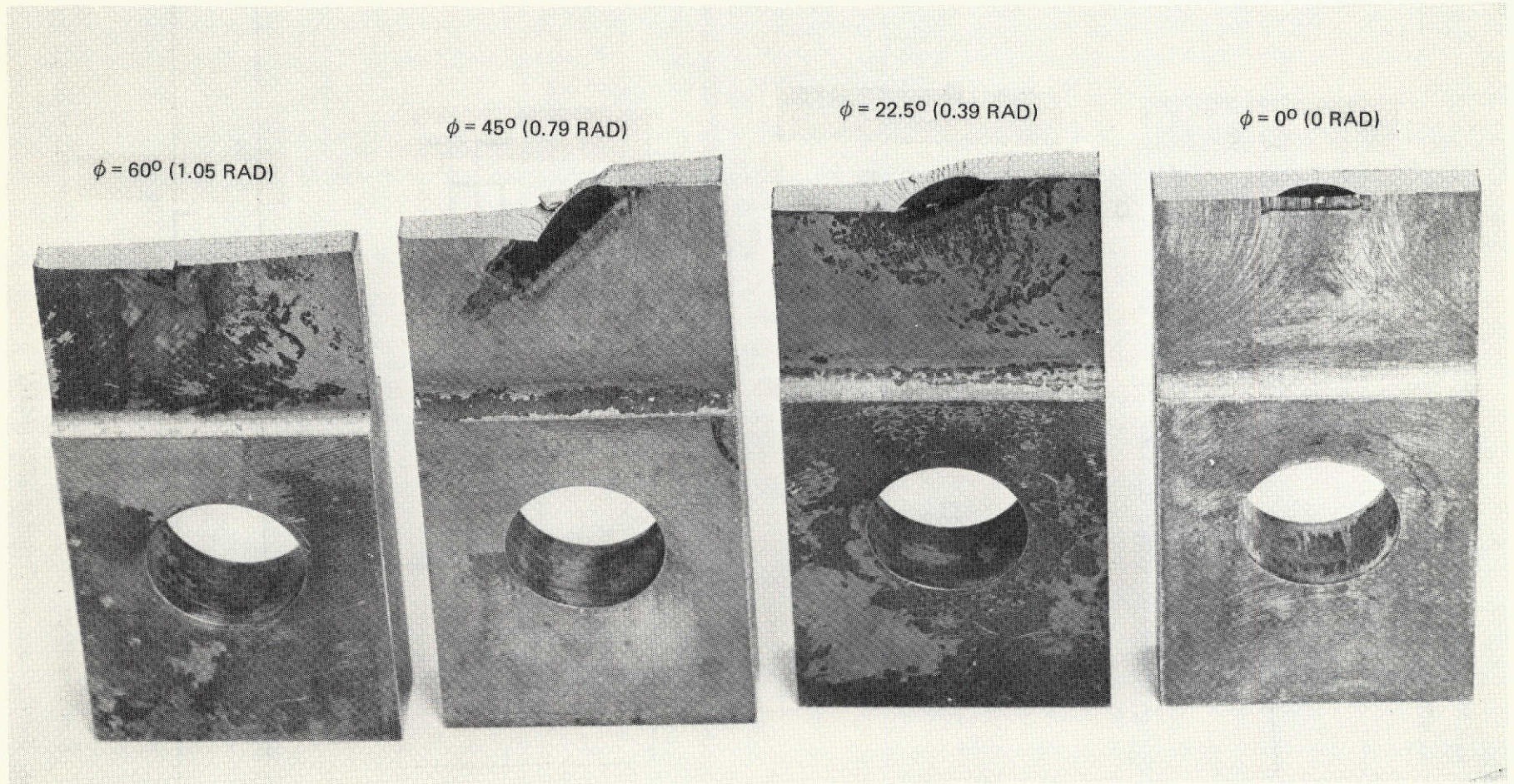


Figure 6-32: Fracture Surfaces of Inclined Surface Flawed Specimens Subjected to Combined Modes I, II and III

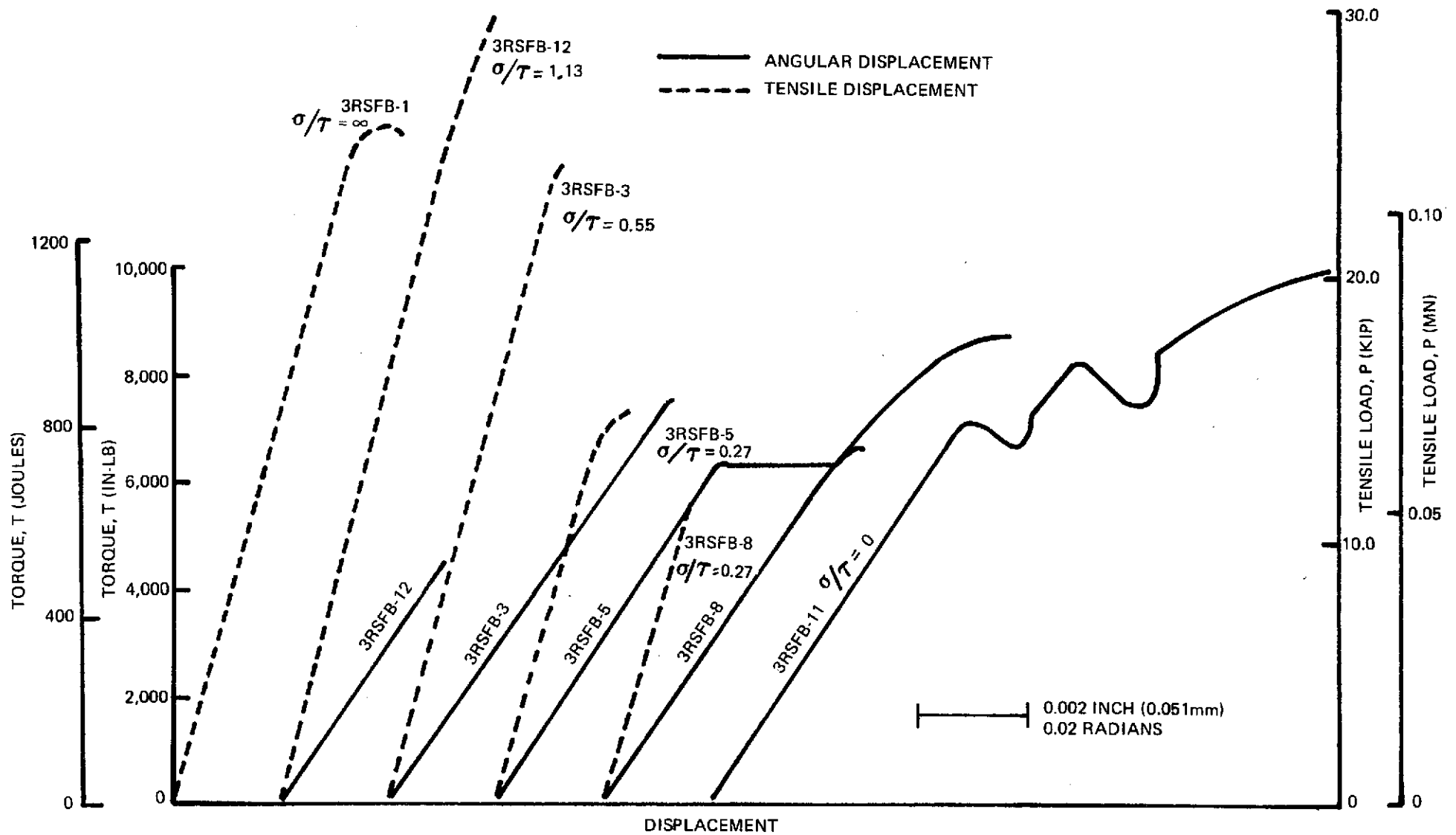


Figure 6-33: Load-Displacement Records for 4340 Steel Cylindrical Specimens Containing Surface Flaws

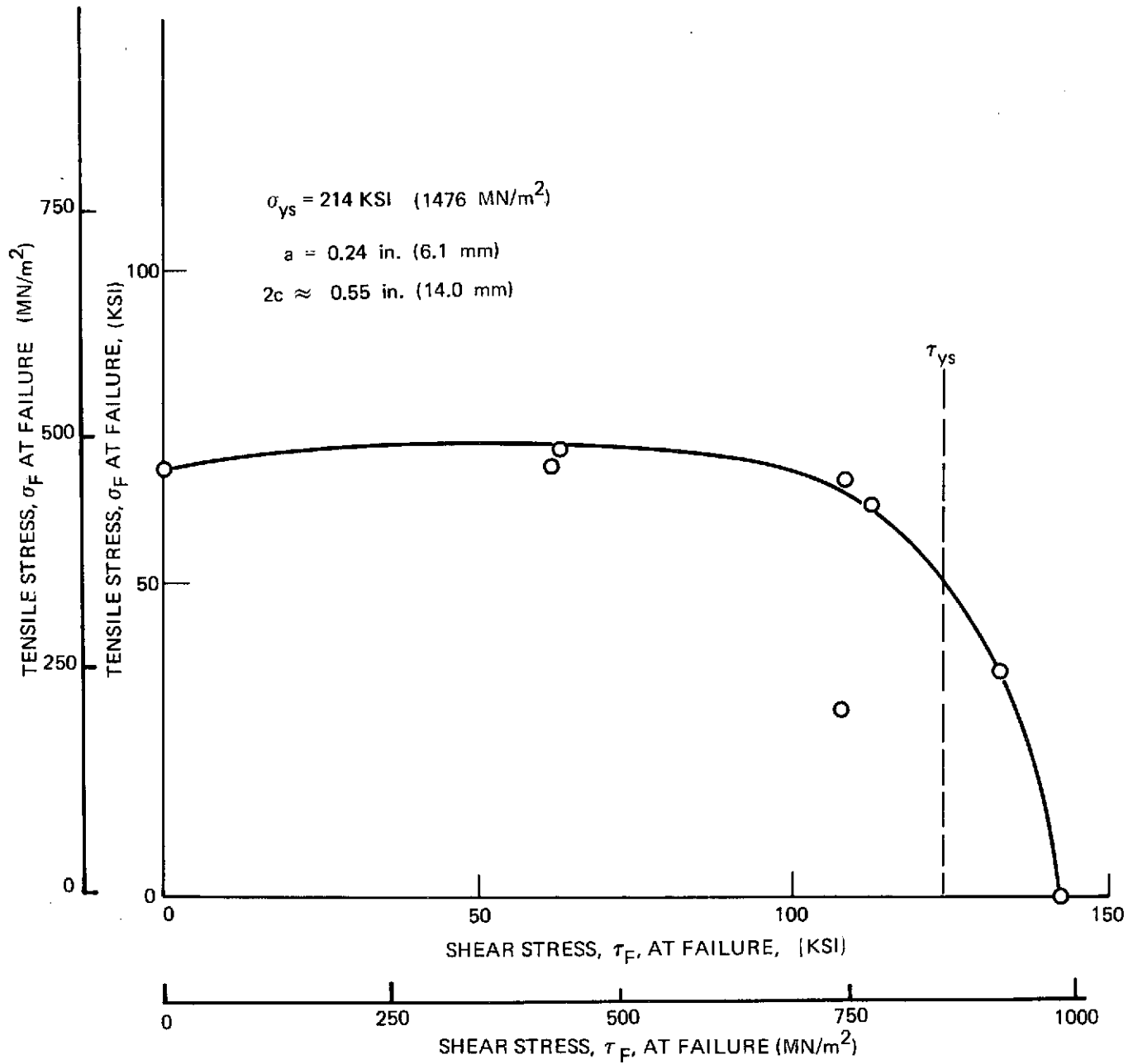


Figure 6-34: Fracture Tests of 4340 Steel Cylindrical Specimens Containing Surface Flaws  
 Subjected to Simultaneous Tension and Torsion

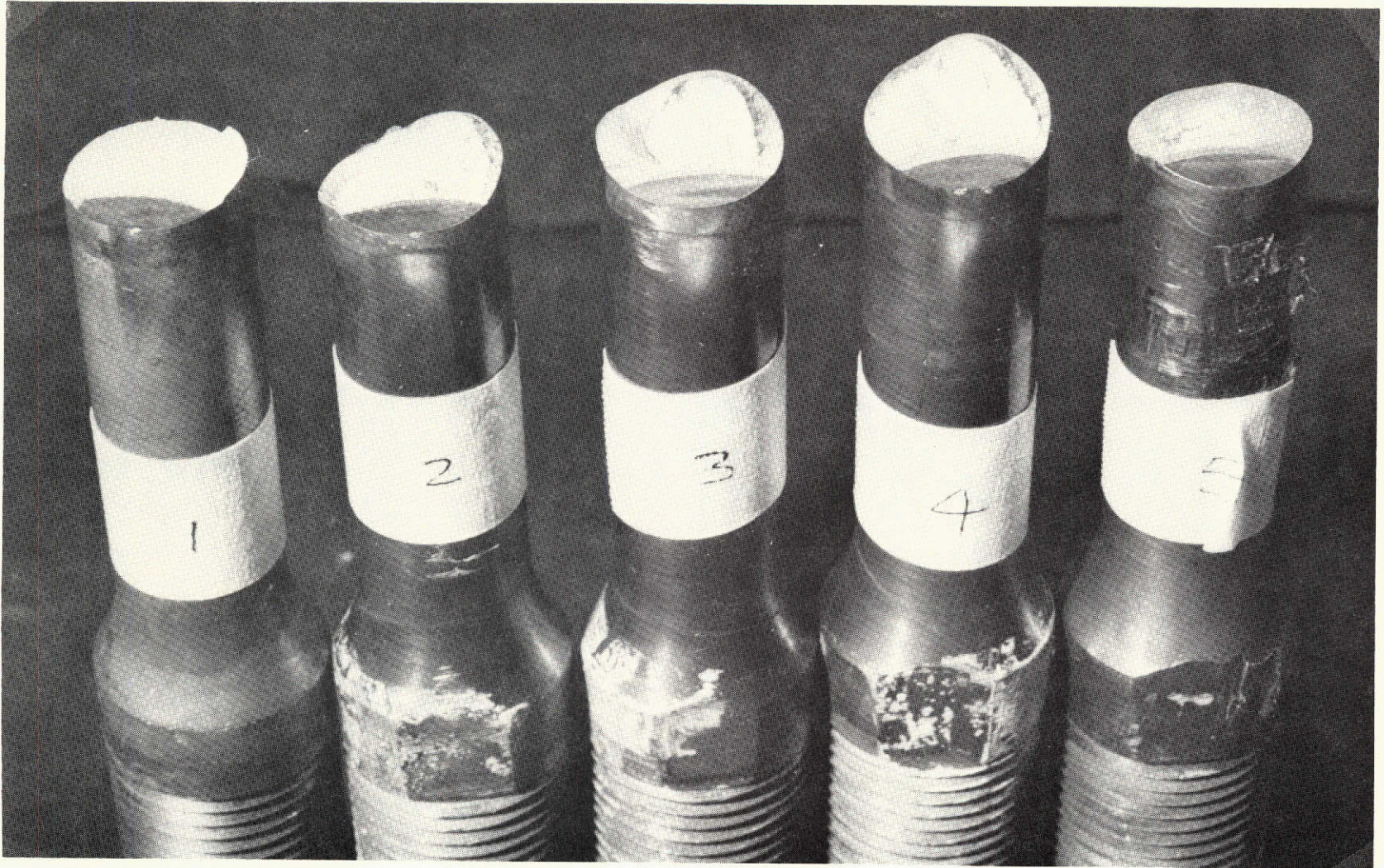


Figure 6-35: Fracture Surfaces of Surface Flawed Round Specimens of 4340 Steel  
(Left to Right  $\sigma_F/\tau_F$  Are  $\infty$ , 1.12, 0.61, 0.27, 0.0)

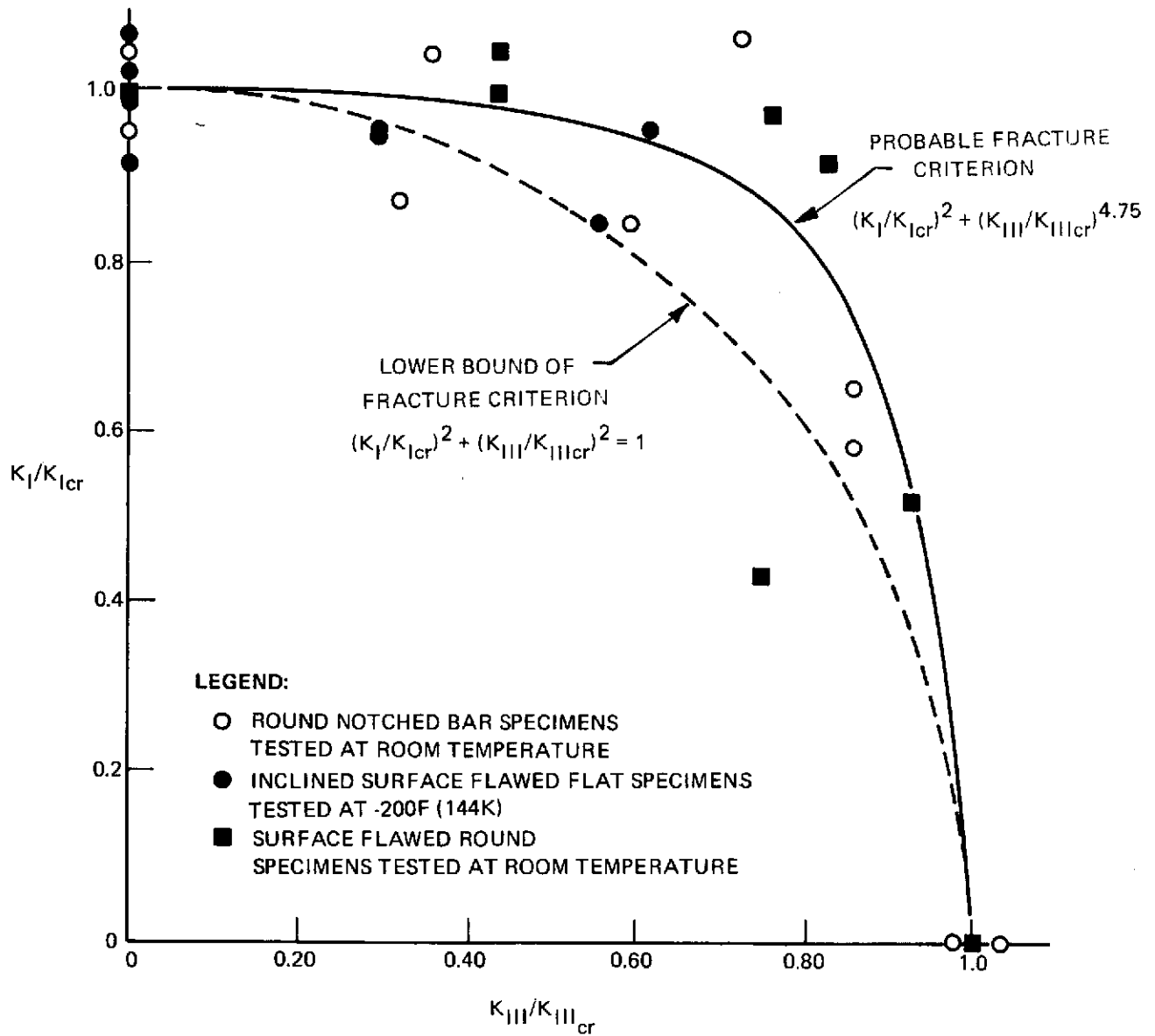


Figure 6-36:  $K_I/K_{Icr}$  Vs.  $K_{III}/K_{IIIcr}$  For Round Notched Bar Specimens, Inclined Surface Flawed Flat Specimens, And Surface Flawed Round Specimens of 4340 Steel



165

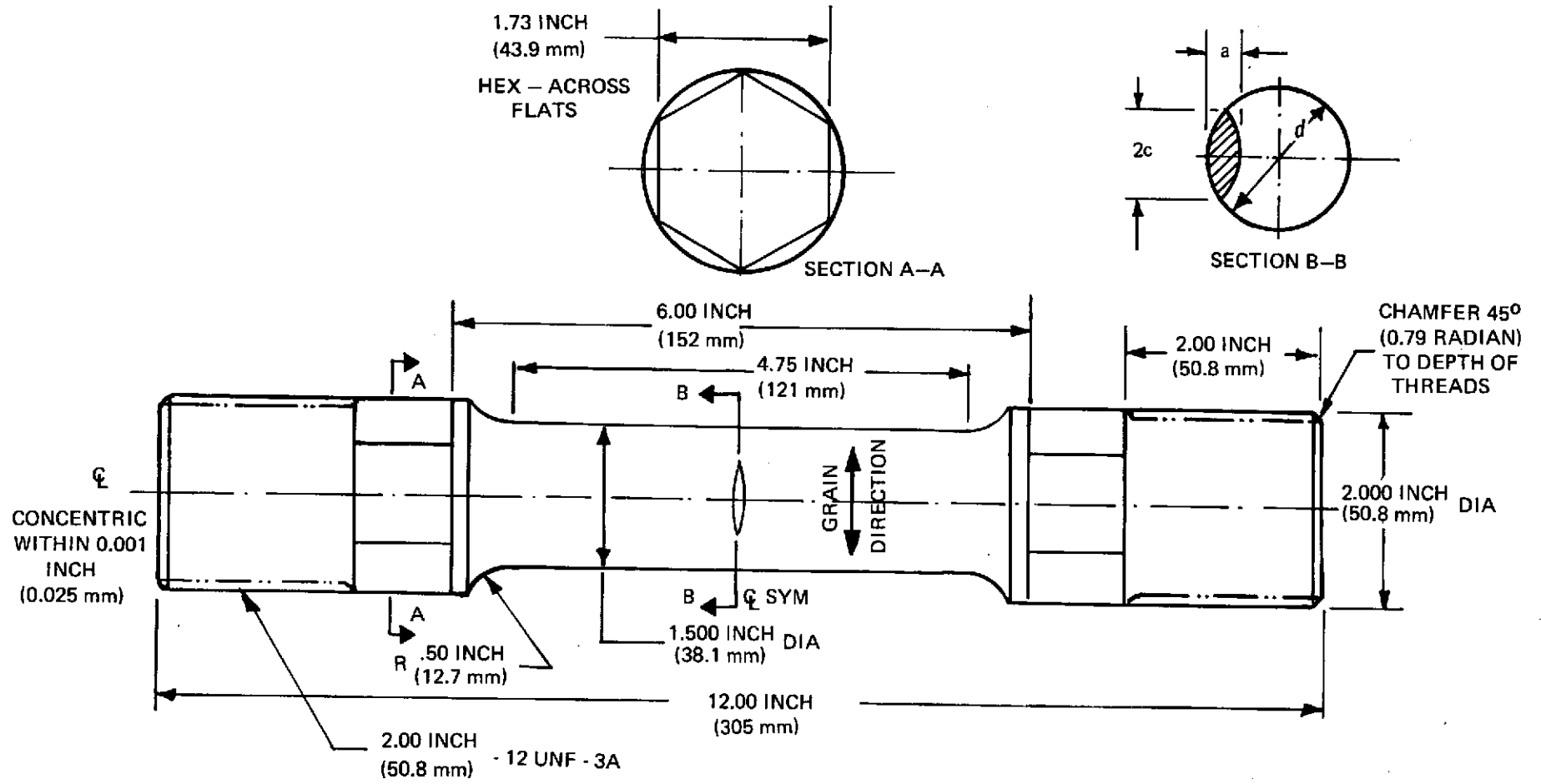
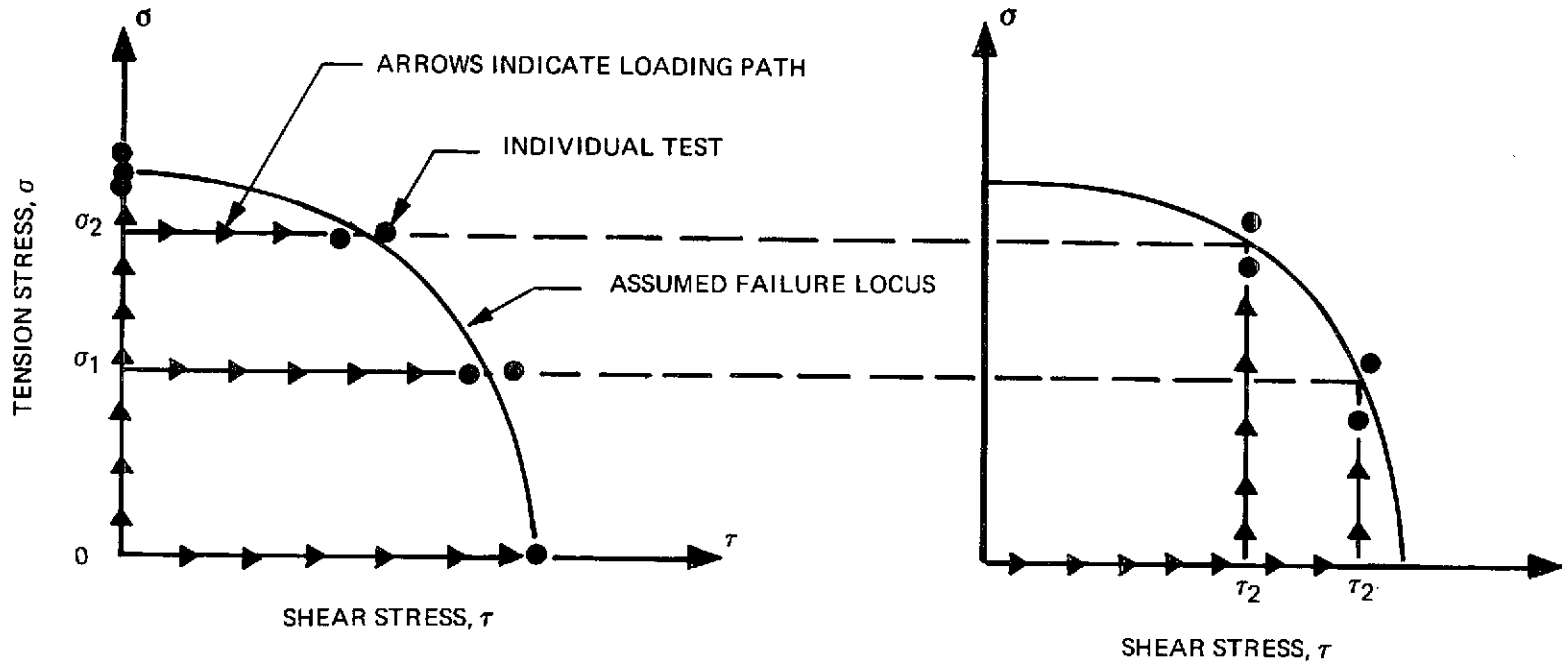


Figure 7-1: Surface Flawed Cylindrical Specimen for 2219-T87 Aluminum for Combined Tension and Torsion Tests



(a) TENSION & TORQUE-TO-FAILURE TESTS

(b) TORQUE & TENSION-TO-FAILURE TESTS

Figure 7-2: Test Program for 2219-T87 Aluminum and 6Al-4V  $\beta$  STA Titanium Static Fracture Tests Under Combined Tension and Shear Stresses

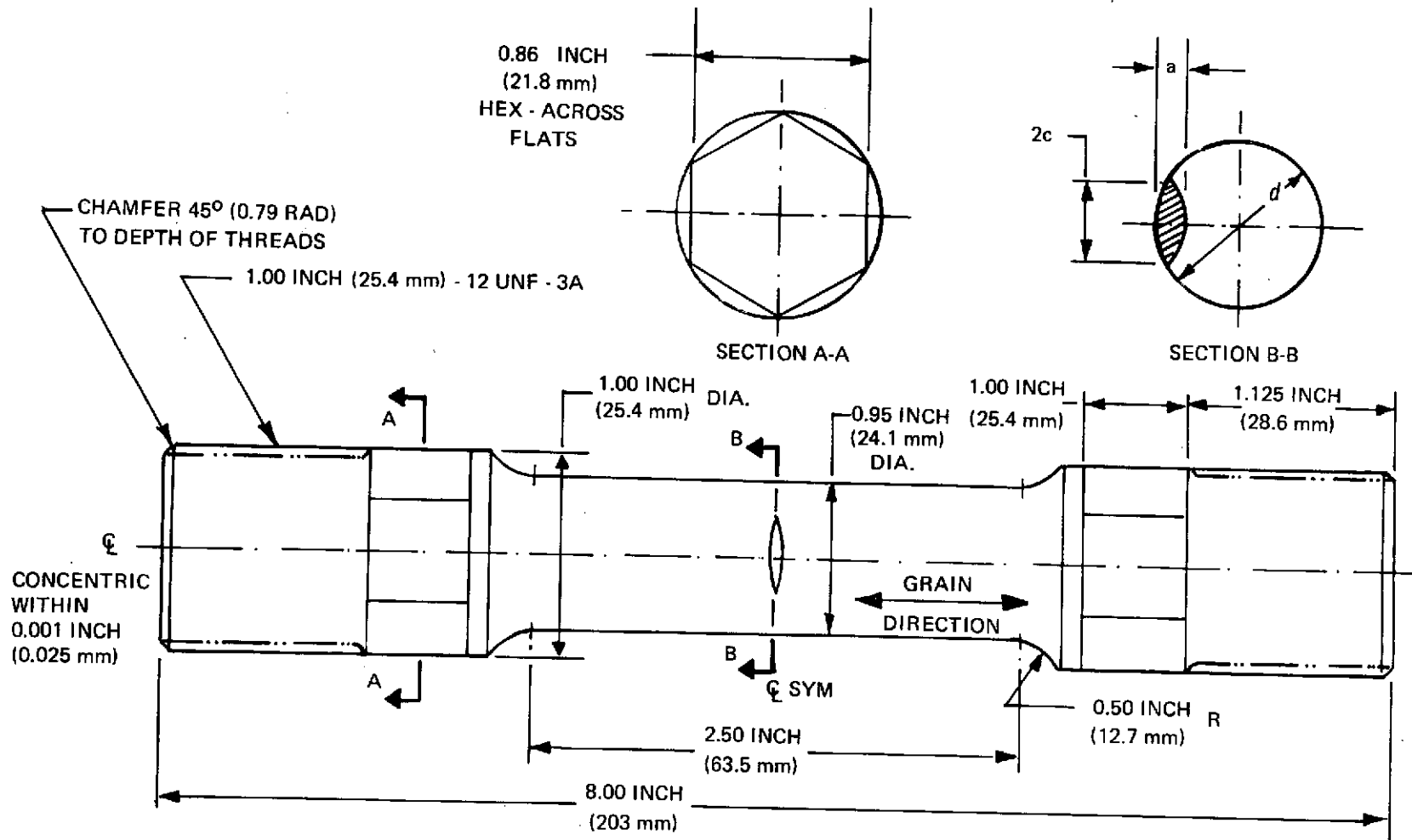
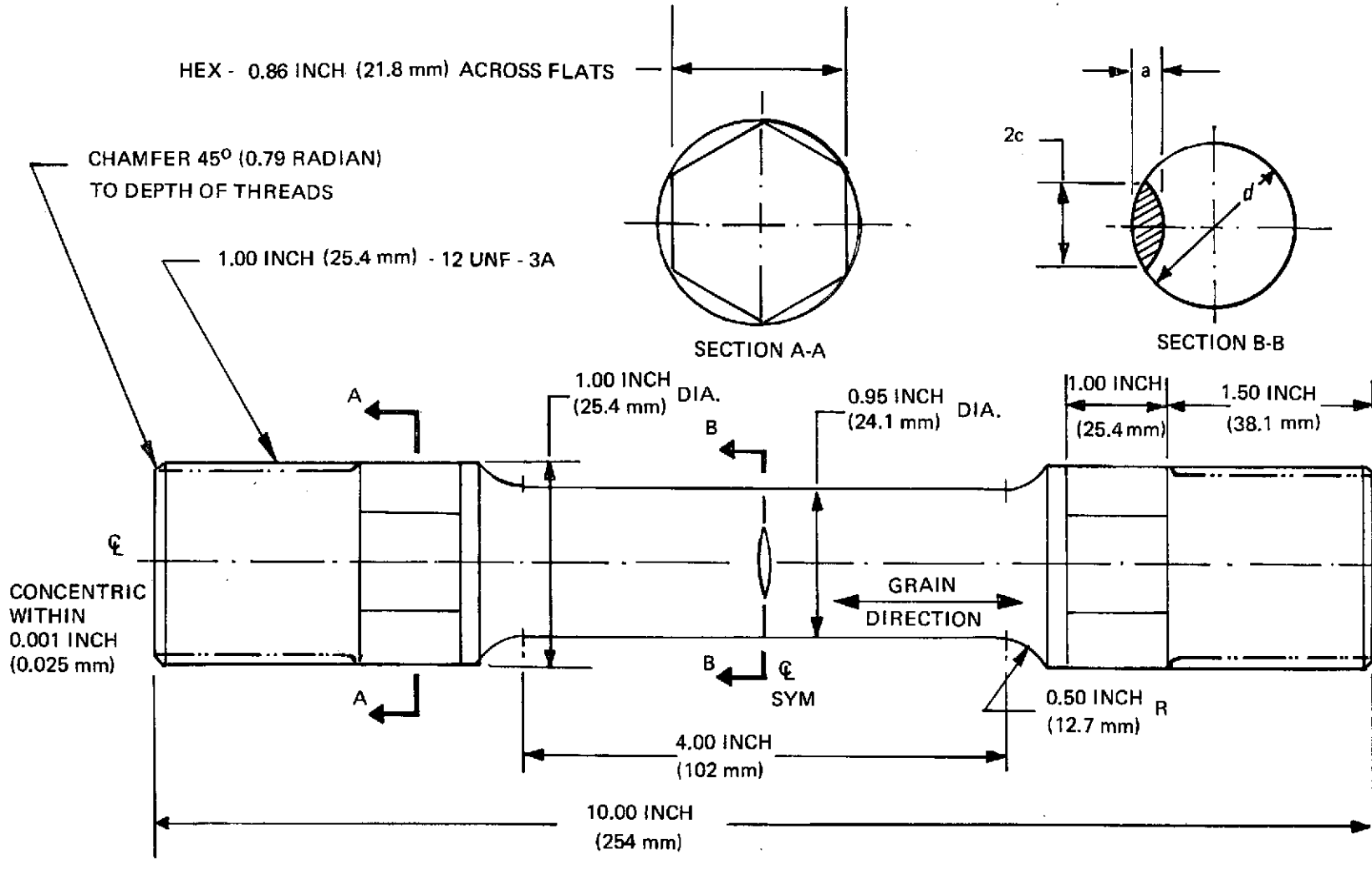


Figure 7-3: Surface Flawed Cylindrical Specimen for 6Al-4V  $\beta$  STA Titanium for Combined Tension and Torsion Static Tests



168

Figure 7-4: Surface Flawed Cylindrical Specimen for 6Al-4V  $\beta$  STA Titanium for Combined Tension and Torsion Cyclic Tests

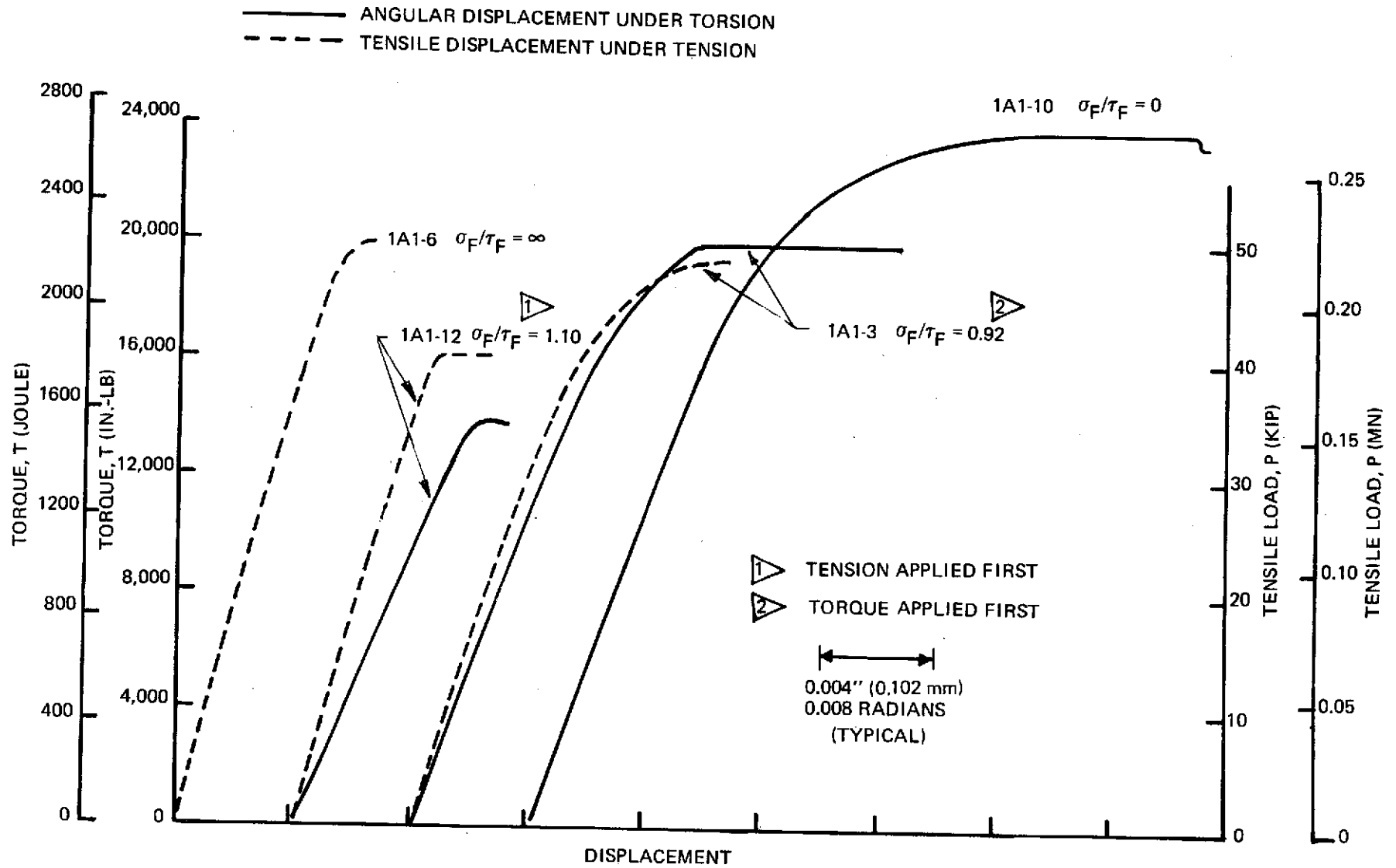


Figure 7-5: Load-Displacement Records for 2219-T87 Aluminum Surface Flawed Cylindrical Specimens

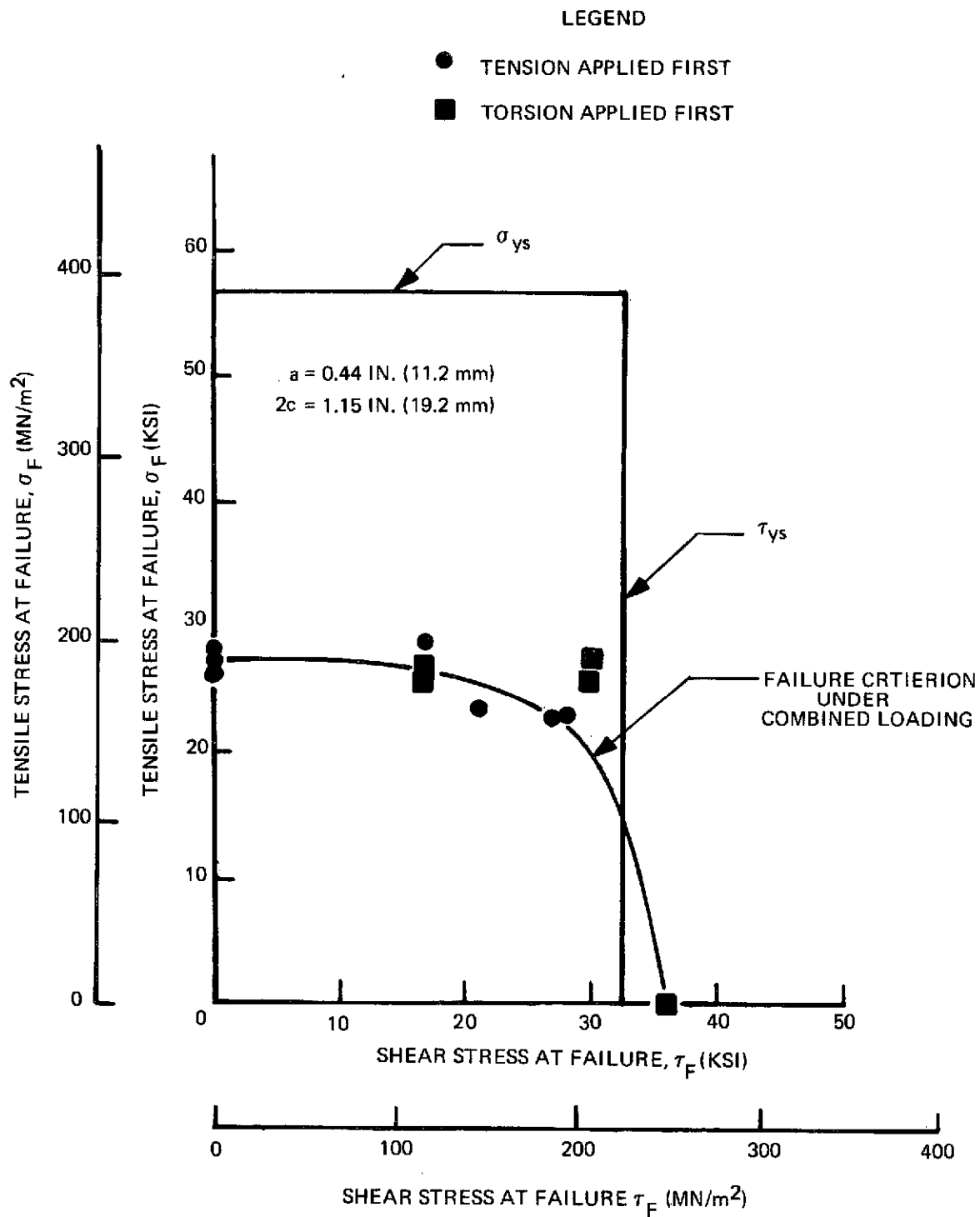


Figure 7-6: Fracture Tests of 2219-T87 Aluminum Cylindrical Specimens Containing Surface Flaws Subjected to Combined Tension and Torsion

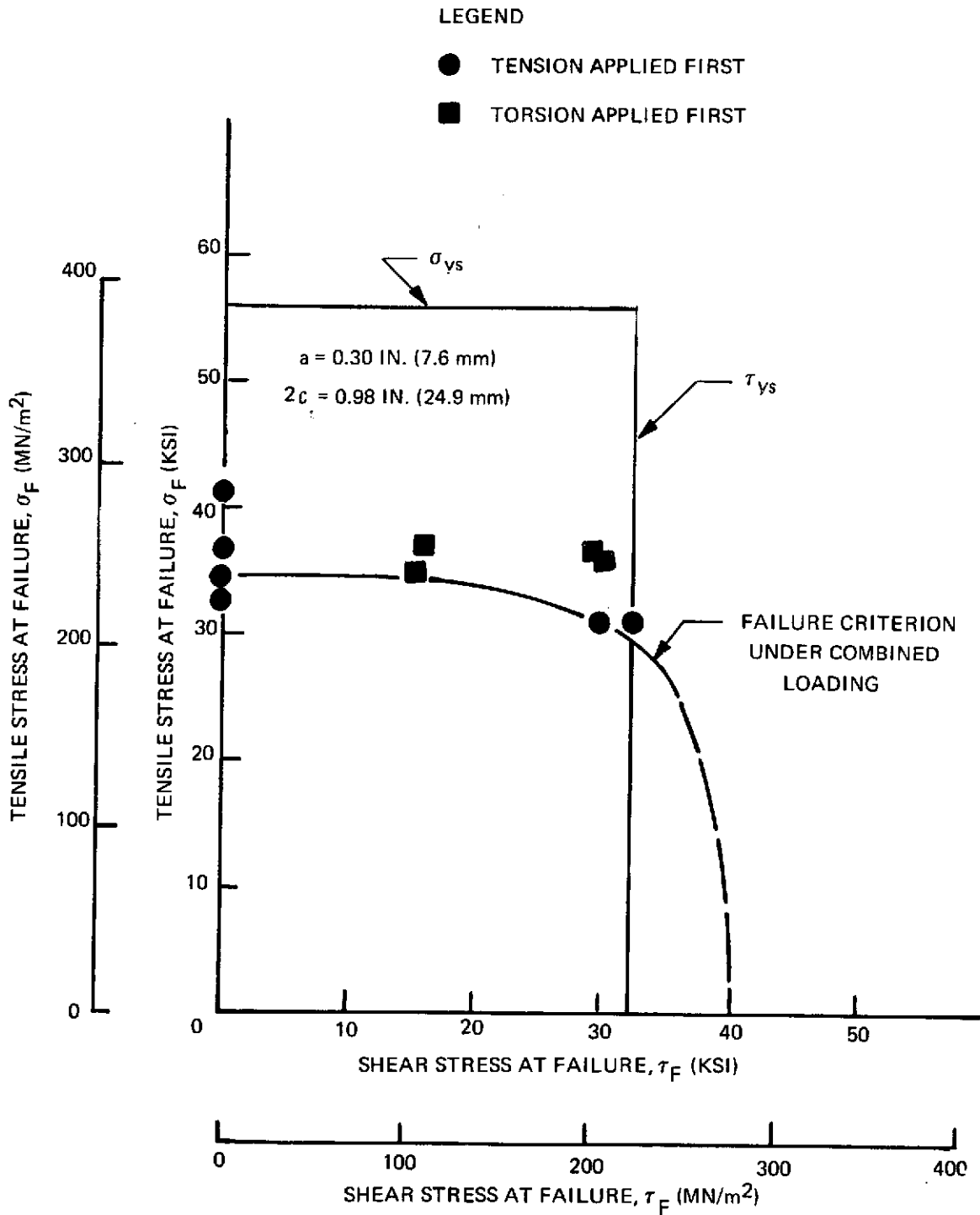


Figure 7-7: Fracture Tests of 2219-T87 Aluminum Cylindrical Specimens Containing Surface Flaws Subjected to Combined Tension and Torsion

LEGEND

- TENSION APPLIED FIRST
- TORSION APPLIED FIRST
- ▲ TENSION AND TORQUE APPLIED SIMULTANEOUSLY

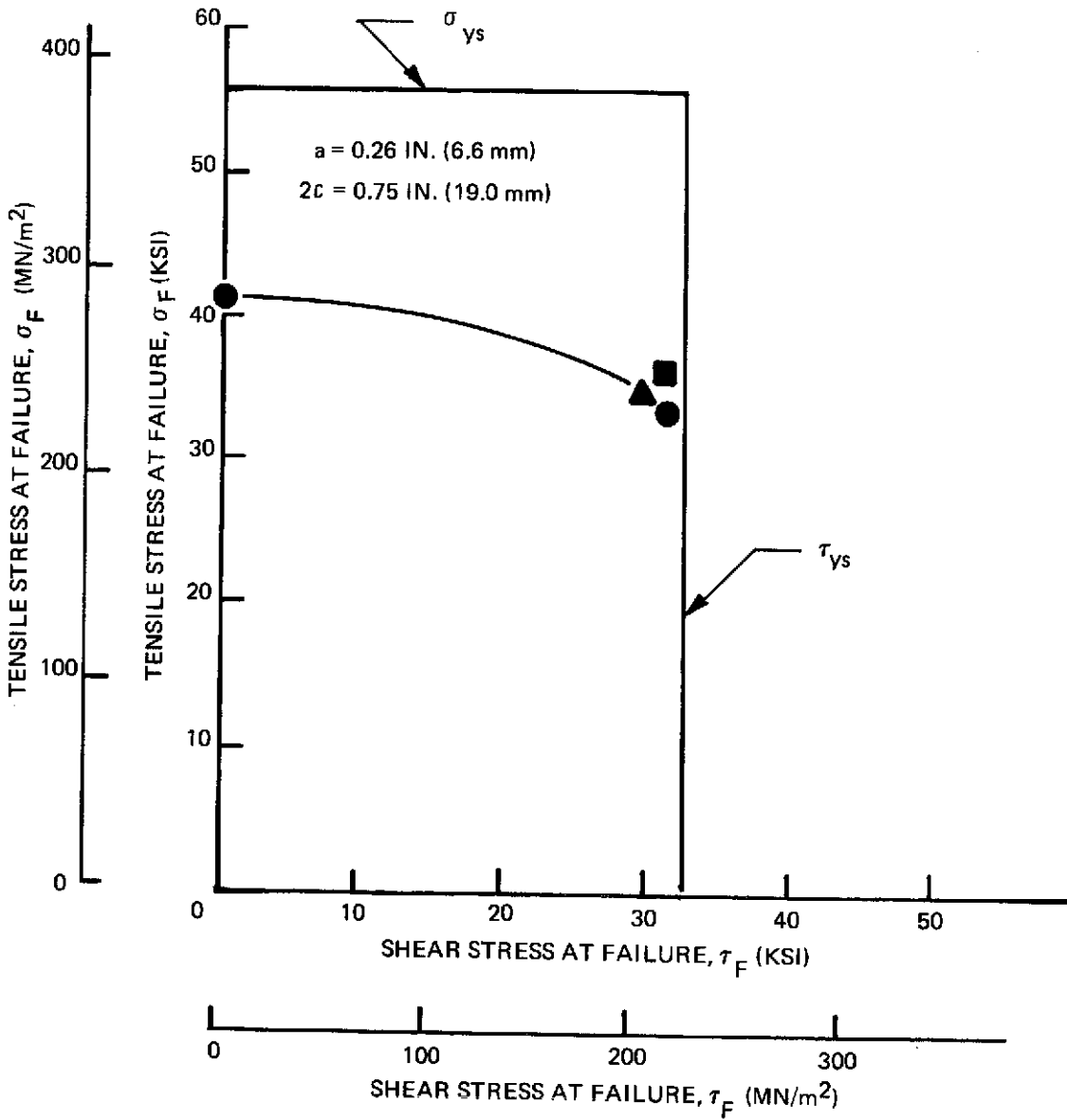


Figure 7-8: Fracture Tests of 2219-T87 Aluminum Cylindrical Specimens Containing Surface Flaws Subjected to Combined Tension and Torsion





$$\sigma_F / \tau_F = \infty$$

(1A1-6)

$$\sigma_F / \tau_F = 1.60$$

(1A1-8)

$$\sigma_F / \tau_F = 0.82$$

(1A1-7)

Figure 7-9: Fracture Surfaces of Surface Flawed Cylindrical Specimens of 2219-T87 Aluminum Subjected to Combined Tension and Torsion (Static Fracture)

LEGEND

FLAW SIZE  $a = 0.44$  IN. (11.2 mm),  $2c = 1.15$  IN (29.2 mm)

- TENSION APPLIED FIRST
- TORSION APPLIED FIRST

FLAW SIZE  $a = 0.30$  IN. (7.6 mm),  $2c = 0.98$  IN. (24.9 mm)

- △ TENSION APPLIED FIRST
- ▲ TORSION APPLIED FIRST

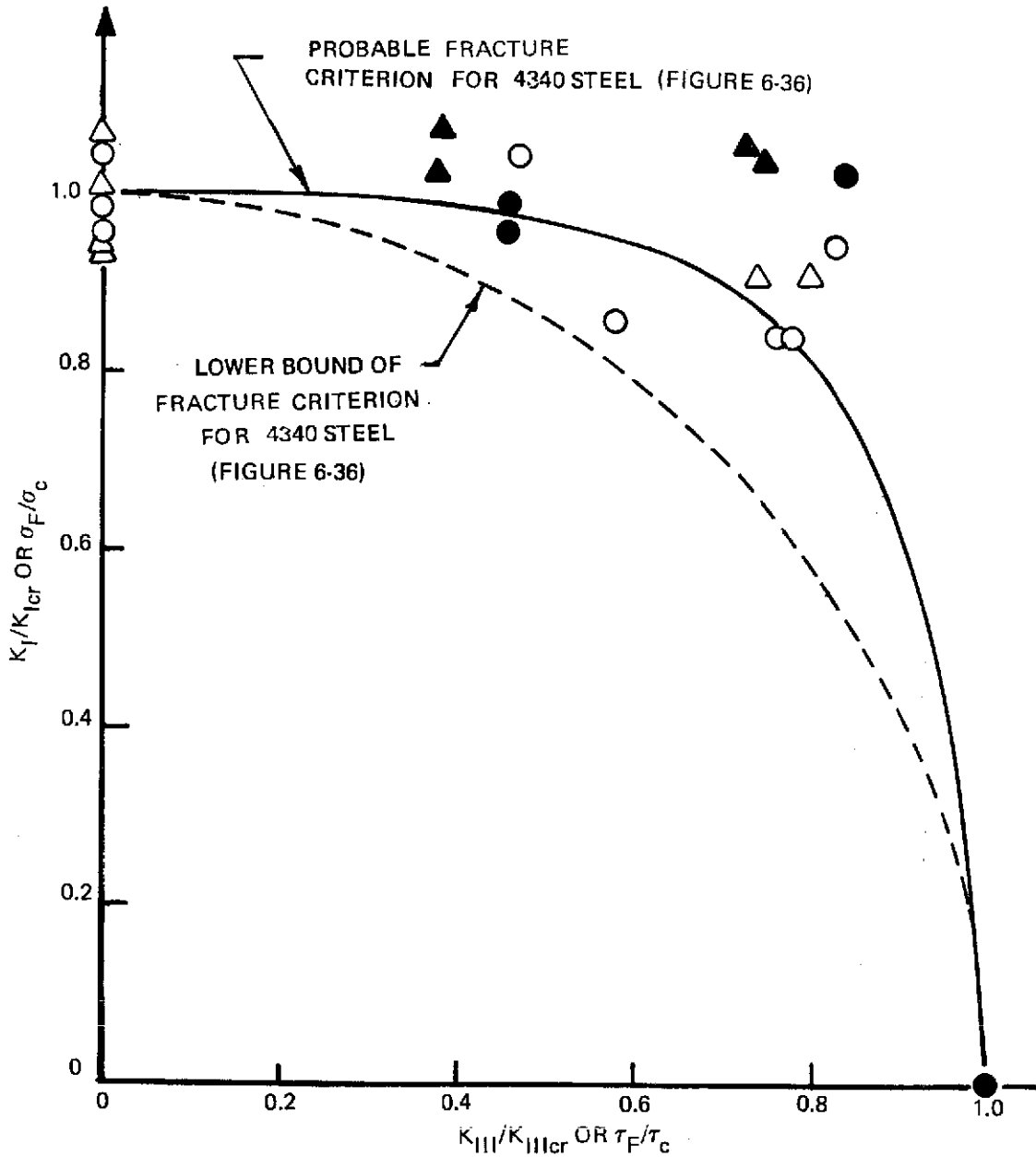


Figure 7-10:  $K_I/K_{Icr}$  vs.  $K_{III}/K_{IIIcr}$  For 2219-T87 Aluminum Cylindrical Specimens Containing Surface Flaws Subjected to Combined Tension and Torsion

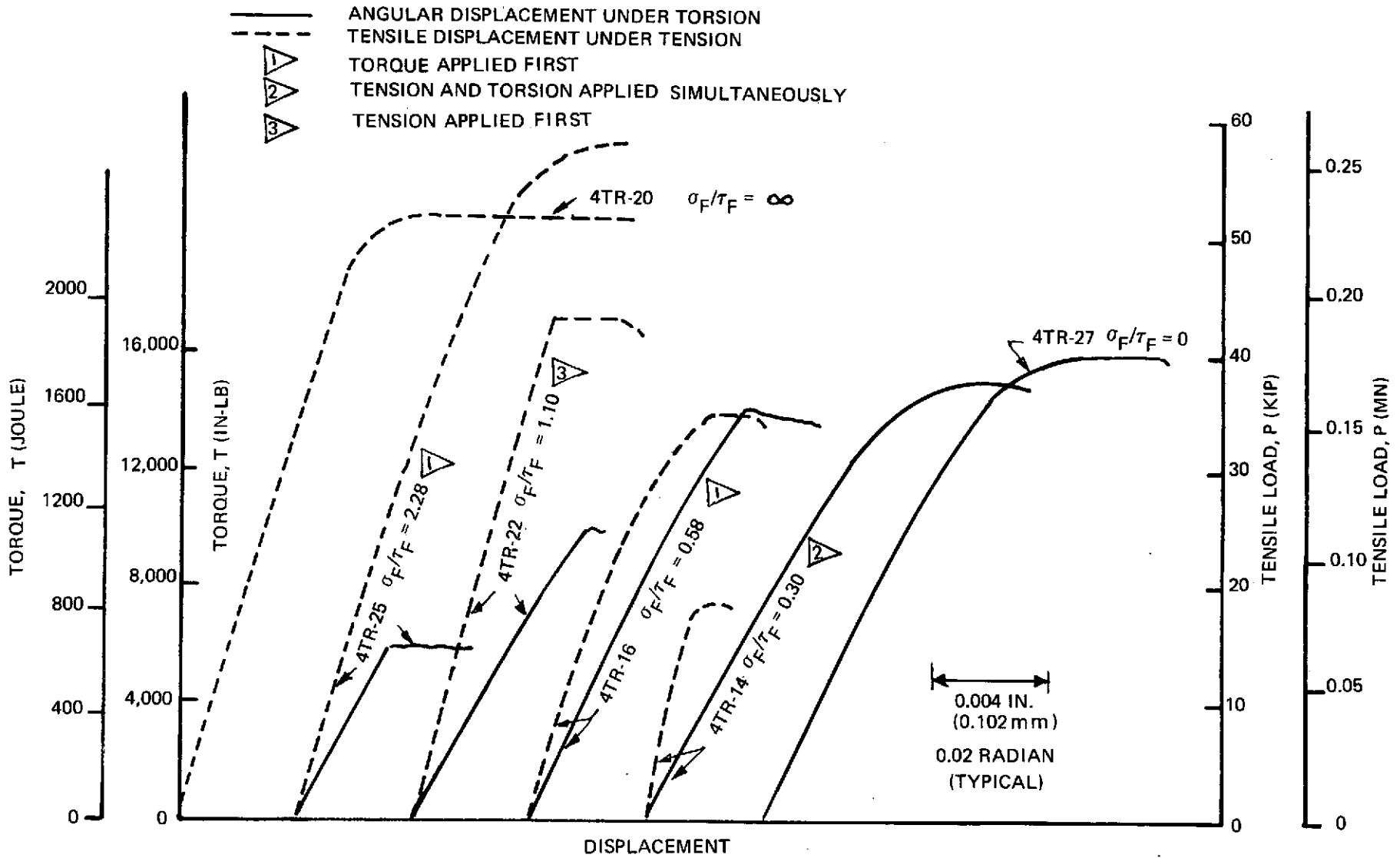


Figure 7-11: Load-Displacement Records for 6Al-4V  $\beta$ STA Titanium Surface Flawed Cylindrical Specimens Subjected to Tension and Torsion

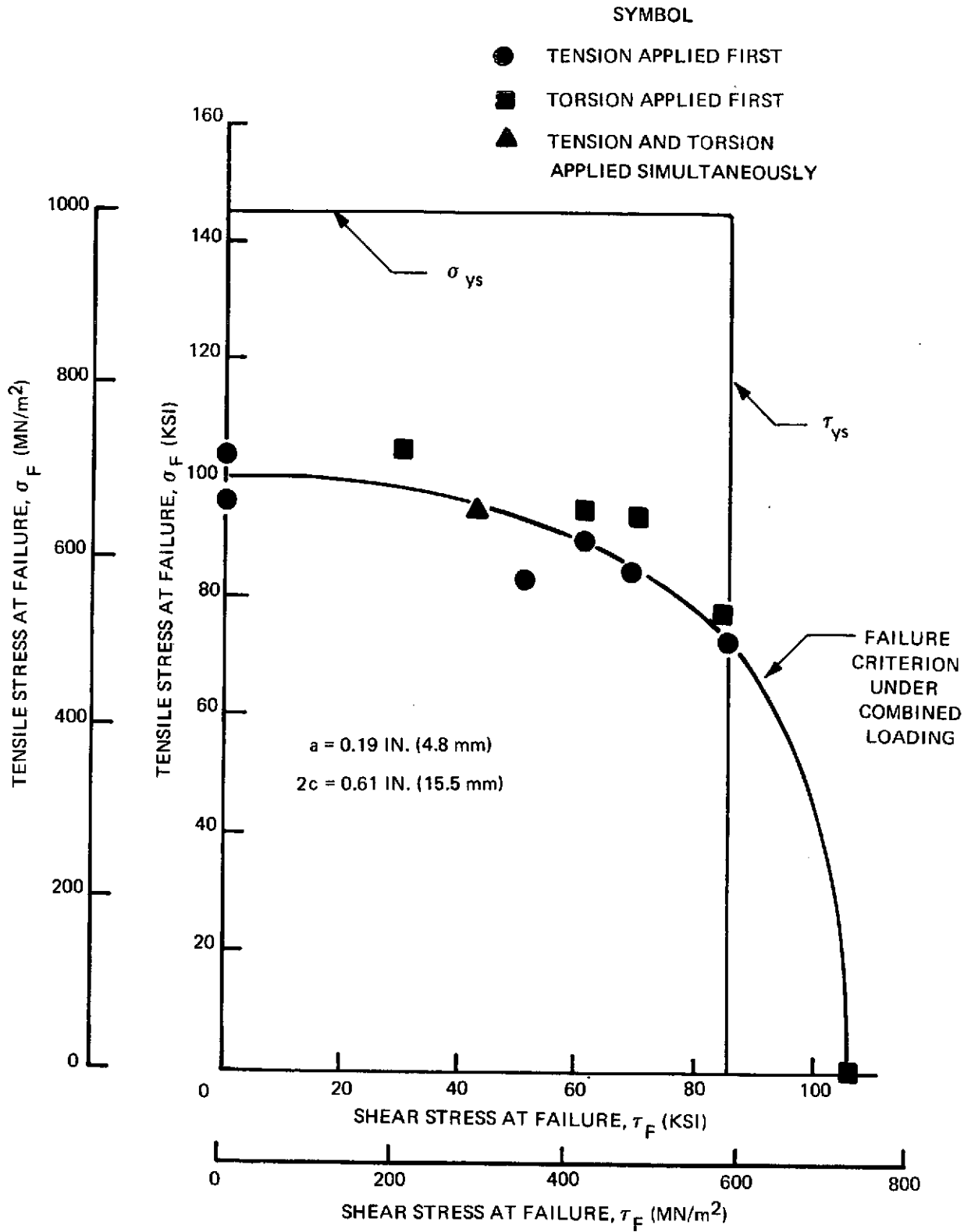


Figure 7-12: Fracture Tests of 6Al-4V  $\beta$  STA Titanium Cylindrical Specimens Containing Surface Flaws Subjected to Combined Tension and Torsion

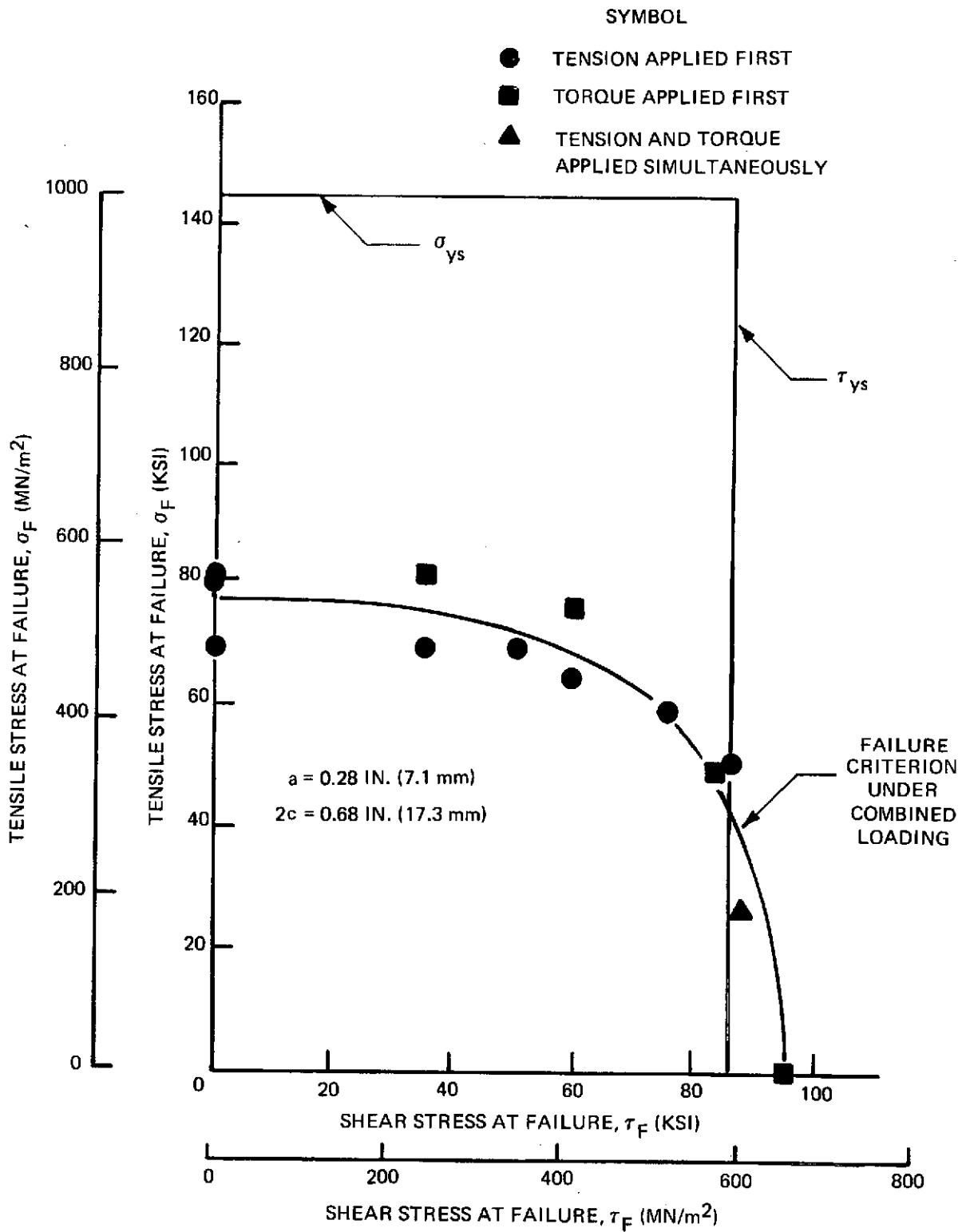


Figure 7-13: Fracture Tests of 6Al-4V  $\beta$  STA Titanium Cylindrical Specimens Containing Surface Flaws Subjected to Combined Tension and Torsion

LEGEND

FLAW SIZE  $a = 0.28$  IN. (7.1 mm) AND  $2c = 0.68$  IN. (17.3 mm)

- TENSION APPLIED FIRST
- TORSION APPLIED FIRST
- ◻ TENSION AND TORSION APPLIED SIMULTANEOUSLY

FLAW SIZE  $a = 0.19$  IN. (4.8 mm) AND  $2c = 0.61$  IN. (15.5 mm)

- TENSION APPLIED FIRST
- TORSION APPLIED FIRST
- ◐ TENSION AND TORSION APPLIED SIMULTANEOUSLY

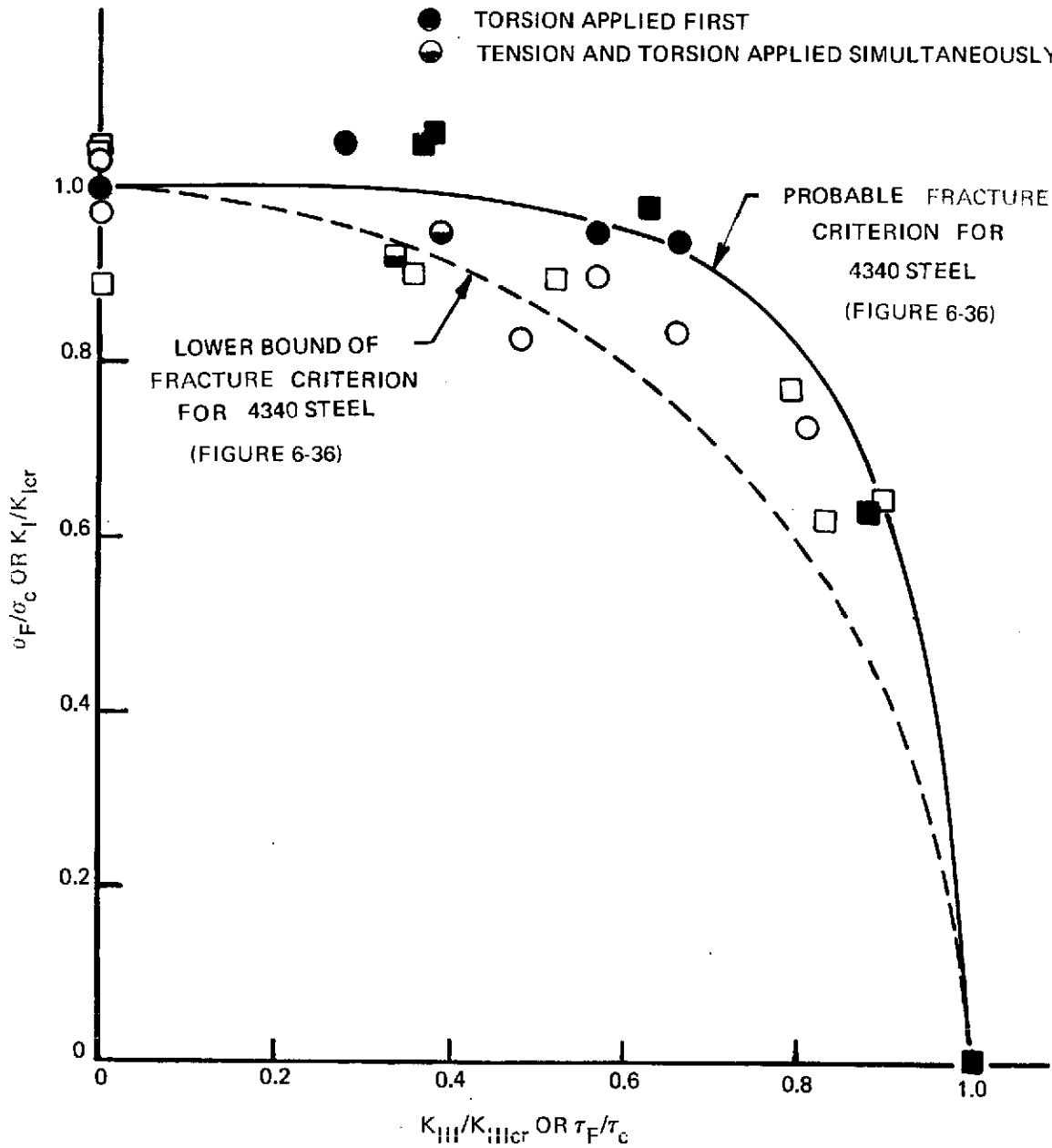
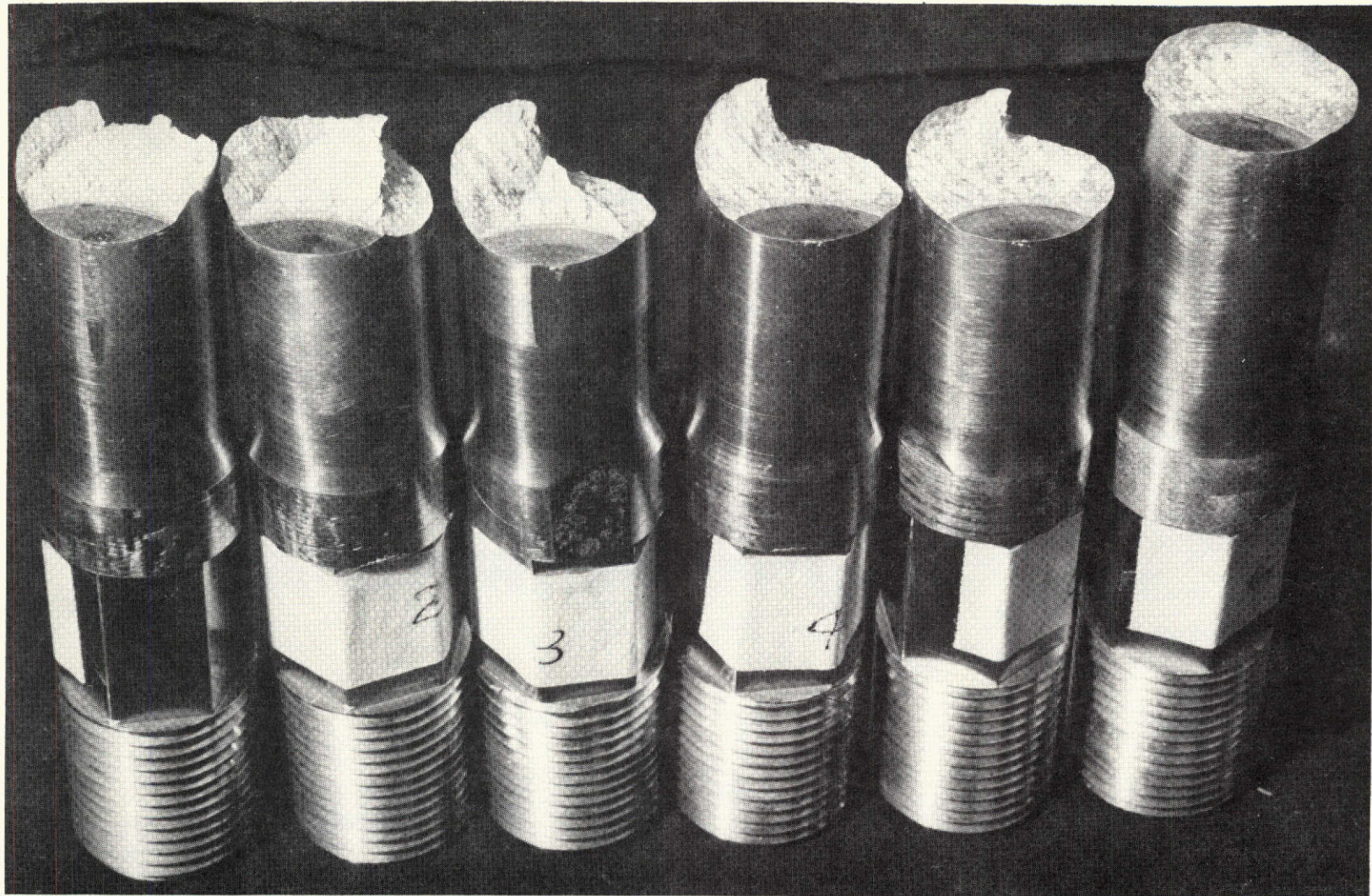


Figure 7-14:  $K_I/K_{Icr}$  Vs.  $K_{III}/K_{IIIcr}$  For 6Al-4V  $\beta$ STA Titanium Cylindrical Specimens Containing Surface Flaws Subjected to Combined Tension and Torsion



$\sigma_F/\tau_F = \infty$   
(4TR-20)

$\sigma_F/\tau_F = 2.28$   
(4TR-25)

$\sigma_F/\tau_F = 1.10$   
(4TR-22)

$\sigma_F/\tau_F = 0.58$   
(4TR-16)

$\sigma_F/\tau_F = 0.30$   
(4 TR-14)

$\sigma_F/\tau_F = 0$   
(4TR-27)

Figure 7-15: Fracture Surfaces of Surface Flawed Cylindrical Specimens of 6Al-4V  $\beta$ STA Titanium Subjected to Combined Tension and Torsion (Static Fracture)

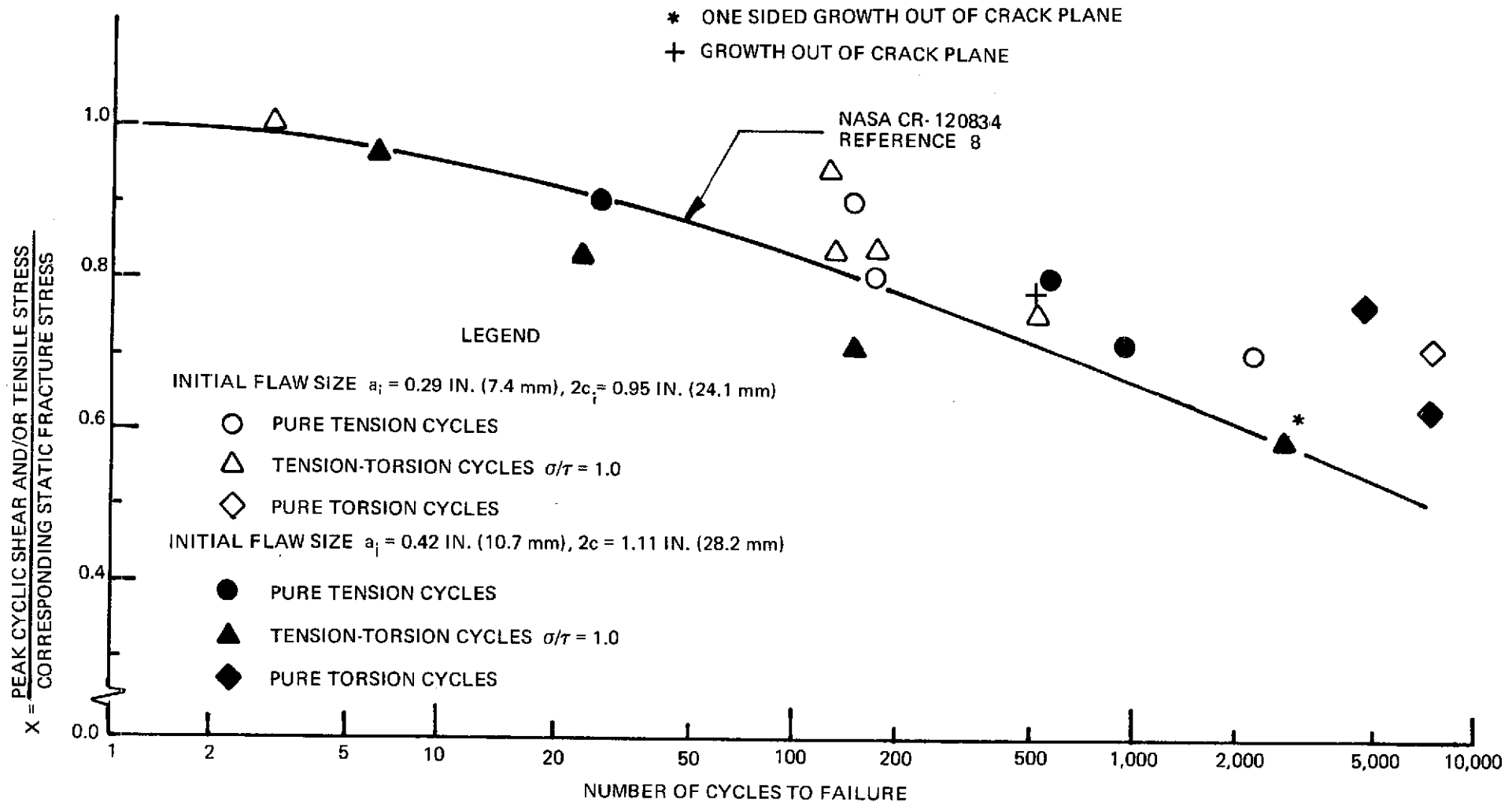


Figure 7-16: Correlation Between Cyclic (Combined Tensile and Shear) Stresses and Cycles to Failure for Surface Flawed Cylindrical Specimens of 2219-T87 Aluminum



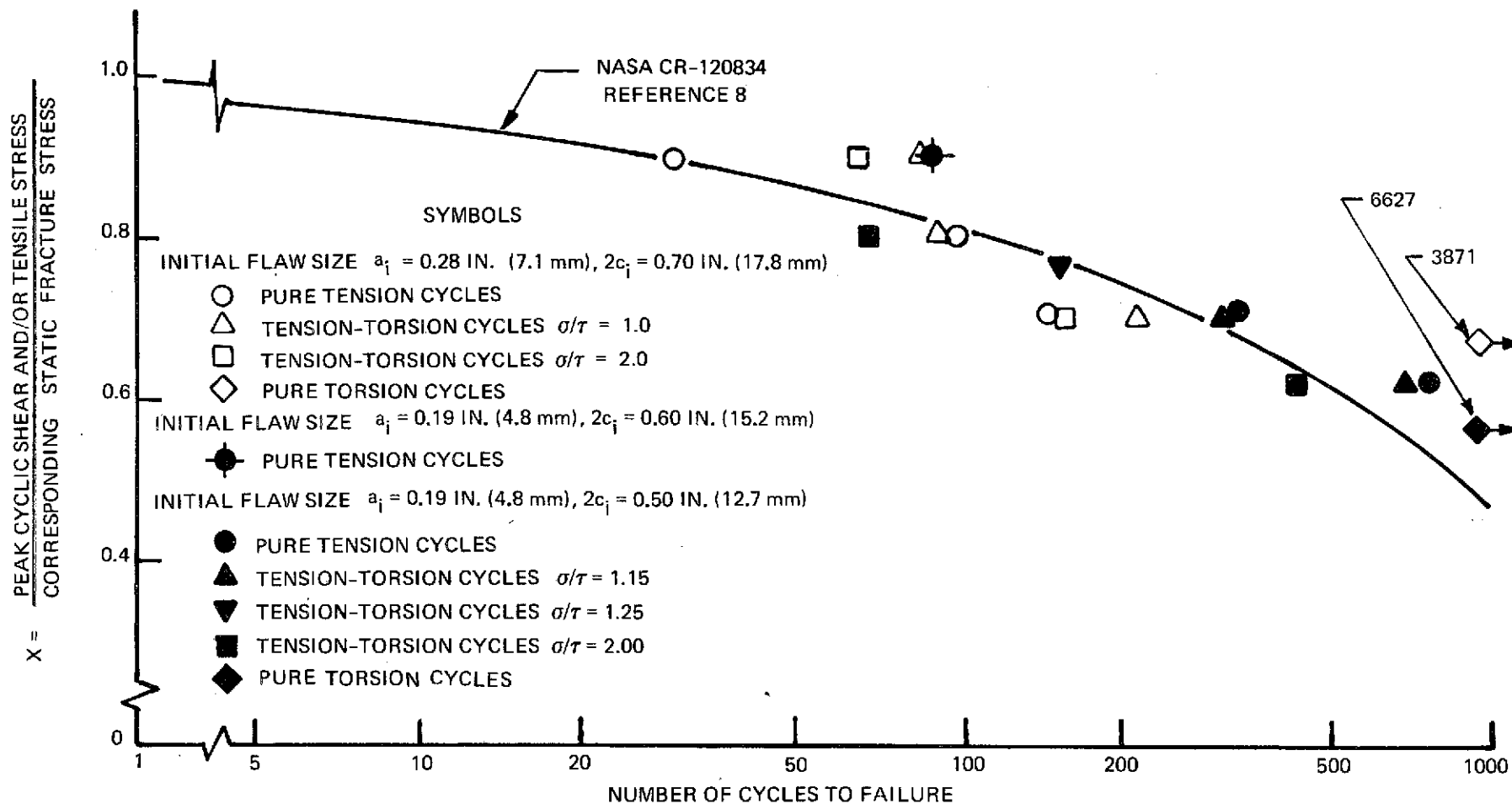
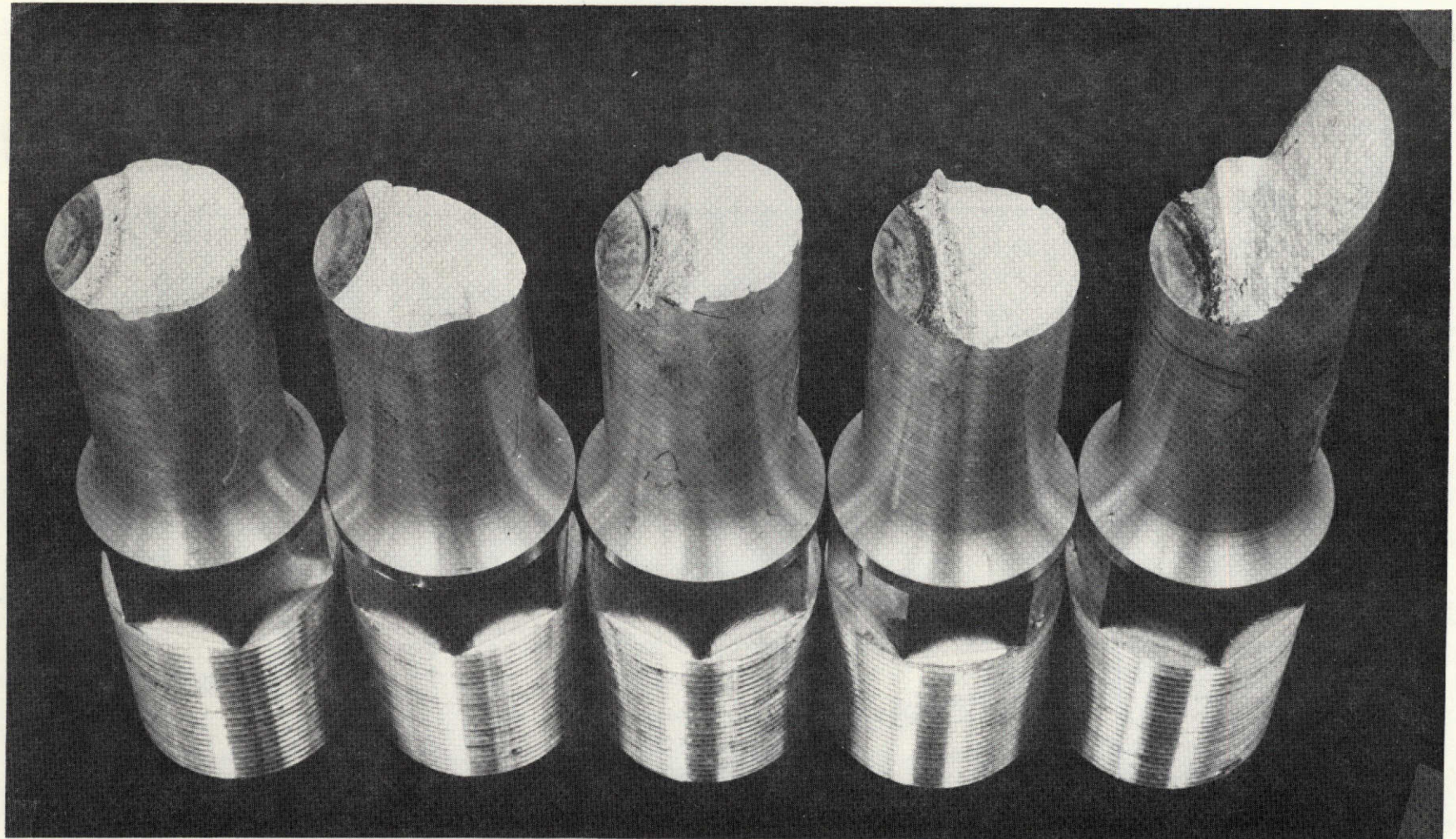
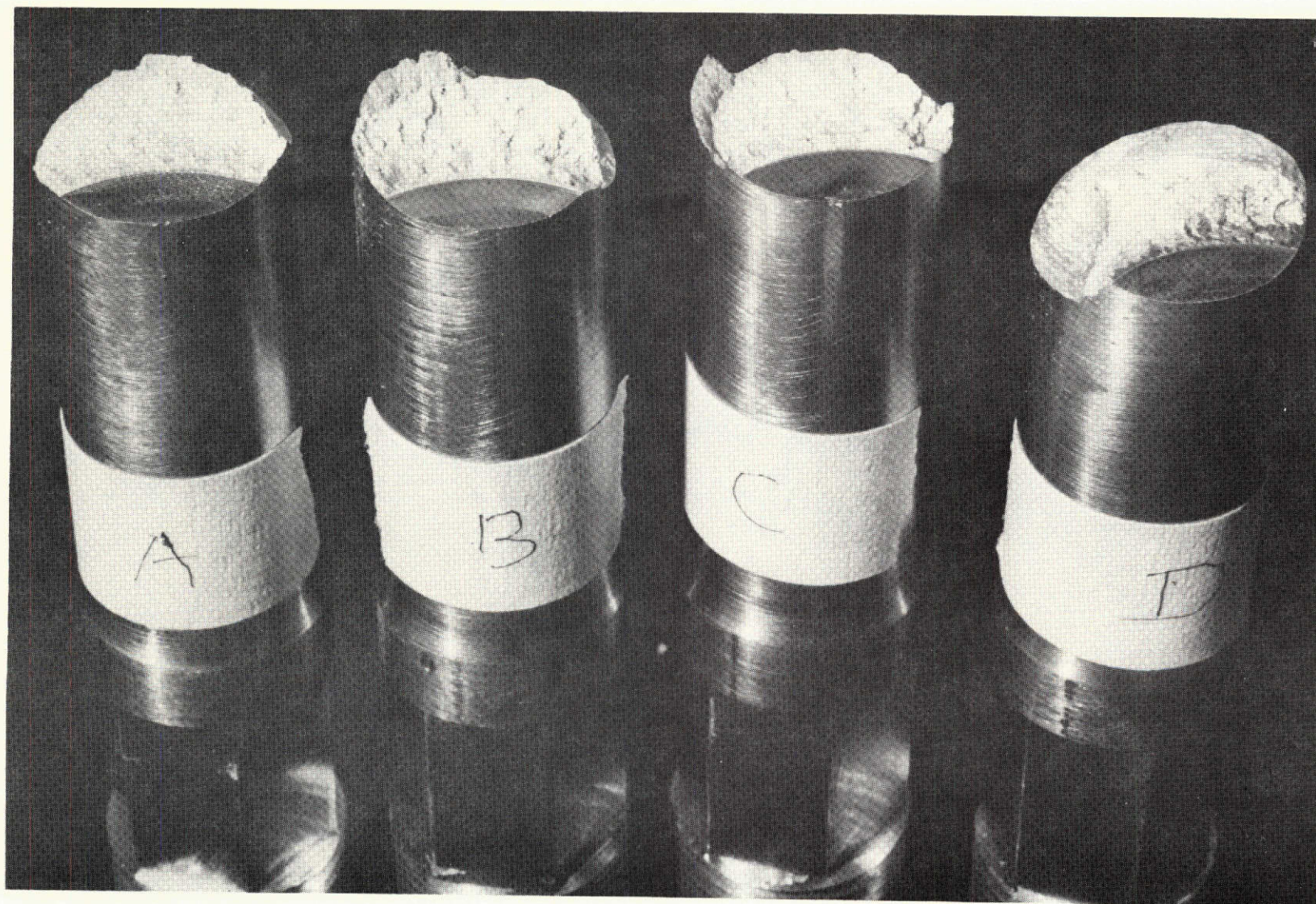


Figure 7-17: Correlation Between Cyclic (Combined Tensile and Shear) Stresses and Cycles to Failure for Surface Flawed Cylindrical Specimens of 6Al-4V  $\beta$ STA Titanium

 $\sigma/\tau =$  $\infty$   
(5A1-12)1.0  
(5A1-15)1.0  
(5A1-18)0  
(5A1-16)0  
(5A1-17)

*Figure 7-18: Fracture Surfaces of Surface Flawed Cylindrical Specimens of 2219-T87 Aluminum Subjected to Cyclic Tensile and Torsional Loadings*



$\sigma/\tau = \infty$   
(5TC-10)

$\sigma/\tau = 1.0$   
(5TC-13)

$\sigma/\tau = 2.0$   
(5TC-16)

$\sigma/\tau = 0$   
(5TC-18)

183

Figure 7-19: Fracture Surfaces of Surface Flawed Cylindrical Specimens of 6A1-4V  $\beta$  STA Titanium Subjected to Combined Tensile and Torsional Cyclic Loadings

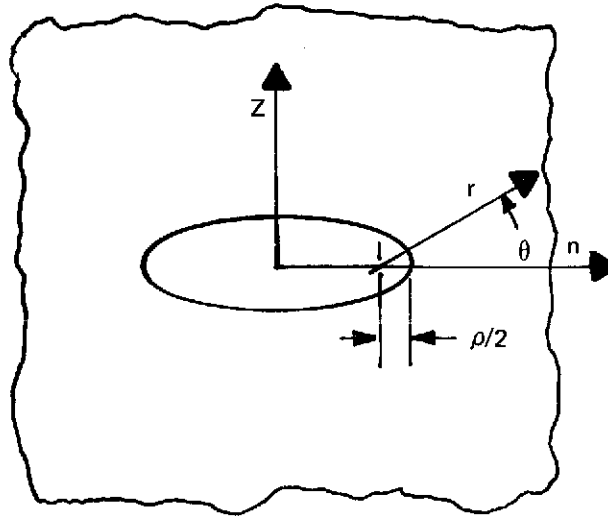


Figure 8-1: Coordinate System for Stress Field for an Elliptical Notch in an Infinite Plate

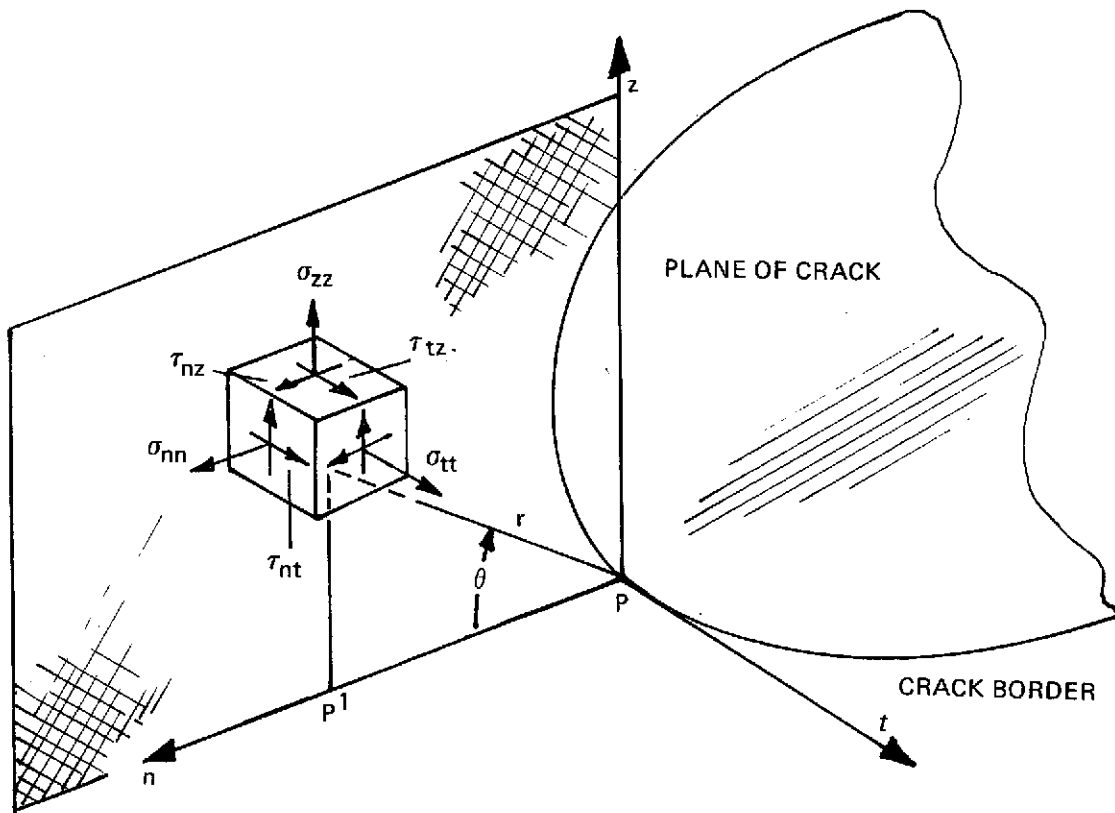
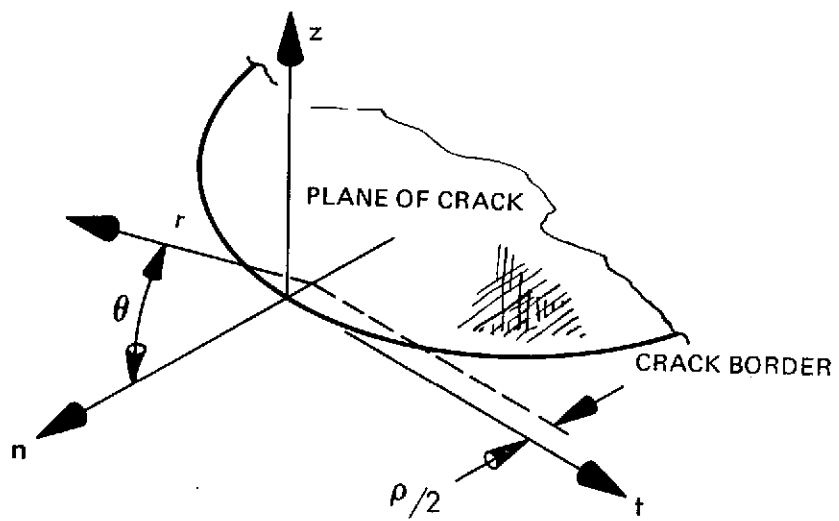


Figure 8-2: Rectangular Stress Components in Plane Normal to Crack Border



$\rho$  = Notch Root Radius

*Figure 8-3: Local Coordinate System for a Notch in a Solid*

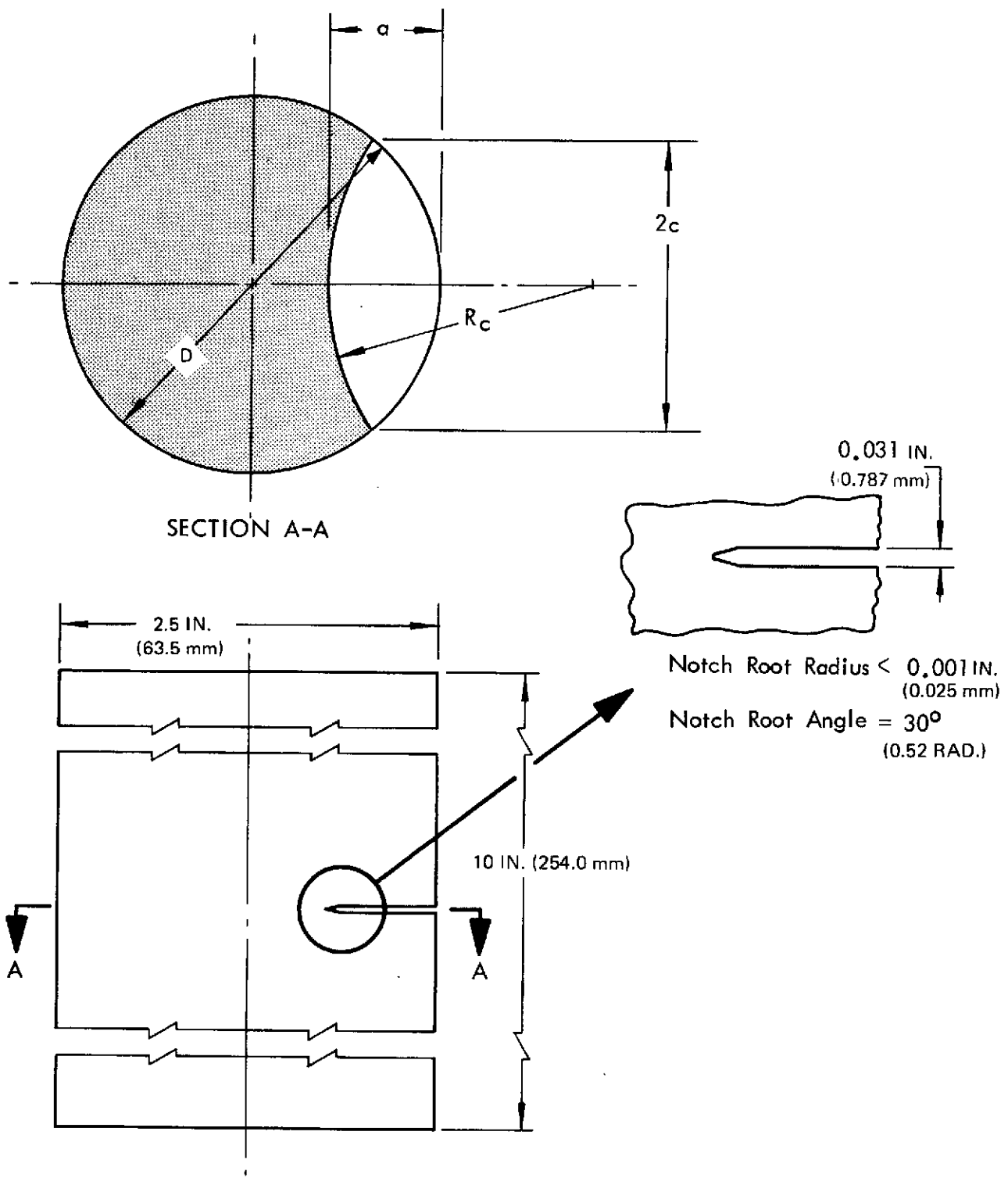
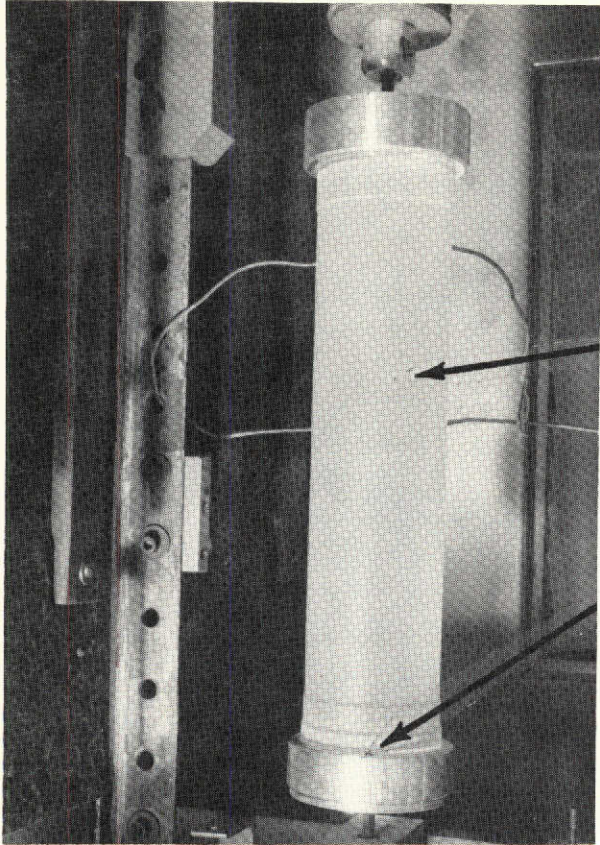
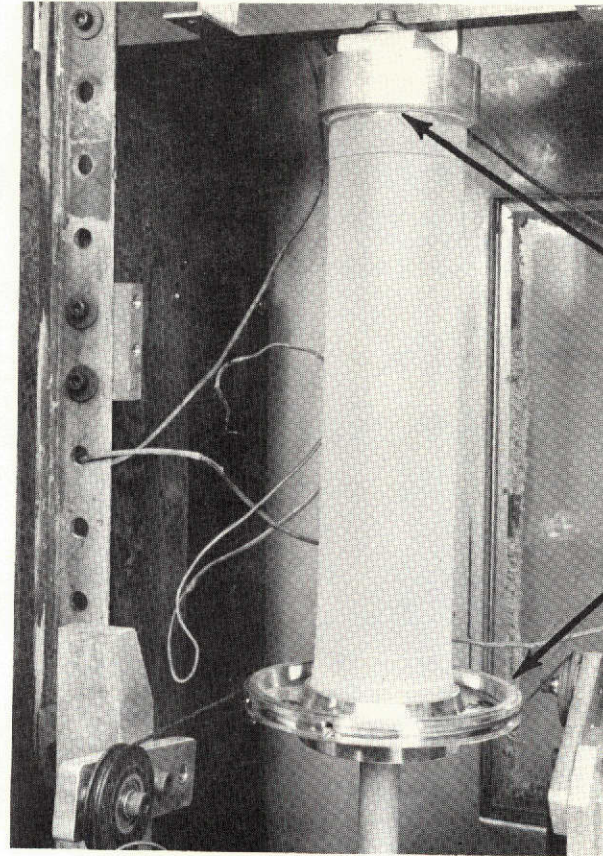


Figure 8-4: Photoelastic Specimen and Notch Configurations



SURFACE NOTCH

END PRESSED  
IN ALUMINUM  
CAP



END CEMENTED  
TO ALUMINUM  
CAP

TORQUE APPLIED  
THROUGH  
ALUMINUM  
PULLEY

*Figure 8-5: Notched Photoelastic Specimens in Tension or Torsion Loading in Stress Freezing Oven*

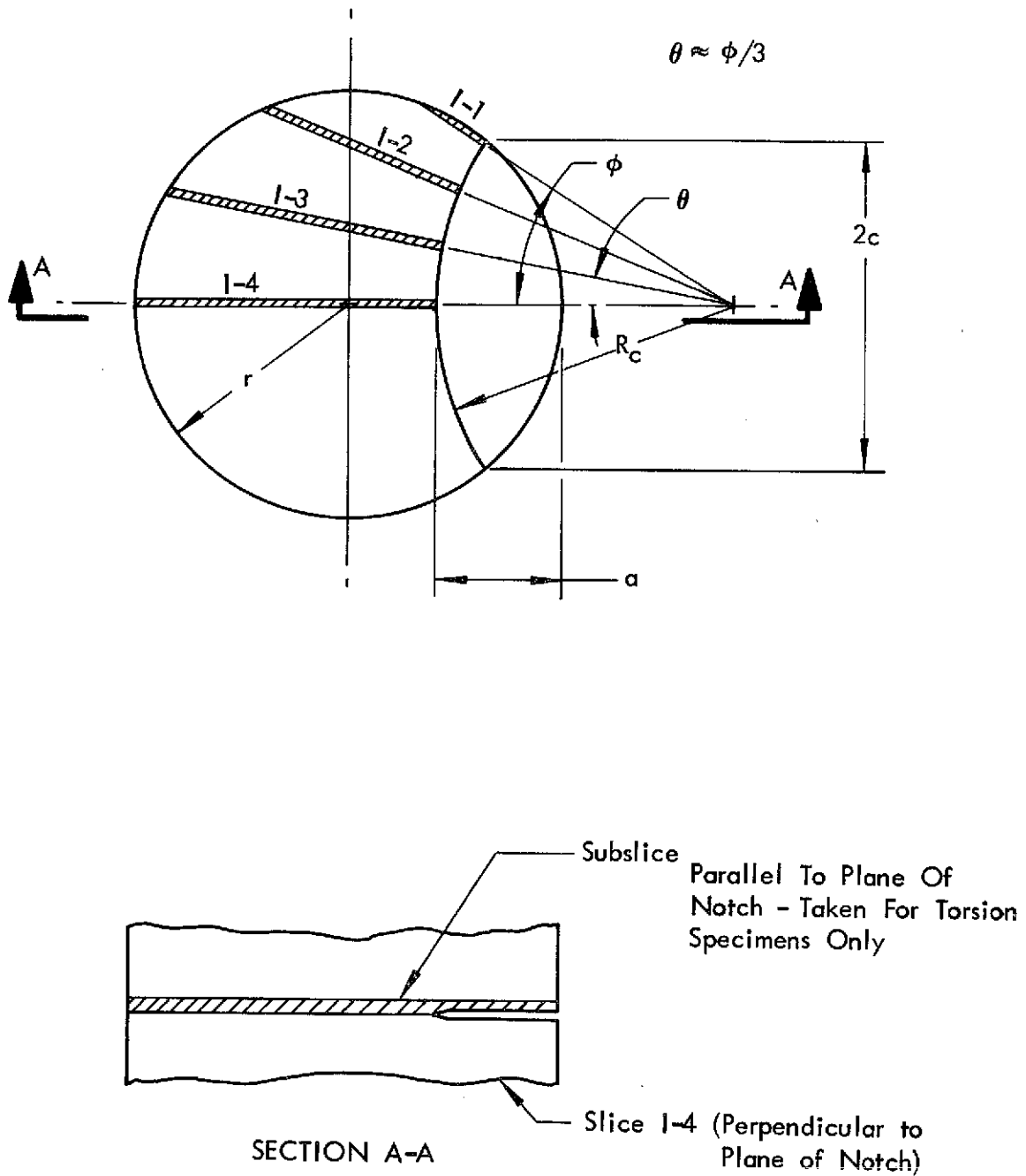
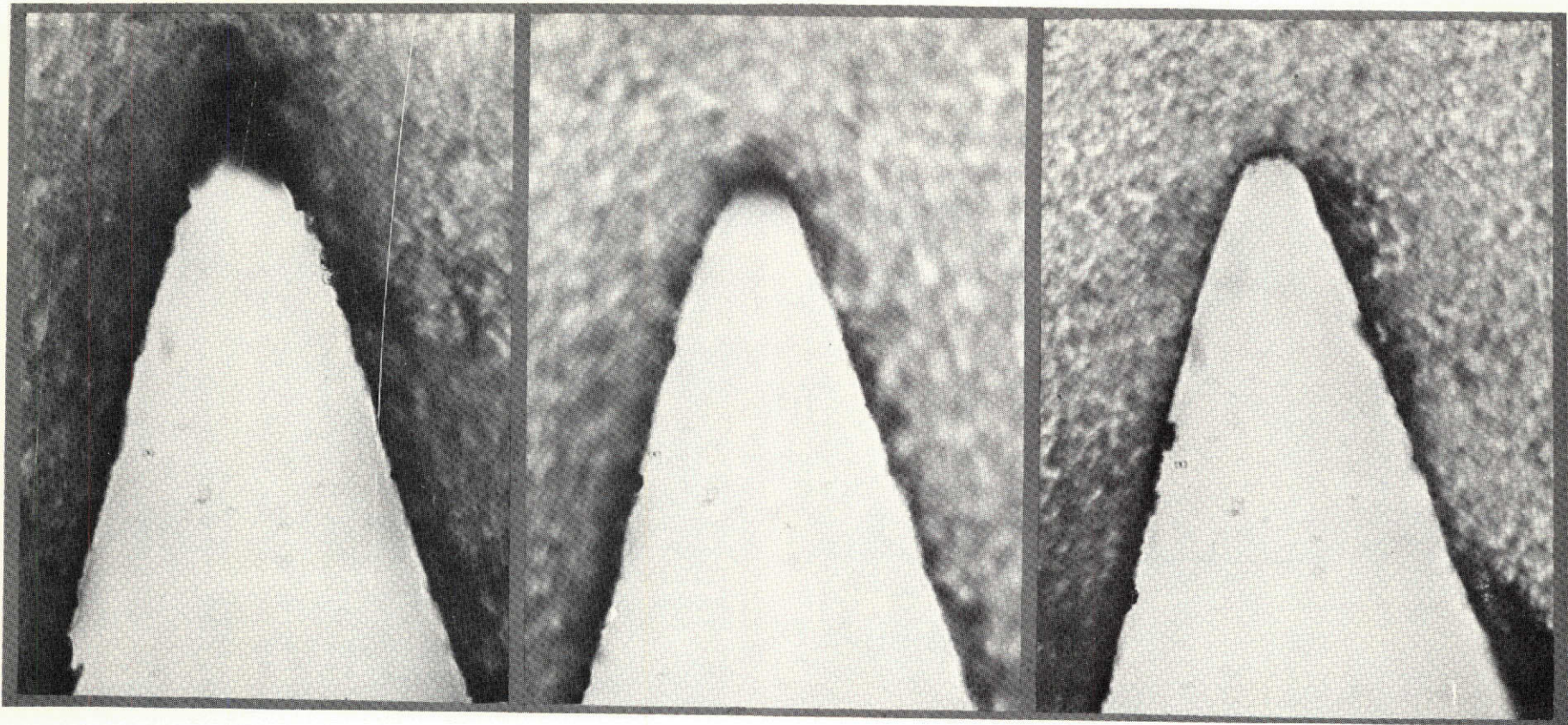


Figure 8-6: Location of Slices for Photoelastic Specimen





SLICE I-1 400X

SLICE I-2 400X

SLICE I-3 400X

*Figure 8-7: Micrographs of Notch Root Radii for Slices in nz Plane of Surface Notched Specimen 1*

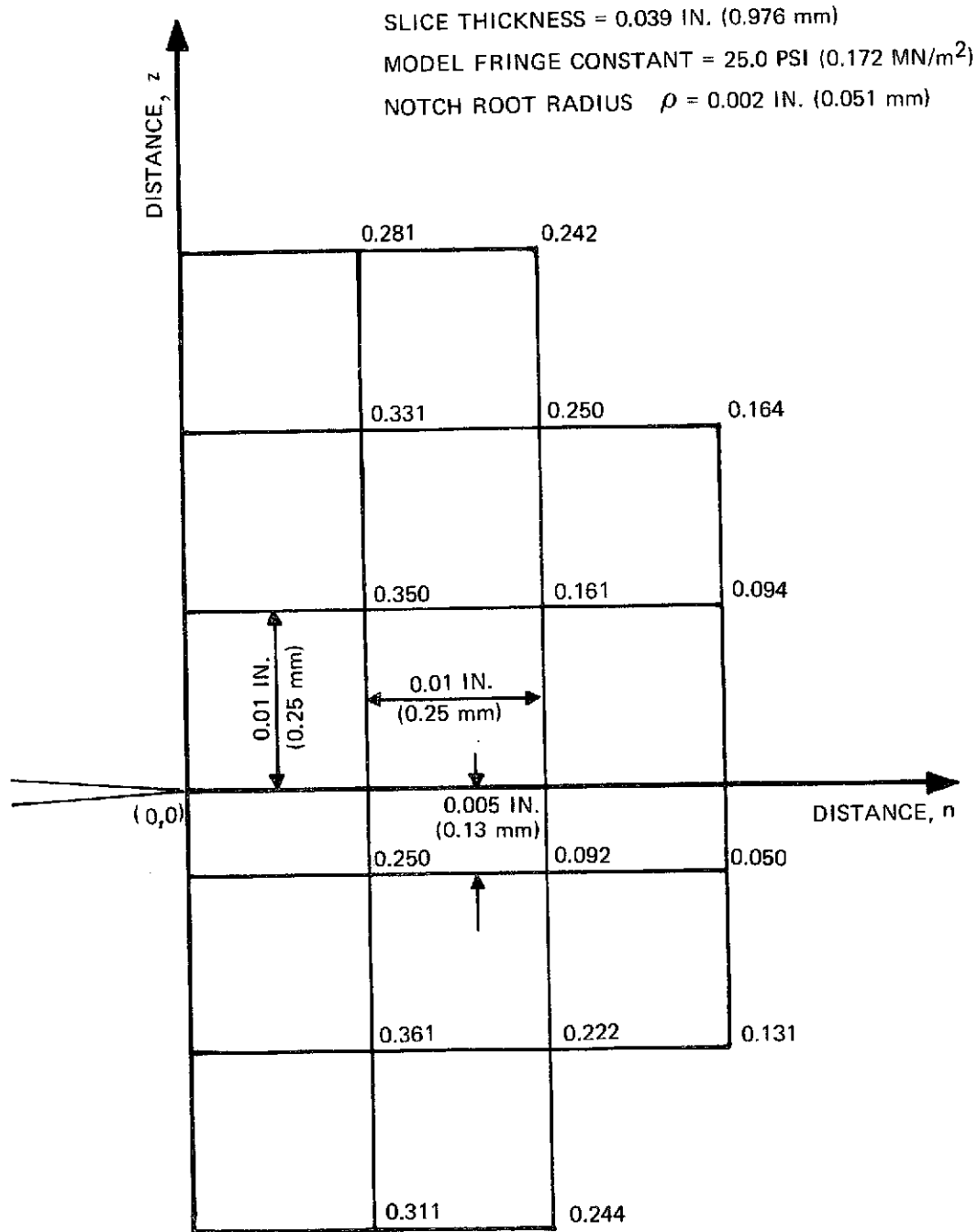


Figure 8-8: Measured Fringe Orders for Circumferentially Notched Round Bar (Specimen 7) in Tension

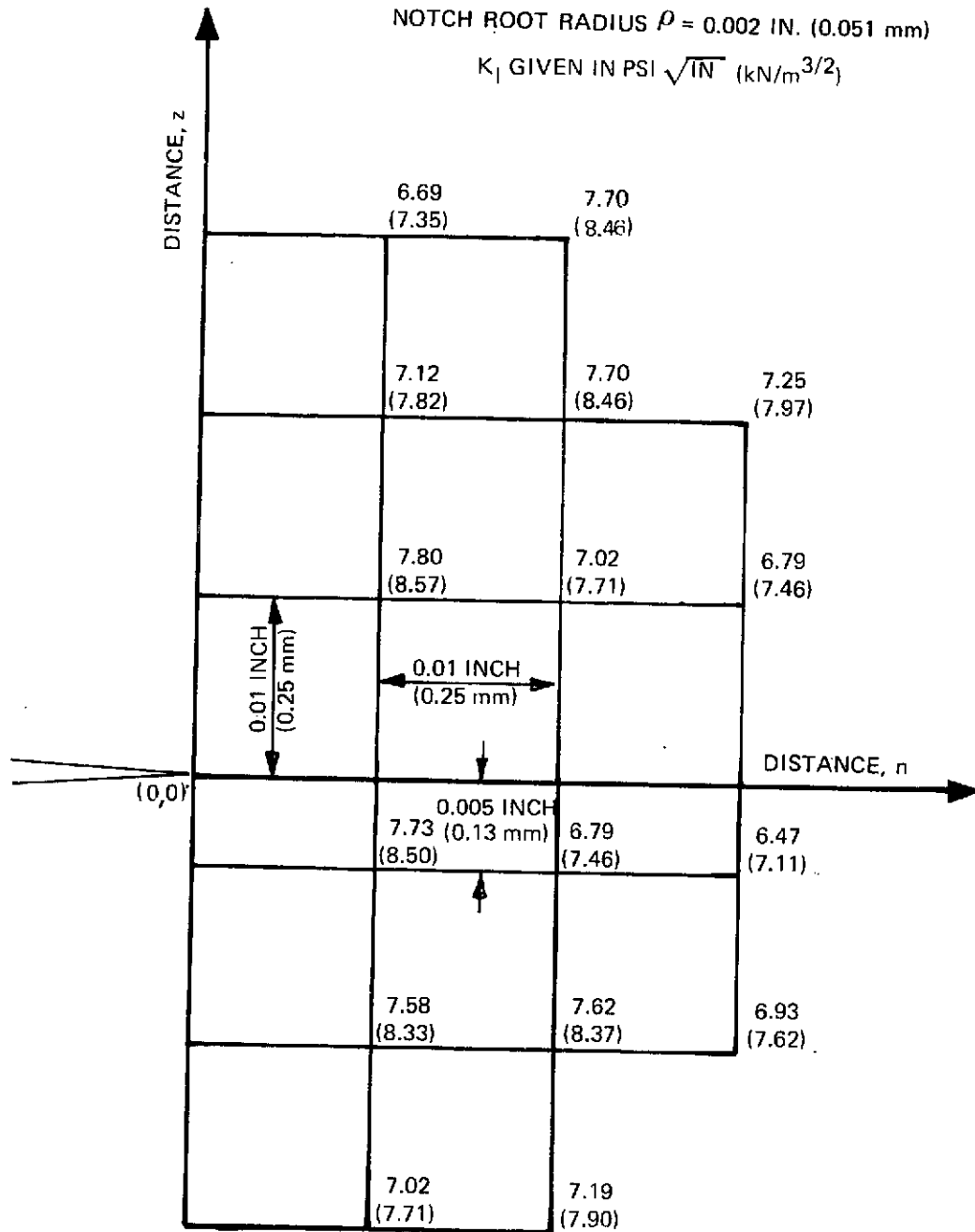


Figure 8-9: Stress Intensity Factors Calculated for a Circumferentially Notched Round Bar (Specimen 7) Neglecting Effect of Remote Stress Field ( $\rho = 0.002$  IN. (0.051 mm))

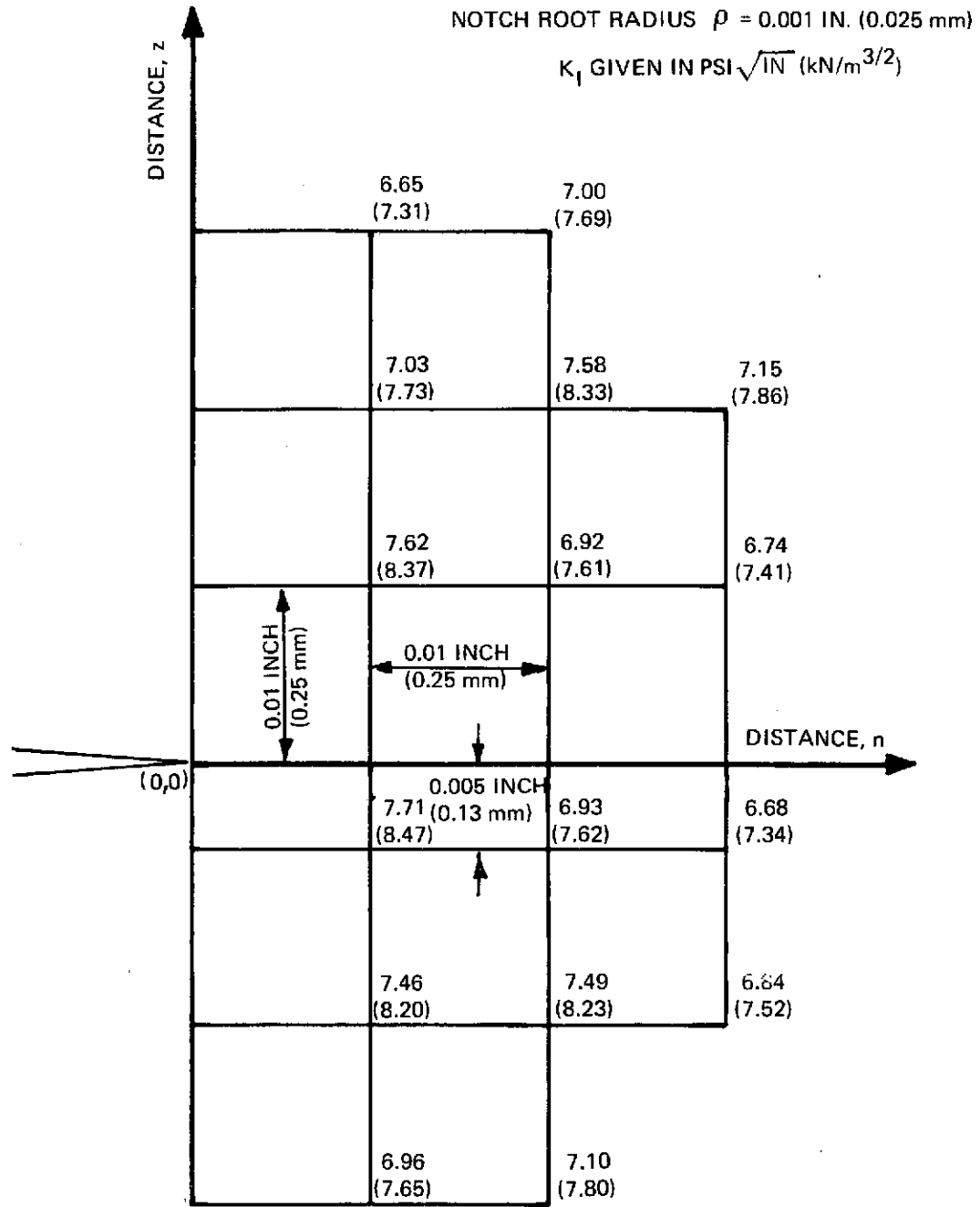


Figure 8-10: Stress Intensity Factors Calculated for a Circumferentially Notched Round Bar (Specimen 7) Neglecting Effect of Remote Stress Field ( $\rho = 0.001$  IN. (0.025 mm))

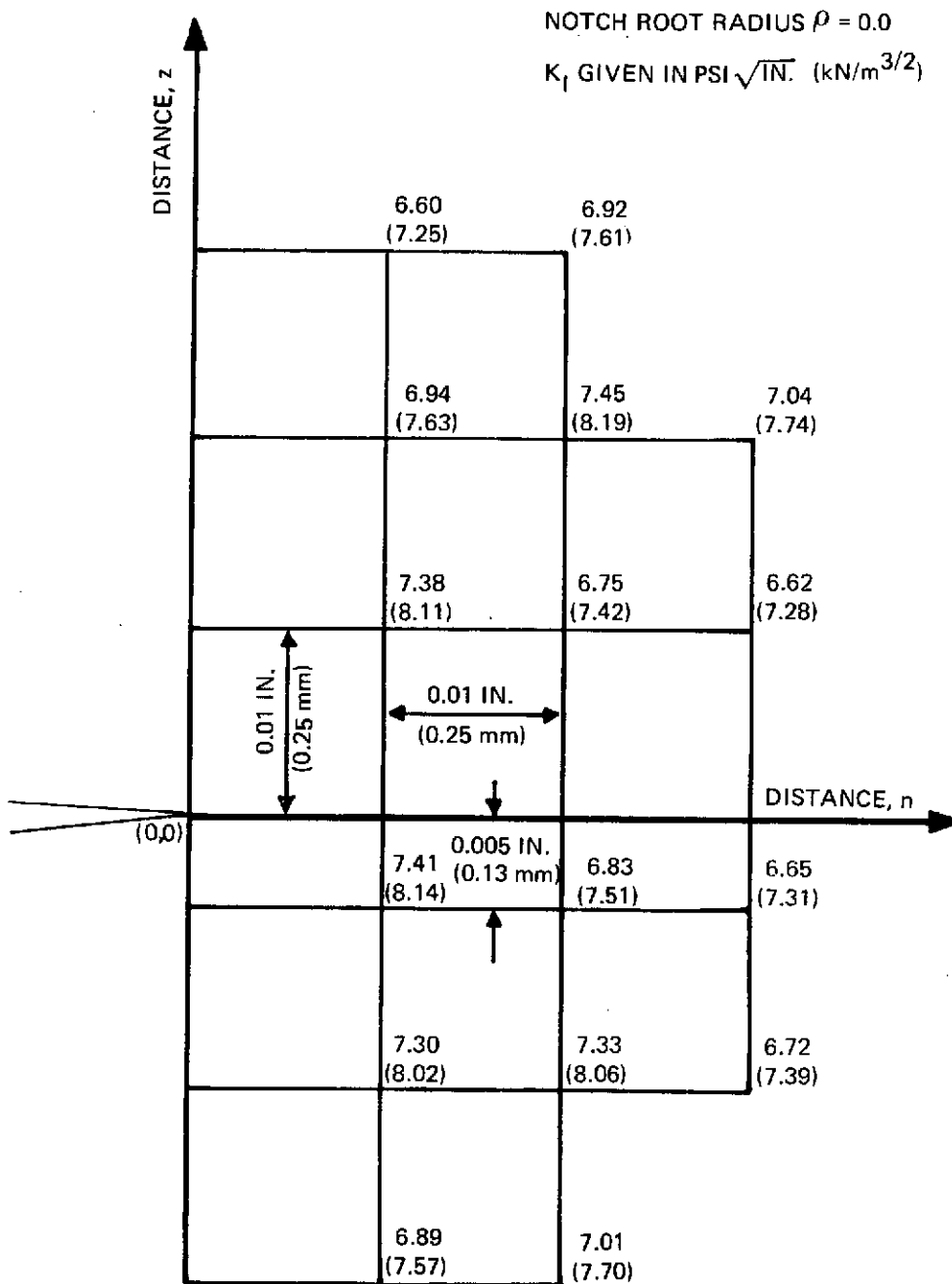


Figure 8-11: Stress Intensity Factors Calculated for a Circumferentially Notched Round Bar (Specimen 7) Neglecting Remote Stress Field ( $\rho = 0.000$ )

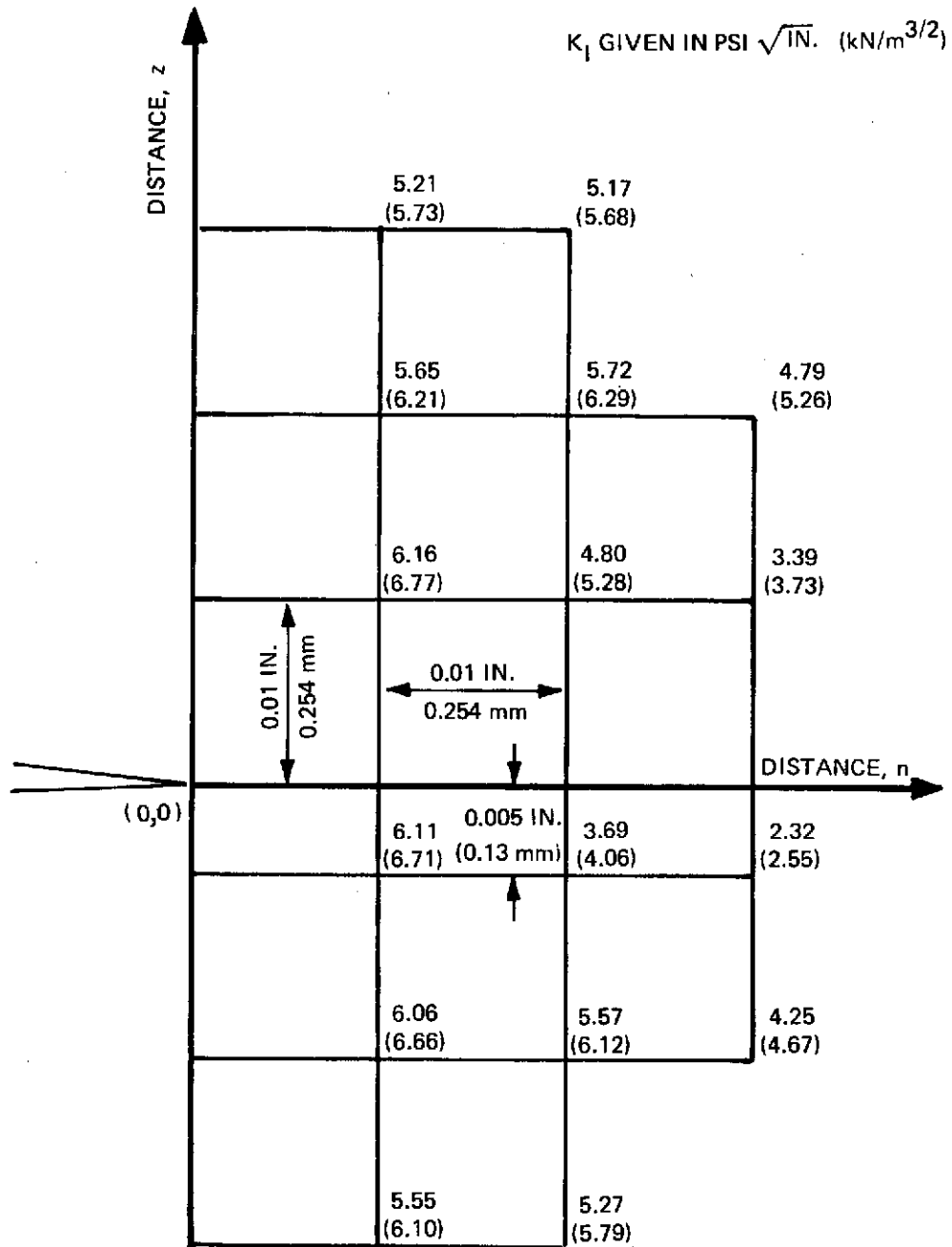


Figure 8-12: Stress Intensity Factors for a Circumferentially Notched Round Bar (Specimen 7) Using Equation (8-12)

Table 3-1: Chemical Composition of Materials Tested

ELEMENT (% BY WEIGHT EXCEPT AS NOTED)	2219-T87 ALUMINUM PLATE (SPECIFICATION LIMITS)		5AI-2.5 SN (ELI) TITANIUM PLATE HEAT NO. 294327	6AI-4V TITANIUM HEAT NO. G-17681-1E	4340 STEEL HEAT NO. SP 4118
	MINIMUM	MAXIMUM			
COPPER	5.80	6.80	-	-	-
SILICON	-	0.20	-	-	0.33
MANGANESE	0.20	0.40	-	-	0.74
MAGNESIUM	-	0.02	0.01	-	-
CHROMIUM	-	-	-	-	0.85
ZINC	-	0.10	-	-	-
VANADIUM	0.05	0.15	-	4.3	-
TIN	-	-	2.50	-	-
CARBON	-	-	0.02	0.03	0.38
NITROGEN	-	-	70 PPM	0.012	-
OXYGEN	-	-	940 PPM	0.14	-
HYDROGEN	-	-	94 PPM	0.0026	-
ZIRCONIUM	0.10	0.25	-	-	-
PHOSPHOROUS	-	-	-	-	0.010
SULPHUR	-	-	-	-	0.012
NICKEL	-	-	-	-	1.95
MOLYBDENUM	-	-	-	-	0.23
IRON	-	0.30	0.19	0.23	BALANCE
TITANIUM	0.10	0.20	BALANCE	BALANCE	-
ALUMINUM	BALANCE	BALANCE	5.10	6.5	-

Table 3-2: Mechanical Properties of Titanium Alloys

ALLOY	PLATE THICKNESS IN. (mm)	TEST TEMPERATURE DEG. F (DEG. K)	LOADING DIRECTION L=LONGITUDINAL T=TRANSVERSE	ULTIMATE TENSILE STRENGTH KSI (MN/m <sup>2</sup> )	0.2% OFFSET YEILD STRENGTH KSI (MN/m <sup>2</sup> )	PERCENT ELONGATION IN 2.0 IN. GAGE LENGTH	PERCENT REDUCTION IN AREA
5Al-2.5 Sn (ELI) TITANIUM	0.80 (20.3)	-320 (78)	L	176 (1214)	173 (1193)	8	—
		-423 (20)	L	201 (1386)	187 (1289)	3	—
6Al-4V (STA) TITANIUM	0.375 (9.5)	72 (295)	L	186 (1282)	174 (1200)	6	16
			T	163 (1124)	149 (1027)	4	18
		-320 (78)	L	260 (1793)	250 (1724)	3	15
			T	237 (1634)	221 (1524)	3	15
		-423 (20)	L	290 (2000)	277 (1910)	2	—
			T	269 (1855)	—	—	—
6Al-4V BETA-ANNEALED (STA) TITANIUM	0.375 (9.5)	72 (295)	L	173 (1193)	156 (1076)	4	7
			T	172 (1186)	155 (1069)	6	9
		-320 (78)	L	247 (1703)	224 (1544)	3	4
			T	245 (1689)	226 (1558)	3	4
		-423 (20)	L	284 (1958)	269 (1855)	3	—
			T	276 (1903)	261 (1800)	3	—
6Al-4V BETA-ANNEALED (STA) TITANIUM	1.0 (25.4)	72 (295)	L	159 (1096)	146 (1007)	8	9
			T	162 (1117)	146 (1007)	8	9



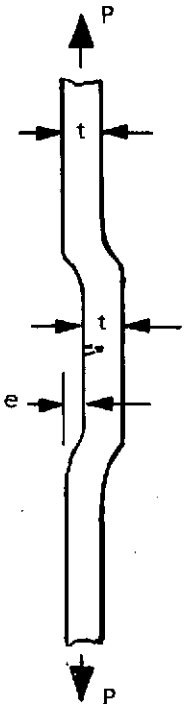
Table 3-3: Mechanical Properties of 4340 Steel Plate

PLATE THICKNESS IN. (mm)	TEST TEMPERATURE DEG. F (DEG. K)	LOADING DIRECTION TENSILE STRENGTH KSI (MN/m <sup>2</sup> )	ULTIMATE TENSILE STRENGTH KSI (MN/m <sup>2</sup> )	0.2% OFFSET YIELD STRENGTH KSI (MN/m <sup>2</sup> )	PERCENT ELONGATION IN 2.0 IN. (50.8 mm) GAGE LENGTH	PERCENT REDUCTION IN AREA
1.0 (25.4)	72 (295)	L	277 (1910)	212 (1462)	10	36
		T	274 (1889)	216 (1489)	11	40
	-200 (144)	L	294 (2027)	225 (1551)	5	5
		T	—	210 (1448)	2	1

Table 3-4: Mechanical Properties of 2219-T87 Aluminum Plate

PLATE THICKNESS IN. (mm)	TEST TEMPERATURE DEG. F (DEG. K)	LOADING DIRECTION L=LONGITUDINAL T=TRANSVERSE	ULTIMATE TENSILE STRENGTH KSI (MN/m <sup>2</sup> )	0.2% OFFSET YIELD STRENGTH KSI (MN/m <sup>2</sup> )	PERCENT ELONGATION IN 2.0 IN. (50.8 mm) GAGE LENGTH	PERCENT REDUCTION IN AREA
1.0 (25.4)	72 (295)	L	68 (469)	55 (379)	10	28
		T	69 (476)	56 (386)	8	15
	-320 (78)	L	83 (572)	65 (448)	13	22
		T	86 (593)	66 (455)	12	14
	-423 (20)	L	97 (669)	67 (462)	15	—
		T	100 (690)	69 (476)	11	13
2-50 (63.5)	72 (295)	L	69 (476)	57 (393)	12	23
		T	69 (476)	55 (379)	10	15

Table 4-1: Test Program for 5Al-2.5 Sn (ELI) Titanium Surface Flawed Specimens Loaded to Fracture in Combined Bending and Tension Stresses at -320F (78 K)

SPECIMEN CONFIGURATION	a/2c	t IN. (mm)	e IN. (mm)	a/t	NO. OF TESTS
	0.25	0.375 (9.5)	0.00	0.3	2
				0.4	2
		0.28 (7.1)	0.045 (1.14)	0.3	2
				0.5	2
		0.090 (2.29)	0.3	2	
			0.5	2	

*Table 4-2: Test Program for 5Al-2,5 Sn (ELI) Titanium Surface Flawed Specimens Loaded to Fracture in Pure Bending at -423F (20 K)*

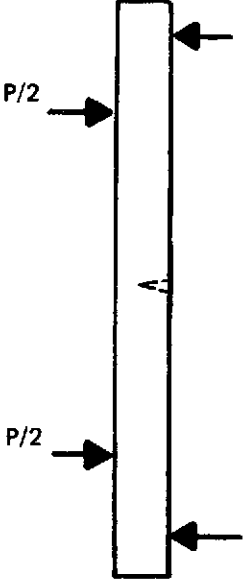
SPECIMEN CONFIGURATION	$a/2c$	$t$ IN. (mm)	$a/t$	NO. OF TESTS
	0.25	0.75 (19.1)	0.2	2
			0.3	2
			0.4	2
			0.5	2

Table 4-3: Static Fracture Toughness Data For 5Al-2.5 Sn (ELI) Titanium at -320F (78 K)

SPECIMEN IDENTIFICATION	SPECIMEN THICKNESS t IN (mm)	SPECIMEN WIDTH W IN (mm)	FLAW DEPTH a IN (mm)	FLAW LENGTH 2c IN (mm)	FRACTURE STRESS $\sigma$ , KSI (MN/m <sup>2</sup> )	FRACTURE TOUGHNESS K <sub>IE</sub> KSI $\sqrt{\text{IN}}$ (MN/m <sup>3/2</sup> )
2TSFN1	0.369 (9.37)	2.001 (50.8)	0.108 (2.74)	0.480 (12.2)	149.4 (1030)	84.1 (92.4)
2TSFN2	0.378 (9.60)	2.002 (50.8)	0.105 (2.67)	0.455 (11.6)	148.2 (1022)	81.6 (89.7)
2TSFN3	0.378 (9.60)	2.500 (63.5)	0.159 (4.04)	0.707 (18.0)	119.3 (823)	81.0 (89.0)
2TSFN4	0.373 (9.47)	2.503 (63.6)	0.158 (4.01)	0.718 (18.2)	130.2 (898)	89.5 (98.4)

Table 4-4: Test Results for 5Al-2.5 Sn (ELI) Titanium Surface Flawed Specimens Subjected to Combined Bending and Tension Stresses at -320F (78 K)

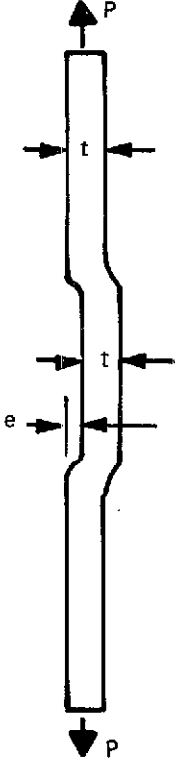
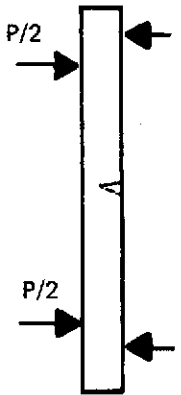
CONFIGURATION	SPECIMEN				FLAW SIZE		RESULTS			
	IDENTIFICATION	THICKNESS	WIDTH	OFFSET	DEPTH	LENGTH	FAILURE LOAD KIPS (MN)	FAILURE TENSILE STRESS $\sigma_T$ , KSI (MN/m <sup>2</sup> )	ESTIMATED FAILURE BENDING STRESS, $\sigma_B$ , KSI (MN/m <sup>2</sup> )	FRACTURE TOUGHNESS, $K_{IC}$ KSI $\sqrt{IN}$ (MN/m <sup>3/2</sup> )
		t IN. (mm)	W IN. (mm)	e IN. (mm)	a IN. (mm)	2c IN. (mm)				
	2TCBN1	0.278 (7.06)	2.503 (63.6)	0.090 (2.29)	0.083 (2.11)	0.340 (8.6)	118.4 (0.527)	170.0 (1172)	30.5 (210)	94.1 (103.4)
	2TCBN6	0.281 (7.14)	2.507 (63.7)	0.090 (2.29)	0.080 (2.03)	0.333 (8.5)	119.5 (0.532)	169.5 (1169)	30.5 (210)	92.9 (102.1)
	2TCBN2	0.253 (6.43)	2.506 (63.7)	0.072 (1.83)	0.081 (2.06)	0.340 (8.6)	105.3 (0.469)	166.1 (1145)	25.1 (173)	89.9 (98.8)
	2TCBN5	0.280 (7.11)	2.507 (63.7)	0.040 (1.02)	0.080 (2.03)	0.335 (8.5)	116.8 (0.520)	166.8 (1150)	15.5 (107)	86.1 (94.6)
	2TCBN3	0.280 (7.11)	2.503 (63.6)	0.097 (2.46)	0.133 (3.38)	0.560 (14.2)	75.2 (0.335)	107.5 (741)	32.6 (225)	77.3 (85.0)
	2TCBN8	0.278 (7.06)	2.502 (63.6)	0.093 (2.36)	0.127 (3.23)	0.555 (14.1)	73.1 (0.325)	105.0 (724)	31.5 (217)	74.4 (81.8)
	2TCBN4	0.281 (7.14)	2.500 (63.5)	0.044 (1.12)	0.141 (3.58)	0.560 (14.2)	100.0 (0.445)	142.4 (982)	16.7 (115)	96.2 (105.7)
	2TCBN7	0.281 (7.14)	2.509 (63.7)	0.053 (1.35)	0.130 (3.30)	0.555 (14.1)	82.4 (0.367)	116.9 (806)	19.4 (134)	78.2 (85.9)

Table 4-5: Test Results For 5Al-2.5 Sn (ELI) Titanium Surface Flawed Specimens Subjected to Pure Bending at -423F (20 K)

CONFIGURATION	SPECIMEN			FLAW SIZE		RESULTS		
	IDENTIFI- CATION	THICKNESS t IN. (mm)	WIDTH W IN (mm)	DEPTH a IN (mm)	LENGTH 2c IN. (mm)	MOMENT AT FRACTURE IN-LB. (JOULE)	MAXIMUM BENDING STRESS AT FRACTURE, $\sigma_B$ KSI (MN/m <sup>2</sup> )	$K_{cr}$ KSI $\sqrt{IN}$ (MN/m <sup>3/2</sup> )
	2TPBH-1	0.750 (19.1)	3.002 (76.3)	0.123 (3.12)	0.575 (14.6)	45,600 (5150)	162.3 (1119)	84.7 (93.1)
	2TPBH-2	0.753 (19.1)	3.003 (76.3)	0.125 (3.18)	0.565 (14.4)	47,175 (5330)	166.2 (1146)	86.5 (95.1)
	2TPBH-3	0.744 (18.9)	3.001 (76.2)	0.200 (5.08)	0.865 (22.0)	37,050 (4190)	133.8 (923)	75.4 (82.9)
	2TPBH-4	0.750 (19.1)	3.003 (76.3)	0.205 (5.21)	0.865 (22.0)	39,225 (4430)	139.3 (960)	78.7 (86.5)
	2TPBH-5	0.751 (19.1)	3.498 (88.9)	0.280 (7.11)	1.150 (29.2)	42,750 (4830)	130.0 (896)	74.2 (81.5)
	2TPBH-6	0.750 (19.1)	3.500 (88.9)	0.280 (7.11)	1.160 (29.5)	41,925 (4740)	127.8 (881)	73.1 (80.3)
	2TPBH-7	0.751 (19.1)	3.500 (88.9)	0.348 (8.84)	1.470 (37.3)	36,940 (4170)	112.6 (776)	63.2* (69.5)
	2TPBH-8	0.750 (19.1)	3.500 (88.9)	0.347 (8.81)	1.450 (36.8)	36,150 (4080)	110.2 (760)	62.1* (68.2)

\*W/2c  $\approx$  2.4 INADEQUATE WIDTH

Table 5-1: Test Program For Proof Test Temperature Effects on 2219-T87 Aluminum

SPECIMEN NUMBER	PROOF LOAD APPLIED AT			STATIC FRACTURE AT			CYCLIC FRACTURE AT			REMARKS
	72F (295K)	-320F (78K)	-423F (20K)	72F (295K)	-320F (78K)	-423F (20K)	72F (295K)	-320F (78K)	-423F (20K)	
6A-18						X				FOR FRACTURE TOUGHNESS
6A-1		P2		X						EFFECTS OF PROOF LOAD TEMPERATURES ON FRACTURE TOUGHNESS
6A-4	P1	P2		X						
6A-7			P3	X						
6A-10	P1		P3	X						
6A-13	P1									
6A-16	P1	P2			X					
6A-19	P1					X				
6A-22	P1		P3			X				
6A-2		P2					C1			EFFECTS OF PROOF LOAD TEMPERATURES ON CYCLIC LIFE AT 72F (295K)
6A-3		P2					C2			
6A-5	P1	P2					C1			
6A-25	P1	P2					C2			
6A-6	P1						C2			
6A-8			P3				C1			EFFECTS OF PROOF LOAD TEMPERATURES ON CYCLIC LIFE AT 72F (295K)
6A-9			P3				C2			
6A-11	P1		P3				C1			
6A-12	P1		P3				C2			
6A-14	P1							C3		EFFECTS OF PROOF LOAD TEMPERATURES ON CYCLIC LIFE AT -320F (78K)
6A-15	P1							C4		
6A-17	P1	P2						C3		
6A-26	P1	P2						C4		
6A-20	P1								C5	EFFECTS OF PROOF LOAD TEMPERATURES ON CYCLIC LIFE AT -423F (20K)
6A-21	P1								C6	
6A-23	P1		P3						C5	
6A-24	P1		P3						C6	



Table 5-2: Test Program For Proof Test Temperature Effects on 6Al-4V  $\beta$  STA Titanium

SPECIMEN NUMBER	PROOF LOAD APPLIED AT			STATIC FRACTURE		CYCLIC CONDITIONS AT			REMARKS
	72F (295K)	-320F (78K)	-423F (20K)	-320F (78K)	-423F (20K)	72F (295K)	-320F (78K)	-423F (20K)	
6T-1 6T-2 6T-33						C1 C2 C2			BASELINE CYCLIC DATA WITHOUT ANY PROOF LOAD EFFECTS
6T-3 6T-3A 6T-4 6T-32							C3 C3 C4 C4		
6T-30 6T-6								C5 C6	
6T-7 6T-8 6T-9 6T-31	P1 P1 P1 P1	P2		X X					
6T-11 6T-12 6T-13 6T-14		P2 P2 P2 P2				C1 C2 C1 C2			EFFECTS OF PROOF LOAD TEMPERATURES ON FLAW GROWTH CHARACTERISTICS AT 72F (295K)
6T-5 6T-27 6T-28 6T-10 6T-29			P3 P3 P3 P3 P3			C1 C1 C2 C1 C2			
6T-19 6T-20 6T-21 6T-22		P2 P2 P2 P2					C3 C4 C3 C4		EFFECTS OF PROOF LOAD TEMPERATURES ON FLAW GROWTH CHARACTERISTICS AT -320F (78K)
6T-23 6T-24 6T-25 6T-26			P3 P3 P3 P3					C5 C6 C5 C6	EFFECTS OF PROOF LOAD TEMPERATURES ON FLAW GROWTH CHARACTERISTICS AT -423F (20K)

FIGURE 5-3 PROOF TEST TEMPERATURE EFFECTS ON THE FLAW GROWTH CHARACTERISTICS OF 2219-T87 ALUMINUM

SPECIMEN			CYCLIC EXTENSION OF EDM FLAW @ R.T.		FLAW SIZE BEFORE PRELOAD		FIRST PRELOAD CYCLE			FLAW SIZE AFTER FIRST PRELOAD		SECOND PRELOAD CYCLE			FLAW SIZE AFTER SECOND PRELOAD		OPERATIONAL CONDITIONS TO FRACTURE									
IDENTIFICATION	THICKNESS, $t$ INCH (mm)	WIDTH, $w$ INCH (mm)	MAX. CYCLIC STRESS KSI (MN/m <sup>2</sup> )	NUMBER OF CYCLES	FLAW DEPTH, $a_1$ INCH (mm)	FLAW LENGTH, $2c_1$ INCH (mm)	TEMPERATURE OF $\sigma_1$ (°K)	MAX STRESS, $\sigma_1$ KSI (MN/m <sup>2</sup> )	STRESS INTENSITY, $K_{I1}$ KSI $\sqrt{IN.}$ (MN/m <sup>3/2</sup> )	FLAW DEPTH, $a_2$ INCH (mm)	FLAW LENGTH, $2c_2$ INCH (mm)	TEMPERATURE OF $\sigma_2$ (°K)	MAX STRESS, $\sigma_2$ KSI (MN/m <sup>2</sup> )	STRESS INTENSITY, $K_{I2}$ KSI $\sqrt{IN.}$ (MN/m <sup>3/2</sup> )	FLAW DEPTH, $a_3$ INCH (mm)	FLAW LENGTH, $2c_3$ INCH (mm)	TEMPERATURE OF $\sigma_{cr}$ (°K)	STATIC FAILURE STRESS, KSI (MN/m <sup>2</sup> )	MAX. CYCLIC STRESS, KSI (MN/m <sup>2</sup> )	NO. OF CYCLES TO FAILURE	FLAW DEPTH, $a_{cr}$ INCH (mm)	FLAW LENGTH, $2c_{cr}$ INCH (mm)	STRESS INTENSITY, $K_{Icr}$ KSI $\sqrt{IN.}$ (MN/m <sup>3/2</sup> )	STRESS INTENSITY, $K_{I1}$ KSI $\sqrt{IN.}$ (MN/m <sup>3/2</sup> )	RATIO, $K_{I1}/K_{Icr}$	
6A-18	0.604 (15.3)	4.999 (127)	12.0 (82.7)	16,000	0.232 (5.89)	0.838 (21.3)	← STATIC FRACTURE TOUGHNESS SPECIMEN →										-423 (20)	63.4 (437)	—	—	0.232 (5.89)	0.838 (21.3)	49.6 (54.5)	—	—	
6A-1	0.603 (15.3)	5.002 (127)	—	15,000	0.230 (5.84)	0.838 (21.3)	-320 (78)	53.8 (371)	41.4 (45.5)	0.236 (5.99)	0.838 (21.3)	—	—	—	—	—	ROOM	51.4 (354)	—	—	DELAMINATION	—	—	40.3 (44.3)	—	—
6A-2	0.602 (15.3)	4.999 (127)	—	16,000	0.222 (5.64)	0.832 (21.1)	-320 (78)	51.4 (354)	39.1 (43.0)	0.232 (5.89)	0.832 (21.1)	—	—	—	—	—	ROOM	—	40.6 (280)	1274	DELAMINATION	—	—	30.9 (34.0)	0.77	
6A-3	0.602 (15.3)	4.999 (127)	—	12,000	0.226 (5.74)	0.830 (21.1)	-320 (78)	55.8 (385)	42.9 (47.1)	0.232 (5.89)	0.830 (21.1)	—	—	—	—	—	ROOM	—	43.9 (303)	956	DELAMINATION	—	—	33.6 (36.9)	0.837	
6A-4	0.602 (15.3)	5.000 (127)	—	13,000	0.226 (5.74)	0.832 (21.1)	ROOM	47.5 (328)	36.5 (40.1)	DELAMINATION		-320 (78)	58.3 (402)	44.8 (49.2)	DELAMINATION		ROOM	51.8 (357)	—	—	DELAMINATION	—	—	39.8 (43.7)	—	—
6A-5	0.602 (15.3)	5.000 (127)	—	14,000	0.224 (5.69)	0.830 (21.1)	ROOM	47.5 (328)	36.4 (40.0)	DELAMINATION		-320 (78)	59.8 (412)	45.9 (50.4)	DELAMINATION		ROOM	—	40.6 (280)	1542	DELAMINATION	—	—	31.1 (34.2)	0.775	
6A-6	0.602 (15.3)	5.000 (127)	—	18,000	0.239 (6.07)	0.830 (21.1)	ROOM	47.5 (328)	36.8 (40.4)	DELAMINATION		—	—	—	—	—	ROOM	—	43.9 (303)	1073	DELAMINATION	—	—	34.0 (37.4)	0.846	
6A-25	0.600 (15.2)	5.000 (127)	—	17,000	0.230 (5.84)	0.832 (21.1)	ROOM	47.7 (329)	36.8 (40.4)	DELAMINATION		-320 (78)	58.5 (403)	45.2 (49.7)	DELAMINATION		ROOM	—	44.0 (303)	1138	DELAMINATION	—	—	33.9 (37.3)	0.845	
6A-7	0.605 (15.4)	5.000 (127)	—	16,000	0.239 (6.07)	0.830 (21.1)	-423 (20)	54.6 (376)	42.0 (46.2)	0.241 (6.12)	0.830 (21.1)	—	—	—	—	—	ROOM	51.8 (357)	—	—	DELAMINATION	—	—	40.6 (44.6)	—	—
6A-8	0.600 (15.2)	5.000 (127)	—	15,000	0.232 (5.89)	0.838 (21.3)	-423 (20)	55.0 (379)	42.3 (46.5)	0.238 (6.05)	0.838 (21.3)	—	—	—	—	—	ROOM	—	40.7 (281)	1946	DELAMINATION	—	—	31.2 (34.3)	0.777	
6A-9	0.605 (15.4)	5.001 (127)	—	14,000	0.228 (5.79)	0.832 (21.1)	-423 (20)	54.7 (377)	41.8 (45.9)	0.236 (5.99)	0.832 (21.1)	—	—	—	—	—	ROOM	—	43.7 (301)	1164	DELAMINATION	—	—	33.6 (36.9)	0.837	
6A-10	0.599 (15.2)	5.002 (127)	—	14,000	0.225 (5.72)	0.830 (21.1)	ROOM	47.7 (329)	36.7 (40.3)	DELAMINATION		-423 (20)	55.1 (380)	42.3 (46.5)	DELAMINATION		ROOM	52.3 (361)	—	—	DELAMINATION	—	—	40.2 (44.2)	—	—
6A-11	0.602 (15.3)	4.999 (127)	—	15,000	0.224 (5.69)	0.837 (21.3)	ROOM	47.7 (329)	36.7 (40.3)	DELAMINATION		-423 (20)	55.0 (379)	42.3 (46.5)	DELAMINATION		ROOM	—	40.6 (280)	1925	DELAMINATION	—	—	31.2 (34.3)	0.777	
6A-12	0.602 (15.3)	5.001 (127)	—	13,000	0.220 (5.59)	0.834 (21.2)	ROOM	47.5 (328)	36.5 (40.1)	DELAMINATION		-423 (20)	54.9 (379)	42.1 (46.3)	DELAMINATION		ROOM	—	43.9 (303)	1597	DELAMINATION	—	—	33.7 (37.0)	0.838	
6A-13	0.600 (15.2)	5.000 (127)	—	12,000	0.220 (5.59)	0.825 (21.0)	ROOM	48.0 (331)	36.7 (40.3)	DELAMINATION		—	—	—	—	—	-320 (78)	62.0 (427)	—	—	DELAMINATION	—	—	47.4 (52.1)	—	—
6A-14	0.601 (15.3)	5.000 (127)	—	11,000	0.226 (5.74)	0.832 (21.1)	ROOM	47.7 (329)	36.7 (40.3)	DELAMINATION		—	—	—	—	—	-320 (78)	—	42.7 (294)	1931	0.470 (11.94)	1.680 (42.7)	52.8 (58.7)	32.9 (36.2)	0.677	
6A-15	0.594 (15.1)	5.001 (127)	—	15,000	0.225 (5.74)	0.828 (21.0)	ROOM	48.5 (334)	37.3 (41.0)	DELAMINATION		—	—	—	—	—	-320 (78)	—	46.5 (321)	1067	DELAM.	1.730 (43.9)	—	35.8 (39.3)	0.737	
6A-16	0.598 (15.2)	5.000 (127)	—	16,000	0.224 (5.69)	0.835 (21.2)	ROOM	47.7 (329)	36.7 (40.3)	DELAMINATION		—	—	—	—	—	-320 (78)	61.2 (422)	—	—	DELAMINATION	—	—	47.1 (51.8)	—	—
6A-17	0.603 (15.3)	5.000 (127)	—	14,000	0.228 (5.74)	0.828 (21.0)	ROOM	47.5 (328)	36.5 (40.1)	DELAMINATION		-320 (78)	57.9 (399)	44.5 (48.9)	GROWTH ON SIDES		-320 (78)	—	42.5 (293)	2101	0.425 (10.80)	1.700 (43.2)	49.7 (54.6)	32.7 (35.9)	0.673	
6A-26	0.598 (15.2)	5.001 (127)	—	16,000	0.230 (5.84)	0.825 (21.0)	ROOM	47.7 (329)	36.7 (40.3)	DELAMINATION		-320 (78)	58.7 (405)	45.2 (49.7)	GROWTH ON SIDES		-320 (78)	—	46.2 (319)	889	0.410 (10.41)	1.45 (36.8)	50.2 (55.2)	35.5 (39.0)	0.731	
6A-19	0.603 (15.3)	5.000 (127)	—	13,000	0.220 (5.59)	0.825 (21.0)	ROOM	47.5 (328)	36.3 (39.9)	DELAMINATION		—	—	—	—	—	-423 (20)	66.1 (456)	—	—	DELAMINATION	—	—	50.5 (55.5)	—	—
6A-20	0.591 (15.0)	5.001 (127)	—	13,000	0.220 (5.59)	0.830 (21.1)	ROOM	48.4 (334)	37.1 (40.8)	DELAMINATION		—	—	—	—	—	-423 (20)	—	51.7 (356)	328	@	1.12 (28.4)	—	39.6 (43.5)	0.799	
6A-21	0.597 (15.2)	5.000 (127)	—	16,000	0.228 (5.74)	0.830 (21.1)	ROOM	48.0 (331)	37.0 (40.7)	DELAMINATION		—	—	—	—	—	-423 (20)	—	47.0 (324)	811	@	1.10 (27.9)	—	35.2 (39.8)	0.730	
6A-22	0.602 (15.3)	5.000 (127)	—	15,500	0.221 (5.61)	0.830 (21.1)	ROOM	47.7 (329)	36.5 (40.1)	DELAMINATION		-423 (20)	55.0 (379)	42.1 (46.3)	DELAMINATION		-423 (20)	65.8 (454)	—	—	DELAMINATION	—	—	50.4 (55.4)	—	—
6A-23	0.604 (15.3)	5.000 (127)	—	12,000	0.220 (5.59)	0.830 (21.1)	ROOM	47.5 (328)	36.3 (39.9)	DELAMINATION		-423 (20)	54.8 (378)	41.9 (46.0)	DELAMINATION		-423 (20)	—	50.6 (349)	481	@	1.20 (30.5)	—	38.7 (42.5)	0.780	
6A-24	0.600 (15.2)	5.001 (127)	12.0 (82.7)	12,000	0.220 (5.59)	0.835 (21.2)	ROOM	47.7 (329)	36.6 (40.2)	DELAMINATION		-423 (20)	55.1 (380)	42.3 (46.5)	DELAMINATION		-423 (20)	—	46.7 (322)	887	0.425 (10.80)	1.25 (31.8)	47.8 (52.5)	36.7 (40.3)	0.740	

\*FOR CASES OF DELAMINATIONS, LAST MEASURED FLAW DIMENSIONS ARE USED FOR  $K_{I2}$  AND  $K_{Icr}$  CALCULATIONS.  
 \*\*  $K_{I1}$  - CALCULATED FROM MAX CYCLIC STRESS AND LAST MEASURABLE FLAW DIMENSIONS ( $a_1, 2c_1$ ; OR  $a_2, 2c_2$ )  
 \*\*\*AV.  $K_{Icr}$  @ R.T. = 40.2 KSI  $\sqrt{IN.}$  (44.2 MN/m<sup>3/2</sup>) FROM STATIC TESTS; AV  $K_{Icr}$  @ -320°F (78°K) = 48.6 KSI  $\sqrt{IN.}$  (53.4 MN/m<sup>3/2</sup>) FROM STATIC AND CYCLIC TESTS;  $K_{Icr}$  = 49.6 KSI  $\sqrt{IN.}$  (54.5 MN/m<sup>3/2</sup>) FROM STATIC AND CYCLIC TEST @ -423°F (20°K)  
 @ NOT CLEARLY DETECTABLE.

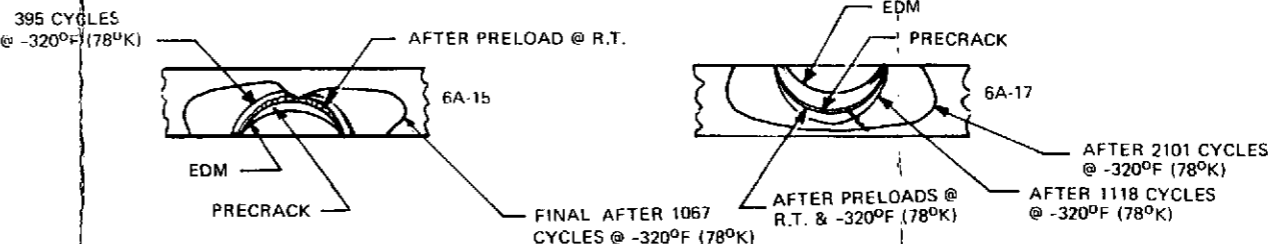


Table 5-4: Fracture Toughness Data For 6Al-4V  $\beta$  STA Titanium

SPECIMEN			FATIGUE CRACK EXTENSION AT ROOM TEMP.					FRACTURE TEST RESULTS				
IDENTIFICATION	THICKNESS, t INCH (mm)	WIDTH, W INCH (mm)	MAXIMUM FATIGUE STRESS KSI (MN/m <sup>2</sup> )	STRESS RATIO, R ( $\sigma_{MIN}/\sigma_{MAX}$ )	TOTAL NUMBER OF CYCLES, N	FLAW DEPTH, a INCH (mm)	FLAW LENGTH, 2c INCH (mm)	TEMPERATURE $\sigma_F$ (°K)	ENVIRONMENT	GROSS AREA STRESS, $\sigma_G$ KSI (MN/m <sup>2</sup> )	$K_{Ic}$ KSI $\sqrt{IN}$ (MN/m <sup>3/2</sup> )	AVG $K_{Ic}$ KSI $\sqrt{IN}$ (MN/m <sup>3/2</sup> )
6BTR -1	0.301 (7.65)	1.998 (50.7)	30.0 (207)	0.25	3000	0.143 (3.63)	0.595 (15.1)	72 (295)	AIR	87.8 (605)	55.3 (60.8)	56.9 (62.5)
6BTR -2	0.301 (7.65)	1.998 (50.7)	30.0 (207)	0.25	3000	0.134 (3.40)	0.591 (15.0)	72 (295)	AIR	94.3 (650)	58.5 (64.3)	
6BTN -1	0.203 (5.11)	1.201 (30.5)	35.0 (241)	0.50	12,000	0.084 (2.13)	0.352 (8.94)	-320 (78)	LN <sub>2</sub>	116.2 (801)	55.4 (60.9)	52.8 (58.0)
6BTN -2	0.204 (5.18)	1.199 (30.5)	35.0 (241)	0.50	13,000	0.091 (2.31)	0.362 (9.19)	-320 (78)	LN <sub>2</sub>	102.7 (708)	50.2 (55.2)	
6BTH -1	0.203 (5.16)	1.199 (30.5)	35.0 (241)	0.50	12,000	0.050 (1.27)	0.220 (5.59)	-423 (20)	LH <sub>2</sub>	120.2 (829)	43.9 (48.2)	44.9 (49.3)
6BTH -2	0.198 (5.03)	1.199 (30.5)	35.0 (241)	0.50	18,000	0.047 (1.19)	0.215 (5.46)	-423 (20)	LH <sub>2</sub>	127.9 (882)	45.9 (50.4)	

FIGURE 5-5 PROOF TEST TEMPERATURE EFFECTS ON THE FLAW GROWTH CHARACTERISTICS OF 6Al-4V-βSTA TITANIUM

IDENTIFICATION	SPECIMEN		CYCLIC EXTENSION OF EDM FLAW AT R.T.		FLAW SIZE BEFORE PRELOAD		FIRST PRELOAD CYCLE		FLAW SIZE AFTER FIRST PRELOAD		SECOND PRELOAD CYCLE		FLAW SIZE AFTER SECOND PRELOAD		OPERATIONAL CYCLIC CONDITIONS						MARKING AT R.T.		AFTER MARKING		STATIC FRACTURE CONDITIONS						
	THICKNESS, t INCH (mm)	WIDTH, W INCH (mm)	MAX CYCLIC STRESS (KSI)	NUMBER OF CYCLES (X 1000)	FLAW DEPTH, a <sub>1</sub> , INCH (mm)	FLAW LENGTH, 2c <sub>1</sub> , INCH (mm)	TEMPERATURE, σ <sub>F</sub> (°K)	MAX STRESS, σ <sub>1</sub> KSI (MN/m <sup>2</sup> )	STRESS INTENSITY, K <sub>11</sub> , KSI √IN. (MN/m <sup>3/2</sup> )	FLAW DEPTH, a <sub>2</sub> , INCH (mm)	FLAW LENGTH, 2c <sub>2</sub> , INCH (mm)	TEMPERATURE (°K)	MAX STRESS, σ <sub>2</sub> KSI (MN/m <sup>2</sup> )	STRESS INTENSITY, K <sub>12</sub> , KSI √IN. (MN/m <sup>3/2</sup> )	FLAW DEPTH, a <sub>3</sub> , INCH (mm)	FLAW LENGTH, 2c <sub>3</sub> , INCH (mm)	TEMPERATURE (°K)	MAX CYCLIC STRESS, σ <sub>3</sub> KSI (MN/m <sup>2</sup> )	NUMBER OF CYCLES APPLIED	FINAL FLAW DEPTH, a <sub>f</sub> , INCH (mm)	FINAL FLAW LENGTH, 2c <sub>f</sub> , INCH (mm)	STRESS INTENSITY, K <sub>13</sub> , KSI √IN. (MN/m <sup>3/2</sup> )	STRESS INTENSITY, K <sub>1f</sub> , KSI √IN. (MN/m <sup>3/2</sup> )	MAX CYCLIC STRESS, KSI (MN/m <sup>2</sup> )	NUMBER OF CYCLES (X 1000)	CRITICAL FLAW DEPTH, a <sub>cr</sub> , INCH (mm)	CRITICAL FLAW LENGTH, (2c) <sub>cr</sub> , INCH (mm)	TEMPERATURE (°K)	STATIC FRACTURE STRESS, σ <sub>cr</sub> KSI (MN/m <sup>2</sup> )	STRESS INTENSITY, K <sub>1cr</sub> , KSI √IN. (MN/m <sup>3/2</sup> )	
6T-1	0.205 (5.21)	1.100 (27.9)	40.0 (276)	22.0	0.019 (0.48)	0.105 (2.67)	—	—	—	—	—	—	—	—	—	R.T.	122.3 (843)	160	0.028 (0.71)	0.105 (2.67)	30.2 (33.2)	32.8 (36.0)	—	—	—	—	—	—	R.T.	169.8 (1170)	—
6T-2	0.199 (5.05)	1.104 (28.0)	—	15.0	0.018 (0.46)	0.103 (2.62)	—	—	—	—	—	—	—	—	—	R.T.	110.4 (761)	2083	0.050 (1.27)	0.128 (3.25)	26.5 (29.1)	33.6 (36.9)	—	—	—	—	—	—	R.T.	167.4 (1154)	—
6T-3	0.204 (5.18)	1.100 (27.9)	—	19.0	0.017 (0.43)	0.099 (2.51)	—	—	—	—	—	—	—	—	—	-320 (78)	155.8 (1074)	294	0.029 (0.74)	0.103 (2.62)	36.4 (40.0)	41.3 (45.4)	—	—	—	—	—	—	R.T.	169.1 (1166)	—
6T-3A	0.202 (5.13)	0.804 (20.4)	—	19.0	0.018 (0.46)	0.106 (2.69)	—	—	—	—	—	—	—	—	—	-320 (78)	159.0 (1096)	370	0.060* (1.52)	0.142** (3.60)	38.4 (42.2)	50.9 (55.9)	—	—	—	—	—	—	-320 (78)	160.6 (1107)	51.4 (56.5)
6T-4	0.201 (5.11)	0.803 (20.4)	—	16.0	0.018 (0.46)	0.104 (2.64)	—	—	—	—	—	—	—	—	—	-320 (78)	138.0 (952)	600*	0.040* (1.02)	0.130 (3.30)	32.8 (36.0)	41.2 (45.3)	—	—	—	—	—	—	—	—	
6T-30	0.203 (5.16)	0.901 (22.9)	—	30.0	0.016 (0.41)	0.110 (2.79)	—	—	—	—	—	—	—	—	—	-423 (20)	138.2 (953)	51	0.077 (1.96)	0.131 (3.33)	31.7 (34.8)	41.4 (45.5)	50.0 (345)	16.0	0.110 (2.79)	0.228 (5.79)	R.T.	140.4 (968)	58.1 (63.9)		
6T-6	0.201 (5.11)	0.706 (17.9)	—	18.0	0.021 (0.53)	0.096 (2.44)	—	—	—	—	—	—	—	—	—	-423 (20)	118.0 (814)	192	0.086 (2.18)	0.176 (4.47)	28.2 (31.0)	41.2 (45.3)	50.0 (345)	4.0	0.098 (2.51)	0.206 (5.23)	R.T.	132.2 (912)	51.4 (56.5)		
6T-7	0.201 (5.11)	0.804 (20.4)	—	18.0	0.020 (0.51)	0.097 (2.46)	R.T.	141.0 (972)	35.2 (38.7)	0.020 (0.51)	0.097 (2.46)	—	—	—	—	—	—	—	—	—	—	—	—	—	—	—	—	-320 (78)	234.2 (1615)	—	
6T-8	0.199 (5.05)	0.805 (20.4)	—	21.0	0.022 (0.56)	0.096 (2.44)	R.T.	141.0 (972)	35.8 (39.3)	0.022 (0.56)	0.096 (2.44)	-320 (78)	180.0 (1241)	45.0 (49.5)	0.022 (0.56)	0.096 (2.44)	—	—	—	—	—	—	—	—	—	—	—	-320 (78)	203.9 (1406)	51.8 (56.9)	
6T-9	0.203 (5.16)	0.700 (17.8)	—	18.0	0.019 (0.48)	0.098 (2.49)	R.T.	141.0 (972)	34.9 (38.4)	0.019 (0.48)	0.098 (2.49)	—	—	—	—	—	—	—	—	—	—	—	—	—	—	—	-423 (20)	226.1 (1559)	55.3 (60.8)		
6T-31	0.195 (4.95)	0.904 (23.0)	—	30.0	0.022 (0.56)	0.110 (2.79)	R.T.	141.6 (976)	37.4 (41.1)	0.022 (0.56)	0.110 (2.79)	-423 (20)	165.3 (1140)	42.0 (46.2)	0.022 (0.56)	0.110 (2.79)	—	—	—	—	—	—	—	—	—	—	-423 (20)	200.2 (1380)	51.5 (56.7)		
6T-15	0.202 (5.13)	0.906 (23.0)	—	20.0	0.020 (0.51)	0.105 (2.67)	-423 (20)	162.7 (1122)	39.8 (43.7)	0.020 (0.51)	0.105 (2.67)	—	—	—	—	—	—	—	—	—	—	—	—	50.0 (345)	30.0	0.037 (0.94)	0.115 (2.92)	R.T.	168.0 (1158)	—	
6T-16	0.202 (5.13)	0.909 (23.1)	—	18.0	0.020 (0.51)	0.102 (2.59)	-423 (20)	162.3 (1119)	39.4 (43.3)	0.020 (0.51)	0.105 (2.67)	—	—	—	—	—	—	—	—	—	—	—	—	50.0 (345)	25.0	0.060 (1.52)	0.123 (3.12)	R.T.	164.0 (1131)	—	
6T-17	0.202 (5.13)	0.901 (22.9)	—	20.0	0.018 (0.46)	0.102 (2.59)	R.T.	141.0 (972)	34.8 (38.2)	0.018 (0.46)	0.102 (2.59)	-423 (20)	164.0 (1131)	38.8 (42.6)	0.018 (0.46)	0.102 (2.59)	—	—	—	—	—	—	—	—	50.0 (345)	140.0	0.048 (1.17)	0.113 (2.87)	R.T.	167.4 (1154)	—
6T-18	0.201 (5.11)	0.903 (22.9)	—	23.0	0.018 (0.46)	0.105 (2.67)	R.T.	141.0 (972)	35.0 (38.5)	0.018 (0.46)	0.105 (2.67)	-423 (20)	164.4 (1134)	39.1 (43.0)	0.018 (0.46)	0.105 (2.67)	—	—	—	—	—	—	—	—	50.0 (345)	100.0	0.042 (1.07)	0.120 (3.05)	R.T.	165.7 (1143)	—
6T-11	0.201 (5.11)	0.905 (23.0)	—	19.0	0.017 (0.43)	0.102 (2.59)	-320 (78)	180.0 (1241)	43.0 (47.3)	0.017 (0.43)	0.102 (2.59)	—	—	—	—	—	R.T.	125.0 (862)	693	0.031 (0.79)	0.108 (2.74)	29.8 (32.8)	34.4 (37.8)	—	—	—	—	—	R.T.	175.3 (1209)	—
6T-12	0.201 (5.11)	0.905 (23.0)	—	18.0	0.016 (0.41)	0.102 (2.59)	-320 (78)	180.0 (1241)	42.2 (46.4)	0.016 (0.41)	0.102 (2.59)	—	—	—	—	—	R.T.	110.0 (758)	2962	0.110 (2.79)	0.264 (6.71)	25.4 (27.9)	48.8 (53.6)	—	—	—	—	—	R.T.	131.9 (909)	59.3 (65.2)
6T-13	0.202 (5.13)	0.902 (22.9)	—	15.0	0.017 (0.43)	0.098 (2.49)	R.T.	141.0 (972)	33.9 (37.3)	0.017 (0.43)	0.098 (2.49)	-320 (78)	180.0 (1241)	42.6 (46.8)	0.017 (0.43)	0.098 (2.49)	R.T.	125.0 (862)	1217	0.041 (1.04)	0.115 (2.92)	29.6 (32.5)	35.2 (39.8)	—	—	—	—	—	R.T.	169.5 (1189)	—
6T-14	0.207 (5.26)	0.901 (22.9)	—	17.5	0.020 (0.51)	0.100 (2.54)	R.T.	141.0 (972)	35.5 (39.0)	0.020 (0.51)	0.100 (2.54)	-320 (78)	180.0 (1241)	44.6 (49.0)	0.020 (0.51)	0.100 (2.54)	R.T.	110.0 (758)	3862	0.132 (3.35)	0.316 (8.03)	27.0 (29.7)	54.8 (60.2)	—	—	—	—	—	R.T.	116.0 (800)	57.9 (63.6)
6T-5	0.202 (5.13)	0.704 (17.9)	—	17.0	0.018 (0.46)	0.097 (2.46)	-423 (20)	163.5 (1127)	38.2 (42.0)	0.018 (0.46)	0.097 (2.46)	—	—	—	—	—	R.T.	125.0 (862)	1761	0.124 (3.15)	0.240 (6.10)	29.9 (32.9)	53.0 (58.2)	—	—	—	—	—	R.T.	135.0 (931)	57.6 (63.3)
6T-27	0.202 (5.13)	0.898 (22.8)	—	29.0	0.018 (0.46)	0.103 (2.62)	-423 (20)	164.5 (1134)	39.0 (42.9)	0.018 (0.46)	0.103 (2.62)	—	—	—	—	—	R.T.	125.0 (862)	1998	0.136 (3.45)	0.290 (7.37)	30.4 (33.4)	59.8 (65.7)	—	—	—	—	—	R.T.	131.5 (907)	63.2 (69.5)
6T-28	0.202 (5.13)	0.904 (23.0)	—	20.0	0.019 (0.48)	0.105 (2.67)	-423 (20)	163.6 (1128)	39.5 (43.4)	0.019 (0.48)	0.105 (2.67)	—	—	—	—	—	R.T.	110.0 (758)	1100	0.050 (1.27)	0.135 (3.43)	26.9 (29.6)	34.3 (37.7)	—	—	—	—	—	R.T.	164.6 (1135)	—
6T-10	0.202 (5.13)	0.700 (17.0)	—	20.0	0.019 (0.48)	0.100 (2.54)	R.T.	141.0 (972)	35.1 (38.6)	0.019 (0.48)	0.100 (2.54)	-423 (20)	164.1 (1131)	39.2 (43.1)	0.019 (0.48)	0.100 (2.54)	R.T.	125.0 (862)	1974	0.122 (3.10)	0.270 (6.86)	30.6 (33.6)	56.9 (62.5)	—	—	—	—	—	R.T.	131.8 (909)	60.2 (66.2)
6T-29	0.203 (5.16)	0.901 (22.9)	—	30.0	0.020 (0.51)	0.104 (2.64)	R.T.	141.0 (972)	35.9 (39.5)	0.020 (0.51)	0.104 (2.64)	-423 (20)	169.4 (1134)	41.5 (45.6)	0.020 (0.51)	0.104 (2.64)	R.T.	110.0 (758)	3034	0.120 (3.05)	0.330 (8.38)	27.2 (29.9)	55.4 (60.9)	—	—	—	—	—	R.T.	118.3 (816)	59.9 (65.8)
6T-19	0.201 (5.11)	0.806 (20.5)	—	19.0	0.023 (0.58)	0.104 (2.64)	-320 (78)	180.0 (1241)	46.5 (51.1)	0.023 (0.58)	0.104 (2.64)	—	—	—	—	—	-320 (78)	159.0 (1096)	339	0.044 (1.12)	0.118 (3.00)	40.6 (44.6)	46.3 (50.9)	—	—	—	—	-320 (78)	176.3 (1216)	51.7 (56.8)	
6T-20	0.202 (5.13)	0.801 (20.3)	—	17.5	0.021 (0.53)	0.105 (2.67)	-320 (78)	180.0 (1241)	45.7 (50.2)	0.021 (0.53)	0.105 (2.67)	—	—	—	—	—	-320 (78)	138.0 (952)	812	0.053 (1.35)	0.129 (3.28)	34.2 (37.6)	41.8 (45.9)	—	—	—	—	—	R.T.	168.3 (1160)	—
6T-21	0.201 (5.11)	0.802 (20.4)	—	16.0	0.020 (0.51)	0.107 (2.72)	R.T.	141.0 (972)	36.1 (39.7)	0.020 (0.51)	0.107 (2.72)	-320 (78)	180.0 (1241)	45.4 (49.9)	0.020 (0.51)	0.107 (2.72)	-320 (78)	159.0 (1096)	618*	0.068 (1.73)	0.163 (4.14)	39.6 (43.5)	54.6 (60.0)	—	—	—	—	-320 (78)	—	54.6 (60.0)	
6T-22	0.202 (5.13)	0.808 (20.5)	—	17.0	0.020 (0.51)	0.104 (2.64)	R.T.	141.0 (972)	35.9 (39.5)	0.020 (0.51)	0.104 (2.64)	-320 (78)	180.0 (1241)	45.0 (49.5)	0.020 (0.51)	0.104 (2.64)	-320 (78)	138.0 (952)	909	0.050 (1.27)	0.132 (3.35)	33.7 (37.0)	42.3 (46.5)	—	—	—	—	—	-320 (78)	162.9 (1123)	50.3 (55.3)
6T-23	0.201 (5.11)	0.898 (17.7)	—	18.0	0.022 (0.56)	0.106 (2.69)	-423 (20)	165.6 (1142)	41.7 (45.8)	0.022 (0.56)	0.106 (2.69)	—	—	—	—	—	-423 (20)	138.3 (954)	52	0.072 (1.83)	0.143 (3.63)	34.5 (37.9)	43.4 (47.7)	50.0 (345)	3.0	0.102 (2.59)	0.210 (5.33)	R.T.	141.2 (974)	55.8 (61.3)	
6T-24	0.200 (5.08)	0.707 (18.0)	—	16.5	0.020 (0.51)	0.103 (2.62)	-423 (20)	164.0 (1131)	40.0 (44.0)	0.020 (0.51)	0.103 (2.62)	—	—	—	—	—	-423 (20)	118.8 (819)	171	0.082 (2.08)	0.166 (4.22)	28.5 (31.3)	40.1 (44.1)	50.0 (345)	4.0	0.110 (2.79)	0.238 (6.05)	R.T.	123.7 (853)	52.1 (57.3)	
6T-25	0.203 (5.16)	0.705 (17.9)	—	25.0	0.021 (0.53)	0.105 (2.69)	R.T.	141.0 (972)	36.5 (40.1)	0.021 (0.53)	0.106 (2.69)	-423 (20)	161.8 (1116)	40.2 (44.2)	0.021 (0.53)	0.106 (2.69)	-423 (20)	135.3 (933)	327	0.074 (1.88)	0.135 (3.43)	33.3 (36.6)	41								

Table 6-1: Test Program for Evaluating Effects of Combined Modes I-II Loading On Fracture in 4340 Steel

SPECIMEN CONFIGURATION	TEST TEMP.	CRACK TYPE	TEST VARIABLES			
			LOADING	2a/W	$\phi$ DEGREES (RADIANS)	NO. OF TESTS
FIGURE 6-3	-200 F (144K) GN <sub>2</sub> ENVIRONMENT	INCLINED CENTER CRACK	UNIFORM TENSION	0.5	0 (0.0)	2
					25 (0.44)	2
					50 (0.87)	2
					75 (1.31)	2
FIGURE 6-4	ROOM TEMP	THROUGH CRACKED TUBE	PURE TORSION	—	—	2

Table 6-2: Test Program for Evaluating Combined Modes I-III Loading Effects On Fracture in 4340 Steel

SPECIMEN CONFIGURATION	TEST TEMP.	CRACK TYPE	TEST VARIABLES			
			LOADING	d/D	$K_I/K_{III}$	NO. OF TESTS
FIGURE 6-5	72 F (295K)	CIRCUMFERENTIAL CRACK	TENSION	0.5 ~ 0.6	1:0	2
			TENSION AND TORSION		2:1	2
					1:1	2
					1:2	2
			TORSION		0:1	2

Table 6-3: Test Program for Evaluating Combined Modes I-II-III Loading Effects On Fracture in 4340 Steel With Surface Flawed Flat Specimens

SPECIMEN CONFIGURATION	TEST TEMP.	CRACK TYPE	TEST VARIABLES				
			LOADING	a/t	a/2c	$\phi$ DEGREES (RADIAN)	NO. OF SPECIMENS
FIGURE 6-6	-200 F (144K) GN <sub>2</sub> ENVIRONMENT	SURFACE FLAW IN A FLAT PLATE	TENSION	0.5~0.6	0.25	0 (0.0)	2
						25 (0.44)	2
						45 (0.79)	2
						60 (1.05)	2

*Table 6-4: Test Program for Evaluating Combined Modes I-II-III Loading Effects On Fracture in 4340 Steel With Surface Flawed Round Specimens*

SPECIMEN CONFIGURATION	TEST TEMP.	CRACK TYPE	TEST VARIABLES				
			LOADING	a/D	a/2C	$\frac{\sigma_{TENSION}}{\tau_{SHEAR}}$	NO. OF TESTS
FIGURE 6-7	72 F (295K)	SURFACE FLAW IN A ROUND SPECIMEN	TENSION	0.3	0.4	1:0	3
			TENSION AND TORSION			1:1	2
						1:2	2
						1:3	2
			TORSION			0:1	1



Table 6-5: Static Fracture Toughness Test Results for 4340 Steel for Various Crack Propagation Directions

SPECIMEN					ENVIRONMENT		CRACK DEPTH $a$ , IN. (mm)	CRACK LENGTH $2c$ (2a), IN. (mm)	GROSS FRACTURE STRESS $\sigma$ , KSI (MN/m <sup>2</sup> )	FRACTURE TOUGHNESS $K_{Ic}$ OR $K_{Ic}$ KSI $\sqrt{IN.}$ (MN/m <sup>3/2</sup> )	AVERAGE FRACTURE TOUGHNESS $K_{Ic}$ OR $K_{Ic}$ KSI $\sqrt{IN.}$ (MN/m <sup>3/2</sup> )
IDENTIFICATION	CONFIGURATION	CRACK PROPAGATION DIRECTION	THICKNESS $t$ , IN. (mm)	WIDTH $W$ , IN. (mm)	MEDIUM	TEMPERATURE $\phi F$ ( $^{\circ}K$ )					
3RSF-1	SURFACE FLAW FIG. 6-21	LS	0.2510 (6.38)	1.8023 (45.8)	AIR	RT	0.123 (3.12)	0.482 (12.2)	124.7 (860)	71.5 (78.6)	72.2 (79.3)
3RSF-2	SURFACE FLAW FIG. 6-21	LS	0.2510 (6.38)	1.8029 (45.8)	AIR	RT	0.138 (3.51)	0.490 (12.4)	125.3 (864)	73.7 (81.0)	
3RSF-5	SURFACE FLAW FIG. 6-6	LS	0.2496 (6.34)	2.0089 (51.0)	AIR	RT	0.130 (3.30)	0.510 (13.0)	120.0 (827)	71.3 (78.4)	
3RCC-1	CENTER CRACK FIG. 6-21	LT	0.2505 (6.36)	1.5011 (38.1)	AIR	RT	—	0.760 (19.3)	59.8 (412)	77.3 (85.0)	73.9 (81.2)
3RCC-2	CENTER CRACK FIG. 6-21	LT	0.2510 (6.38)	1.5005 (38.1)	AIR	RT	—	0.770 (19.6)	53.4 (368)	70.5 (77.5)	
3LSF-1	SURFACE FLAW FIG. 6-6	LS	0.2480 (6.30)	2.0026 (50.9)	GN <sub>2</sub>	-200 (144)	0.140 (3.56)	0.605 (15.4)	59.8 (412)	37.0 (40.7)	40.1 (44.1)
3LSF-2	SURFACE FLAW FIG. 6-6	LS	0.2521 (6.40)	2.0020 (50.9)			0.140 (3.56)	0.590 (15.0)	70.2 (484)	43.2 (47.5)	
3TSF-1	SURFACE FLAW FIG. 6-6	TS	0.2523 (6.41)	2.0032 (50.9)			0.136 (3.45)	0.595 (15.1)	65.3 (450)	39.9 (43.9)	40.6 (44.6)
3TSF-2	SURFACE FLAW FIG. 6-6	TS	0.2446 (6.21)	2.0036 (50.9)			0.120 (3.05)	0.510 (13.0)	72.4 (499)	41.4 (45.5)	
3LCC-1	CENTER CRACK FIG. 6-3	LT	0.2532 (6.43)	1.4957 (38.0)	GN <sub>2</sub>	-200 (144)	—	0.748 (19.0)	33.0 (228)	42.5 (46.7)	41.6 (45.7)
3LCC-2	CENTER CRACK FIG. 6-3	LT	0.2560 (6.50)	1.5012 (38.1)			—	0.760 (19.3)	31.4 (217)	40.8 (44.8)	

Table 6-6: Static Fracture Test Data from Combined Mode I-II Inclined Center Cracked Specimens of 4340 Steel

SPECIMEN					PRECRACKING AT 72 F (295K)				FRACTURE TESTS & RESULTS AT-200 F(144K)		
NUMBER	THICKNESS, t IN. (mm)	WIDTH, W IN. (mm)	MACHINED NOTCH LENGTH IN. (mm)	ANGLE, $\phi$ (FIG. 6-3) DEGREE (RADIAN)	MAX. FATIGUE STRESS KSI (MN/m <sup>2</sup> )	STRESS RATIO, R ( $\sigma_{MIN}/\sigma_{MAX}$ )	TOTAL NUMBER OF CYCLES	CRACK LENGTH, 2a, IN. (mm)	GROSS FRACTURE STRESS, $\sigma$ KSI (MN/m <sup>2</sup> )	MODE I STRESS INTENSITY, K <sub>I</sub> KSI $\sqrt{IN.}$ (MN/m <sup>3/2</sup> )	MODE II STRESS INTENSITY, K <sub>II</sub> KSI $\sqrt{IN.}$ (MN/m <sup>3/2</sup> )
3LCC-1	0.253 (6.43)	1.500 (38.1)	0.50 (12.7)	0 (0.0)	25.0 (172)	0.7	40,000	.748 (19.0)	33.0 (228)	42.5 (46.7)	0.0
3LCC-2	0.256 (6.50)	1.501 (38.1)	↑	0 (0.0)	35.0 (241)	0.5	34,000	.760 (19.3)	31.4 (217)	40.8 (44.8)	0.0
3LCC-3	0.256 (6.50)	1.497 (38.0)		25 (0.44)	25.0 (172)	0.4	32,000	.700 (17.8)	30.5 (210)	30.9 (33.9)	12.8 (14.1)
3LCC-4	0.252 (6.40)	1.498 (38.0)		25 (0.44)	30.0 (207)	0.3	25,000	.760 (19.3)	27.5 (190)	29.8 (32.7)	12.2 (13.4)
3LCC-5	0.255 (6.48)	1.502 (38.1)	↓	50 (0.87)	20.0 (138)	0.27	28,000	.660 (16.8)	47.0 (324)	23.1 (25.4)	25.1 (27.6)
3LCC-6	0.256 (6.50)	1.501 (38.1)		50 (0.87)	20.0 (138)	0.27	38,500	.630 (16.0)	38.2 (263)	18.0 (19.8)	19.7 (21.7)
3LCC-7	0.254 (6.45)	1.500 (38.1)		75 (1.31)	20.0 (138)	0.27	40,000	.790 (20.1)	110.1 (759)	10.5 (11.5)	35.0 (38.4)
3LCC-8	0.256 (6.50)	1.472 (37.4)	0.50 (12.7)	75 (1.31)	20.0 (138)	0.27	37,000	.690 (17.5)	115.2 (794)	9.9 (10.9)	33.7 (36.9)

Table 6-7: Fracture Testing of 4340 Steel Hollow Tubes Containing Through Cracks In Pure Torsion

SPECIMEN			FATIGUE CRACK EXTENSION AT ROOM TEMPERATURE				FRACTURE TEST RESULTS					
IDENTIFICATION	TEST SECTION OUTSIDE DIAMETER $d_o$ , INCH (mm)	TEST SECTION INSIDE DIAMETER $d_i$ , INCH (mm)	MAXIMUM CYCLIC STRESS, KSI (MN/m <sup>2</sup> )	STRESS RATIO ( $\sigma_{MIN}/\sigma_{MAX}$ )	NUMBER OF CYCLES	CRACK LENGTH $2a$ , INCH (mm)	TEMPERATURE $\phi_F$ (°K)	TEST ENVIRONMENT	TORQUE AT FRACTURE, $T_F$ IN.-LB (JOULE)	TORQUE AT POP-IN, $T_P$ IN.-LB (JOULE)	MODE II STRESS INTENSITY AT POP-IN, $K_{II}$ KSI $\sqrt{IN.}$ (MN/m <sup>3/2</sup> )	MODE II STRESS INTENSITY AT FRACTURE, $K_{IIc}$ KSI $\sqrt{IN.}$ (MN/m <sup>3/2</sup> )
TUBE A	0.903 (22.9)	0.706 (17.9)	20 (138)	0.06	43,000	0.280 (7.11)	72 (295)	AIR	9375 (1060)	11,250 (1270)	65.5 (72.0)	78.5 (86.3)
TUBE B	0.900 (22.9)	0.710 (18.0)	20 (138)	0.06	34,000	0.292 (7.42)	72 (295)	AIR	9200 (1040)	11,250 (1270)	67.5 (74.2)	82.4 (90.6)

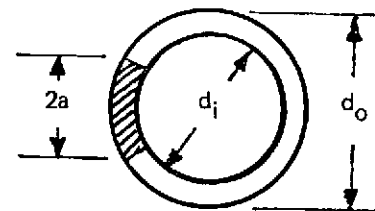


Table 6-8: Fracture Data From Combined Mode I-III Tests of Round Notched Bar Specimens of 4340 Steel

SPECIMEN			PRECRACKING AT 72 F (295K)						FRACTURE RESULTS AT 72 F (295K)				
IDENTIFICATION	DIAMETER OF BAR D, IN. (mm)	DIAMETER OF NOTCH d <sub>1</sub> IN. (mm)	MAX. TENSION FATIGUE STRESS (BASED ON d <sub>1</sub> ) KSI, (MN/m <sup>2</sup> )	STRESS RATIO (σ <sub>MIN</sub> /σ <sub>MAX</sub> )	NUMBER OF CYCLES	MIN. DIAMETER AT CRACKED SECTION, d, IN. (mm)	MAX. FATIGUE CRACK DEPTH, IN. (mm)	MIN. FATIGUE CRACK DEPTH, IN. (mm)	APPROXIMATE LOADING RATIO, P/T	FRACTURE LOAD, P <sub>F</sub> LBS (MN)	FRACTURE TORQUE, T <sub>F</sub> IN.-LB (JOULE)	STRESS INTENSITY K <sub>I</sub> AT FRACTURE KSI √IN. (MN/m <sup>3/2</sup> )	STRESS INTENSITY K <sub>III</sub> AT FRACTURE KSI √IN. (MN/m <sup>3/2</sup> )
3RNB-2	0.904 (23.0)	0.556 (14.1)	30.0 (207)	0.06	11,000	0.466 (11.8)	0.084 (2.13)	0.006 (0.15)	8	23,200 (0.103)	—	55.8 (61.3)	—
3RNB-10	0.903 (22.9)	0.554 (14.1)	↑	↑	8,000	0.538 (13.7)	0.010 (0.25)	0.006 (0.15)	8	32,600 (0.145)	—	61.3 (67.3)	—
3RNB-6	0.901 (22.9)	0.567 (14.4)	↑	↑	17,000	0.535 (13.6)	0.024 (0.61)	0.006 (0.15)	0.075	32,000 (0.142)	2260 (255)	61.1 (67.2)	25.0 (27.5)
3RNB-11	0.902 (22.9)	0.556 (14.1)	↑	↑	12,000	0.524 (13.3)	0.030 (0.76)	0.002 (0.05)	0.075	25,900 (0.115)	1895 (214)	51.1 (56.1)	22.1 (24.3)
3RNB-12	0.902 (22.9)	0.552 (14.0)	↑	↑	9,000	0.524 (13.3)	0.024 (0.61)	0.004 (0.10)	0.15	25,000 (0.111)	3585 (405)	49.7 (54.6)	41.8 (45.9)
3RNB-8	0.901 (22.9)	0.564 (14.3)	↑	↑	9,000	0.542 (13.8)	0.020 (0.51)	0.002 (0.05)	0.15	33,700 (0.150)	4770 (539)	62.3 (68.4)	51.2 (56.3)
3RNB-7	0.902 (22.9)	0.552 (14.0)	↑	↑	16,000	0.512 (13.0)	0.032 (0.81)	0.008 (0.20)	0.30	16,600 (0.074)	4860 (549)	34.0 (37.3)	60.1 (66.0)
3RNB-9	0.902 (22.9)	0.551 (14.0)	↑	↑	11,000	0.533 (13.5)	0.012 (0.30)	0.006 (0.15)	0.30	19,980 (0.089)	5400 (610)	38.1 (41.8)	60.4 (66.3)
3RNB-5	0.902 (22.9)	0.548 (13.9)	↓	↓	6,000	0.510 (13.0)	0.030 (0.76)	0.008 (0.20)	0	—	5480 (619)	—	68.4 (79.1)
3RNB-3	0.901 (22.9)	0.552 (14.0)	30.0 (207)	0.06	8,000	0.498 (12.6)	0.050 (1.27)	0.004 (0.10)	0	—	5460 (617)	—	72.3 (79.5)

① STRESS INTENSITY FACTORS CALCULATED FROM  
MIN DIAMETER AT CRACKED SECTION, d.

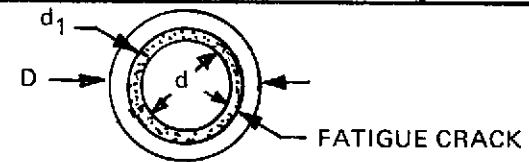


Table 6-9: Fracture Data From Combined Mode I-II-III Tests of 4340 Steel Flat Specimens Containing Inclined Surface Flaws

SPECIMEN				PRECRACKING AT 72 F (295K)					FRACTURE TESTS & RESULTS AT -200 F (144K)					
IDENTIFICATION	THICKNESS, $t$ IN. (mm)	WIDTH, $w$ IN. (mm)	ANGLE, $\phi$ (FIG. 6-6) DEGREES (RADIAN)	MAX FATIGUE STRESS KSI (MN/m <sup>2</sup> )	STRESS RATIO ( $\sigma_{MIN}/\sigma_{MAX}$ )	NUMBER OF CYCLES	FLAW DEPTH $a$ , IN. (mm)	FLAW LENGTH $2c$ , IN. (mm)	GROSS FRACTURE STRESS, $\sigma$ KSI (MN/m <sup>2</sup> )	STRESS INTENSITY $K_I$ AT A, $K_{IIA}$ KSI $\sqrt{IN.}$ (MN/m <sup>3/2</sup> )	STRESS INTENSITY $K_{III}$ AT A, $K_{IIIA}$ KSI $\sqrt{IN.}$ (MN/m <sup>3/2</sup> )	STRESS INTENSITY $K_I$ AT B, $K_{IIB}$ KSI $\sqrt{IN.}$ (MN/m <sup>3/2</sup> )	STRESS INTENSITY $K_{II}$ AT B, $K_{IIB}$ KSI $\sqrt{IN.}$ (MN/m <sup>3/2</sup> )	
3LSF-1	0.248 (6.30)	2.005 (50.9)	0 (0.0)	30.0 (207)	0.30	8000	0.140 (3.56)	0.605 (15.4)	59.8 (412)	37.0 (40.6)	0.0	25.4 (27.9)	0.0	
3LSF-2	0.252 (6.40)	2.002 (50.9)	0 (0.0)	↑ ↓	0.30	7000	0.140 (3.56)	0.590 (15.0)	70.2 (484)	43.2 (47.4)	0.0	30.0 (32.9)	0.0	
3LSF-3	0.260 (6.60)	2.003 (50.9)	25 (0.44)		0.23	21,000	0.144 (3.66)	0.590 (15.0)	75.6 (521)	38.3 (42.1)	14.4 (15.8)	27.0 (29.6)	15.2 (16.6)	
3LSF-4	0.259 (6.58)	2.003 (50.9)	26 (0.45)		0.20	2500	0.187 (4.75)	0.650 (16.5)	70.1 (483)	38.4 (42.1)	14.4 (15.8)	22.3 (24.5)	16.2 (17.7)	
3LSF-5	0.254 (6.45)	2.002 (50.8)	45 (0.79)		0.15	1500	0.148 (3.76)	0.600 (15.2)	120.2 (829)	38.5 (42.3)	30.1 (33.0)	27.3 (30.0)	31.8 (34.9)	
3LSF-6	0.254 (6.45)	1.998 (50.8)	45 (0.79)		0.15	2000	0.142 (3.61)	0.590 (15.0)	110.0 (758)	34.1 (37.4)	27.1 (29.7)	23.9 (26.2)	28.5 (31.3)	
3LSF-7	0.258 (6.55)	2.000 (50.8)	61 (1.06)		0.18	3000	0.150* (3.81)	0.600* (15.2)	157.0 (1083)	23.2* (25.4)	33.1* (36.3)	16.4* (18.0)	35.0* (38.4)	
3LSF-8	0.253 (6.43)	2.001 (50.8)	60 (1.05)		30.0 (207)	0.18	4000	0.150* (3.81)	0.600* (15.2)	173.6 (1197)	28.4* (31.2)	37.7* (41.4)	20.1* (22.1)	40.0* (44.0)

\* FRACTURE DID NOT OCCUR ALONG THE FLAW PLANE. FLAW DIMENSIONS ARE ESTIMATED.

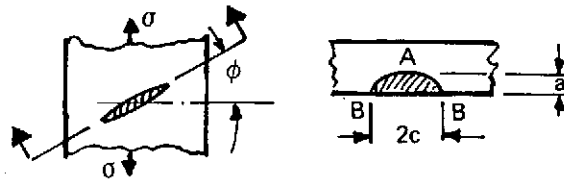


Table 6-10: Test Results Obtained from Surface Flawed Cylindrical Specimens of 4340 Steel Subjected to Combined Tension and Torsion

SPECIMEN		FATIGUE CRACK EXTENSION AT ROOM TEMPERATURE					FRACTURE TEST RESULTS				FAILURE STRESS ADJUSTED FOR FLAW DEPTH a = 0.240 IN. (6.10 mm)	
IDENTIFICATION	TEST SECTION DIAMETER d, INCH (mm)	MAXIMUM CYCLIC STRESS KSI (MN/m <sup>2</sup> )	STRESS RATIO $\sigma_{MIN}/\sigma_{MAX}$	NUMBER OF CYCLES X 1000	FLAW DEPTH a, INCH (mm)	FLAW LENGTH 2c, INCH (mm)	TEMPERATURE	TEST ENVIRON.	FAILURE STRESS IN TENSION $\sigma_F$ , KSI (MN/m <sup>2</sup> )	FAILURE STRESS IN SHEAR (TORQUE) $\tau_F$ , KSI (MN/m <sup>2</sup> )	$\sigma_F$ KSI (MN/m <sup>2</sup> )	$\tau_F$ KSI (MN/m <sup>2</sup> )
3RSFB-1	0.703 (17.9)	30.0 (207)	0.40	2.0	0.260 (6.60)	0.545 (13.8)	RT	AIR	65.4 (451)	—	68.1 (470)	—
3RSFB-2	0.701 (17.8)	25.0 (172)	0.50	2.8	0.465 (11.81)	0.645 (16.4)	↑	↑	33.6 (232)	—	—	—
3RSFB-4	0.703 (17.9)	↑	↑	3.5	0.562 (14.27)	0.630 (16.0)	↑	↑	23.4 (161)	—	—	—
3RSFB-11	0.701 (17.8)	↑	↑	5.1	0.220 (5.59)	0.550 (14.0)	↑	↑	—	149.1 (1028)	—	142.8 (985)
3RSFB-7	0.701 (17.8)	↑	↑	3.0	0.192 (4.88)	0.530 (13.5)	↑	↑	77.5 (534)	69.3 (478)	69.3 (478)	62.0 (427)
3RSFB-12	0.702 (17.8)	↑	↑	3.0	0.210 (5.33)	0.530 (13.5)	↑	↑	76.3 (526)	67.4 (465)	71.4 (492)	63.0 (434)
3RSFB-3	0.704 (17.9)	↑	↑	4.0	0.244 (6.20)	0.550 (14.0)	↑	↑	62.0 (427)	111.9 (772)	62.5 (431)	112.8 (778)
3RSFB-6	0.703 (17.9)	↑	↑	3.0	0.222 (5.64)	0.555 (14.1)	↑	↑	69.0 (476)	112.5 (776)	66.4 (458)	108.2 (746)
3RSFB-5	0.703 (17.9)	↓	↓	4.5	0.248 (6.30)	0.575 (14.6)	↓	↓	35.1 (242)	130.9 (903)	35.7 (246)	133.1 (918)
3RSFB-8	0.699 (17.8)	25.0 (172)	0.50	2.0	0.280 (7.11)	0.610 (15.5)	RT	AIR	27.2 (188)	99.6 (687)	29.4 (203)	107.6 (742)

Table 7-1: Test Program for Static Fracture Specimens at Room Temperature Under Combined Tension and Shear Stresses

MATERIAL	SPECIMEN AND FLAW CONFIGURATION	FLAW DEPTH, a IN. (mm)	FLAW LENGTH, 2c IN. (mm)	NUMBER OF STATIC FRACTURE TESTS IN				
				TENSION ALONE	TORQUE ALONE	TENSION FIRST AND TORQUED TO FRACTURE	TORQUE FIRST AND FAILED IN TENSION	SIMULTANEOUS TENSION AND TORSION APPLIED
2219-T87 ALUMINUM	FIGURE 7-1	0.44 (11.2)	1.15 (29.2)	3	1	4	4	—
		0.30 (7.6)	0.98 (24.9)	3	—	4	5	—
		0.26 (6.6)	0.75 (19.0)	1	—	1	1	1
6Al-4V $\beta$ STA TITANIUM	FIGURE 7-3	0.28 (7.1)	0.78 (17.3)	3	1	5	4	1
		0.19 (4.8)	0.61 (15.5)	3	1	4	5	1

*Table 7-2: Test Program for Cyclic Specimens at Room Temperature  
Subjected to Combined Tension and Shear Stresses*

MATERIAL	SPECIMEN AND FLAW CONFIGURATION	FLAW DEPTH, a IN. (mm)	FLAW LENGTH, 2c IN. (mm)	$\frac{\sigma_{\text{TENSION}}}{\tau_{\text{SHEAR}}}$	NUMBER OF TESTS
2219-T87 ALUMINUM	FIGURE 7-1	0.29 (7.4)	0.95 (24.1)	1:0	3
				1:1	5
				0:1	1
		0.42 (10.7)	1.11 (28.2)	1:0	3
		1:1	4		
		0:1	2		
6Al-4V $\beta$ STA TITANIUM	FIGURE 7-4	0.19 (4.8)	0.50 (12.7)	1:0	3
				2:1	2
				1:1	3
				0:1	1
		0.28 (7.1)	0.70 (17.8)	1:0	3
				2:1	2
		1:1	3		
		0:1	1		



Table 7-3: Results for Fracture Tests of 2219-T87 Aluminum Surface Flawed Cylindrical Specimens Subjected to Combined Tension and Torsion

SPECIMEN		PRECRACKING AT ROOM TEMP.					FRACTURE TEST RESULTS AT ROOM TEMP.		
IDENTIFICATION	TEST SECTION DIAMETER, d IN. (mm)	MAX CYCLIC STRESS KSI (MN/m <sup>2</sup> )	STRESS RATIO, R ( $\sigma_{MIN}/\sigma_{MAX}$ )	NUMBER OF CYCLES	FLAW DEPTH, a IN. (mm)	FLAW LENGTH, 2c IN. (mm)	LOADING SEQUENCE FOR TEST *	FAILURE STRESS IN TENSION, $\sigma_F$ KSI (MN/m <sup>2</sup> )	FAILURE STRESS IN TORSION, $\tau_F$ KSI (MN/m <sup>2</sup> )
2AI-1	1.747 (44.4)	8.0 (55.2)	0.2	12,000	0.425 (10.8)	1.190 (30.2)	P	25.9 (179)	—
2AI-2	1.752 (44.5)	↑	0.2	13,000	0.430 (10.9)	1.200 (30.5)	P	26.8 (185)	—
1AI-3	1.499 (38.1)	↓	0.3	7,000	0.420 (10.7)	1.130 (28.7)	T-P	27.5 (190)	30.2 (208)
1AI-4	1.499 (38.1)	↓	↑	22,000	0.430 (10.9)	1.130 (28.7)	P-T	22.7 (157)	28.0 (193)
1AI-5	1.500 (38.1)	↓	↓	30,000	0.440 (11.2)	1.140 (29.0)	P-T	28.3 (195)	16.9 (117)
1AI-6	1.500 (38.1)	↓	↓	32,000	0.470 (11.9)	1.170 (29.7)	P	28.3 (195)	—
1AI-7	1.498 (38.0)	↓	↓	32,000	0.440 (11.2)	1.130 (28.7)	P-T	22.7 (157)	27.6 (190)
1AI-8	1.501 (38.1)	↓	↓	10,000	0.425 (10.8)	1.120 (28.4)	T-P	26.7 (184)	16.7 (115)
1AI-9	1.503 (38.2)	↓	↓	12,500	0.430 (10.9)	1.120 (28.4)	T-P	25.5 (176)	30.1 (208)
1AI-10	1.502 (38.2)	↓	↓	14,000	0.435 (11.0)	1.130 (28.7)	T	—	36.1 (249)
1AI-11	1.501 (38.1)	↓	↓	13,000	0.430 (10.9)	1.120 (28.4)	T-P	26.0 (179)	16.6 (114)
1AI-12	1.500 (38.1)	8.0 (55.2)	0.3	12,000	0.430 (10.9)	1.120 (28.4)	P-T	23.2 (160)	21.1 (145)

\* P-T = TENSION APPLIED FIRST, THEN TORQUED TO FAILURE  
T-P = TORQUE APPLIED FIRST, THEN LOADED TO FAILURE IN TENSION  
S = TENSION AND TORSION APPLIED SIMULTANEOUSLY

Table 7-4: Results for Fracture Tests of 2219-T87 Aluminum Surface Flawed Cylindrical Specimens Subjected to Combined Tension and Torsion

SPECIMEN		PRECRACKING AT ROOM TEMP					FRACTURE TEST RESULTS AT ROOM TEMP.		
IDENTIFICATION	TEST SECTION DIAMETER, d IN. (mm)	MAX CYCLIC STRESS KSI (MN/m <sup>2</sup> )	STRESS RATIO, R ( $\sigma_{MIN}/\sigma_{MAX}$ )	NUMBER OF CYCLES	FLAW DEPTH, a IN. (mm)	FLAW LENGTH, 2c IN. (mm)	LOADING SEQUENCE FOR TEST *	FAILURE STRESS IN TENSION, $\sigma_F$ KSI (MN/m <sup>2</sup> )	FAILURE STRESS IN TORSION, $\tau_F$ KSI (MN/m <sup>2</sup> )
1AI-1	1.751 (44.5)	8.0 (55.2)	0.2	22,000	0.296 (7.52)	0.990 (25.1)	P	36.7 (253)	-
1AI-2	1.751 (44.5)	10.0 (69.0)	↑	16,000	0.308 (7.82)	0.990 (25.1)	P	34.6 (238)	-
2AI-3	1.501 (38.1)	8.0 (55.2)		12,000	0.300 (7.62)	0.980 (24.9)	T-P	29.6** (204)	15.1** (104)
2AI-4	1.501 (38.1)	↑	↓	10,000	0.300 (7.62)	0.990 (25.1)	P	41.3 (285)	-
2AI-5	1.503 (38.2)			11,000	0.300 (7.62)	0.980 (24.9)	P-T	31.0 (214)	30.0 (207)
2AI-6	1.498 (38.0)	↓	↓	12,000	0.300 (7.62)	0.980 (24.9)	P-T	31.2 (215)	32.2 (222)
2AI-7	1.499 (38.1)			0.2	12,000	0.307 (7.80)	0.980 (24.9)	T-P	35.6 (245)
2AI-8	1.500 (38.1)	↓	↑	30,000	0.295 (7.49)	0.940 (23.9)	T-P	36.8 (254)	15.7 (108)
2AI-9	1.502 (38.2)			35,000	0.300 (7.62)	0.960 (24.4)	T-P	36.1 (249)	29.4 (203)
2AI-10	1.503 (38.2)	↓	↓	45,000	0.300 (7.62)	0.940 (23.9)	P	32.6 (225)	-
2AI-11	1.498 (38.0)			45,000	0.295 (7.49)	0.945 (24.0)	T-P	35.2 (243)	15.2 (105)
2AI-12	1.497 (38.0)	8.0 (55.2)	0.3	50,000	0.305 (7.75)	0.945 (24.0)	P	32.6 (225)	-

\* P-T = TENSION APPLIED FIRST, THEN TORQUED TO FAILURE  
 T-P = TORQUE APPLIED FIRST, THEN LOADED TO FAILURE IN TENSION  
 S = TENSION AND TORSION APPLIED SIMULTANEOUSLY

\*\*THIS SPECIMEN HAS GONE THROUGH COMPLEX LOAD HISTORY PREVIOUSLY

Table 7-5: Results for Fracture Tests of 2219-T87 Aluminum Surface Flawed Cylindrical Specimens Subjected to Combined Tension and Torsion

SPECIMEN		PRECRACKING AT ROOM TEMP.					FRACTURE TEST RESULTS AT ROOM TEMP.		
IDENTIFICATION	TEST SECTION DIAMETER, d IN. (mm)	MAX CYCLIC STRESS KSI (MN/m <sup>2</sup> )	STRESS RATIO, R ( $\sigma_{MIN}/\sigma_{MAX}$ )	NUMBER OF CYCLES	FLAW DEPTH, a IN. (mm)	FLAW LENGTH, 2c IN. (mm)	LOADING SEQUENCE FOR TEST *	FAILURE STRESS IN TENSION, $\sigma_F$ KSI (MN/m <sup>2</sup> )	FAILURE STRESS IN TORSION, $\tau_F$ KSI (MN/m <sup>2</sup> )
3AI-1	1.503 (38.2)	10.0 (69.0)	0.25	12,000	0.270 (6.86)	0.750 (19.1)	P	41.0 (283)	-
3AI-2	1.496 (38.0)	↕	↕	10,000	0.265 (6.73)	0.760 (19.3)	P-T	33.0 (228)	31.3 (216)
3AI-3	1.501 (38.1)	↕	↕	11,000	0.260 (6.60)	0.750 (19.1)	T-P	36.2 (250)	31.3 (216)
3AI-4	1.498 (38.0)	10.0	0.25 (69.0)	12,000	0.260 (6.60)	0.760 (19.3)	S	34.6 (239)	29.6 (204)

- \* P-T = TENSION APPLIED FIRST, THEN TORQUED TO FAILURE
- T-P = TORQUE APPLIED FIRST, THEN LOADED TO FAILURE IN TENSION
- S = TENSION AND TORSION APPLIED SIMULTANEOUSLY

Table 7-6: Fracture Toughness Data of 1.00 Inch Thick 6Al-4V  $\beta$ -STA Titanium

SPECIMEN			FATIGUE CRACK EXTENSION AT ROOM TEMP.					FRACTURE TEST RESULTS				
IDENTIFICATION	THICKNESS, t INCH (mm)	WIDTH, W INCH (mm)	MAX FATIGUE STRESS KSI (MN/m <sup>2</sup> )	STRESS RATIO, R ( $\sigma_{MIN}/\sigma_{MAX}$ )	TOTAL NUMBER OF CYCLES	FLAW DEPTH, a INCH (mm)	FLAW LENGTH, 2c INCH (mm)	TEMPERATURE	ENVIRONMENT	GROSS AREA STRESS, $\sigma$ , KSI (MN/m <sup>2</sup> )	FRACTURE TOUGH- NESS, K <sub>IE</sub> (KSI $\sqrt{IN.}$ (MN/m <sup>3/2</sup> ))	AVERAGE K <sub>IE</sub> KSI $\sqrt{IN.}$ (MN/m <sup>3/2</sup> )
4TFR-1	0.199 (5.05)	1.204 (30.6)	40.0 (276)	0.5	2500	0.096 (0.44)	0.354 (8.99)	RT	AIR	131.4 (906)	68.2 (75.0)	69.2 (76.1)
4TFR-2	0.205 (5.21)	1.205 (30.6)	40.0 (276)	0.5	2500	0.097 (0.47)	0.354 (8.99)	RT	AIR	134.9 (930)	70.2 (77.1)	

Table 7-7: Results for Fracture Tests of 6Al-4V  $\beta$ -STA Titanium Surface Flawed Cylindrical Specimens Subjected to Combined Tension and Torsion

SPECIMEN		PRECRACKING AT ROOM TEMP.					FRACTURE TEST RESULTS AT ROOM TEMP.				
IDENTIFICATION	TEST SECTION DIAMETER, d IN. (mm)	MAX CYCLIC STRESS KSI (MN/m <sup>2</sup> )	STRESS RATIO, R ( $\sigma_{MIN}/\sigma_{MAX}$ )	NUMBER OF CYCLES	FLAW DEPTH, a IN. (mm)	FLAW LENGTH, 2c IN. (mm)	LOADING SEQUENCE FOR TEST *	FAILURE STRESS IN TENSION, $\sigma_F$ KSI (MN/m <sup>2</sup> )	FAILURE STRESS IN TORSION, $\tau_F$ KSI (MN/m <sup>2</sup> )		
4TR-1	0.916 (23.3)	31.5 (217)	0.2	5400	0.183 (4.65)	0.500 (12.7)	P	117.5 (810)	—		
4TR-2	0.891 (22.6)	↑	↑	3000	0.187 (4.75)	0.600 (15.2)	P	103.4 (713)	—		
4TR-3	0.950 (24.1)			3500	0.187 (4.75)	0.605 (15.4)	P-T	72.8 (502)	85.5 (590)		
4TR-4	0.953 (24.2)			3000	0.190 (4.83)	0.615 (15.6)	P-T	82.7 (570)	50.7 (350)		
4TR-5	0.940 (23.9)			2000	0.186 (4.72)	0.604 (15.3)	P	96.7 (667)	—		
4TR-6	0.951 (24.2)			2600	0.196 (4.98)	0.615 (15.6)	P-T	84.2 (581)	69.6 (480)		
4TR-7	0.953 (24.2)			2600	0.194 (4.93)	0.618 (15.7)	T-P	94.0 (648)	70.0 (483)		
4TR-8	0.951 (24.2)			4500	0.190 (4.83)	0.616 (15.6)	T-P	77.4 (534)	84.0 (579)		
4TR-9	0.952 (24.2)			2600	0.188 (4.78)	0.610 (15.5)	P-T	90.0 (621)	60.7 (419)		
4TR-10	0.950 (24.1)			3500	0.204 (5.18)	0.618 (15.7)	T-P	94.7 (653)	60.3 (416)		
4TR-11	0.952 (24.2)			3600	0.200 (5.08)	0.612 (15.5)	T-P	104.8 (723)	30.0 (207)		
4TR-12	0.953 (24.2)			↓	↓	7000	0.210 (5.33)	0.615 (15.6)	T	—	106.2 (732)
4TR-13	0.949 (24.1)			31.5 (217)	0.2	6000	0.220 (5.59)	0.610 (15.5)	S	94.8 (654)	41.8 (288)

\* P-T = TENSION APPLIED FIRST, THEN TORQUED TO FAILURE  
T-P = TORQUE APPLIED FIRST, THEN LOADED TO FAILURE IN TENSION  
S = TENSION AND TORSION APPLIED SIMULTANEOUSLY

Table 7-8: Results for Fracture Tests of 6Al-4V  $\beta$ -STA Titanium Surface Flawed Cylindrical Specimens Subjected to Combined Tension and Torsion

SPECIMEN		PRECRACKING AT ROOM TEMP.					FRACTURE TEST RESULTS AT ROOM TEMP.				
IDENTIFICATION	TEST SECTION DIAMETER, d IN. (mm)	MAX CYCLIC STRESS KSI (MN/m <sup>2</sup> )	STRESS RATIO R ( $\sigma_{MIN}/\sigma_{MAX}$ )	NUMBER OF CYCLES	FLAW DEPTH <sup>a</sup> IN. (mm)	FLAW LENGTH <sup>2c</sup> IN. (mm)	LOADING SEQUENCE FOR TEST *	FAILURE STRESS IN TENSION, $\sigma_F$ KSI (MN/m <sup>2</sup> )	FAILURE STRESS IN TORSION, $\tau_F$ KSI (MN/m <sup>2</sup> )		
4TR-14	0.954 (24.2)	25.0 (172)	0.25	6000	0.298 (6.81)	0.698 (17.7)	S	26.4 (182)	88.0 (607)		
4TR-15	0.948 (24.1)	↑	↑	4500	0.280 (7.11)	0.680 (17.3)	P-T	50.0 (345)	86.3 (595)		
4TR-16	0.952 (24.2)			5000	0.304 (7.72)	0.720 (18.3)	T-P	49.2 (339)	84.0 (579)		
4TR-17	0.950 (24.1)			10,000	0.304 (7.72)	0.688 (17.5)	P-T	70.0 (483)	49.9 (344)		
4TR-18	0.946 (24.0)			0.25	3500	0.284 (7.21)	0.690 (17.5)	T-P	76.8 (530)	59.8 (412)	
4TR-19	0.949 (24.1)			0.20	3000	0.264 (6.71)	0.667 (16.9)	P	81.3 (561)	-	
4TR-20	0.916 (23.3)			↑	3000	0.268 (6.81)	0.660 (16.8)	P	81.3 (561)	-	
4TR-21	0.886 (22.5)				4000	0.268 (6.81)	0.672 (17.1)	P-T	70.1 (483)	34.4 (237)	
4TR-22	0.920 (23.4)			25.0 (172)		3500	0.270 (6.86)	0.665 (16.9)	P-T	65.0 (448)	58.9 (406)
4TR-23	0.950 (24.1)			31.5 (217)		2500	0.288 (7.32)	0.665 (16.9)	P-T	69.3 (478)	-
4TR-24	0.950 (24.1)			31.5 (217)	↓	3500	0.280 (7.11)	0.670 (17.0)	P-T	60.0 (414)	75.3 (519)
4TR-25	0.945 (24.0)	31.5 (217)	0.20	3500	0.294 (7.47)	0.680 (17.3)	T-P	82.4 (568)	36.1 (249)		
4TR-26	0.951 (24.2)	25.0 (172)	0.25	5000	0.268 (6.81)	0.655 (16.6)	T-P	81.6 (563)	35.0 (241)		
4TR-27	0.949 (24.1)	25.0 (172)	0.25	6000	0.300 (7.62)	0.682 (17.3)	T	-	95.4 (658)		

\* P-T = TENSION APPLIED FIRST, THEN TORQUED TO FAILURE  
 T-P = TORQUE APPLIED FIRST, THEN LOADED TO FAILURE IN TENSION  
 S = TENSION AND TORSION APPLIED SIMULTANEOUSLY

Table 7-9: Results for Fatigue Tests of 2219-T87 Aluminum Surface Flawed Cylindrical Specimens Subjected to Combined Tension and Torsion Loadings

SPECIMEN IDENTIFICATION	TEST SECTION DIAMETER, d IN. (mm)	INITIAL FLAW DEPTH, a <sub>i</sub> IN. (mm)	INITIAL FLAW LENGTH, 2 c <sub>i</sub> IN. (mm)	MAXIMUM CYCLIC TENSILE STRESS, σ KSI (MN/m <sup>2</sup> )	MAXIMUM CYCLIC SHEAR STRESS, τ KSI (MN/m <sup>2</sup> )	TENSION STRESS RATIO (σ <sub>MIN</sub> /σ <sub>MAX</sub> )	SHEAR STRESS RATIO (τ <sub>MIN</sub> /τ <sub>MAX</sub> )	NUMBER OF APPLIED LOADING CYCLES, N	FINAL FLAW DEPTH, a <sub>f</sub> IN. (mm)	FINAL FLAW LENGTH, 2 c <sub>f</sub> IN. (mm)	REMARKS
5AI-1	1.499 (38.1)	0.298 (7.57)	0.940 (23.9)	30.0 (207)	—	0.05	0.0	160	0.435 (11.0)	0.980 (24.9)	T
5AI-2	1.501 (38.1)	0.295 (7.49)	0.940 (23.9)	26.9 (185)	—	↑	↑	172	0.440 (11.2)	0.960 (24.4)	T
5AI-3	1.500 (38.1)	0.285 (7.24)	0.936 (23.8)	23.5 (162)	—	↑	↑	2224	0.522 (13.3)	1.135 (28.8)	T
5AI-4	1.502 (38.2)	0.290 (7.37)	0.945 (24.0)	28.8 (199)	28.6 (197)	↑	↑	127	0.335 (8.51)	1.110 (27.9)	F, DELAMINATION TYPE OF GROWTH
5AI-5	1.502 (38.2)	0.290 (7.37)	0.950 (24.1)	25.7 (177)	25.6 (177)	↑	↑	176	0.360 (9.14)	1.140 (29.0)	T, OUT OF PLANE GROWTH
5AI-6	1.501 (38.1)	0.290 (7.37)	0.945 (24.0)	22.6 (156)	22.6 (156)	↑	↑	524	0.360 (9.14)	1.060 (26.9)	F, OUT OF PLANE GROWTH
5AI-7	1.500 (38.1)	0.285 (7.24)	0.935 (23.7)	25.8 (178)	25.7 (177)	↑	↑	133	0.325 (82.6)	1.095 (27.8)	F
5AI-8	1.503 (38.2)	0.285 (7.24)	0.940 (23.9)	30.4 (210)	30.3 (209)	↑	↑	3	—	—	F, I
5AI-9	1.500 (38.1)	0.295 (7.49)	0.945 (24.0)	—	28.8 (199)	↑	↑	7533	0.430 (10.9)	1.320 (33.5)	T
5AI-10	1.500 (38.1)	0.428 (10.9)	1.120 (28.4)	24.3 (168)	—	↑	↑	27	0.472 (12.0)	1.135 (28.8)	F
5AI-11	1.501 (38.1)	0.420 (10.7)	1.105 (28.1)	21.5 (148)	—	↓	↓	569	0.562 (14.3)	1.265 (32.1)	T

T = TEST TERMINATED COUPLE OF CYCLES PRIOR TO FAILURE  
 F = FAILURE OCCURED WHILE CYCLING THE SPECIMEN  
 I = FLAW SIZE AT FAILURE COULD NOT BE SEEN DISTINCTLY

Table 7-9: (Continued)

SPECIMEN IDENTIFICATION	TEST SECTION DIAMETER, d IN. (MM)	INITIAL FLAW DEPTH, a <sub>i</sub> IN. (MM)	INITIAL FLAW LENGTH, 2c IN. (MM)	MAXIMUM CYCLIC TENSILE STRESS, σ KSI (MIN/m <sup>2</sup> )	MAXIMUM CYCLIC SHEAR STRESS, KSI (MIN/m <sup>2</sup> )	TENSION STRESS RATIO (σ <sub>MIN</sub> /σ <sub>MAX</sub> )	SHEAR STRESS RATIO (τ <sub>MIN</sub> /τ <sub>MAX</sub> )	NUMBER OF APPLIED LOADING CYCLES, N	FINAL FLAW DEPTH, a <sub>f</sub> IN. (MM)	FINAL FLAW LENGTH, 2c <sub>f</sub> IN. (MM)	REMARKS
5AI-12	1.502 (38.2)	0.424 (10.8)	1.110 (28.2)	19.2 (132)	—	0.05	0.0	924	0.530 (13.5)	1.295 (32.9)	T
5AI-13	1.500 (38.1)	0.425 (10.8)	1.115 (28.3)	23.2 (160)	23.1 (159)	↑	↑	6	—	—	F, I
5AI-14	1.501 (38.1)	0.416 (10.6)	1.110 (28.2)	20.4 (141)	20.4 (141)	↑	↑	24	0.435 (11.0)	1.160 (29.5)	F, I
5AI-15	1.499 (38.1)	0.420 (10.7)	1.115 (28.3)	17.3 (119)	17.4 (120)	↑	↑	158	0.460 (11.7)	1.170 (29.7)	F, I
5AI-16	1.501 (38.1)	0.415 (10.5)	1.120 (28.4)	—	23.0 (159)	↑	↑	7500	0.480 (12.2)	1.370 (34.8)	T
5AI-17	1.503 (38.2)	0.420 (10.7)	1.115 (28.3)	—	27.5 (190)	↓	↓	4879	0.515 (13.1)	1.400 (35.6)	F
5AI-18	1.496 (38.0)	0.418 (10.6)	1.110 (28.2)	14.2 (98)	14.4 (99)	0.05	0.0	2791	0.770 (19.6)	1.360 (34.5)	T, ONE SIDED OUT OF PLANE GROWTH

T = TEST TERMINATED COUPLE OF CYCLES PRIOR TO FAILURE  
 F = FAILURE OCCURRED WHILE CYCLING THE SPECIMEN  
 I = FLAW SIZE AT FAILURE COULD NOT BE SEEN DISTINCTLY



Table 7-10: Results For Fatigue Tests of 6Al-4V  $\beta$ STA Titanium Surface Flawed Cylindrical Specimens  
 Subjected to Combined Tension and Torsion Loadings

SPECIMEN IDENTIFICATION	TEST SECTION DIAMETER, d IN. (mm)	INITIAL FLAW DEPTH, a <sub>i</sub> IN. (mm)	INITIAL FLAW LENGTH, 2c <sub>i</sub> IN. (mm)	MAXIMUM CYCLIC TENSILE STRESS, $\sigma$ KSI (MN/m <sup>2</sup> )	MAXIMUM CYCLIC SHEAR STRESS, $\tau$ KSI (MN/m <sup>2</sup> )	TENSION STRESS RATIO ( $\sigma_{MIN}/\sigma_{MAX}$ )	SHEAR STRESS RATIO ( $\tau_{MIN}/\tau_{MAX}$ )	NUMBER OF APPLIED LOADING CYCLES, N	FINAL FLAW DEPTH, a <sub>f</sub> IN. (mm)	FINAL FLAW LENGTH, 2c <sub>f</sub> IN. (mm)	REMARKS
5TC-1	0.950 (24.1)	0.190 (4.83)	0.601 (15.3)	90.0 (621)	—	0.05	0.0	88	0.270 (6.86)	0.622 (15.8)	T
5TC-2	0.951 (24.2)	0.200 (5.08)	0.505 (12.8)	80.0 (552)	—	↑	↑	334	0.358 (9.09)	0.690 (17.5)	T
5TC-3	0.951 (24.2)	0.192 (4.88)	0.502 (12.8)	70.0 (483)	—	↑	↑	752	0.380 (9.65)	0.690 (17.5)	T
5TC-4	0.948 (24.1)	0.190 (4.83)	0.495 (12.6)	75.0 (517)	60.0 (414)	↑	↑	152	0.320 (8.13)	0.670 (17.0)	T
5TC-5	0.953 (24.2)	0.196 (4.98)	0.501 (12.7)	58.8 (405)	51.1 (352)	↑	↑	678	0.380 (9.65)	0.695 (17.7)	T
5TC-6	0.952 (24.2)	0.192 (4.88)	0.500 (12.7)	85.6 (590)	43.0 (296)	↑	↑	69	0.292 (7.42)	0.550 (14.0)	T
5TC-7	0.949 (24.1)	0.194 (4.93)	0.508 (12.9)	65.8 (454)	33.0 (228)	↑	↑	427	0.336 (8.53)	0.690 (17.5)	T
5TC-8	0.948 (24.1)	0.192 (4.88)	0.505 (12.8)	67.0 (462)	58.0 (480)	↓	↓	316	0.352 (8.94)	0.715 (18.2)	T
5TC-9	0.938 (23.8)	0.196 (4.98)	0.495 (12.6)	—	66.0 (455)	0.05	0.0	6627	—	—	F, I

T = TEST TERMINATED COUPLE OF CYCLES PRIOR TO FAILURE  
 F = FAILURE OCCURRED WHILE CYCLING THE SPECIMEN  
 I = FLAW SIZE AT FAILURE COULD NOT BE SEEN DISTINCTLY

Table 7-10: (Continued)

SPECIMEN IDENTIFICATION	TEST SECTION DIAMETER, d IN. (mm)	INITIAL FLAW DEPTH, a <sub>i</sub> IN. (mm)	INITIAL FLAW LENGTH, 2c <sub>i</sub> IN. (mm)	MAXIMUM CYCLIC TENSILE STRESS, σ KSI (MN/m <sup>2</sup> )	MAXIMUM CYCLIC SHEAR STRESS, τ KSI (MN/m <sup>2</sup> )	TENSION STRESS RATIO (σ <sub>MIN</sub> /σ <sub>MAX</sub> )	SHEAR STRESS RATIO (τ <sub>MIN</sub> /τ <sub>MAX</sub> )	NUMBER OF APPLIED LOADING CYCLES, N	FINAL FLAW DEPTH, a <sub>f</sub> IN. (mm)	FINAL FLAW LENGTH, 2c <sub>f</sub> IN. (mm)	REMARKS
5TC-10	0.949 (24.1)	0.282 (7.16)	0.718 (18.2)	69.0 (476)	—	0.05	0.0	30	0.340 (8.64)	0.755 (19.2)	T
5TC-11	0.950 (24.1)	0.276 (7.01)	0.696 (17.7)	61.6 (425)	—	↑	↑	99	0.384 (9.75)	0.748 (19.0)	T
5TC-12	0.950 (24.1)	0.280 (7.11)	0.702 (17.8)	54.0 (372)	—	↑	↑	149	0.394 (10.0)	0.785 (19.9)	T
5TC-13	0.945 (24.0)	0.280 (7.11)	0.702 (17.8)	59.4 (410)	59.4 (410)	↑	↑	86	0.380 (9.65)	0.805 (20.4)	T
5TC-14	0.869 (22.1)	0.272 (6.91)	0.675 (17.1)	52.8 (364)	52.8 (364)	↑	↑	93	0.374 (9.50)	0.790 (20.1)	T
5TC-15	0.951 (24.2)	0.276 (7.01)	0.705 (17.9)	46.2 (319)	46.2 (319)	↑	↑	218	—	—	F, I
5TC-16	0.948 (24.1)	0.280 (7.11)	0.699 (17.8)	67.5 (465)	34.0 (234)	↑	↑	65	0.372 (9.45)	0.795 (20.2)	T
5TC-17	0.951 (24.2)	0.286 (7.26)	0.702 (17.8)	52.5 (362)	26.0 (179)	↓	↓	159	0.384 (9.75)	0.817 (20.8)	T
5TC-18	0.950 (24.1)	0.282 (7.16)	0.700 (17.8)	—	60.0 (414)	0.05	0.0	3871	—	—	F, I

T = TEST TERMINATED COUPLE OF CYCLES PRIOR TO FAILURE

F = FAILURE OCCURRED WHILE CYCLING THE SPECIMEN

I = FLAW SIZE AT FAILURE COULD NOT BE SEEN DISTINCTLY.

Table 8-1: Notch Dimensions and Applied Loading for Photoelastic Test Specimens

SPECIMEN		TYPE OF NOTCH	NOTCH		CUTTER RADIUS $R_c$ IN. (mm)	RANGE OF MEASURED NOTCH ROOT RADIUS IN. (mm)	APPLIED	
NUMBER	DIAMETER, D IN. (MM)		DEPTH $a$ IN (mm)	LENGTH $2c$ IN (mm)			LOAD lbf (N)	TORQUE IN-LB (JOULE)
1	2.50 (63.5)	SURFACE	0.50 (12.7)	1.65 (41.9)	1.75 (44.5)	0.0006 — 0.0008 (0.015 — 0.020)	15.4 (68.5)	—
2	2.50 (63.5)	SURFACE	0.50 (12.7)	1.65 (41.9)	1.75 (44.5)	—	—	10.0 (1.13)
3	2.50 (63.5)	SURFACE	0.75 (19.1)	1.90 (48.3)	1.75 (44.5)	0.0004 (0.010)	11.9 (52.9)	—
4	2.50 (63.5)	SURFACE	0.75 (19.1)	1.90 (48.3)	1.75 (44.5)	—	—	7.5 (0.85)
5	1.50 (38.1)	SURFACE	0.30 (7.6)	1.00 (25.4)	1.06 (26.9)	0.0004 (0.010)	10.3 (45.8)	—
6	1.50 (38.1)	SURFACE	0.30 (7.6)	1.00 (25.4)	1.06 (26.9)	—	—	5.6 (0.63)
7	2.50 (63.5)	CIRCUM-FERENTIAL	0.50 (12.7)	—	—	0.002 (0.051)	15.1 (67.2)	—

Table 8-2: Stress Intensity Factors  $K_I$  at Various Locations of Surface Flaws in Cylindrical Specimens Subjected to Tension from Photoelastic Tests

SPECIMEN NUMBER	STRESS INTENSITY FACTOR, $K_I$ FROM PHOTOELASTIC RESULTS					$K_{I 1-1} / K_{I 1-4}$	$\sqrt{a/c}$	OTHER DETAILS
	AT LOCATION	I-1	I-2	I-3	I-4			
1	$K_I$ KSI $\sqrt{IN}$ (KN/m <sup>3/2</sup> )	2.45 (2.68)	—	3.39 (3.73)	3.71 (4.08)	0.66	0.79	a = 0.50 IN. (12.7 mm) a/D = 0.20 a/2c = 0.31
	$K_I / (Y\sigma \sqrt{a})$	0.46	—	0.64	0.70			
	$K_I / (1.95\sigma \sqrt{a})$	0.57	—	0.78	0.86			
	$K_I / (1.95\sigma \sqrt{a/Q})$	0.71	—	0.99	1.08			
3	$K_I$ KSI $\sqrt{IN}$ (KN/m <sup>3/2</sup> )	4.80 (5.28)	—	5.22 (5.74)	5.40 (5.94)	0.89	0.88	a = 0.75 IN. (19.1 mm) a/D = 0.30 a/2c = 0.39
	$K_I / (Y\sigma \sqrt{a})$	0.78	—	0.85	0.88			
	$K_I / (1.95\sigma \sqrt{a})$	1.18	—	1.28	1.32			
	$K_I / (1.95\sigma \sqrt{a/Q})$	1.65	—	1.80	1.86			
5	$K_I$ KSI $\sqrt{IN}$ (KN/m <sup>3/2</sup> )	4.14 (4.55)	5.34 (5.87)	5.99 (6.59)	6.14 (6.75)	0.67	0.79	a = 0.30 IN. (7.6 mm) a/D = 0.20 a/2c = 0.31
	$K_I / (Y\sigma \sqrt{a})$	0.54	0.70	0.78	0.80			
	$K_I / (1.95\sigma \sqrt{a})$	0.67	0.86	0.96	0.99			
	$K_I / (1.95\sigma \sqrt{a/Q})$	0.85	1.10	1.23	1.26			

Table 8-3: Stress Intensity Factors  $K_{II}$  at Various Locations of Surface Flaws in Cylindrical Specimens Subjected to Torsion From Photoelastic Tests

SPECIMEN NUMBER	MAX APPLIED SHEAR STRESS $\tau = 16T/(\pi D^3)$ PSI (KN/m <sup>2</sup> )	STRESS INTENSITY FACTOR $K_{II}$ AT LOCATION				$\frac{K_{II} I-4}{\tau\sqrt{\pi a}}$	$\frac{K_{II} I-4}{K_{II} I-1}$	OTHER DETAILS
		I-1, $K_{II} I-1$ PSI $\sqrt{IN.}$ (KN/m <sup>3/2</sup> )	I-2, $K_{II} I-2$ PSI $\sqrt{IN.}$ (KN/m <sup>3/2</sup> )	I-3, $K_{II} I-3$ PSI $\sqrt{IN.}$ (KN/m <sup>3/2</sup> )	I-4, $K_{II} I-4$ PSI $\sqrt{IN.}$ (KN/m <sup>3/2</sup> )			
2	3.26 (3.59)	3.46 (3.81)	2.52 (2.77)	—	0.26 (0.29)	0.80	0.08	a = 0.50 IN. (12.7 mm) a/D = 0.20 a/2c = 0.31
4	2.45 (2.69)	3.20 (3.52)	2.51 (2.76)	1.36 (1.50)	0.17 (0.19)	0.85	0.05	a = 0.75 IN. (19.1 mm) a/D = 0.30 a/2c = 0.39
6	8.45 (9.29)	5.47 (6.02)	4.21 (4.63)	2.35 (2.58)	0.29 (0.32)	0.67	0.05	a = 0.30 IN. (7.6 mm) a/D = 0.20 a/2c = 0.31

## APPENDIX A: PHOTOELASTIC DATA

Fringe orders measured at various locations of local coordinates  $n$  and  $z$  (Figures 8-3 and 8-6) for slices taken in  $n$ - $z$  plane of Specimens 1, 3 and 5 loaded in tension and Specimens 2, 4 and 6 loaded in pure torsion are shown in Figure A-1 to A-21. Each figure also shows slice location, slice thickness and model fringe constant.

For Specimens 2, 4 and 6, which were loaded in pure torsion, a subslice in the form of a rectangular parallelepiped was prepared from each of the  $n$ - $z$  plane slice, as shown in Figure 8-6. Rectangular subslices were taken at  $z = 0.02$  in. (0.51 mm) away from the notch plane. Measured maximum shear stress  $\tau_{nt}$  at various locations of distance  $n$  are given in Table A-1 for these subslices.

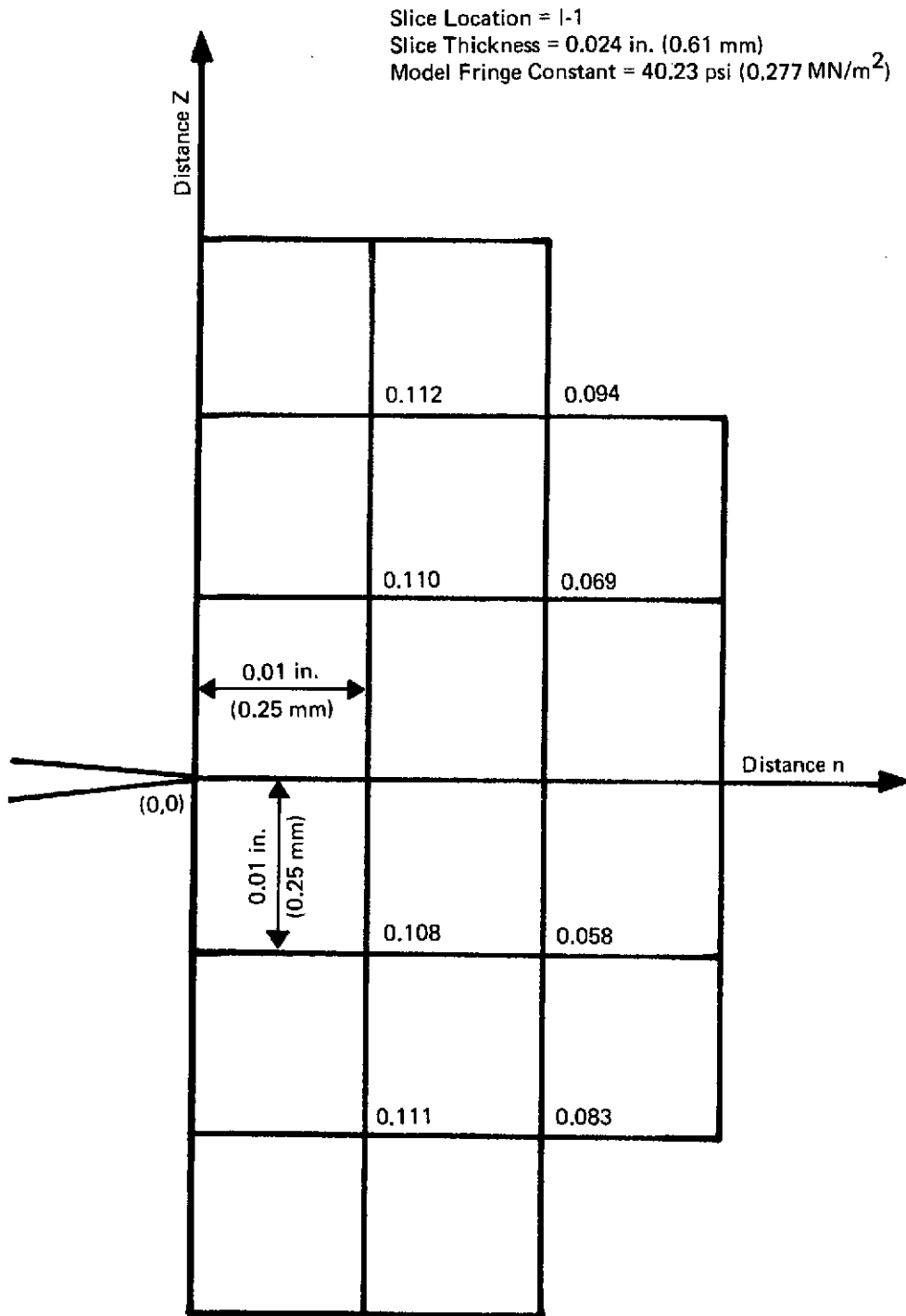


Figure A-1: Measured Fringe Orders for the Cylindrical Specimen 1 in Tension at Slice Location I-1

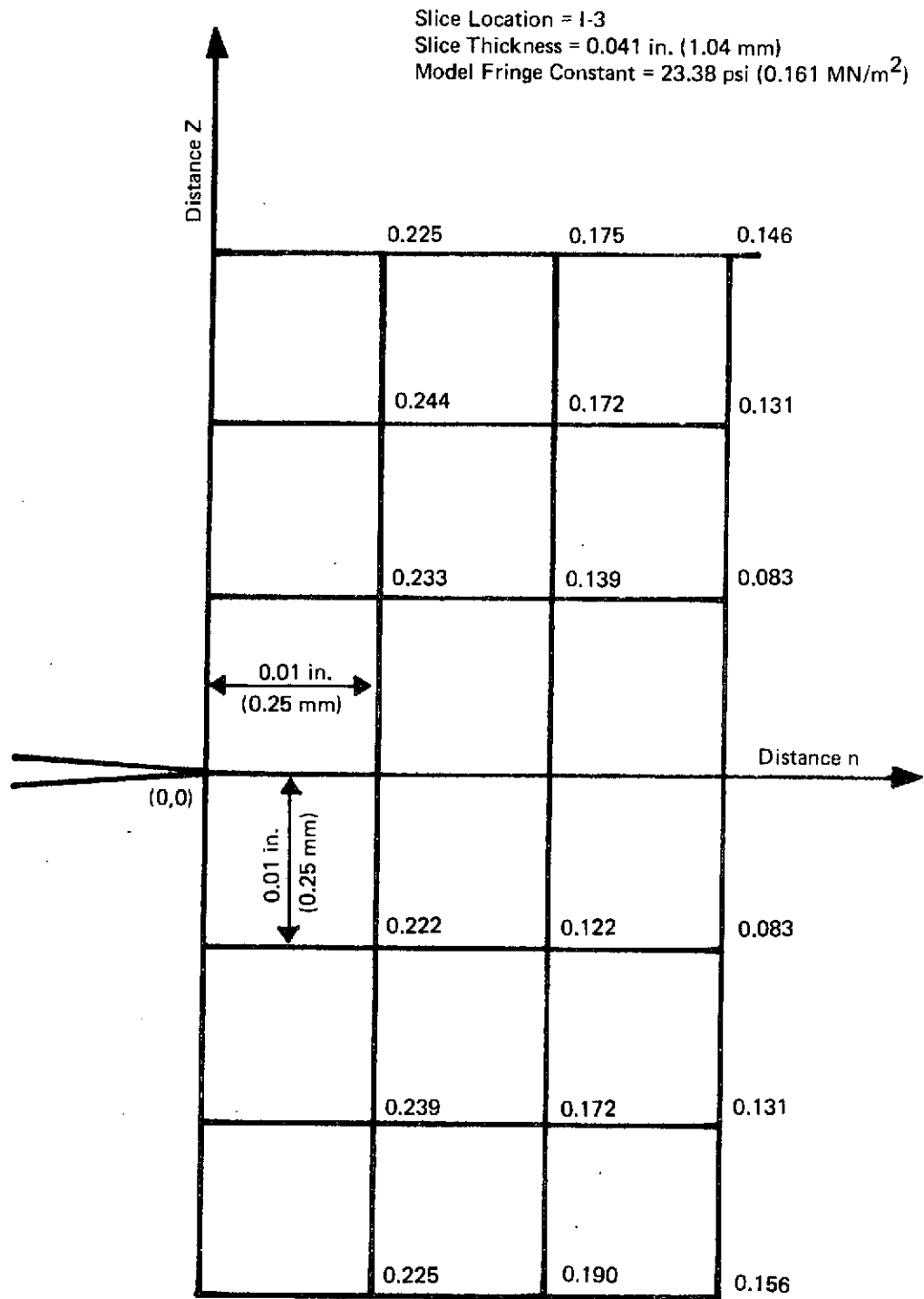


Figure A-2: Measured Fringe Orders for the Cylindrical Specimen 1 in Tension at Slice Location 1-3



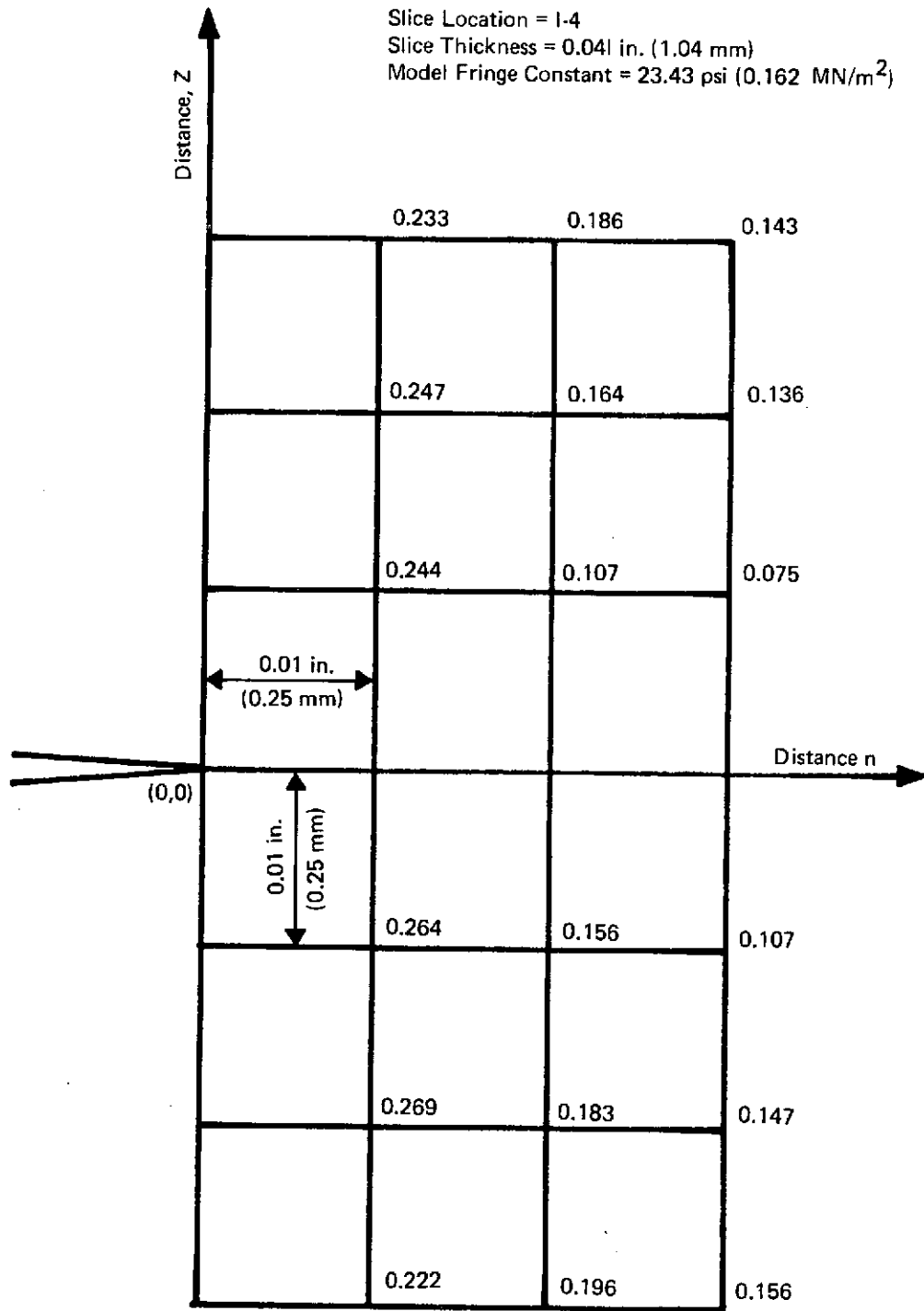


Figure A-3: Measured Fringe Orders for the Cylindrical Specimen 1 in Tension at Slice Location 1-4

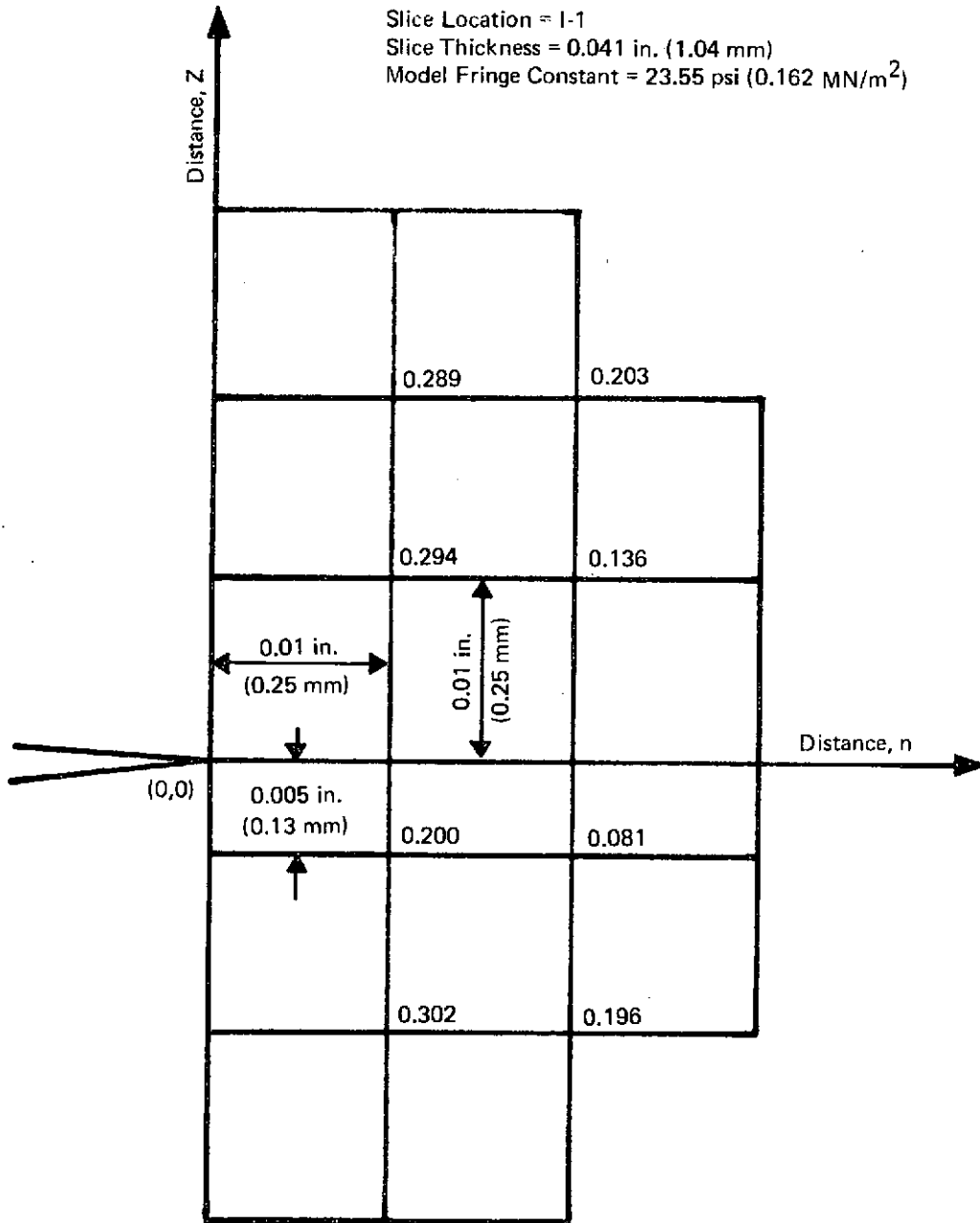


Figure A-4: Measured Fringe Orders for the Cylindrical Specimen 3 in Tension at Slice Location I-1

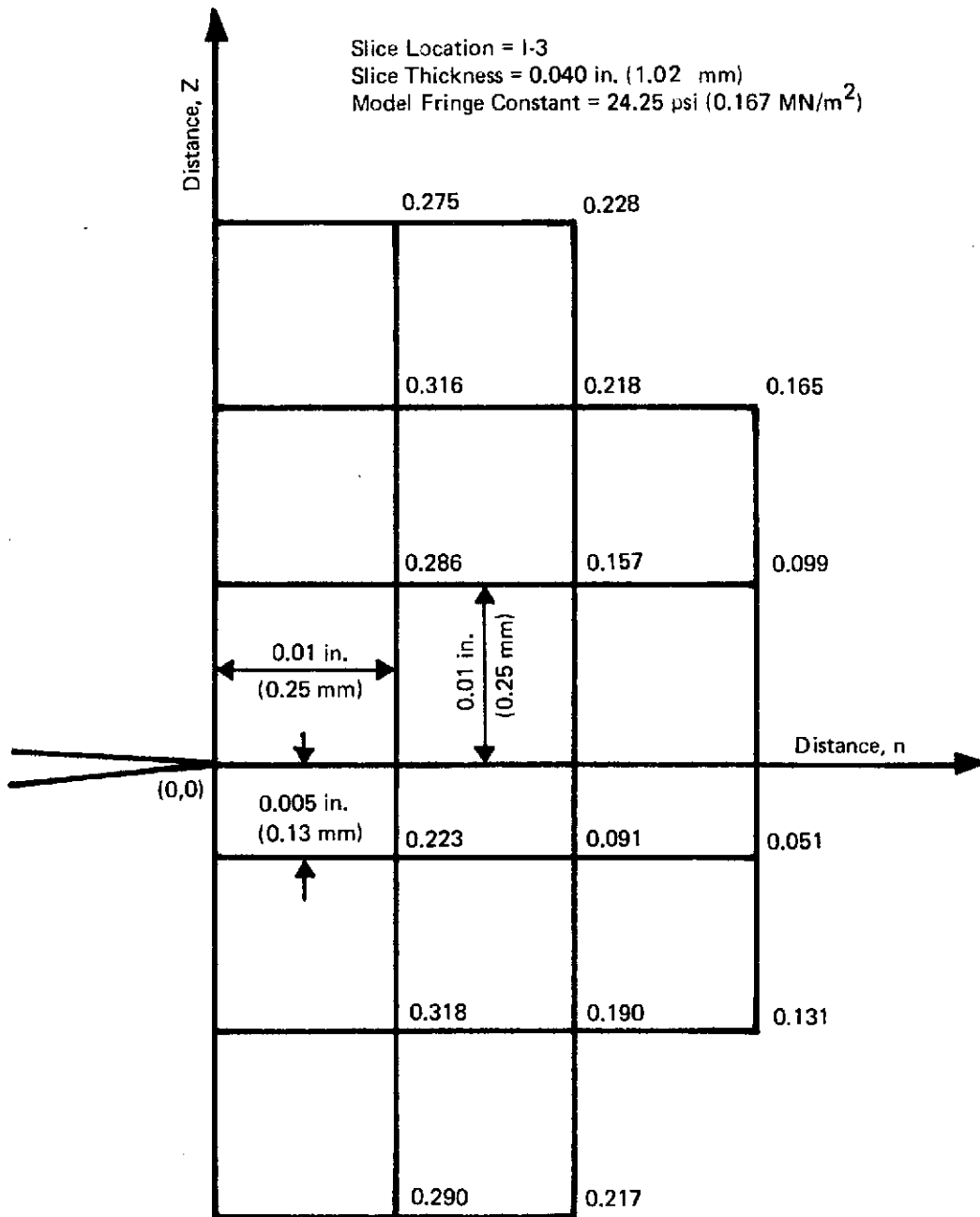


Figure A-5: Measured Fringe Orders for the Cylindrical Specimen 3 in Tension at Slice Location I-3

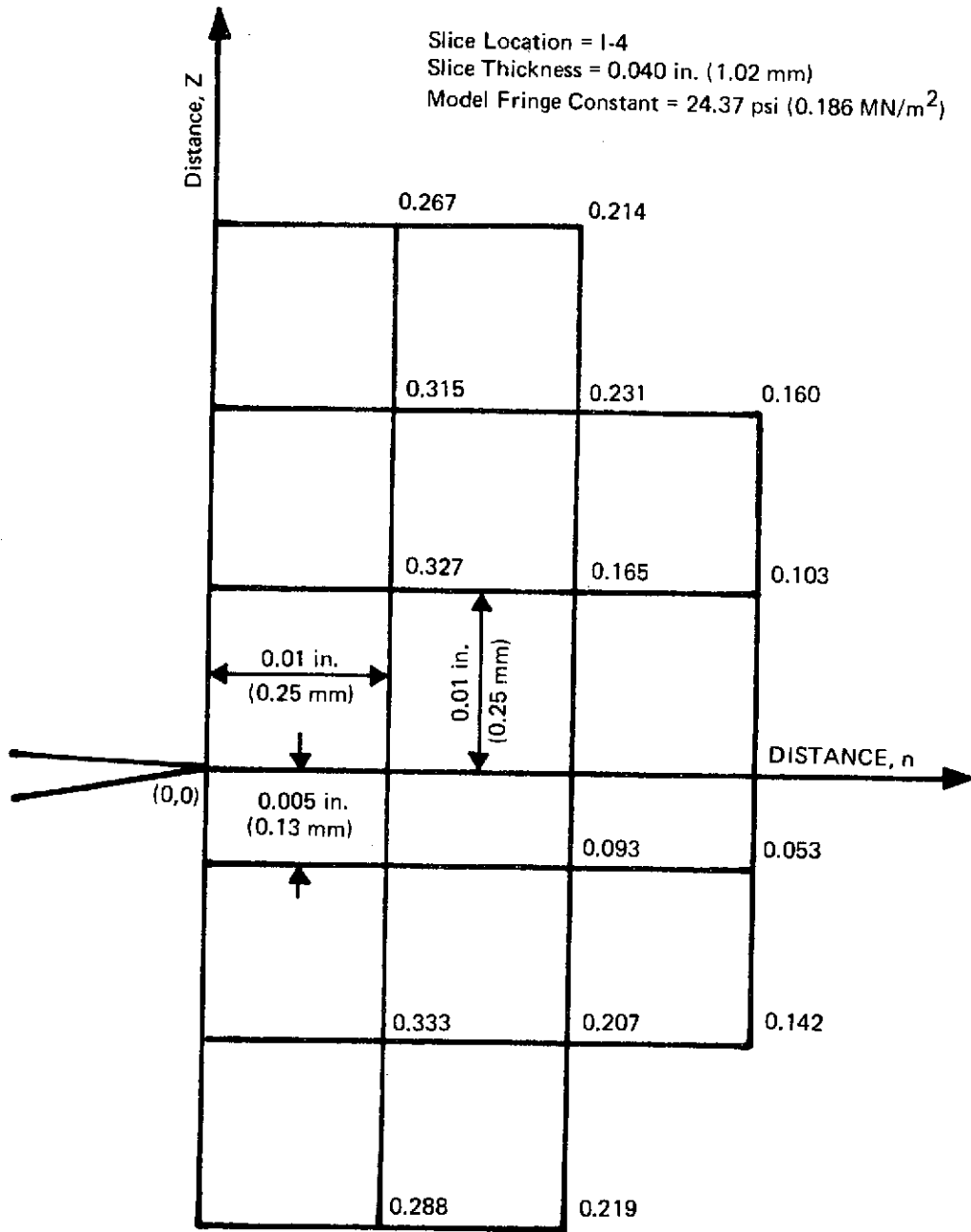


Figure A-6: Measured Fringe Orders for the Cylindrical Specimen 3 in Tension at Slice Location I-4

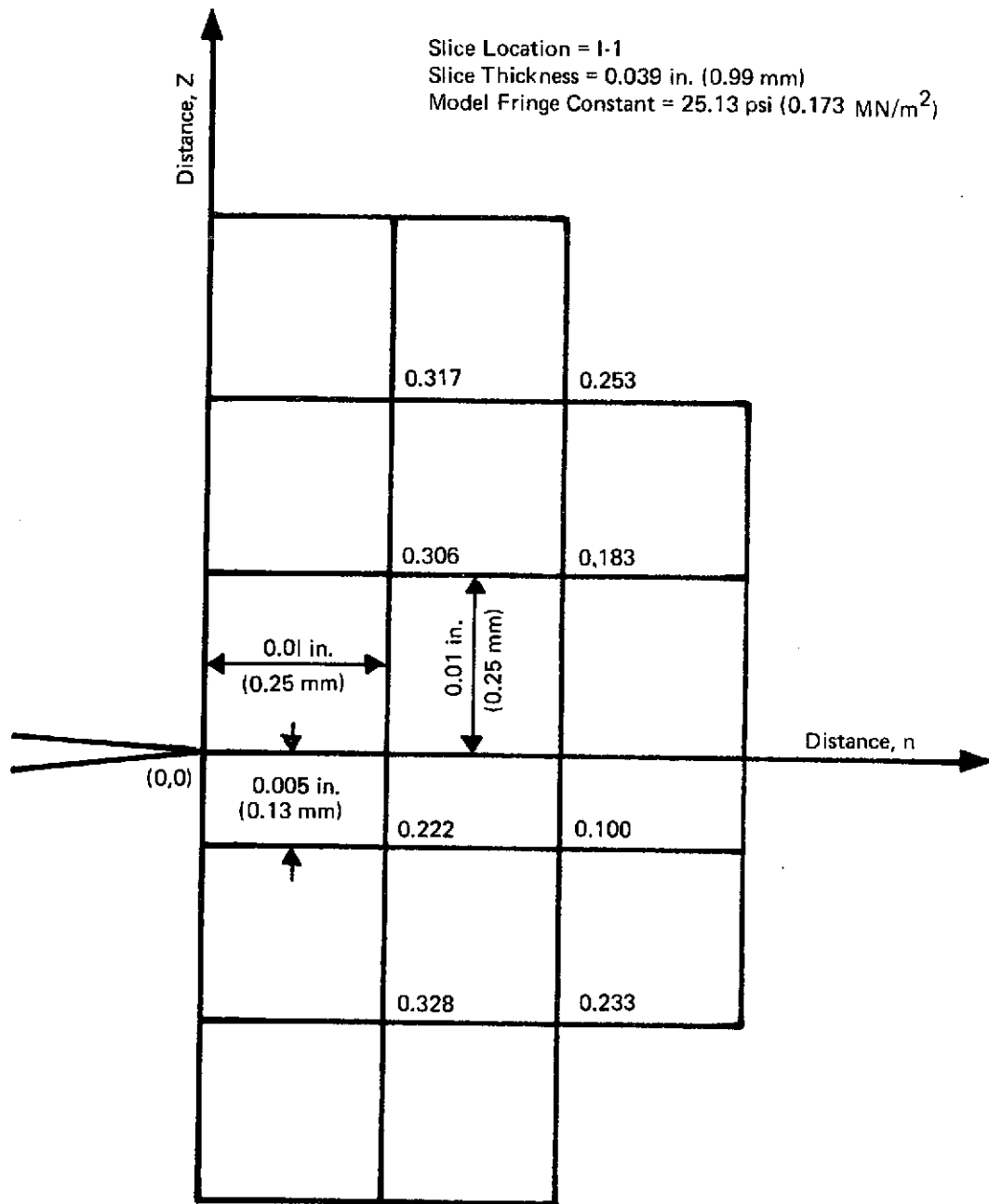


Figure A-7: Measured Fringe Orders for the Cylindrical Specimen 5 in Tension at Slice Location I-1

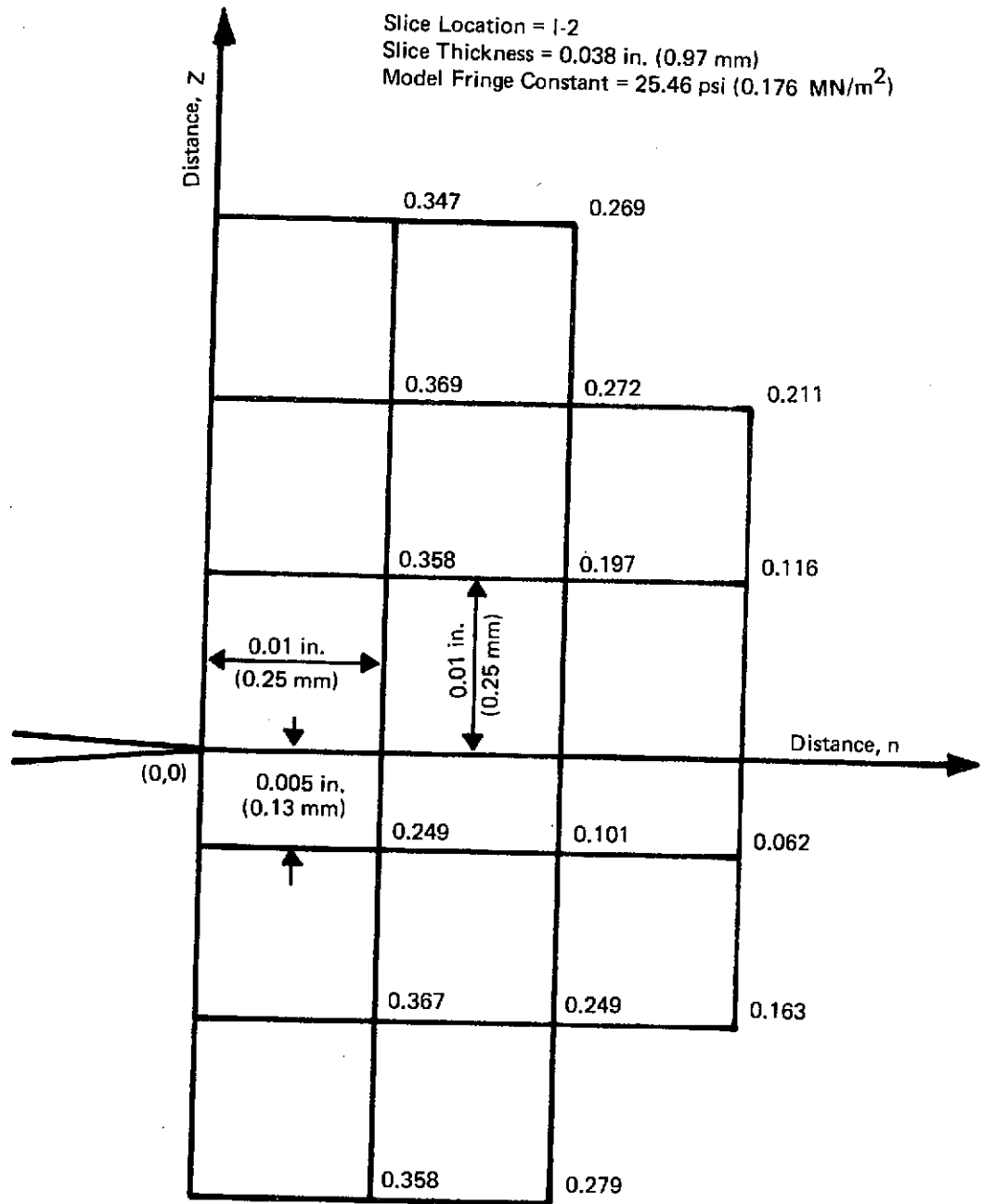


Figure A-8: Measured Fringe Orders for the Cylindrical Specimen 5 in Tension at Slice Location 1-2

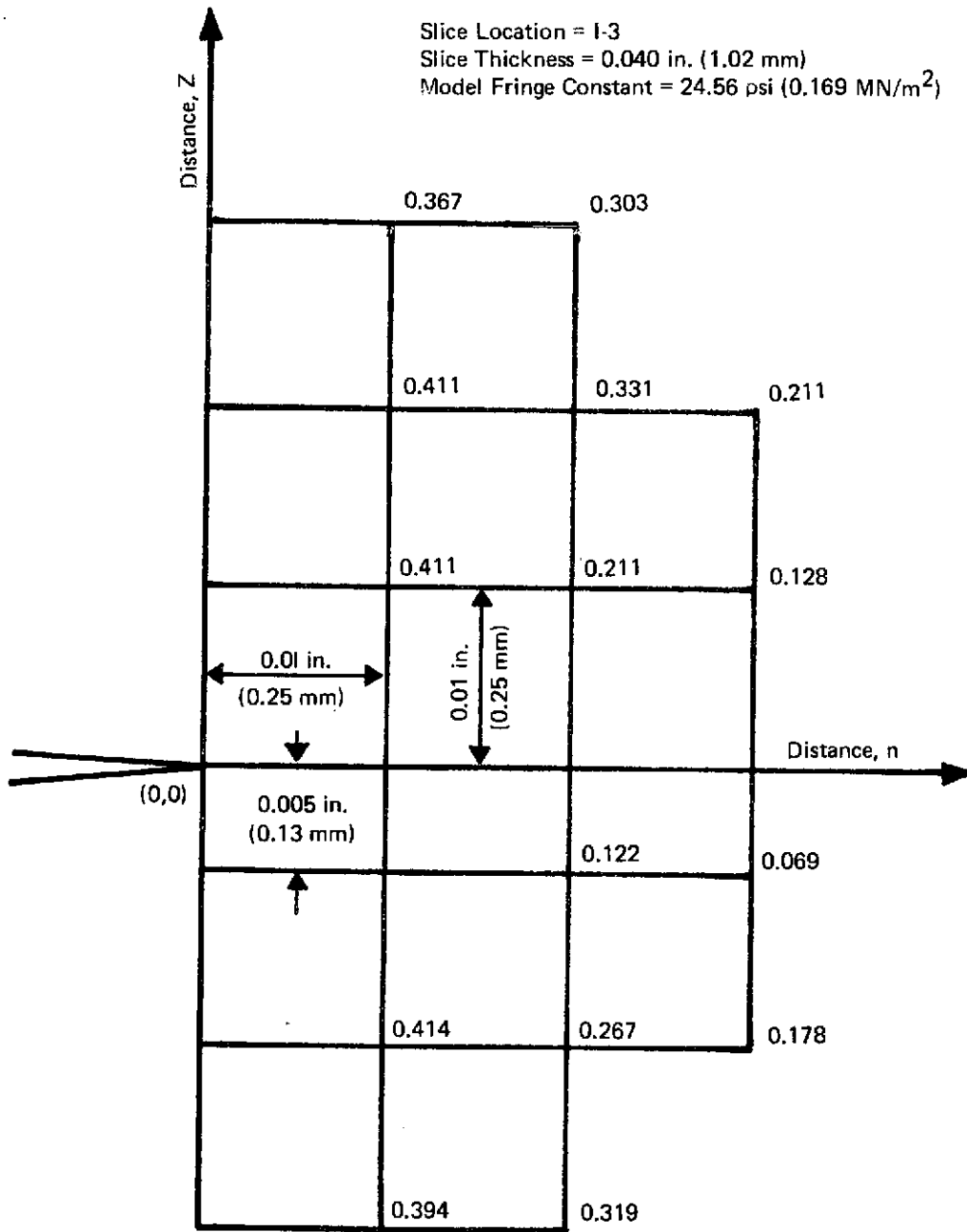


Figure A-9: Measured Fringe Orders for the Cylindrical Specimen 5 in Tension at Slice Location I-3

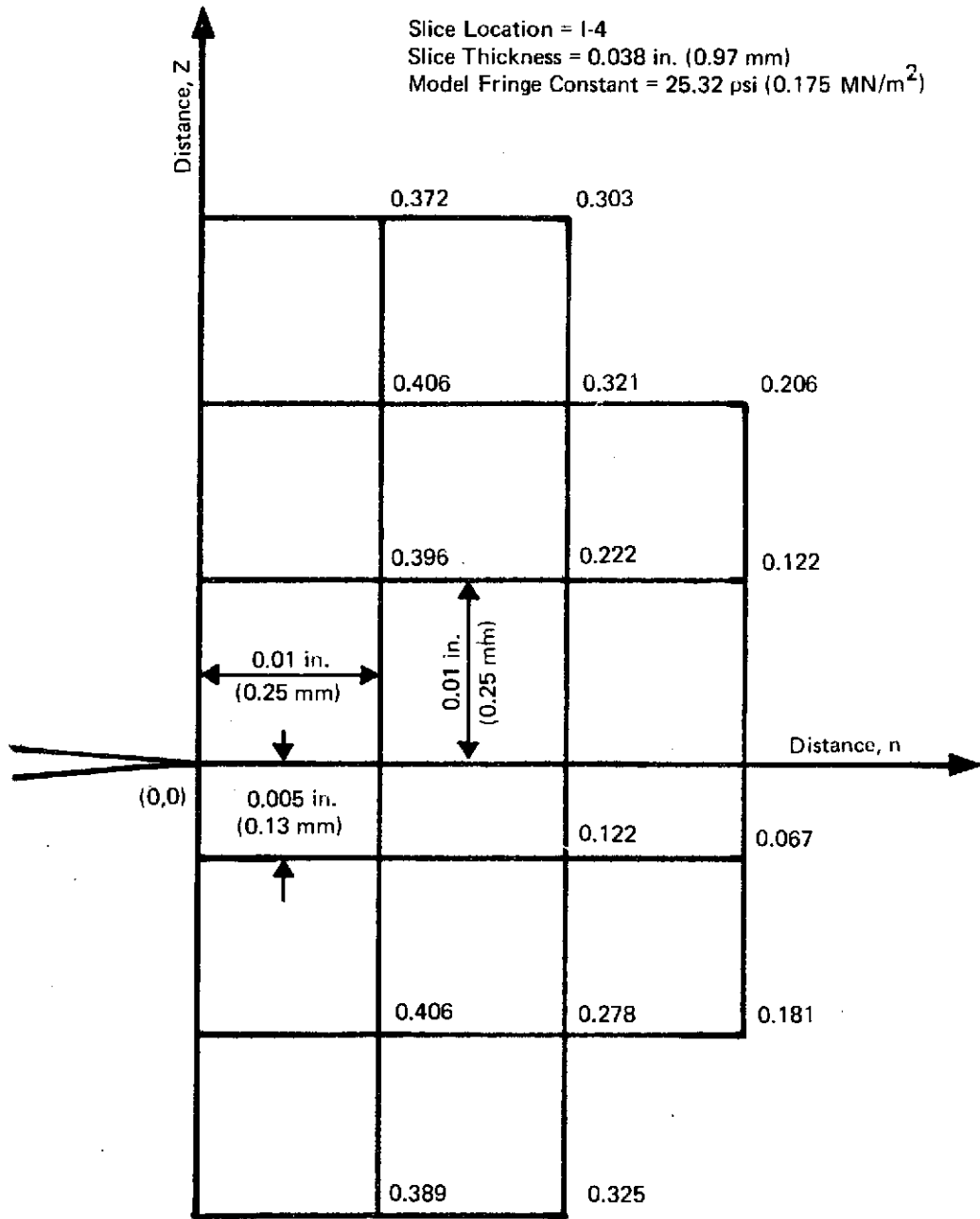


Figure A-10: Measured Fringe Orders for the Cylindrical Specimen 5 in Tension at Slice Location I-4



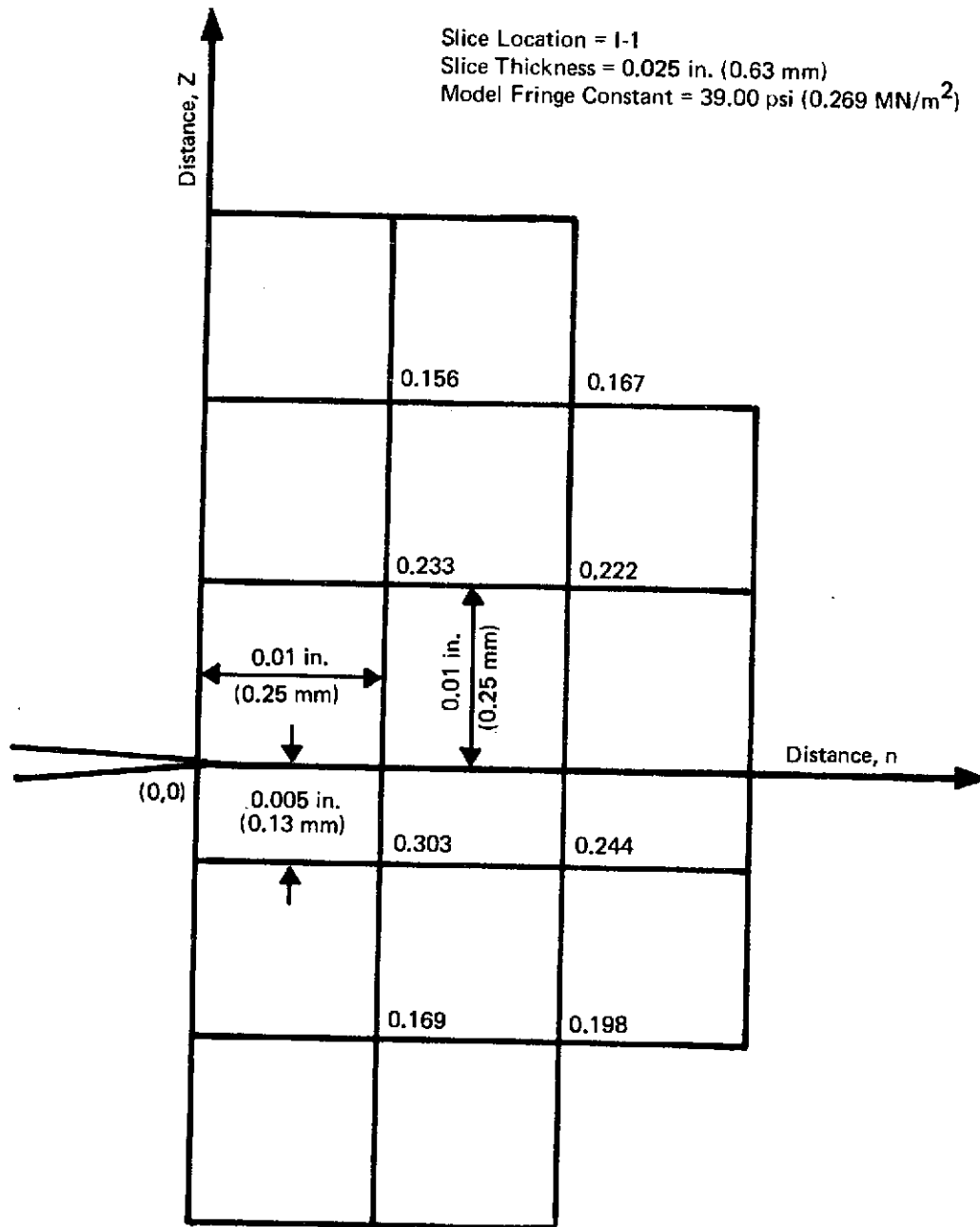


Figure A-11: Measured Fringe Orders for the Cylindrical Specimen 2 in Torsion at Slice Location I-1

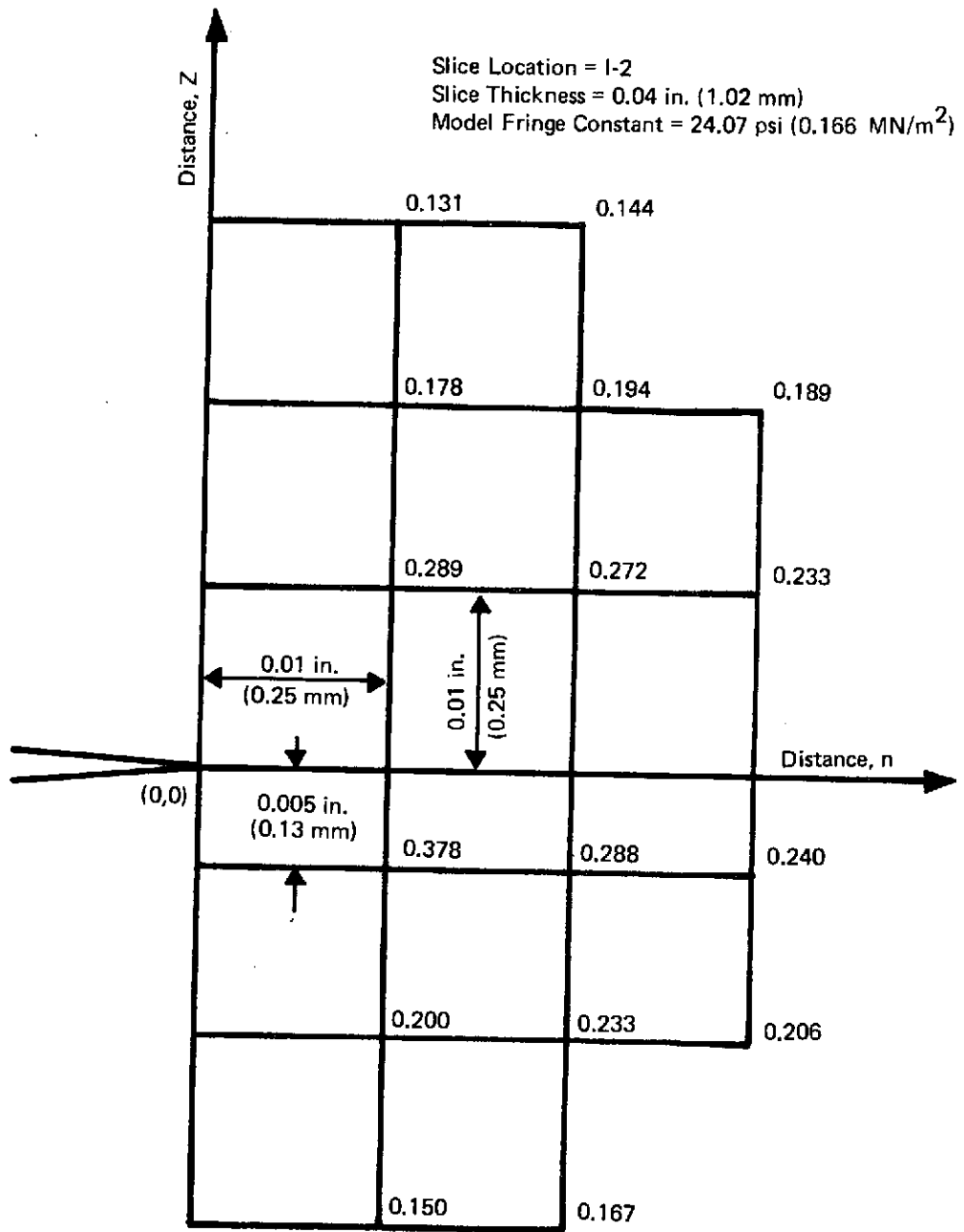


Figure A-12: Measured Fringe Orders for the Cylindrical Specimen 2 in Torsion at Slice Location I-2

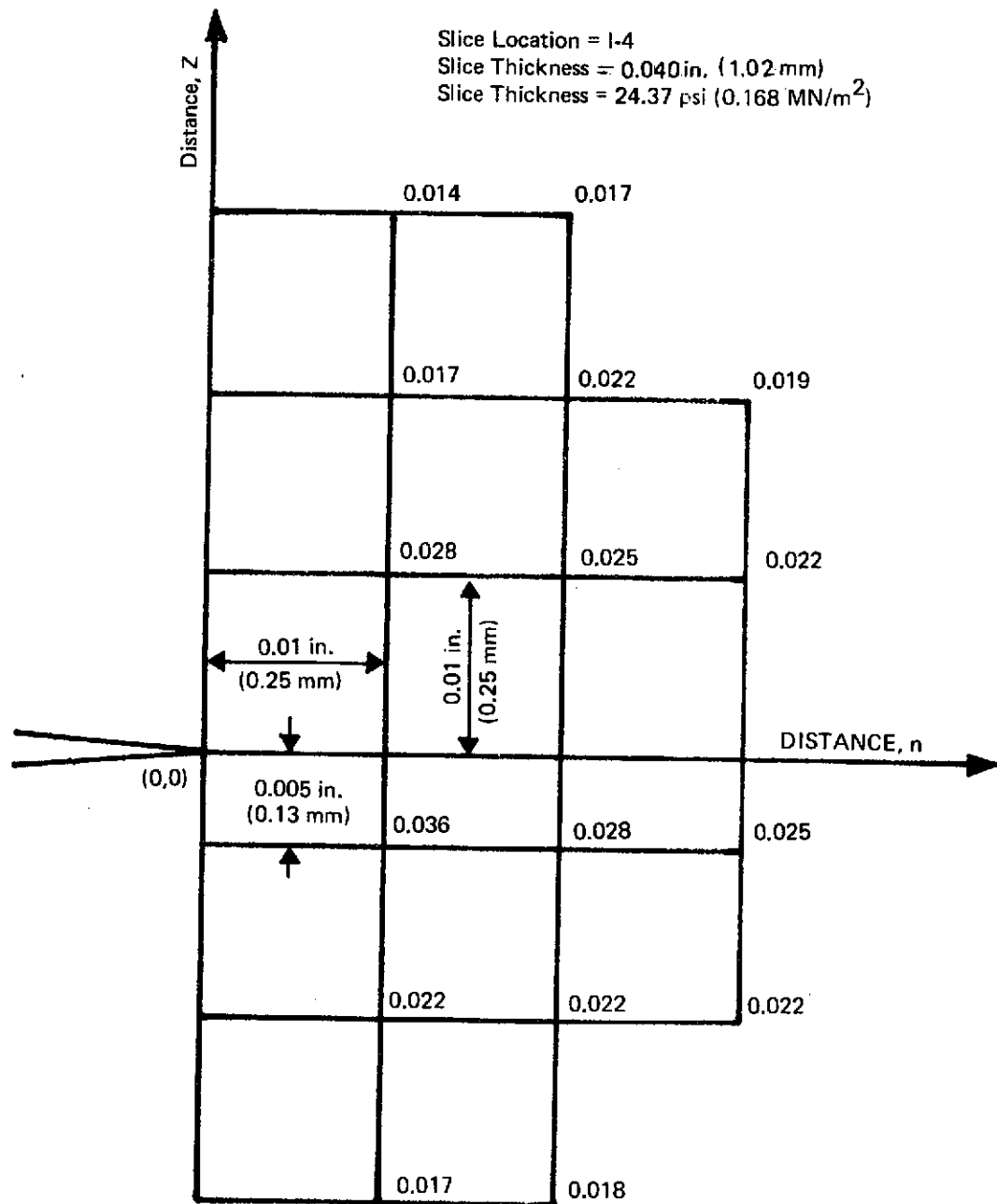


Figure A-13: Measured Fringe Orders for the Cylindrical Specimen 2 in Torsion at Slice Location I-4

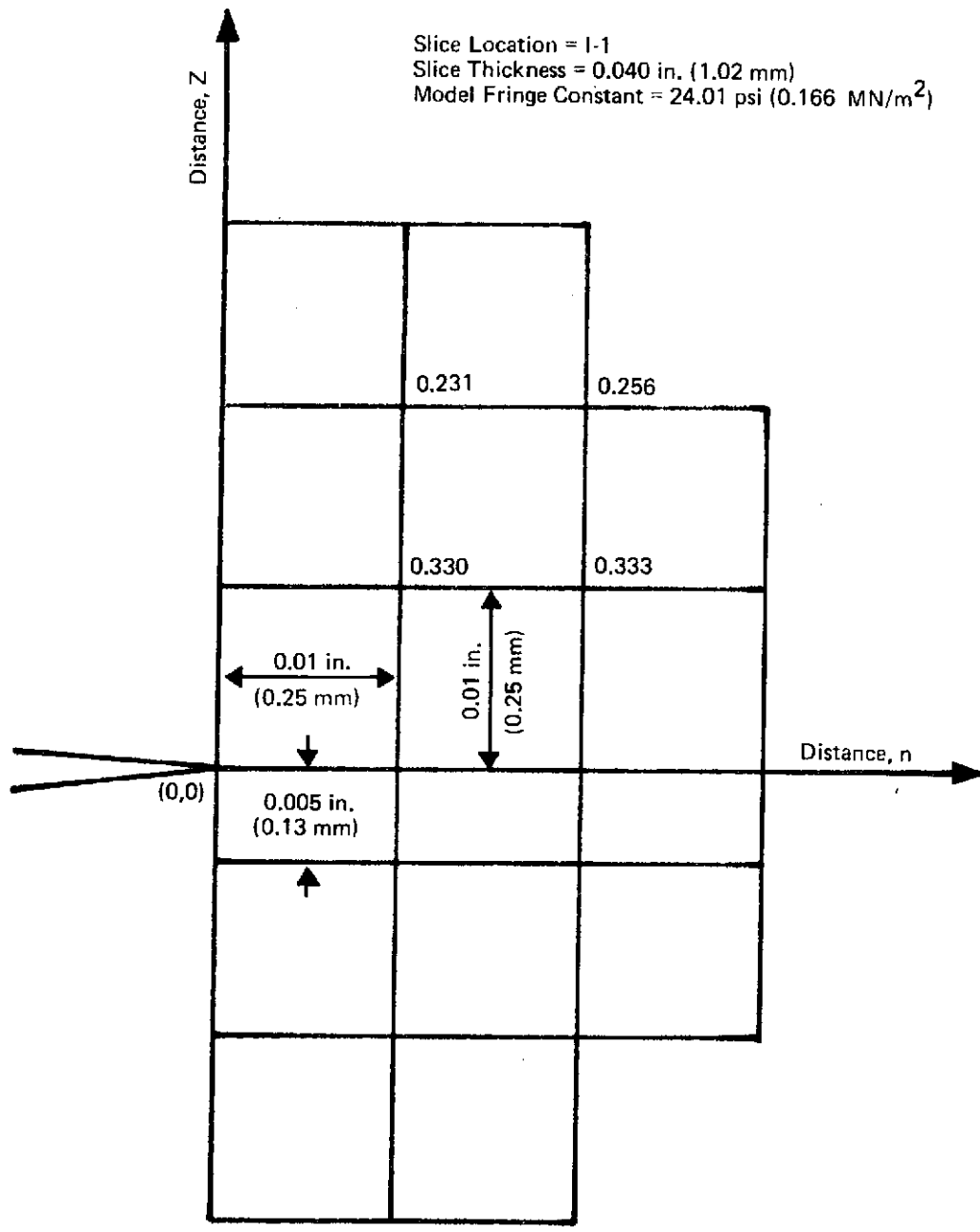


Figure A-14: Measured Fringe Orders for the Cylindrical Specimen 4 in Torsion at Slice Location I-1

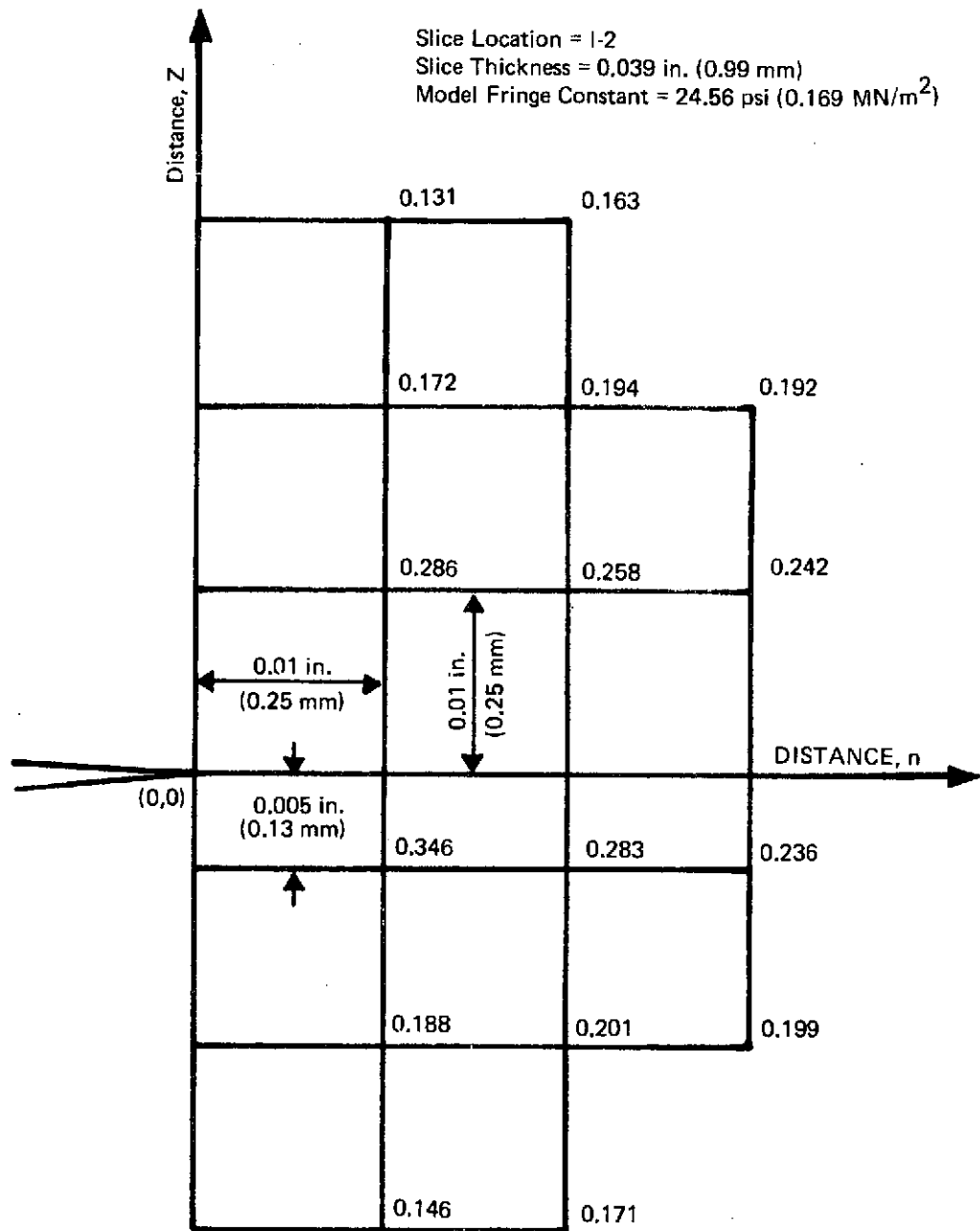


Figure A-15: Measured Fringe Orders for the Cylindrical Specimen 4 in Torsion at Slice Location I-2

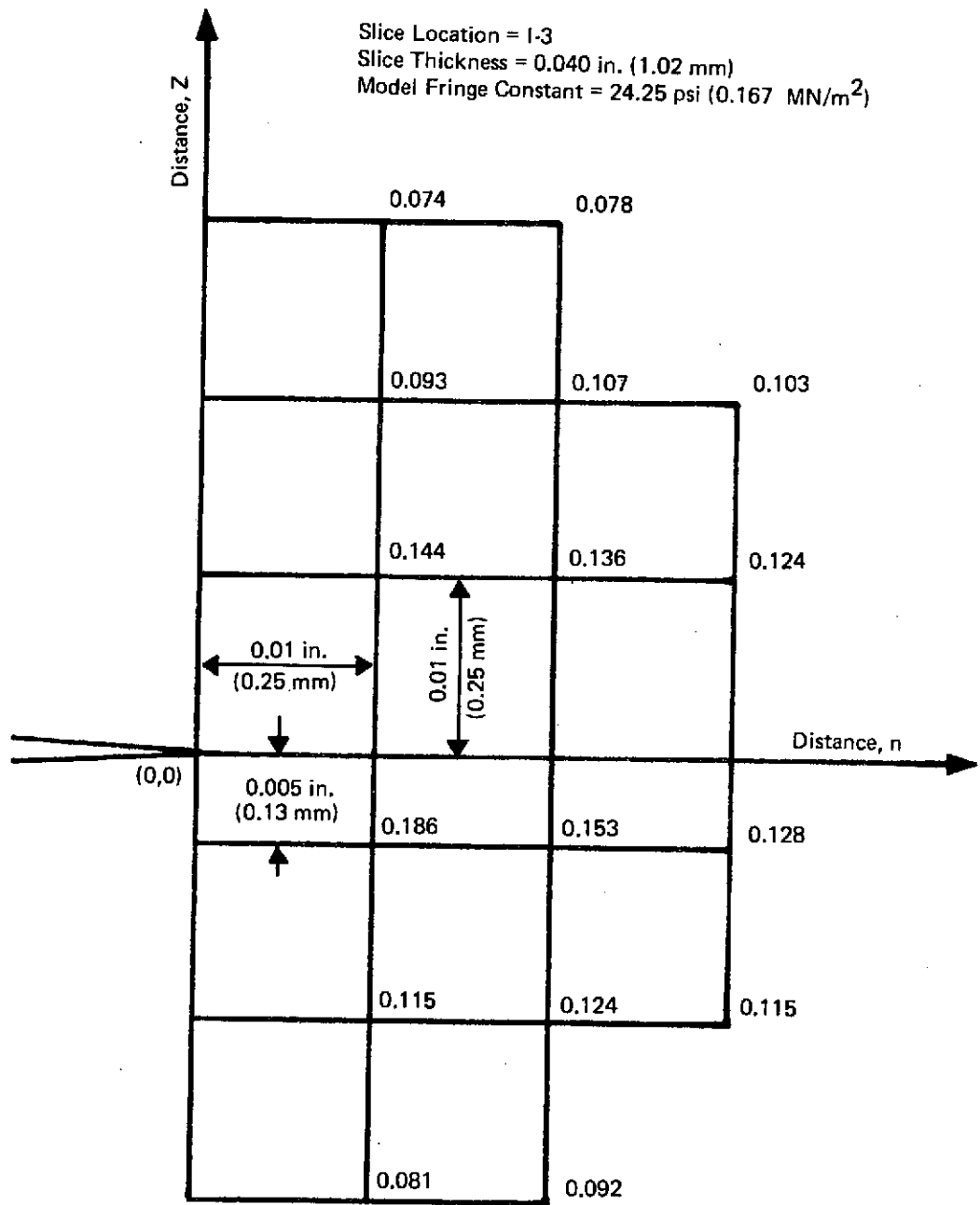


Figure A-16 : Measured Fringe Orders for the Cylindrical Specimen 4 in Torsion at Slice Location I-3

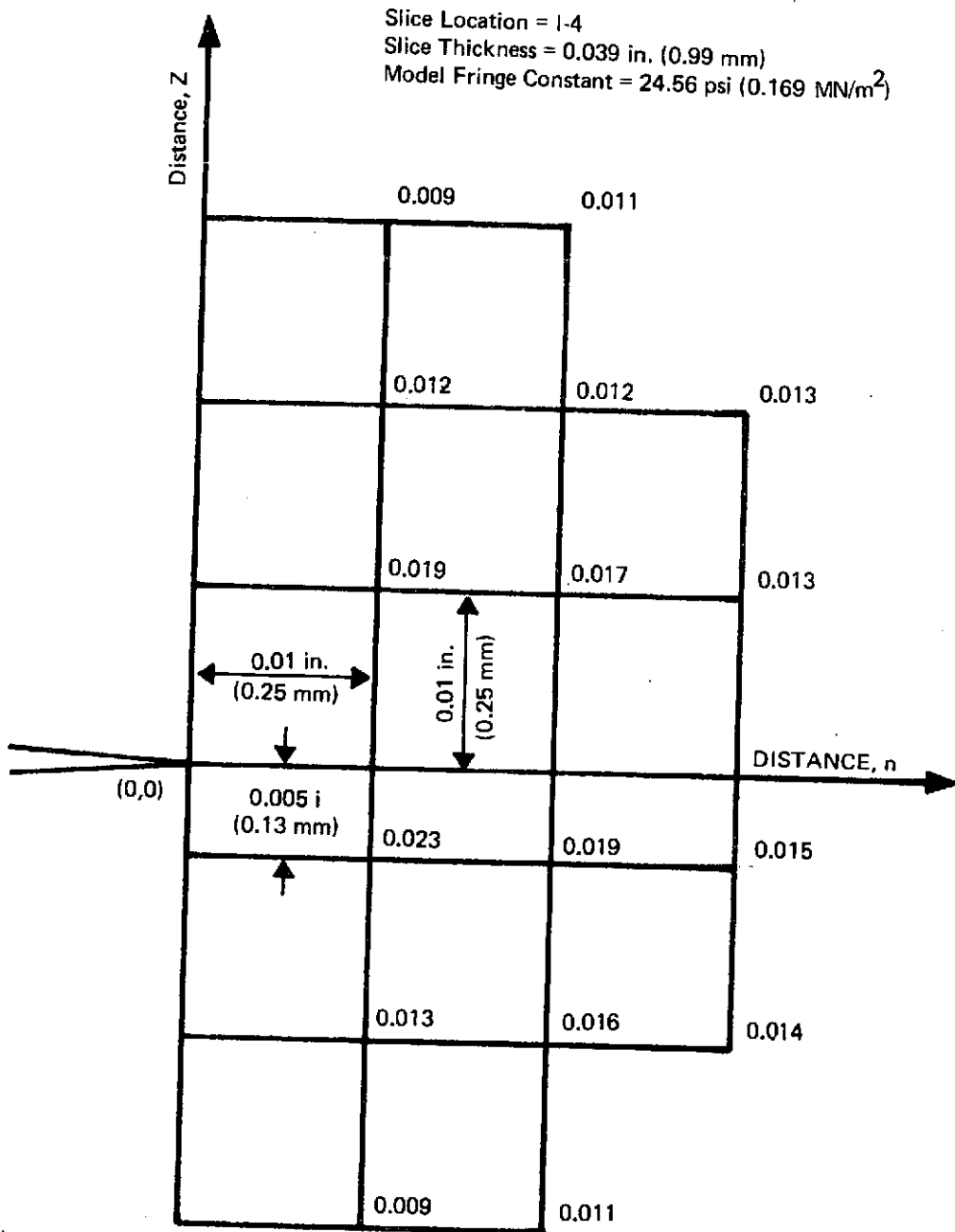


Figure A-17: Measured Fringe Orders for the Cylindrical Specimen 4 in Torsion at Slice Location 1-4

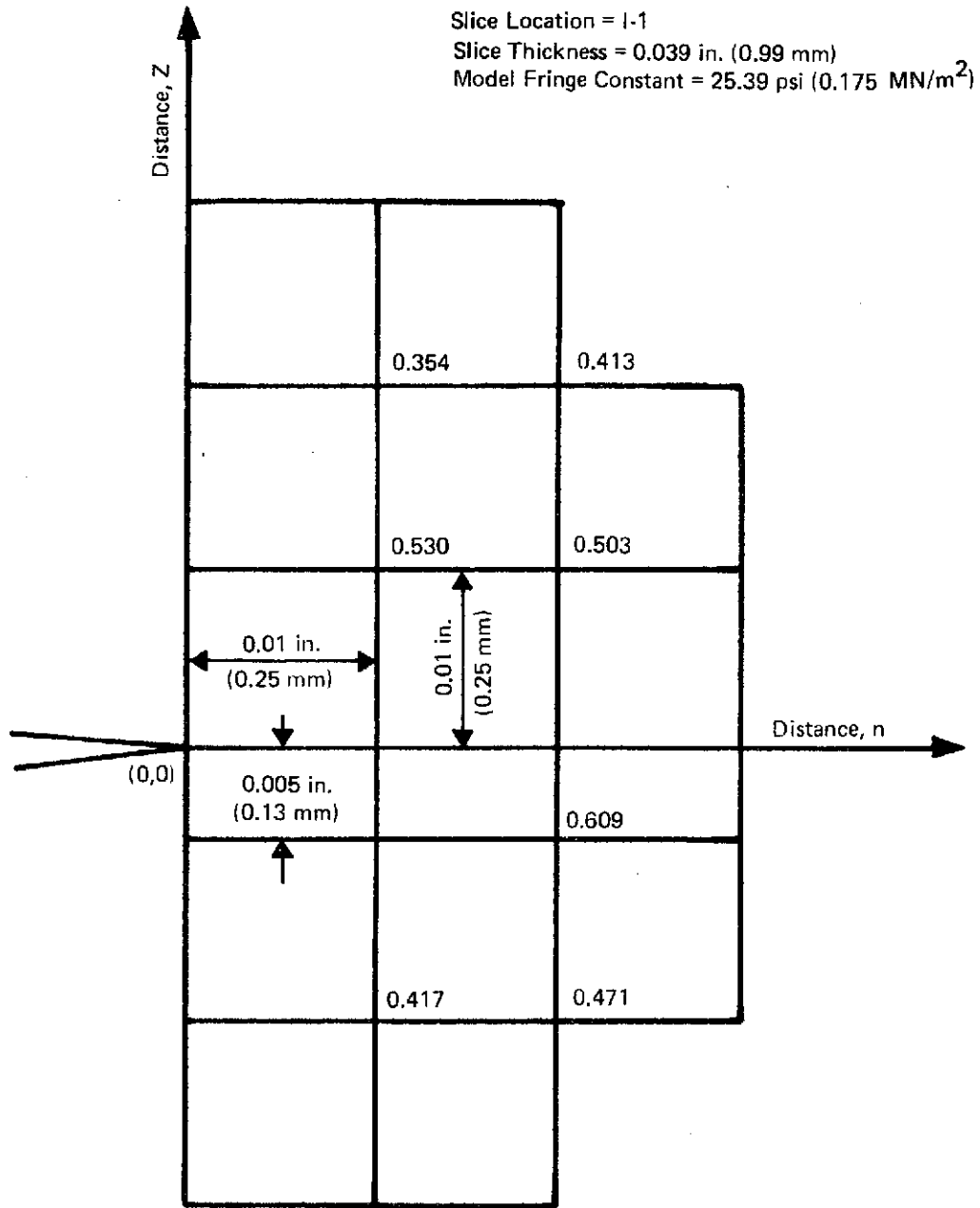


Figure A-18: Measured Fringe Orders for the Cylindrical Specimen 6 in Torsion at Slice Location 1-1



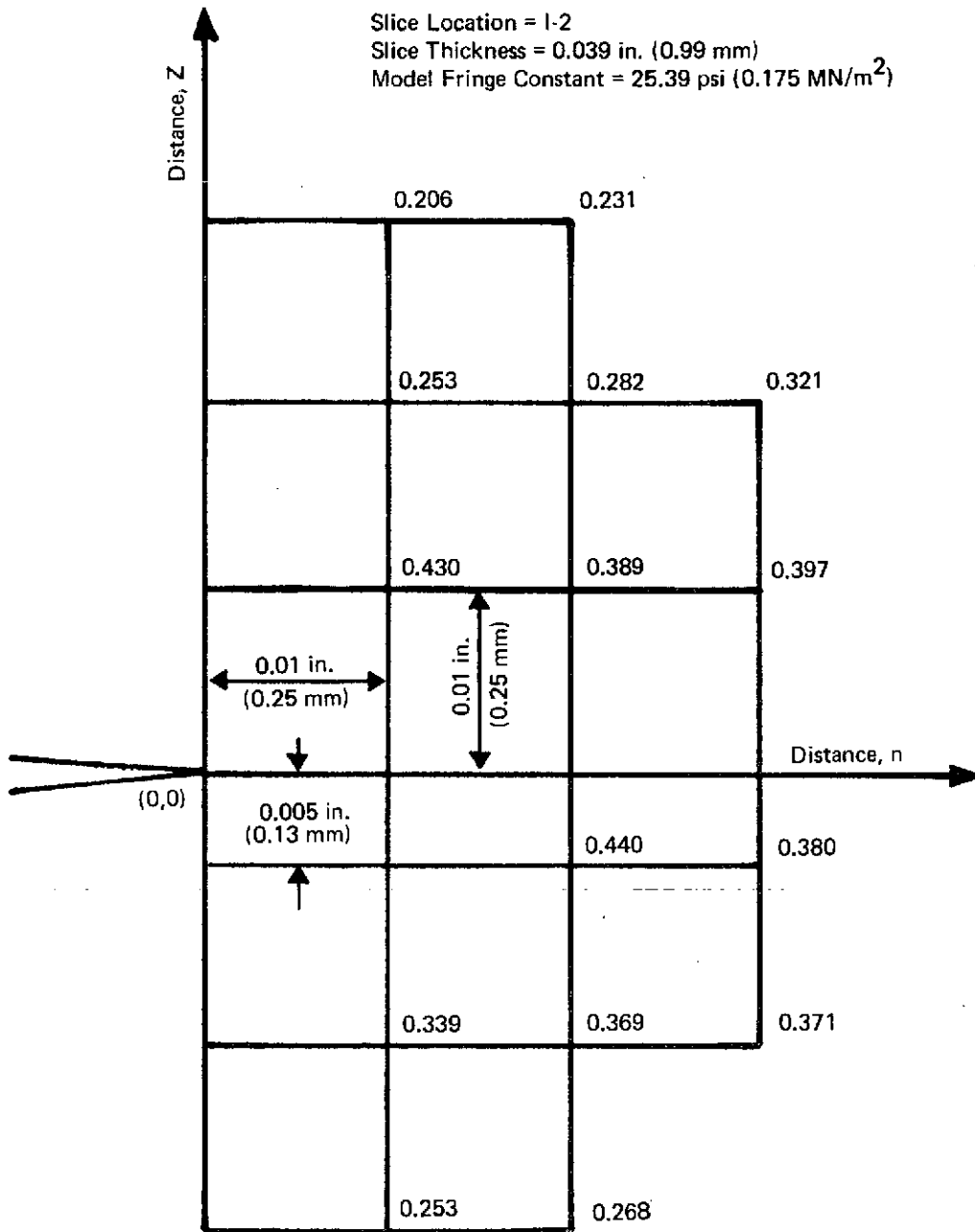


Figure A-19: Measured Fringe Orders for the Cylindrical Specimen 6 in Torsion at Slice Location 1-2

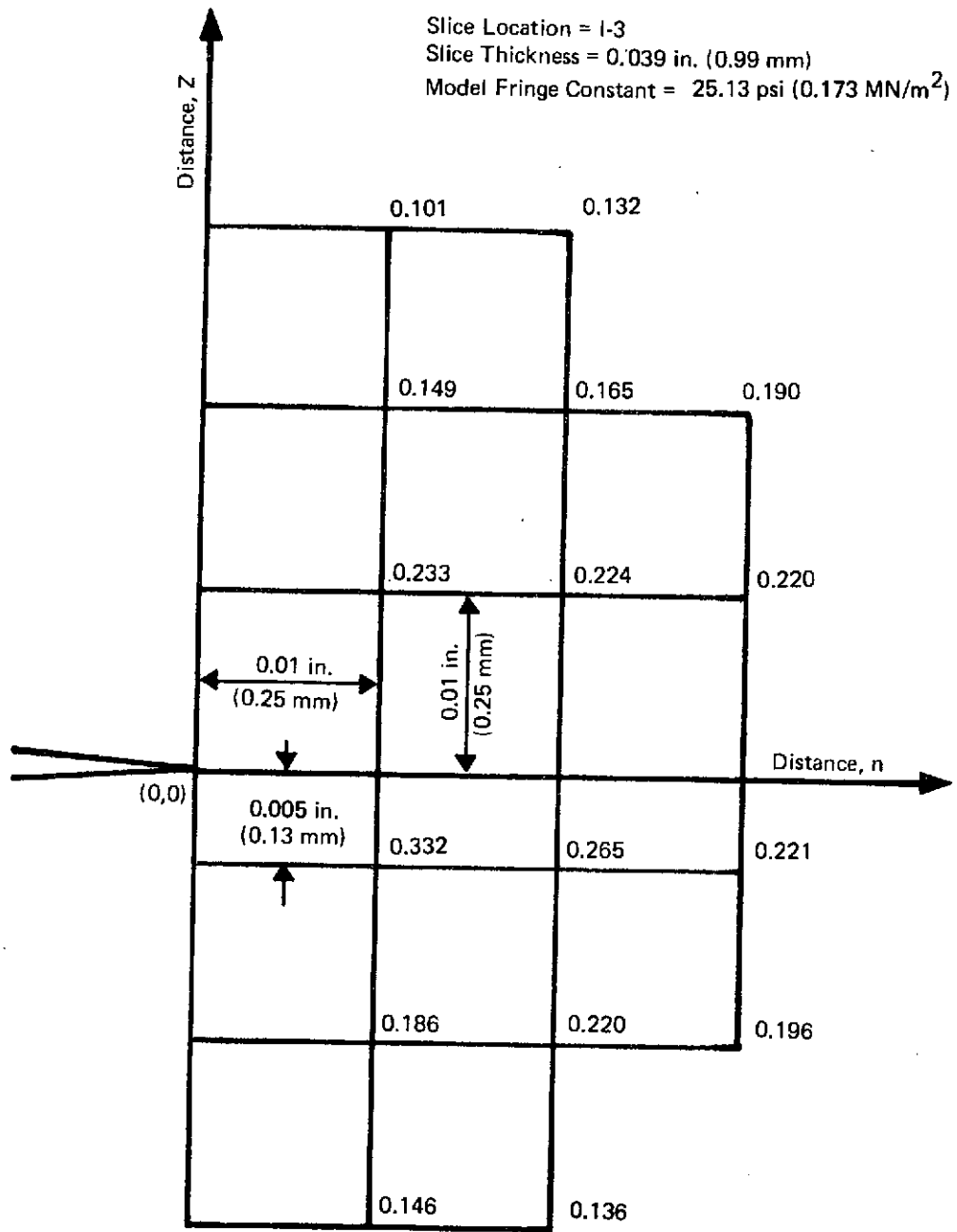


Figure A-20: Measured Fringe Orders for the Cylindrical Specimen 6 in Torsion at Slice Location I-3

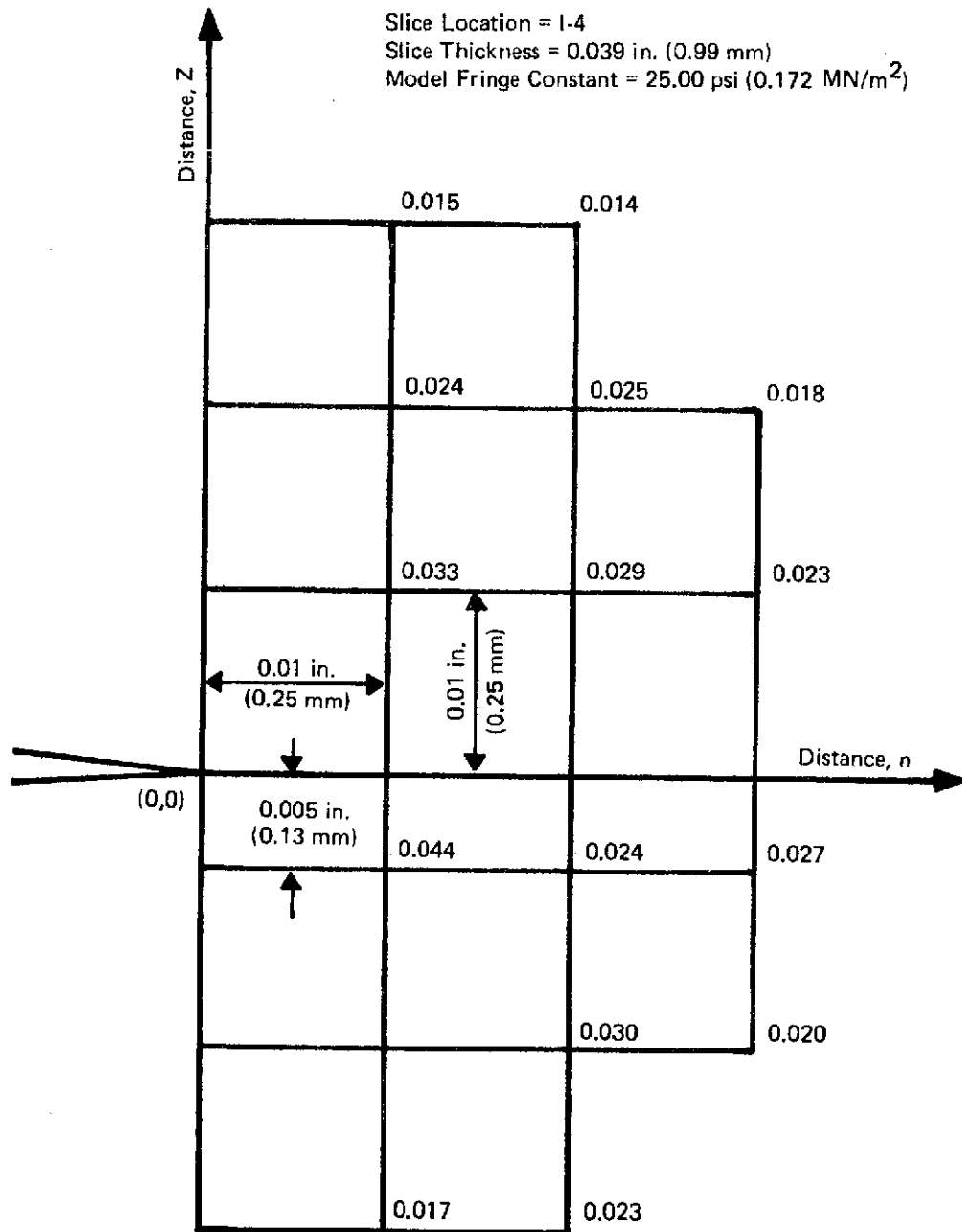


Figure A-21: Measured Fringe Orders for the Cylindrical Specimen 6-4 in Torsion at Slice Location I-4

Table A-1: Measured Maximum Shear Stress  $\tau_{nt}$  at Various Locations of Distance  $n$  for Cylindrical Specimens Subjected to Torsion

SPECIMEN NUMBER	SUBSLICE LOCATION	MAX SHEAR STRESS $\tau_{nt}$ IN PSI (KN/m <sup>2</sup> ) AT Z = 0.02 IN. (0.51 mm), t = 0.0, AND AT					
		n = 0.005 IN. = (0.127 mm)	n = 0.010 IN. = (0.254 mm)	n = 0.015 IN. = (0.381 mm)	n = 0.020 IN. = (0.508 mm)	n = 0.025 IN. = (0.635 mm)	n = 0.030 IN. = (0.762 mm)
2	I-1	3.73 (25.7)	3.22 (22.2)	2.72 (18.8)	2.01 (13.9)	—	—
	I-2	2.93 (20.2)	2.49 (17.2)	2.00 (13.8)	1.70 (11.7)	1.22 (8.4)	1.00 (6.9)
	I-4	3.45 (23.8)	2.96 (20.4)	2.26 (15.6)	1.90 (13.1)	1.55 (10.7)	1.30 (9.0)
4	I-1	3.58 (24.7)	3.01 (20.8)	2.25 (15.5)	1.82 (12.5)	—	—
	I-2	3.92 (27.0)	3.25 (22.4)	3.01 (20.8)	2.48 (17.1)	1.82 (12.5)	1.53 (10.5)
	I-3	3.34 (23.0)	2.82 (19.4)	2.29 (15.8)	1.77 (12.2)	1.43 (9.9)	1.15 (7.9)
	I-4	2.39 (16.5)	1.86 (12.8)	1.53 (10.5)	1.15 (7.9)	0.91 (6.3)	—
6	I-1	3.50 (24.1)	2.84 (19.6)	2.32 (16.0)	1.85 (12.8)	—	—
	I-2	2.97 (20.5)	2.48 (17.1)	1.96 (13.5)	1.64 (11.3)	1.24 (8.5)	—
	I-3	2.50 (17.2)	2.10 (14.5)	1.56 (10.8)	1.23 (8.5)	1.00 (6.9)	—
	I-4	2.30 (15.9)	1.90 (13.1)	1.49 (10.3)	1.14 (7.9)	0.95 (6.6)	—

APPENDIX B: LIST OF SYMBOLS

a	Crack depth of surface flaw or semi-minor axis of ellipse or half crack length for through cracks.
b	Half width of through cracked specimens.
2c	Crack length of surface flaw or major axis of ellipse.
d	Diameter of the round bar in the plane of the crack.
D	Diameter of the round bar.
E	Young's modulus.
$E(k)$	Complete elliptical integral of the second kind.
I	Moment of inertia
$k, k'$	Modulus and complementary modulus for elliptical integrals given by $k^2 = 1 - a^2/c^2$ and $k'^2 = a^2/c^2$ .
$K(k)$	Complete elliptical integral of the first kind.
$K_I$	Opening mode or Mode I stress intensity factor.
$K_{II}$	Sliding mode or Mode II stress intensity factor.
$K_{III}$	Tearing mode or Mode III stress intensity factor.
$K_{Ic}$	Plane strain fracture toughness for Mode I.
$K_{IIc}$	Plane strain fracture toughness for Mode II
$K_{IIIc}$	Plane strain fracture toughness for Mode III.
$K_{IE}$	Plane strain fracture toughness for Mode I from surface flawed specimens.
$K_{Ib}$	Mode I stress intensity factor due to pure bending.
$K_{It}$	Mode I stress intensity factor due to extensional (tensile) loading only.
$M_B$	Parameter for stress intensity factor for a semi-elliptical surface crack in a plate subjected to bending.
$M_K$	Stress intensity magnification factor for a semi-elliptical surface crack in a plate subjected to uniform tension.

n,t,z	Local curvilinear orthogonal coordinate system at the crack front.
P	Applied load.
Q	$[E(k)]^2 - 0.212 (\sigma/\sigma_{ys})^2$
r	Radial distance from crack front in x-y or n-z plane.
t	Thickness of flat specimen or tube.
T	Applied torque.
W	Width of flat specimens.
x,y,z	Cartesian coordinates.
Y	Dimensionless stress intensity coefficient for single edge cracks.
$\alpha$	Proof test factor.
$\delta$	Crack opening displacement at the diametral center for an elliptical crack or flaw opening displacement for a surface flaw.
$\theta$	Angle in polar coordinates.
$\lambda$	Shell parameter.
$\mu$	Shear modulus.
$\nu$	Poisson's ratio.
$\rho$	Notch root radius.
$\sigma$	Gross applied tensile stress.
$\sigma_B$	Maximum bending stress at outer fibers of the flat specimen.
$\tau$	Maximum shear stress at outer fibers (surface) of a cylindrical specimen subjected to torque T. $\tau = 16T/(D^3)$ .
$\sigma_{ys}$	Uniaxial tensile yield strength.
$\phi$	Angle between the crack plane and specimen cross section.

## SUBSCRIPTS

- i at initial conditions
- cr at critical conditions
- f at final conditions
- F at fracture

DISTRIBUTION LIST FOR FINAL REPORT NASA CR-134611

CONTRACT NAS3-14346

EFFECTS OF PROOF LOADS AND COMBINED MODE LOADINGS  
ON FRACTURE AND FLAW GROWTH CHARACTERISTICS OF AEROSPACE ALLOYS

BOEING AEROSPACE COMPANY  
SEATTLE, WASHINGTON

Copies

NASA-Lewis Research Center 21000 Brookpark Rd. Cleveland, OH 44135	
Attn: Contracting Officer, MS 500-313	1
Technical Report Control Office, MS 5-5	1
Technology Utilization Office, MS 3-16	1
AFSC Liaison Office, MS 501-3	1
Library, MS 60-3	1
R. H. Johns, MS 49-3	1
G. T. Smith, Project Manager, MS 49-3	20
R. H. Kemp, MS 49-3	1
W. F. Brown, Jr., MS 105-1	1
J. E. Srawley, MS 105-1	1
J. C. Freche, MS 49-1	1
R. W. Hall, MS 49-1	1
National Aeronautics and Space Administration Washington, DC 20546	
Attn: RPX/Chief, Liquid Experimental Engineering	1
KT/Technology Utilization Office	1
RW/G. C. Deutsch	1
Library	1
National Technical Information Service	18
Springfield, VA 22151	
Attn: NASA Representative	
Box 333	
College Park, MD 20740	2
NASA-Ames Research Center Moffett Field, CA 94035	
Attn: Library	1
D. Williams	1
NASA-Flight Research Center P.O. Box 273 Edwards, CA 93523	
Attn: Library	1



NASA-Goddard Space Flight Center  
Greenbelt, MD 20771  
Attn: Library 1

NASA-John F. Kennedy Space Center  
Kennedy Space Center, FL 32931  
Attn: Library 1

NASA-Langley Research Center  
Hampton, VA 23365  
Attn: Library 1  
R. W. Leonard 1  
H. Hardrath 1  
W. Elber 1

NASA-Manned Spacecraft Center  
Houston, TX 77001  
Attn: Library 1  
R. E. Johnson 1  
S. V. Glorioso 1

NASA-Marshall Space Flight Center  
Marshall Space Flight Center, AL 35812  
Attn: Library 1  
S&E-ASTN/AA/C. Lifer 1  
S&E-ASTN/ASR/C. Crockett 1  
S&E-ASTN-AS/H. Coldwater 1

Air Force Office of Scientific Research  
Washington, DC 20333  
Attn: Library 1

Air Force Rocket Propulsion Laboratory (RPM)  
Edwards, CA 93523  
Attn: Library 1

Air Force Systems Command  
Aeronautical Systems Division  
Wright-Patterson AFB, OH 45433  
Attn: Library 1  
C. F. Tiffany, Code ENF 1

Air Force Systems Command  
Andrews Air Force Base  
Washington, DC 20332  
Attn: Library 1

Air Force Systems Command  
Arnold Engineering Development Center  
Tallahoma, TN 37389  
Attn: Library 1

Wright-Patterson Air Force Base  
Wright-Patterson Air Force Base, OH 45433  
Attn: H. A. Wood  
N. G. Tupper

Frankford Arsenal  
Philadelphia, PA 19137  
Attn: 1320/Library  
C. Carman

Department of the Army  
U.S. Army Material Command  
Washington, DC 20315  
Attn: AMCRD-RC

U.S. Army Missile Command  
Redstone Scientific Information Center  
Redstone Arsenal, AL 35808  
Attn: Document Section

Commanding Officer  
U.S. Army Research Office (Durham)  
Box CM, Duke Station  
Durham, NC 27706  
Attn: Library

Bureau of Naval Weapons  
Department of the Navy  
Washington, DC 20360  
Attn: RRRE-6

Commander  
U.S. Naval Ordnance Laboratory  
White Oak  
Silver Springs, MD 20910  
Attn: Library

Director, Code 6180  
U.S. Naval Research Laboratory  
Washington, DC 20390  
Attn: Library  
J. M. Krafft

Atomic Energy Commission  
Division of Reactor Development and Technology  
Washington, DC 20767

National Science Foundation  
Engineering Division  
1800 G Street, NW  
Washington, DC 20540  
Attn: Library

Battelle Memorial Institute 505 King Avenue Columbus, OH 43201 Attn: Library	1
E. Hulbert (Dr.)	1
G. Hahn (Dr.)	1
C. Federson	1
 IIT Research Institute Technology Center Chicago, IL 60616 Attn: Library	   1
 Stanford Research Institute 3333 Ravenswood Ave. Menlo Park, CA 94025 Attn: Library	   1
 Brown University Providence, RI Attn: Technical Library	   1
J. R. Rice (Dr.)	1
 California Institute of Technology Pasadena, CA Attn: Technical Library	   1
V. F. Zackay	1
 Case Western Reserve University 10090 Euclid Ave. Cleveland, OH 44115 Attn: Technical Library	   1
 Carnegie Institute of Technology Department of Civil Engineering Pittsburgh, PA 15213 Attn: Library	   1
 Colorado State University Dept. of Mechanical Engineering Ft. Collins, CO 80521 Attn: F. Smith (Dr.)	   1
 Cornell University Dept. of Materials Science and Engineering Ithaca, NY 14830 Attn: Library	   1
 Massachusetts Institute of Technology Cambridge, MA Attn: Library	   1

Pennsylvania State University State College, PA Attn: Library	1
University of Denver Denver Research Institute P.O. Box 10126 Denver, CO 80210 Attn: Library	1
Aerojet Liquid Rocket Company P.O. Box 15847 Sacramento, CA 95813 Attn: Technical Library, 2484-2115A	1
Aerospace Corp. 2400 E. El Segundo Blvd. Los Angeles, CA 90045 Attn: Library - Documents	1
Bell Aerosystems, Inc. Box 1 Buffalo, NY 14240 Attn: J. Davis	1
Brunswick Corp. Defense Products Division P.O. Box 4594 43000 Industiral Ave. Lincoln, NE Attn: Library	1
Chrysler Corp. Space Division P.O. Box 29200 New Orleans, LA 70129 Attn: P. Munafo Library	1 1
Del Research Corp. 427 Main St. Hellertown, PA 18055 Attn: P. Paris (Dr.)	1
Del West Associates, Inc. 6324 Variel Ave. Suite C Woodland Hill, CA 91364 Attn: M. Creager (Dr.)	1

General American Transportation Corp.  
General American Research Division  
7449 N. Natchez Ave.  
Niles, IL 60648  
Attn: R. N. Johnson (Dr.) |

General Dynamics  
P.O. Box 748  
Ft. Worth, TX 76101  
Attn: Library |  
C. D. Little |

General Dynamics/Convair Aerospace  
P.O. Box 1128  
San Diego, CA 92112  
Attn: Library |  
J. Jensen |  
W. Witzel |  
J. Haskins |

General Electric Co.  
Missiles and Space Systems Center  
Valley Forge Space Technology Center  
P.O. Box 8555  
Philadelphia, PA 19101  
Attn: Library |

Grumman Aircraft Engineering Corp.  
Bethpage, Long Island, NY  
Attn: Library |  
W. Judwig |

Jet Propulsion Laboratory  
4800 Oak Grove Dr.  
Pasadena, CA 91102  
Attn: Library |  
J. Lewis |

Ling-Temco-Vought Corp.  
P.O. Box 5907  
Dallas, TX 75222  
Attn: Library |

Lockheed Missiles and Space Co.  
P.O. Box 504  
Sunnyvale, CA 94087  
Attn: Library |  
R. E. Lewis |

Martin-Marietta Corp.  
 Denver Division  
 P.O. Box 179  
 Denver, CO 80201  
 Attn: P. Lorenz, MS 0431 1  
       F. Schwartzberg, MS 0430 1  
       A. Holsten, MS 0430 1  
       D. Bolstad (Michoud) (MAF) 1

McDonnell Douglas Aircraft Corp.  
 P.O. Box 516  
 Lambert Field, MO 63166  
 Attn: Library 1  
       B. Whiteson 1

McDonnell Douglas Astronautics  
 Western Division  
 5301 Bolsa Ave.  
 Huntington Beach, CA 92647  
 Attn: Library 1  
       H. Babel 1  
       R. Rawe 1

Northrop Space Laboratories  
 3401 West Broadway  
 Hawthorne, CA  
 Attn: Library 1

North American Rockwell, Inc.  
 Rocketdyne Division  
 6633 Canoga Ave.  
 Canoga Park, CA 91304  
 Attn: Library, Dept. 596-306 1  
       G. Vorman 1

North American Rockwell, Inc.  
 Space and Information Systems Division  
 12214 Lakewood Blvd.  
 Downey, CA 90241  
 Attn: Library 1  
       J. E. Collipriest 1

Republic Aviation  
 Fairchild Hiller Corp.  
 Farmington, Long Island, NY  
 Attn: Library 1

Thiokol Chemical Corp.  
 Wasatch Division  
 P.O. Box 524  
 Brigham City, UT 84302  
 Attn: Library Section 1

TRW Systems, Inc.  
One Space Park  
Redondo Beach, CA 90278  
Attn: Technical Library, Document Acquisitions 1

United Aircraft Corp.  
Corporate Library  
400 Main St.  
East Hartford, CT 06108  
Attn: Library 1

United Aircraft Corp.  
Pratt and Whitney Division  
Florida Research and Development Center  
P.O. Box 2691  
West Palm Beach, FL 33402  
Attn: Library 1

Westinghouse Research Laboratories  
Beulah Rd., Churchill Borough  
Pittsburgh, PA 15235  
Attn: Library 1  
    W. K. Wilson 1  
    E. T. Wessel 1

Aluminum Company of America  
1200 Ring Bldg.  
Washington, DC 20036  
Attn: G. B. Bauthold 1